

Thermal Transport in Cuprates, Cobaltates, and Manganites

Inaugural Dissertation

zur

Erlangung des Doktorgrades
der mathematisch-naturwissenschaftlichen Fakultät
der Universität zu Köln

vorgelegt von

Kai Berggold

aus Rottweil

Köln, im September 2006

Berichterstatter: Prof. Dr. A. Freimuth
Prof. Dr. M. Braden

Vorsitzender
der Prüfungskommission: Prof. Dr. A. Rosch

Tag der mündlichen Prüfung: 5. Dezember 2006

Some years ago I had a conversation with a layman about flying saucers - because I am scientific I know all about flying saucers! I said "I don't think there are flying saucers." So my antagonist said, "Is it impossible that there are flying saucers? Can you prove that it's impossible?". "No", I said, "I can't prove it's impossible. It's just very unlikely". At that he said, "You are very unscientific. If you can't prove it impossible then how can you say that it's unlikely?" But that is the way that is scientific. It is scientific only to say what is more likely and what less likely, and not to be proving all the time the possible and impossible. To define what I mean, I might have said to him, "Listen, I mean that from my knowledge of the world that I see around me, I think that it is much more likely that the reports of flying saucers are the results of the known irrational characteristics of terrestrial intelligence than of the unknown rational efforts of extra-terrestrial intelligence." It is just more likely. That is all.

R.P. Feynman

Für Anja

Contents

1. Introduction	1
2. Theory	3
2.1. Thermal Conductivity	3
2.1.1. Lattice Contribution	3
2.1.2. Extended Debye Model	4
2.1.3. Electronic Contribution	5
2.1.4. Other Contributions to κ	5
2.1.5. Minimum Thermal Conductivity	6
2.1.6. Resonant Phonon Scattering	6
2.2. Thermopower	8
2.3. Figure of Merit	9
2.4. $4f$ Orbitals in the Crystal Field	10
2.4.1. Orthorhombic Perovskites	11
2.4.2. Specific Heat and Susceptibility	12
3. Experimental	15
3.1. Measurement of Transport Properties	15
3.1.1. Experimental Framework	15
3.1.2. Measurements with fixed Temperature and Field	15
3.1.3. Measurements with Temperatures and Field Sweeps	16
3.1.4. Probes	16
3.2. Thermal Conductivity	16
3.2.1. Error Sources	17
3.2.2. Thermal Conductivity Measurements in the Heliox ^3He Insert	19
3.3. Thermopower	21
3.4. Figure of Merit	22
3.5. Electrical Polarization and κ in an Electrical Field	23
3.6. Check of the Thermocouple Calibration	24
3.6.1. Magnetic Field Dependence	26
4. Thermal Conductivity in $R_2\text{CuO}_4$	27
4.1. Heat Transport by Magnetic Excitations	27
4.2. Structural and Magnetic Properties of $R_2\text{CuO}_4$	29
4.2.1. Crystal Structure	30
4.2.2. Cu Magnetism in $R_2\text{CuO}_4$ for $R = \text{Pr, Nd, Sm, Eu, and Gd}$	31
4.2.3. Structural Distortions and Magnetism for $R = \text{Gd, Eu}$	32
4.2.4. Néel Ordering of the R -Moments at low Temperatures	34
4.2.5. Spin Waves	34

4.3.	Thermal Conductivity of $R_2\text{CuO}_4$: Literature Data	35
4.3.1.	Thermal conductivity by Nd Spin Waves in Nd_2CuO_4 ?	35
4.4.	Samples	38
4.4.1.	Contributions by Paramagnetic Impurities	41
4.4.2.	Thermal Expansion	43
4.5.	Experimental Results: Zero Field	44
4.5.1.	Gd_2CuO_4 and Pr_2CuO_4	44
4.5.2.	Nd_2CuO_4 , Sm_2CuO_4 , and Eu_2CuO_4	45
4.5.3.	$\text{La}_2\text{CuO}_{4+\delta}$	45
4.5.4.	Discussion: Zero Field	46
4.5.5.	Mean Free Path and Magnetic Correlation Length	50
4.5.6.	Comparison to 1D systems	51
4.6.	Magnetic-Field Dependence of κ	52
4.6.1.	Magnetic Field Dependence at High Temperatures	59
4.6.2.	Discussion: Low-temperature Magnetic-Field Dependence of κ	60
4.7.	Conclusions	66
5.	Thermal Conductivity in Cubic Cobaltates	69
5.1.	The Spin-state Transition in $R\text{CoO}_3$ with $R = \text{La, Pr, Nd, and Eu}$	69
5.1.1.	Jahn-Teller Effect	71
5.2.	Samples	72
5.3.	Susceptibility Analysis	72
5.3.1.	CF Analysis of the Susceptibility of PrCoO_3 and NdCoO_3	73
5.3.2.	Spin-State Transition with variable Energy Gap	73
5.3.3.	Impurity Contribution in LaCoO_3	75
5.4.	Results	79
5.4.1.	LaCoO_3	79
5.4.2.	$R\text{CoO}_3$ with $R = \text{La, Pr, Nd, and Eu}$	80
5.4.3.	$R\text{CoO}_3$: Comparison to the Literature	82
5.4.4.	LaCoO_3 : Low Temperatures	82
5.4.5.	LaCoO_3 : Field Dependence of κ	85
5.4.6.	LaCoO_3 : Comparison Zero Field	85
5.4.7.	LaCoO_3 : Influence of the Spin-State Transition on κ	88
5.4.8.	$R\text{CoO}_3$ with $R=\text{Pr, Nd, and Eu}$: Low Temperatures	95
5.4.9.	PrCoO_3 and NdCoO_3 : Influence of the Spin-State Transition on κ	95
5.4.10.	Resonant Scattering in PrCoO_3	97
5.5.	Conclusions	99
6.	Thermal Transport of $\text{La}_{1-x}\text{Sr}_x\text{CoO}_3$ and $\text{La}_{0.75-x}\text{Eu}_{0.25}\text{Sr}_x\text{CoO}_3$	101
6.1.	Introduction	101
6.2.	Samples	102
6.3.	Experimental Results	103
6.4.	$\text{La}_{1-x}\text{Sr}_x\text{CoO}_3$	103
6.4.1.	Resistivity	103
6.4.2.	Thermal Conductivity	104
6.4.3.	Thermopower	106
6.4.4.	Figure of Merit	109

6.5.	$\text{La}_{0.75-x}\text{Eu}_{0.25}\text{Sr}_x\text{CoO}_3$	109
6.6.	Conclusions	113
7.	Thermal Conductivity of Orthorhombic Manganites	115
7.1.	Orthorhombic RMnO_3 Perovskites	115
7.2.	Samples	118
7.3.	Thermal Conductivity of RMnO_3 : Overview	118
7.4.	NdMnO_3	120
7.4.1.	Thermal Conductivity of NdMnO_3 : Zero Field	121
7.4.2.	Thermal Expansion of NdMnO_3 in Magnetic Fields	122
7.4.3.	Magnetostriction	124
7.4.4.	Analysis: Thermal Expansion and Susceptibility	126
7.4.5.	The Spin-Flop Transition	133
7.4.6.	Uniaxial Pressure Dependences	134
7.4.7.	Specific Heat	135
7.4.8.	Thermal Conductivity of NdMnO_3 : Scattering by Magnetic Excitations	136
7.4.9.	Thermal Conductivity of NdMnO_3 : Influence of Magnetic Fields	138
7.5.	TbMnO_3	139
7.5.1.	Thermal Conductivity	140
7.6.	Conclusions	144
8.	Summary	145
A.	Additional Measurements	149
A.1.	TbMnO_3	149
A.2.	GdMnO_3	157
A.3.	$\text{GdFe}_3(\text{BO}_3)_4$	160
A.4.	Bechgaard Salts	163
A.5.	Spin Ladders	164
A.6.	$\text{Ca}_3\text{Co}_2\text{O}_6$	165
A.7.	LaCoO_3	166
	List of Figures	169
	List of Tables	171
	Bibliography	173
	Publikationsliste	189
	Danksagung	191
	Offizielle Erklärung	193
	Zusammenfassung	195
	Abstract	197
	Lebenslauf	199

1. Introduction

Transition-metal oxides with perovskite- and related structures are well known for their unusual physical properties arising from strong correlations. La_2CuO_4 is a parent compound of high-temperature superconductors [1]. LaMnO_3 shows the colossal magnetoresistance upon doping [2]. In LaCoO_3 , the rare example of a temperature-induced spin-state transition is realized. The interpretation of the complex phenomena observed in these compounds is difficult and often controversially discussed in the literature. A useful tool is to investigate, how the properties of the systems change, if the La ion is replaced by a smaller rare-earth ion. The resulting structural changes often give additional information, since the key parameters determining the physical properties are tuned. The interpretation of the results obtained from these compounds is often complicated by the presence of the rare-earth $4f$ moments. A key for the data interpretation is therefore a reliable distinction of the effects caused by the rare-earth ions and the transition-metal complex. Moreover, interactions between these different magnetic subsystems may lead to additional phenomena. The thermal conductivity of transition-metal oxides often reflects the complex properties of these systems. Frequently, unusual temperature- and magnetic-field dependences are observed. There are various reasons for these phenomena: In the quasi one-dimensional spin-ladder systems large contributions to the heat transport are caused by magnetic excitations [3, 4]. In magnetic systems with large spin-phonon coupling an unusual suppression of the thermal conductivity is observed [5]. The thermal conductivity is a powerful tool to investigate these phenomena arising from phononic, electronic, and spin excitations and their interactions

The unusual behavior of the thermal conductivity of La_2CuO_4 was discovered already more than one decade ago [6]. In this publication the possibility of a magnetic contribution to the heat transport was discussed. However, the mechanism of the heat transport in La_2CuO_4 is still under debate [7–9]. One aim of the present work is to clarify this issue. Therefore, a systematic study of the thermal conductivity of the related rare-earth cuprates $R_2\text{CuO}_4$ with $R = \text{La, Pr, Nd, Sm, Eu, and Gd}$ will be presented. It will be shown that a magnetic contribution to the heat transport is a very fundamental property of the layered cuprates. The results will be compared to one-dimensional systems, and the principal differences of the magnetic contribution to the heat transport between 1D and 2D will be discussed. Moreover, the low-temperature behavior under application of large magnetic fields will be addressed. It has been proposed in the literature that at low temperatures an additional magnetic contribution of Nd spin waves to the heat conductivity of Nd_2CuO_4 is induced by the application of magnetic fields [10, 11]. The magnetic-field dependences of the thermal conductivity for the $R_2\text{CuO}_4$ compounds will be presented. The analysis of the data gives new insight, since another mechanism causing the field-dependences is preferred.

The spin-state transition in LaCoO_3 is a long-standing issue in solid-state physics since the 1950's. The question, whether a high-spin state or an intermediate spin-state is thermally populated, is discussed controversially up to now. Whereas initially a high-spin state was proposed, an intermediate-spin state scenario became popular during the last decade [12].

However, very recent results indicate that a high-spin scenario taking into account large spin-orbit coupling effects is a more appropriate description [13]. The thermal conductivity of LaCoO_3 has shown to be quite sensitive to the spin-state transition [9]. However, a quantitative analysis of this phenomenon lacks so far. This work presents a systematic study of the thermal conductivity on several LaCoO_3 single crystals, to obtain a clear picture of the intrinsic features. A detailed quantitative treatment of the influence of the spin-state transition to the thermal conductivity is carried out. A consistent picture will be obtained, including the related compounds where La is replaced by the rare-earth ions Pr, Nd, or Eu. In addition, the reason for the observed complex field-dependent low-temperature behavior of the thermal conductivity will be clarified.

Upon charge-carrier doping the physical properties of LaCoO_3 substantially change. We present a systematic study of the thermal conductivity κ and the thermopower S of single crystals of $\text{La}_{1-x}\text{Sr}_x\text{CoO}_3$ with $0 \leq x \leq 0.3$. For all Sr concentrations $\text{La}_{1-x}\text{Sr}_x\text{CoO}_3$ has rather low κ values, whereas S strongly changes as a function of x . We discuss the influence of the temperature- and the doping-induced spin-state transitions of the Co^{3+} ions on both, S and κ . From S , κ , and the electrical resistivity ρ we derive the thermoelectric figure of merit $Z = S^2 / \kappa \rho$. A high figure of merit is a pre-condition for the applicability in thermoelectric devices. Moreover, the influence of an additional replacement of La by Eu is investigated.

The orthorhombic manganates RMnO_3 with $R = \text{La} \dots \text{Ho}$ have attracted much interest, since in GdMnO_3 , TbMnO_3 , and DyMnO_3 ferroelectric ordering phenomena embedded in a magnetically ordered phase are observed [14, 15]. This phenomenon is often referred to as multiferroism. Since ferroelectricity is a structural phenomenon and therefore strongly coupled to the lattice, thermal conductivity is expected to be a useful probe to obtain new insights in the multiferroic properties of these compounds. This work presents thermal conductivity measurements of NdMnO_3 , GdMnO_3 , and TbMnO_3 . The experimental focus is a systematic investigation of the magnetic-field dependence of the heat transport by applying the field along the different crystallographic axes. In combination with thermal expansion and magnetization measurements it will be shown that resonant scattering by the $4f$ orbitals has, however, a much larger influence on the thermal conductivity, than the magnetic and electric ordering transitions at low temperatures.

This thesis is organized in the following way: In chapter 2, a brief introduction to the theoretical framework is given. Chapter 3 gives a description of the used setup and experimental methods. In chapter 4 a systematic study of the thermal conductivity of the rare-earth cuprates will be presented. Chapter 5 is devoted to the thermal conductivity of rare-earth cobaltates with spin-state transitions. Chapter 6 deals with the thermoelectric properties of Sr doped Cobaltates. The topic of chapter 7 is the heat transport in perovskite-type manganates. In the appendix the results of additional measurements are documented.

2. Theory

In this chapter a brief introduction into the thermal conductivity and the thermopower of solids will be given. The focus will be to give an overview about conventional mechanisms established in the literature, and to quote some important basic relations. For a more detailed introduction see Refs. [16–20]. Finally, we will present a short introduction into the treatment of the $4f$ orbitals of the rare-earth ions in low-symmetry crystals.

2.1. Thermal Conductivity

In a crystal, the thermal conductivity is determined by heat carrying quasiparticles. The thermal conductivity κ can be generally expressed by the equation [16]:

$$\kappa = \frac{1}{d} c v \ell \quad (2.1)$$

where d denotes the dimensionality, c the specific heat, v the group velocity, and ℓ the mean free path of the respective heat carrying excitations. In most cases two kinds of excitations are responsible for the heat transport: phonons and electrons. The theoretical description is usually based on the Debye model in the first case, and on the electronic gas theory for the latter case.

2.1.1. Lattice Contribution

The heat carrying excitations in an insulating crystal lattice are phonons. For $T \ll \Theta_D$, where Θ_D denotes the Debye temperature, the specific heat can be calculated by the Debye formula [16]

$$c_V = \frac{3k_B}{2\pi^2 v^3} \left(\frac{k_B}{\hbar} \right)^3 T^3 \int_0^{\Theta_D/T} \frac{x^4 e^x}{(e^x - 1)^2} dx. \quad (2.2)$$

Here, v is the sound velocity, which is identical to the group velocity in Eq. 2.1. The main problem in the calculation of the lattice contribution to κ is the estimation of the mean free path ℓ . Three kind of scattering processes usually determine ℓ , scattering of phonons by phonons, scattering by lattice imperfections, and scattering at the crystal surface.

At very low temperatures only the latter process is relevant. Then ℓ is given by a constant which is determined by the sample dimension L_0 . In this case¹, it follows from Eqs. 2.1 and 2.2:

$$\kappa = \frac{2}{15} \pi^2 k_B \left(\frac{k_B T}{\hbar} \right)^3 \frac{L_0}{v^2}. \quad (2.3)$$

According to Ref. [17], here the averaged sound velocity can be calculated via

$$\bar{v} = v_l \left(2 \left(\frac{v_l}{v_t} \right)^2 + 1 \right) / \left(2 \left(\frac{v_l}{v_t} \right)^3 + 1 \right) \quad (2.4)$$

¹At low temperatures the integrand gets small for large x . Therefore one sets $\Theta_D/T \rightarrow \infty$ and uses $\int_0^\infty \frac{x^4 e^x}{(e^x - 1)^2} dx = \frac{4\pi^4}{15}$.

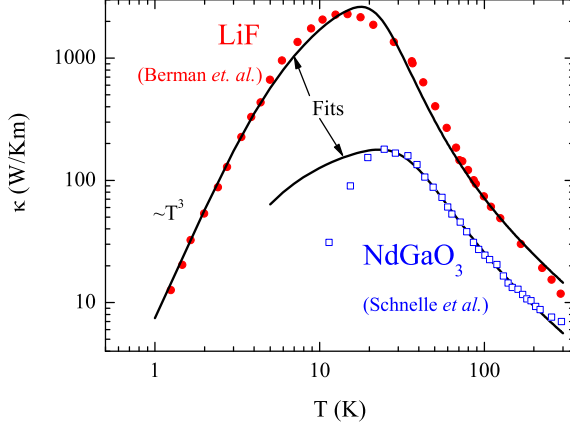


Figure 2.1.: Thermal conductivity of LiF (Berman *et al.* [21]) and NdGaO₃ (Schnelle *et al.* [22]). Lines are fits by Eq. 2.5. The parameters were $L = 7(1)$ mm, $\Theta_D = 700(680)$ K, $v = 6000(4800)$ m/s, $P = 0.07(3.3) 10^{-43}$ s³, $U = 2.2(6.8) 10^{-18}$ s, and $u = 6(5.6)$ for LiF (NdGaO₃). [22, 23].

from the measured longitudinal and transverse sound velocities v_l and v_t , respectively. In this limit the thermal conductivity follows the T^3 dependence of the specific heat. At high temperatures ℓ is mainly determined by Umklapp processes, which result from phonon-phonon interactions. Since at high temperatures the number of excited phonons is proportional to T , $\ell \sim 1/T$ follows. The specific heat becomes temperature independent for $T \rightarrow \Theta_D$. Thus, $\kappa \approx 1/T$ follows at high temperatures.

2.1.2. Extended Debye Model

To describe the thermal conductivity more quantitatively, Eqs. 2.1 and 2.2 can be written as

$$\kappa_{ph} = \frac{k_B}{2\pi^2 v_s} \left(\frac{k_B}{\hbar} \right)^3 T^3 \int_0^{\Theta_D/T} \frac{x^4 e^x \tau(\omega, T)}{(e^x - 1)^2} dx \quad (2.5)$$

where $\tau(\omega, T) = v/\ell$ is a temperature and frequency dependent scattering rate. Under the assumption that the different scattering processes act independently, one can write τ^{-1} as a sum of the different scattering rates:

$$\tau^{-1} = \tau_{bd}^{-1} + \tau_{pt}^{-1} + \tau_{um}^{-1} + \tau_D^{-1} + \dots \quad (2.6)$$

The used scattering rates have the following meanings:

- $\tau_{bd}^{-1} = v/L$: This is the boundary scattering term, which describes the reflection of phonons by the crystal surface.
- $\tau_{pt}^{-1} = P\omega^4$: This term describes point defect scattering, and is the most effective term in the temperature range, where the phononic maximum of κ occurs. At lower temperatures, phonons with larger wave length and therefore small ω are the dominant heat carriers, and τ_{pt}^{-1} is less effective. The physical picture is, that the long wave length phonons do not "see" the small point defects. At high temperatures τ_{pt}^{-1} is less important, because Umklapp scattering is much more effective. In the data analysis we use P as an adjustable parameter describing the scattering strength.
- $\tau_{um}^{-1} = UT \exp(\Theta_D/uT)$. This term describes Umklapp scattering. The factor U gives the scattering strength, the parameter u determines at which temperature Umklapp scattering sets in.

- In some cases other scattering rates may be introduced, as e.g. scattering on planar defects $\tau_D^{-1} = D\omega^2$, which is useful for systems with layered structures (e.g. the cuprates).

For a detailed survey of different scattering rates see e.g. Ref. [24].

To illustrate the data analysis by Eqs. 2.5 and 2.6, Fig. 2.1 shows literature data for LiF and, closer to the compounds investigated in this thesis, NdGaO₃ [21, 22]. The Debye temperatures and sound velocities were taken from the literature [22, 23], and the other parameters were adjusted to the data. For LiF the general temperature dependence is modelled very well, particularly the low-temperature T^3 behavior. Around the maximum larger deviations between the fit and the data are observed, which come from the oversimplification of the used scattering terms. In NdGaO₃ the temperature dependence above the maximum is modeled well, but the fit is much too high for lower temperatures. Here, additional scattering mechanisms, like e.g. scattering on spin waves, paramagnetic impurities, etc. play also a role, which are not included in Eq. 2.6.

2.1.3. Electronic Contribution

Electrons carry a specific heat which is proportional to $k_B T$. Eq. 2.1 is valid for electronic heat transport, too. Here, the Fermi velocity v_f is used for the velocity of the electrons, which yields [16]

$$\kappa_{el} = \frac{\pi^2 n k_B^2 T \ell}{3 m v_f}. \quad (2.7)$$

Here, n is the electron density and m the electron mass. Because the electron carries charge and heat simultaneously, usually the Wiedemann-Franz law holds, which connects electrical and thermal conductivity:

$$\kappa = L \sigma T, \quad (2.8)$$

where L denotes the Lorenz number. The free electron gas theory yields the value $L_0 = 2.45 \cdot 10^{-8} \text{ W}/\Omega \text{ K}^2$. The Wiedemann-Franz law is valid, if only elastic scattering processes occur, which is usually the case for low temperatures (only boundary scattering) and for high temperatures. For intermediate temperatures charge carriers are mainly scattered by phonons which lowers the value of L .

In good metals, only the electronic contribution to κ is relevant. The reason is that the absolute values of κ_{el} are large, and that phonons are strongly scattered by the electrons. For bad metals electronic and phononic contributions can be of the same size. For bad insulators often only the phononic contribution is relevant at low temperatures, but through the thermal activation of electrons the electronic contribution becomes more and more important for high temperatures.

2.1.4. Other Contributions to κ

In principle, every quasiparticle carrying specific heat and a non-vanishing group velocity can contribute to the heat transport. Often, the latter condition is the limiting factor, as it is e.g. the case for optical phonons which have only a small dispersion. Furthermore, the additional quasiparticles can scatter phonons, or are scattered by phonons, which may even overcompensate the additional contribution to the heat transport.

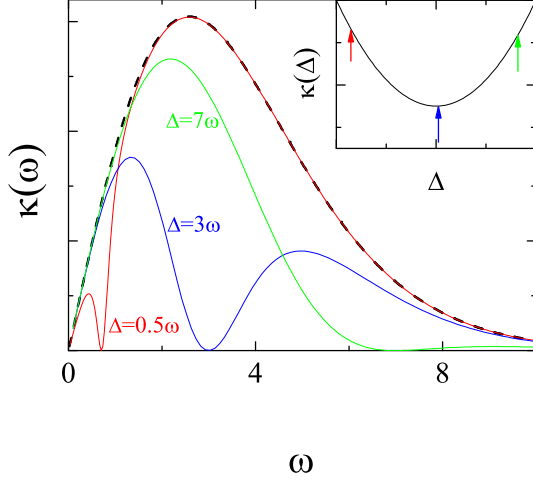


Figure 2.2.: Frequency dependent thermal conductivity without resonant scattering or $\Delta = 0$ (dashed line) and for resonant scattering with different level spacings Δ (solid lines). Inset: Sketch of the resulting thermal conductivity $\kappa(\Delta)$.

2.1.5. Minimum Thermal Conductivity

In the Debye model discussed above, ℓ is not limited to a lowest value, and the $1/T$ behavior of κ continues up to highest temperatures. In reality, however, the interatomic distances give a lower limit to ℓ . It follows, that κ will not drop below a minimum value κ_{\min} . In this limit, the concept of well defined phonons is no longer a good approximation, and therefore other treatments of the minimum thermal conductivity were carried out in the literature. In Ref. [25] the authors discuss a model originally based on Einstein, which uses coupled local oscillators to describe κ . The physical picture is that the energy makes "random walks", with energy exchange between nearest and next-nearest neighbors. This treatment results in

$$\kappa_{\min} = \left(\frac{\pi}{6}\right)^{1/3} k_B n^{2/3} \sum_i v_i \left(\frac{T}{\Theta_i}\right)^2 \int_0^{\Theta_D/T} \frac{x^3 e^x}{(e^x - 1)^2} dx, \quad (2.9)$$

where $n = N/V$ denotes the atomic density and i sums up the different polarizations. The Debye temperatures Θ_i for the different polarization directions i are given by

$$\Theta_i = (\hbar v_i / k_B) (6\pi^2 n)^{1/3}. \quad (2.10)$$

The comparison of the calculated values κ_{\min} to the measured κ at high temperatures yields an underestimation of κ_{\min} up to a factor of 2 [25]. The minimum thermal conductivity can be taken into account in Eq. 2.5 by introducing a minimum mean free path ℓ_{\min} , and replacing $\tau(\omega, T)$ by $\max\{\tau_{\Sigma}(\omega, T), \ell_{\min}/v_s\}$.

2.1.6. Resonant Phonon Scattering

Resonant scattering processes can further suppress the phononic heat transport, in addition to the already discussed mechanisms. For resonant processes a two (or multi) -level system is necessary. The idea is that a phonon with an energy exactly equal to the level splitting Δ is absorbed by stimulating a transition, and later on it is remitted. This process is also possible for the excited state, then a de-excitation process absorbs the incoming phonon. Because the direction of the re-emitted phonon is not correlated to the absorbed phonon, both processes suppress the heat transport. A quantum mechanical treatment of this mechanism [27] gives

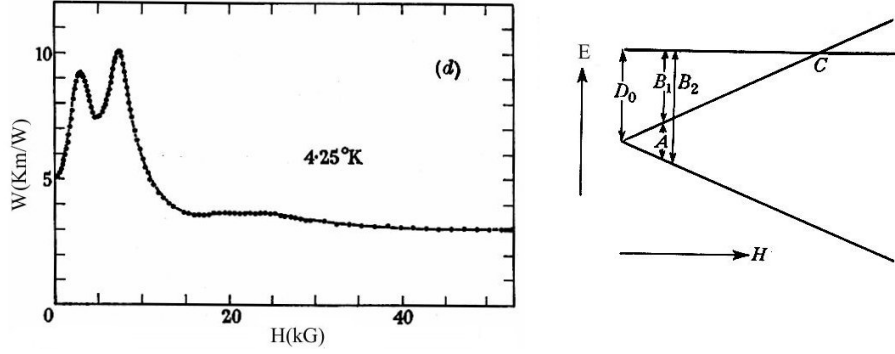


Figure 2.3.: Left panel: Thermal resistance $W = 1/\kappa$ for Holmium ethylsulfate at Helium temperature. The data are taken from Ref. [26]. Right panel: Level scheme of the paramagnetic impurities in Holmium ethylsulfate. The upper level is a singlet and the lower level a doublet which splits in a magnetic field due to the Zeeman effect.

the scattering rate of such a resonant scattering process:

$$\tau_{\text{res}}^{-1} = R \frac{4\omega^4 \Delta^4}{(\Delta^2 - \omega^2)^2} \cdot (N_0 + N_1). \quad (2.11)$$

Here, R gives the overall coupling strength, Δ the energy splitting and N_0 and N_1 the population factors of the resonating levels. For a two-level system it directly follows $N_0 + N_1 = 1$, which means that τ_{res}^{-1} becomes temperature independent. The effect of Eq. 2.11 is illustrated in Fig. 2.2. The ω dependent thermal conductivity is 0 for $\omega = 0$ and for $\omega \rightarrow \infty$, and shows a maximum inbetween. The resonance term is effective in a narrow frequency range. Fig 2.2 illustrates the influence of a resonant process for the case of a two level system, with an increasing gap Δ . For $\Delta = 0$ no resonance occurs, and with increasing Δ the resonance suppresses $\kappa(\omega)$, leading to a suppression of $\kappa(\Delta)$ (see inset). If Δ reaches the maximum of $\kappa(\omega)$ the suppression is most effective again, and for further increasing Δ the resonance becomes less effective, and $\kappa(\Delta)$ increases again. There are various possible origins of the resonance processes. In Refs. [27, 28] a double-peak structure of κ in $\text{SrCu}_2(\text{BO}_3)_2$ could be successfully explained by resonant scattering of phonons by magnetic excitations. Another frequent source of resonances is the presence of paramagnetic impurity levels [26, 29, 30]. A prominent example in this context is holmium ethylsulphate [26]. Fig. 2.3 shows the thermal resistance ($1/\kappa$) of holmium ethylsulphate at 4.25 K in magnetic fields up to 5.3 T. A strong nonmonotonic field dependence is observed. The resonant process is caused by phonons inducing transitions of the paramagnetic ions. The level scheme of holmium ethylsulphate contains a singlet and a doublet, the latter splits in a magnetic field by the Zeeman effect. Because of the four different transitions, which all have a field-dependent energy gap, the complex field dependence of κ arises. Note, that Eq. 2.11 describes only the simplest case of a so-called direct resonance process. Processes of higher order, where e.g. two phonons are involved, an inelastic processes, where incoming and outgoing phonons have different energies, are also possible [31].

2.2. Thermopower

The thermopower S is defined by

$$S = \frac{\vec{\mathcal{E}}}{\nabla T} \quad (2.12)$$

and describes the electrical field² caused by a heat gradient, with the additional condition that no electrical current is allowed to flow. This effect can be reverted. The generation of a heat gradient by an electrical current is called Peltier effect. The Peltier constant Π and the thermopower S are connected via the Onsager relation

$$\Pi = ST. \quad (2.13)$$

A simple picture of the thermopower in metals can be given as follows: In principle, electrons and holes contribute to charge transport. First, we regard only electrons. If a temperature gradient is applied along the sample, the electrons are faster in the hot side of the sample. Therefore, electrons coming from the hot side of the sample have a larger velocity, which causes an electron diffusion from the hot side to the cold side. Since no current flows, a voltage is generated which leads to a steady state.

If electrons and holes are present, the thermovoltage would vanish, if both types of charge carriers move in the same way. This is not the case in reality because of the different mobilities of the quasiparticles. For metals an estimation of the thermopower can be given by

$$S_D = -\frac{\pi^2 k_B^2 T}{3q} \left(\frac{\partial(\ln \sigma(E))}{\partial E} \right)_{E=E_F} \quad (2.14)$$

where $\sigma(E)$ is the electrical conductivity [32]. The thermopower vanishes for $T \rightarrow 0$, which follows from the vanishing of the entropy according to the third law of thermodynamics. A complication occurs, since the mean free path is generally energy dependent, which causes a different scattering for the electrons coming from the hot end of the sample compared to the electrons with the opposite direction. The energy dependence of the mean free path is not known well in general, and can cause a complex behavior of S . At low temperatures a further effect becomes important: the phonon drag. The considerations above assume random scattering centers for the electrons. In fact, the temperature gradient over the sample leads to a phonon flow from the hot end to the cold end of the sample, because in the hot end more phonons are excited. Although the phonons itself do not contribute to the thermopower, they can "drag" charge carriers by the phonon-electron interaction, and enhance the thermopower in this way. At high temperatures this effect is negligible, because phonon-phonon interaction dominates.

The measurement of the thermopower is not straightforward, since the usual setup (see Chp. 3) always measures the sum of the thermopower of the sample and the wires used to measure the voltage:

$$S_{\text{meas}} = S_{\text{Sample}} - S_{\text{wire}} \quad (2.15)$$

Note, that the thermopower of the wires has a negative sign (see e.g. Ref. [33]. At low temperatures one can avoid this problem by the use of superconducting wires, which have a vanishing thermopower. It is, however, possible to measure the absolute S directly by the use

² $\vec{\mathcal{E}} = \vec{E} + (1/e)\vec{\nabla}\mu$ is the sum of the electrostatic field \vec{E} and the gradient of the chemical potential μ [32].

of the Thompson effect [18]. Herefore, the heating power of a wire is measured, with a heat current and a electrical current applied at the same time. The heating power is given by [32]:

$$P = \frac{dq}{dt} \rho j^2 + \frac{d\kappa}{dT} (\nabla T)^2 - T \frac{dS}{dT} (\nabla T) \cdot j \quad (2.16)$$

The Thompson heating of the wire can be distinguished from Joule heating, since it changes sign, if the sign of the electrical current is changed. Since only the derivative of S is determined, one has to integrate dS/dT and to measure one absolute value to obtain the integration constant. This can be done at low temperatures by the use of superconducting wires. This method is complex, and has to be performed very accurately, since the integration of dS/dT is very sensitive to measurement uncertainties. Therefore one usually uses the literature data for the thermopower of Pb estimated by this method in the literature, and calibrates the used wires against Pb [18]. For a detailed introduction to the thermopower I refer to Refs. [18–20]

2.3. Figure of Merit

The thermoelectric figure of merit ZT gives a measure for the efficiency of a material for thermoelectric cooling. A simple derivation can be given as follows: A thermoelectric cooler transports heat from a cold to a hot reservoir. The total heat removal rate is given by [19]

$$q_c = ST_c I - \frac{1}{2} I^2 R - K \Delta T, \quad (2.17)$$

where S is the thermopower, T_c the temperature of the cold reservoir, I the current, $R = \rho l/A$ the resistivity, $K = \kappa A/l$ the thermal conductance, and ΔT the temperature difference between the two reservoirs. The first term of Eq. 2.17 is the heat flow caused by the Peltier effect. The second term is the Joule heating, which has a negative sign, since it warms the cold reservoir. The factor $1/2$ comes from the fact that one half of the heat flows to the warm reservoir. The third term describes the zero-current heat transport, which is determined by the thermal conductivity, and also counteracts the Peltier effect. From Eq. 2.17 it is directly clear that S has to be maximized, and κ and ρ to be minimized to obtain a high efficiency. Furthermore, an optimal current can be obtained by resolving Eq. 2.17 with respect to $\Delta T(I)$ and calculating the maximum value

$$\Delta T(I)_{\max} = \frac{\frac{(ST)^2}{2R} - q_c}{K} \quad (2.18)$$

with the optimum current $I = ST/R$. Finally one obtains from Eq. 2.18 the relation

$$q_c^{\max} \sim \frac{S^2}{KR} \quad (2.19)$$

which motivates the definition of the dimensionless figure merit

$$ZT = \frac{S^2 T}{\kappa \rho}. \quad (2.20)$$

For a more detailed introduction into the efficiency of thermoelectric devices, see Ref. [19].

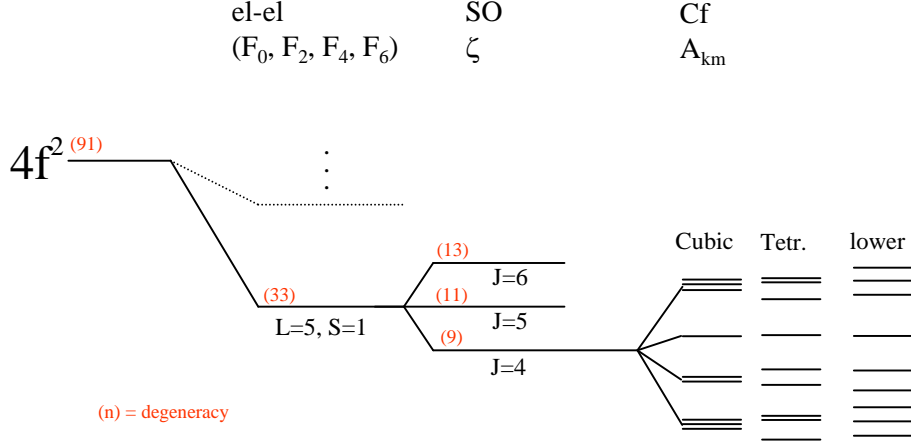


Figure 2.4.: Schematic level splittings of a $4f^2$ system due to electron-electron repulsion, spin-orbit (SO) coupling and crystal field (CF). Note, that the order of the levels of the split $J = 4$ multiplet in the crystal field is exemplary.

2.4. $4f$ Orbitals in the Crystal Field

The dimension D of the Hamiltonian of a f^n level system is given by $\binom{14}{14-n}$, which can reach values up to $D = 4004$ for $n = 7$. This means also a degeneracy D of the energy levels without any interaction. In a crystal (without magnetic field) the Hamiltonian consists of three parts,

$$\mathcal{H} = \mathcal{H}_{el-el} + H_{\zeta} + \mathcal{H}_{CF}. \quad (2.21)$$

The first two terms are the same as for a free ion and describe the electron-electron interaction and the spin-orbit (SO) coupling. The third term gives the influence of the crystal field. The el-el interaction is usually described by Slater integrals $A^{i=0,2,4,6}$, and the SO coupling by the energy ζ . In most cases the relation $F^i (> 5\text{eV}) \gg \zeta (\approx 0.1\text{eV}) \gg E_{CF} (\approx \text{meV})$ holds, which allows to take into account only a small sub-space of the original Hamiltonian. This is illustrated for a $4f^2$ system in Fig. 2.4. Without interaction, one starts with 91 degenerate levels. The dominant energy scale of the el-el interaction gives a $S = 1, L = 5$ state according to Hunds rules, with $11 \times 3 = 33$ degenerate energy levels. If SO coupling is turned on, the levels further split into three levels with $J = 4, 5, 6$. The level spacing between the $J = 4$ and $J = 5$ state³ is $\approx 0.3\text{eV} \approx 3000\text{K}$, and usually only the lowest 3H_4 state has to be taken into account. However, in many systems (e.g. Sm^{3+}) the higher multiplets are important, too.

In a crystal, the ligand-field further splits the 3H_4 multiplet. The energy scales are hereby much smaller than in the d systems, since the $4f$ states are highly screened. The crystal field Hamiltonian can be written as [34]:

$$\mathcal{H}_{CF} = \sum_m \sum_{k=-m}^m A_m^k C_m^k, \quad k, m = 0, 2, 4, 6 \quad (2.22)$$

with the crystal field parameters A_m^k and the tensor operators C_m^k . The parameters A_m^k can be complex for $m \neq 0$, further the relation $A_{-m}^k = (-1^m)(A_m^k)^*$ generally holds. For higher

³Calculated for a Pr^{3+} ion.

symmetries most of the parameters A_m^k vanish, or depend on each other. For the cubic O_h symmetry 2 independent energies remain. In the tetragonal D_{4h} symmetry one has to deal with 5 and for the orthorhombic C_s symmetry with 15 independent parameters. The splitting of the ground state multiplet is different for systems with odd and with even $2J$. If $2J$ is odd, the Kramer's degeneracy tells, that the J multiplets splits into quartets and doublets. In the lowest symmetry only doublets are realized. If $2J$ is even, the multiplet splits into singlets, doublets and triplets. Here, only singlets are realized for the lowest symmetry. For a given $4f^i$ system and a given symmetry one can determine the principle splitting of the ground state multiplet. Tab. 2.2 shows these results for the rare earth ions R^{3+} [35]. Note, that these results reflect only the symmetry of the system, and give no information about the order of the different levels.

The data analysis was performed with the Mathematica⁴ package "CrystalFieldTheory" (CFT) developed by M. Haverkort [36]. This package solves the Hamiltonian Eq. 2.21 by exact diagonalization of the full multiplet. The used Slater integrals F^i and the SO coupling constant ζ obtained from Hartree-Fock calculations by M. Haverkort are listed in Tab. 2.3.

The crystal field is usually investigated by neutron scattering. These measurements yield the level scheme, since the transitions between different CF levels are measured. To get the parameters A_m^k , a CF model has to be used and the A_m^k values are usually fitted to obtain the best description of the energy level scheme. Here, the analysis is often simplified by only taking the ground state multiplet into account. In this case, so-called Stevens operators are frequently used, which yield a different parameterization of the CF Hamiltonian. The conversion of the parameters of the Stevens formalism to the A_m^k parameters is complex in lower symmetry systems.

In this work, tetragonal and orthorhombic systems with R^{3+} ions were investigated. The crystal field was studied in detail in the literature for the tetragonal cuprates, which will be discussed in more detail in Chp. 4.

2.4.1. Orthorhombic Perovskites

In the orthorhombic perovskites one has to deal with 15 independent CF parameters, but usually only a few energy levels are present for the fitting of the A_m^k values. Therefore, usually additional assumptions are made in the data analysis, which restrict the number of free parameters (see e.g. Refs. [37, 38]). To my knowledge no systematic crystal field investigations of orthorhombic cobaltates and manganates are available⁵. However, such investigations have been made for related compounds RMO_3 , with $R = \text{Pr, Nd, and Eu}$; and $M = \text{Al, Ga, Fe, and Ni}$. The structural distortions are similar in these compounds, which leads to similar CF effects for the same R and different M . We will explore this for the comparison of the available data of CF splitting energies for various PrMO_3 and NdMO_3 compounds.

In PrMO_3 , the 3H_4 multiplet of the Pr^{3+} ion splits into 9 singlets (see Tab. 2.3). The measured crystal-field splitting is indeed very similar for different orthorhombic PrMO_3 compounds. In Tab. 2.1 the energy levels for various PrMO_3 compounds measured by neutron scattering experiments are listed. Note, that because of the different sizes of the scattering cross section, only 5 or 6 energies can be resolved. According to Tab. 2.1, the energies E_2 to E_5 are almost identical for $M = \text{Fe, Ga and Ni}$. Larger differences mainly occur for the first

⁴Mathematica 5.2, Wolfram Research.

⁵In Ref. [39] the authors observe some CF excitations in their investigation of the spin-wave spectrum of TbMnO_3 and PrMnO_3 .

excited level, the energy E_1 ranges from 23 K to 74 K. To resolve this issue, the M -O- M bond angle is also listed in Tab. 2.1. This parameter is useful to characterize the distortion (see also Chp. 7). From the comparison with E_1 a direct correlation can be made, E_1 increases with increasing bond angle M -O- M . This systematic also holds for PrCoO_3 and PrMnO_3 , where the energies of the first (second) excited level is known from other measurements, see Tab. 2.1.

In NdMO_3 , the $^4\text{H}_{9/2}$ multiplet of Nd^{3+} splits into 5 doublets. Here, all transitions are observed, and the energy splitting is very similar for the different compounds, too. The smaller value of E_1 in NdFeO_3 may indicate a similar dependence on the M -O- M angle as in PrMO_3 , but this is not clear from the available data. No direct information of the level schemes of NdCoO_3 and NdMnO_3 is available.

2.4.2. Specific Heat and Susceptibility

From the eigensystem calculated from Eq. 2.21 the specific heat and the magnetic susceptibility of the $4f^i$ system is calculated straightforwardly:

$$C_{fi}(T) = \frac{\partial}{\partial E} \frac{\sum_{n=1}^{D_i} E_n \exp(-\frac{E_n}{k_B T})}{Z} \quad (2.23)$$

with

$$Z = \sum_{n=1}^{D_i} \exp(-\frac{E_n}{k_B T}). \quad (2.24)$$

and

$$\chi(T, H) = \frac{M(T, H)}{H} = \frac{\sum_{n=1}^{D_i} M_n(H) \exp(-\frac{E_n}{k_B T})}{ZH} \quad (2.25)$$

with

$$M_n(H) = \langle n | (L_z + 2S_z) | n \rangle. \quad (2.26)$$

Note, that usually the specific heat is much less sensitive to the CF, since here only the energies are relevant.

	R_M (Å)	M -O- M (°)	E_1 (K)	E_2 (K)	E_3 (K)	E_4 (K)	E_5 (K)	E_6 (K)	Ref.
PrFeO ₃	0.645	152 [40]	23	171	270	418	673		[41]
PrGaO ₃	0.62	154 [42]	55	171	232	429	754		[41]
PrGaO ₃			59	186	249	441	777	908	[38]
PrNiO ₃	0.56	159 [43]	74	174	235	440	696		[44]
PrCoO ₃	0.545	159 [45]	70 *						
PrMnO ₃	0.645	150	19 †						
PrMnO ₃			20 ‡	185 ‡					
NdGaO ₃	0.62	153 [46]	132	261	611	789			[47]
NdGaO ₃		153	132	262	606	788			[48]
NdFeO ₃	0.645	151 [49]	120	263	526	705			[37, 50]
NdNiO ₃	0.56	156 [51]	129	220	765	835			[44]
NdCoO ₃	0.545	156 [52]							
NdMnO ₃	0.645	150 [53]							

Table 2.1.: Ionic radii M [54], M -O- M bond angles, and crystal field energies of PrMO_3 and NdMO_3 . *) Value estimated by thermal expansion, see Sec. 5.4.10. †) Value estimated by specific heat [55]. ‡) Value estimated by neutron scattering from Ref. [39].

R^{3+}	S	L	J	GS	D	d_{free}	d_{cubic}				d_{tet}		d_{low}	
							sg	db	tr	qt	sg	db	sg	db
Ce	1/2	3	5/2	$^2F_{5/2}$	14	6		1		1		3		3
Pr	1	5	4	3H_4	91	9	1	1	2		5	2	9	
Nd	3/2	6	9/2	$^4I_{9/2}$	364	10		1		2		5		5
Pm	2	6	4	5I_4	1001	9	1	1	2		5	2	9	
Sm	5/2	5	5/2	$^6H_{5/2}$	2002	6		1		1		3		3
Eu	3	3	0	7F_0	3003	1	1				1		1	
Gd	7/2	0	7/2	$^8S_{7/2}$	3432	8		2		1		4		4
Tb	3	3	6	7F_6	3003	13	2	1	3		7	3	13	
Dy	5/2	5	15/2	$^6H_{15/2}$	2002	16		2		3		8		8
Ho	2	6	8	5I_8	1001	17	1	2	4		9	4	17	
Er	3/2	6	15/2	$^4I_{15/2}$	364	16		2		3		8		8
Tm	1	5	6	3H_6	91	13	2	1	3		7	3	13	
Yb	1/2	3	7/2	$^2F_{7/2}$	14	8		2		1		4		4

Table 2.2.: S , L , J , ground state multiplet (GS), dimensionality of the full multiplet D , degeneracies of the ground multiplet for the free ion, cubic, tetragonal, and lower symmetry (sg: singlet, db: doublet, tr: triplet, qt: quartet) [35].

Atom#	Atom R^{3+}	Conf	r^2 (\AA^2)	r^4 (\AA^4)	r^6 (\AA^6)	ζ (eV)	F^0 (eV)	F^2 (eV)	F^4 (eV)	F^6 (eV)
58	Ce	$4f^1$	0.367	0.312	1.208	0.087	0.000	0.000	0.000	0.000
59	Pr	$4f^2$	0.337	0.265	1.230	0.102	25.711	12.221	7.666	5.515
60	Nd	$4f^3$	0.312	0.229	1.252	0.119	26.739	12.719	7.981	5.742
61	<i>Pm</i>	$4f^4$	0.291	0.200	1.274	0.136	27.719	13.191	8.278	5.956
62	Sm	$4f^5$	0.273	0.177	1.296	0.155	28.665	13.643	8.562	6.161
63	Eu	$4f^6$	0.257	0.158	1.318	0.175	29.581	14.079	8.836	6.357
64	Gd	$4f^7$	0.243	0.143	1.339	0.197	30.474	14.501	9.100	6.548
65	Tb	$4f^8$	0.230	0.129	1.361	0.221	31.344	14.911	9.357	6.732
66	Dy	$4f^9$	0.219	0.118	1.383	0.246	32.200	15.312	9.608	6.912
67	Ho	$4f^{10}$	0.208	0.108	1.405	0.273	33.040	15.704	9.853	7.088
68	Er	$4f^{11}$	0.199	0.099	1.427	0.302	33.865	16.089	10.093	7.260
69	Tm	$4f^{12}$	0.190	0.092	1.449	0.333	34.679	16.467	10.328	7.429
70	Yb	$4f^{13}$	0.182	0.085	1.471	0.366	35.483	16.839	10.560	7.596

Table 2.3.: Radial distributions $r^{2,4,6}$, SO coupling constants ζ , and Slater integrals F^i for the rare earth ions R^{3+} , calculated by a Hartree-Fock approximation [56].

3. Experimental

In this section the used experimental methods will be introduced. The general setup will be discussed only briefly, since it is the same as used in Ref. [57], where a detailed description is given. Extensions of the setup, as the use of a new sample holder for measurements of κ down to 250 mK in a ^3He system, will be described in more detail. Furthermore, test measurements to check the used thermocouple calibration will be presented.

3.1. Measurement of Transport Properties

In this thesis measurements of thermal conductivity, thermopower, and resistivity were performed. Generally, transport measurements are done providing an external perturbation to the sample and measuring the response of the sample. In our case, the external perturbation is either an electrical current, or a heat supply. The response is either an electrical voltage or a heat gradient over the sample. Here, only longitudinal effects are regarded, so the response of the samples is measured in the same spacial direction as the perturbation.

3.1.1. Experimental Framework

The main purpose of the experimental setup is to provide the desired control parameters, as pressure, temperature and magnetic field. Here, pressure is no adjustable control parameter¹.

The temperature / the magnetic field is usually either kept fixed, or changed with a constant rate. The control of the magnetic field is in principle easy, since it is based on the control of electrical currents, and so static magnetic fields, or magnetic field sweeps are possible simply by giving the magnet power supply the right commands (within the limits given by the used magnet and magnet control system). No further measurement of the field is necessary. In contrast, the temperature needs a control loop, usually realized by a temperature controller using a PID algorithm. This requires the measurement of the temperature, and for measurements with fixed temperature it has to be checked, if the temperature is stable enough. For temperature sweeps, a stabilization is only needed for the starting value, a constant rate is then achieved by the controller.

One can group the measurements in those where the data points are taken with fixed temperature and magnetic field, and those where one of these quantities is continuously changed during the measurement.

3.1.2. Measurements with fixed Temperature and Field

Thermal conductivity is usually measured with fixed temperature and field. The procedure is here as follows: First, the required magnetic field and temperature are set, with the external

¹Resistivity measurements are usually done in a gas atmosphere, since here no vacuum is needed, and a faster temperature control and a better thermalization of the sample is possible. The influence of the atmospheric pressure is, however, negligible.

perturbation of the sample (sample heater) turned off. Then it is waited until certain stability criteria are fulfilled, while data points are continuously taken. This is achieved by taking the last n (usually $n = 150$) points and calculating the average, the slope, and the standard deviation. For the measurement signal(s) the slope and the standard deviation are checked, for the temperature additionally the set point deviation. If all criteria are fulfilled, average values of all measured quantities are calculated over the n points. Then the sample heater is turned on, and again it is waited for all stabilization criteria to be fulfilled, yielding a second set of values. From the two sets one can calculate the measured quantities, either by averaging both values (temperature) or by taking the difference. The latter procedure eliminates the offset values, which are always present due to thermovoltages in the wiring and in the plug connections. This is especially important for the low-voltage signals, as the thermocouple voltage. This procedure is basically the same for all measurements with fixed temperatures and fields. Resistivity could be performed in the same way, however a factor of $\sqrt{2}$ in the resolution can be gained if the current is switched between positive and negative values, instead of just turning it off.

3.1.3. Measurements with Temperatures and Field Sweeps

The disadvantage of measurements with fixed temperature and field is, that they are very time consuming. An accurate temperature stabilization can take a lot of time. Furthermore, only a small amount of the measurement time is used to take actual data points. Therefore it is desirable to stabilize only temperature or field, and to sweep the other quantity with a constant rate, taking the measured values continuously. This requires that the response time of the sample is not too slow and that the correction of offset values is still possible. Therefore the offset values should not change too fast as a function of temperature / magnetic field. For the regarded transport properties, this requirements are usually only fulfilled for resistivity measurements. Here, the offsets can be either neglected (insulators), or are taken into account by changing the sign of the current periodically in blocks of typically 10 – 20 s [33].

3.1.4. Probes

For the thermal transport properties six basically identical probes are available, which allow measurements between room temperature and ≈ 5 K. The lowest achievable temperature can be improved to $\approx 2.5 \dots 3$ K by pumping on the lambda plate. The probes are described in detail in Ref. [57]. For the resistivity measurements either a quick measurement device [33], or a variable temperature insert was used. For the latter a new probe was built up which covers the temperature range of 1.5 – 300 K and allows the measurement of two samples simultaneously.

3.2. Thermal Conductivity

The setup used for the thermal conductivity measurements is sketched in Fig. 3.1. The sample holder is kept on a temperature T_0 . A chip heater is mounted on the top of the sample, which can produce a heat gradient over the sample. This heat gradient is measured by a thermocouple attached to the sample. The thermal conductivity is calculated with the following equation

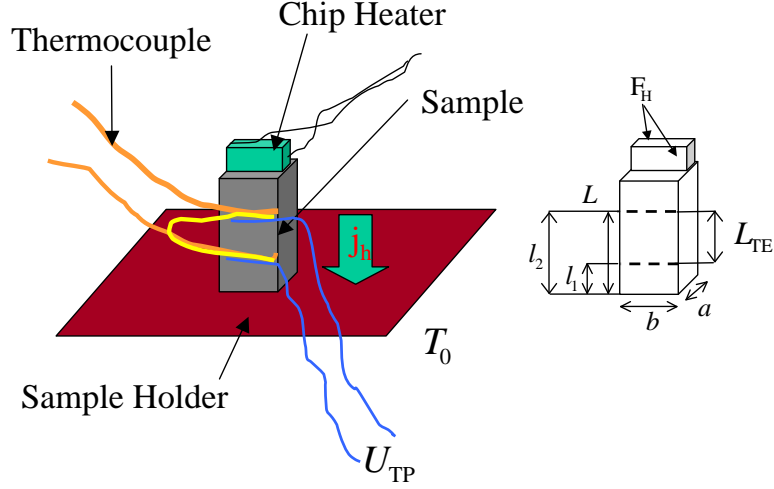


Figure 3.1.: Left: Setup for thermal conductivity measurements. Right: geometry used for the estimation of the radiation losses.

[57]:

$$\kappa = \frac{U_H \cdot I_H \cdot S(T, B)}{\Delta U_{TE}} \frac{l}{A}. \quad (3.1)$$

Here, U_H denotes the Voltage of the sample heater, I_H the current of the sample heater, $S(T, B)$ the temperature and field dependent calibration curve of the thermocouple, U_{TE} the voltage of the thermocouple, l the distance between the thermocouple ends, and A the cross section of the sample. $S(T, B)$ was determined carefully in Ref. [57], and checked with several reference samples, see Sec. 3.6.1. The used thermocouples were in most cases Chromel-Au+0.07%Fe, which are preferably used at low temperatures, and in some cases Constantan-Chromel, which have a higher sensitivity at high temperatures.

3.2.1. Error Sources

Whereas the voltage and current measurements are very precisely, the determination of the geometric factors l and A is affected by a large error of $\approx 5 - 20\%$, depending on the sample geometry. This can be neglected in most cases, since the qualitative behavior of the curves is not affected. Furthermore, the thermopower of the used thermocouples gives an error up to 5%, see Sec. 3.6.1. More crucial are, however, systematic errors which can cause large effects. These are mainly caused by thermal shortcuts by the wiring, or by radiation losses at high temperatures. Both effects are discussed in detail in Ref. [57]. The error through thermal shortcuts can be minimized by the use of proper wiring, in most cases manganin wires by a diameter of $50 \mu\text{m}$. For the measured samples in this thesis the influence of thermal shortcuts has been carefully checked and can be neglected in all cases. Radiation losses depend on the thermal conductivity of the samples and the geometry, and are usually large for samples with a small κ and a large ratio of sample length and cross section, L/A . The latter parameters are often restricted, and therefore radiation losses are often not to avoid. An estimation of the radiation losses was e.g. done in [58]. In this reference only the sample surface and the heater surface are taken into account. However, this is not sufficient because the wiring is a

3. Experimental

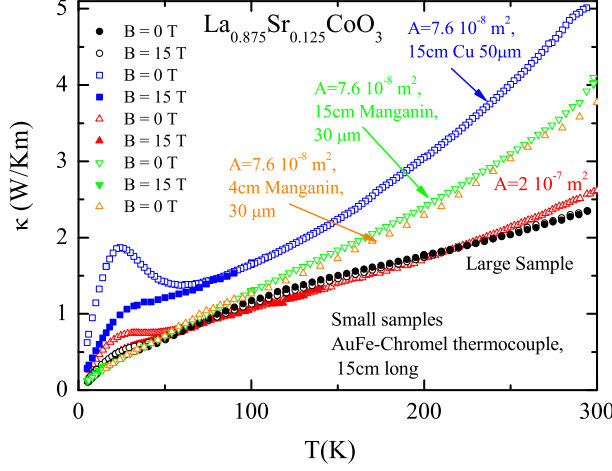


Figure 3.2.: Influence of radiation losses and thermal shortcuts on $\text{La}_{0.875}\text{Sr}_{0.125}\text{CoO}_3$ with different sample sizes and different heater wires. The large sample has a cross section $A = 4 \times 3 \text{ mm}^2$ and a length of 8 mm. The small sample had a length of 3 mm. The cross section of the small sample was modified by lapping the sample and is given in the plot.

radiating surface, too. If one considers a typical sample with $a \times b \times c = 1 \times 1 \times 2 \text{ mm}^3$, one obtains a surface of 9 mm^2 (without the bottom side). If heater wires with a length of 5 cm and a diameter of $50 \mu\text{m}$ are taken, these have a surface of $2 \times 50 \times 0.05 \times \pi = 15.7 \text{ mm}^2$, which is larger than the sample surface. This shows, that the wiring has to be taken into account for an estimation of the radiation losses. Fig. 3.2 shows test measurements of small samples with different setups using different wire length. The radiation effects cause large errors at high temperatures². A similar estimation as for the sample heater wires can be made for the other used wires. This can be easily done by extending the approach used in Ref. [58]. Herefore, it has to be taken into account that the thermocouple is not under the influence of the total heat gradient. One obtains the following relations:

$$\kappa_R = 4\sigma_{SB}T_0^3 \frac{L}{A} \sum_i S_i. \quad (3.2)$$

Here, σ_{SB} is the Stefan Boltzmann constant. The radiation losses lead to an additional term proportional to T^3 to the measured thermal conductivity, i.e. $\kappa_{\text{meas}} = \kappa_{\text{real}} + \kappa_R$. The factors S_i are determined by the surface areas S_i and the absorption coefficients ϵ_i of the different radiating surfaces. Summing over all contributions $S = \sum_i S_i$ we obtain:

$$\begin{aligned} S = & (a + b)L\epsilon_p \\ & + S_H\epsilon_H \\ & + d_{\text{Hw}}l_{\text{Hw}}\pi\epsilon_{\text{Hw}} \\ & + \frac{l_1 + l_2}{2L}d_{\text{Tp}}l_{\text{Tp}}\pi\epsilon_{\text{Tp}} \\ & + \frac{l_1 + l_2}{2L}d_{\text{Chr}}l_{\text{Chr}}\pi\epsilon_{\text{ch}} \\ & + \frac{l}{2L}d_{\text{AuFe}}l_{\text{AuFe}}\pi\epsilon_{\text{AuFe}}. \end{aligned} \quad (3.3)$$

Here, ϵ_i , d_i , and l_i denote the absorption coefficients, diameters and length of the heater wires (Hw), thermopower wires (Tp), Chromel wires of the thermocouple (Chr), and the gold-iron

²The peaks at low temperatures, and the field dependences are systematic errors due to the use of copper wires, which cause thermal shortcuts (see Ref. [57]).

Sample		l_{Tp}	$\kappa_{rad}(300\text{ K})(\text{W/Km})$	$\kappa_{rad}(300\text{ K})/\kappa(300\text{ K})$
LaCoO ₃	Mar5a_08	×	0.7	15%
LaCoO ₃	Mar5b_07	×	0.6	16%
LaCoO ₃	Mar5_09	×	0.6	19%
LaCoO ₃	Zo104	×	0.7	33%
LaCoO ₃	EKParis	×	0.7	18%
TbMnO ₃	S1	×	0.2	6%
TbMnO ₃	S2		2.0	51%
Nd ₂ CuO ₄			1.1	9%

Table 3.1.: Estimated radiation losses for various samples calculated by Eq. 3.2 and the used parameters. Additional parameters are: $l_{AuFe} = l_{Chr} = 0.05\text{ m}$, $l_{Hw} = 0.1\text{ m}$, $d_{Hw} = 50 \cdot 10^{-6}\text{ m}$, $d_{Chr} = d_{Chr} = 78 \cdot 10^{-6}\text{ m}$. The parameter l_{Tp} tells, if thermopower wires were used. No thermopower was measured in S1 of TbMnO₃, but a similar wiring for the voltage wires was used (see Sec. 7.5.1).

wire of the thermocouple (AuFe). S_H is the surface are of the heater. For the meaning of the other geometric factors see Fig. 3.1. In Tab. 3.1 estimations made for the samples with the worst geometric factors for the different series are shown. Herefore the individual sample dimensions and wire thicknesses are used. Since the exact length of the wiring was not known, so typical values were used. The absorption coefficients were set so 1 to obtain an upper limit. In most cases the radiation losses are below 10% at room temperature. Larger radiation losses occur for the LaCoO₃ samples, which have a very low high-temperature thermal conductivity, and for one sample of TbMnO₃. For TbMnO₃, some of the measurements were corrected. Herefore the factor $\sum S_i$ was estimated by the comparison with the reference measurement of the larger sample (see Chp. 7 and Fig. A.6). The difference of κ_{rad} for the two TbMnO₃ samples is estimated to 1.8 W/KM, which is equal to the observed difference of $\kappa(300\text{K})$ for the different samples. This shows, that the estimation with Eq. 3.2 gives a good estimate of the radiation losses. However, since most of the parameters were not exactly known (e.g typical wire length), the result should not be taken too literally. Without a reference measurement the correction of radiation losses is affected by a large uncertainty, and is not recommended. Another error which is relevant at low-temperatures is the heating of the sample with respect to the sample holder, which can get large due to a bad thermal anchoring of the sample [57]. If magnetic-field dependent measurements are performed in a transverse-field cryostat (see e.g. Ref. [59]) the probe has to be oriented with respect to the field. Due to the construction of the probe, this error can be up to 20% if the probe is oriented by visual judgement. This error can be reduced by mounting a Hall probe close to the sample. If only measurements along two axes perpendicular to each other are performend, it is sufficient to determine the minimum / maximum of the hall voltage to orient the sample, which can be easily done.

3.2.2. Thermal Conductivity Measurements in the Heliox ³He Insert

The lowest temperature of the used setup is restricted to $\approx 2.5 - 3\text{ K}$, and the measurements below 5 K are extensive, since pumping on the lambda plate is required. To extent the measurement range to lower temperatures, a Heliox³ ³He evaporation insert was used. The Heliox

³Oxford Instruments

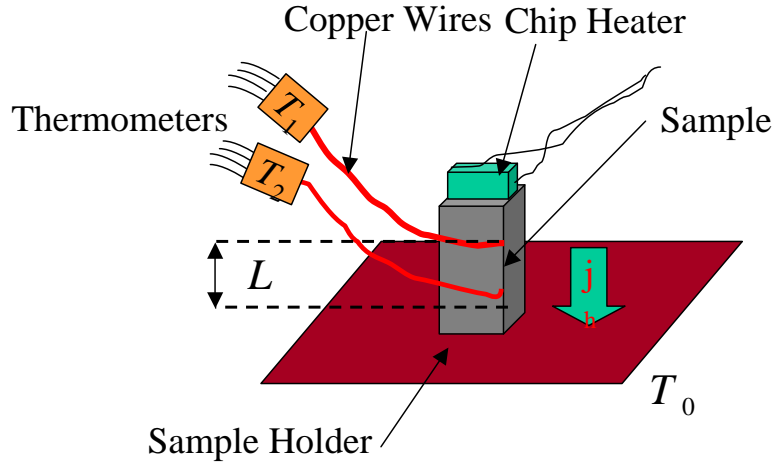


Figure 3.3.: Setup low-temperature thermal conductivity measurements.

has a temperature range from ≈ 250 mK to 60 K [60]. T. Zabel and O. Heyer have built up a sample holder for transport measurements [60, 61]. The sample holder basically consists of a copper plate with a calibrated sample thermometer, and contains 16 pins for the electrical connections, see Fig. 3.4. Below 3 K, the use of two thermometers is required to determine the temperature gradient. This has two main reasons. First, the thermopower vanishes for $T \rightarrow 0$, and the signal of the thermocouples gets too small. Second, heating of the sample requires an exact determination of the sample temperature, because large differences between sample holder and sample can occur [57]. Note, that radiation losses are negligible in the relevant temperature range, and therefore the much larger surfaces of the thermometers / wires play no role.

The used setup is sketched in Fig. 3.5. Two short pieces of copper wires are attached to the sample with silver epoxy. Small Ruthenium oxide thermometers are used, which are glued to the copper wires with silver paint. The thermometers are conducted with a 4-wire setup using thin ($30 \mu\text{m}$) manganin wires. For the measurement of the thermometer resistivity an AVS-47 resistance bridge is used. The bridge measures the resistivity by an AC method which gives the required high accuracy. Since only one bridge was available, the built-in scanner of the AVS-47 was used, and the thermometers are measured consecutively.

A data point is taken as follows: First, the lower thermometer is chosen via the scanner, and it is waited until both, the sample holder and the sample thermometer are stable, and n (usually $n = 50 \dots 100$) data points are taken. Then the scanner is switched to the upper thermometer, and immediately another set of n values is taken. These two values of the thermometer resistivity are used for an in-situ calibration of the thermometers, since with the sample heater turned off, the sample thermometers have the same temperature as the sample holder. Then it is switched again to the lower thermometer, and the sample heater is turned on. Again it is waited until the temperature is stable, and the n values of the lower, and afterwards the upper thermometer are taken. From these two values the temperature gradient is calculated, using the in-situ calibration. The average of these two temperatures gives the temperature to which κ is assigned, what rules out errors due to samples heating. This method requires a stable base temperature. The used temperature gradients are in the order of a few percent of the absolute temperature. For the in-situ calibration a function

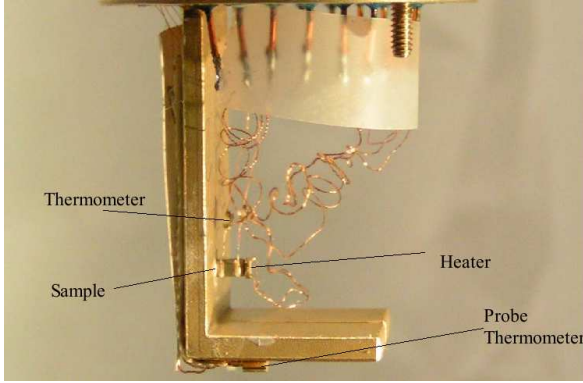


Figure 3.4.: Heliox samples holder with a LaCoO_3 sample prepared for a thermal conductivity measurement [62].

$$T(R) = \exp\left(\sum_{i=1}^6 c_i \cdot \log(R)^i\right) \quad (3.4)$$

is used, what gives a good approximation [63]. If no calibration values are available for new thermometers, one first has to perform a run without using the sample heater to get a preliminary calibration. This is necessary for two reasons: First, the appropriate currents are calculated from the previous temperature gradient, which requires the knowledge of the calibration. This is important, because the thermal conductivity at low temperatures changes drastically with the temperature. For a useful temperature gradient, the thermal conductivity has to be known, and the best approximation is to use the thermal conductivity of the previous measurement point. Second, an estimate of the thermal conductivity is necessary, to plan the further measurements. For thermometers, which have been already used, one can take a calibration curve from a previous curve, even if these may have slightly changed, since for the final data analysis the in-situ calibration is used.

For field dependent measurements at fixed temperatures one has to take into account the field dependence of the thermometers. Since a complete calibration would be very time consuming, a different way was chosen: The field dependent resistivity was measured at the required temperature and at a slightly higher temperature, and for the calibration a linear interpolation was used, which is a good approximation in a narrow temperature range. A comparison with points of the temperature dependent measurements proved the validity of this method.

3.3. Thermopower

To measure the thermopower two additional wires are attached to the sample. For the measurements in this thesis copper wires were used. The thermopower is calculated by

$$S_{\text{TP}} = U_{\text{TP}}/\Delta T + S_{\text{Cu}} \quad (3.5)$$

where $\Delta T = U_{\text{TC}}/S_{\text{TC}}$ is measured analogously to the thermal conductivity measurements. The thermopower of the copper wires has to be added to get the pure sample contribution, see Sec. 2.2. Therefore calibrated copper wires were used [64]. In most cases the thermocouples were attached to the thermopower wires close to the sample, which turned out to give very reliable contacts. The validity of this method was checked by a comparison with a measurement of the same sample with the thermocouple attached directly to the sample.

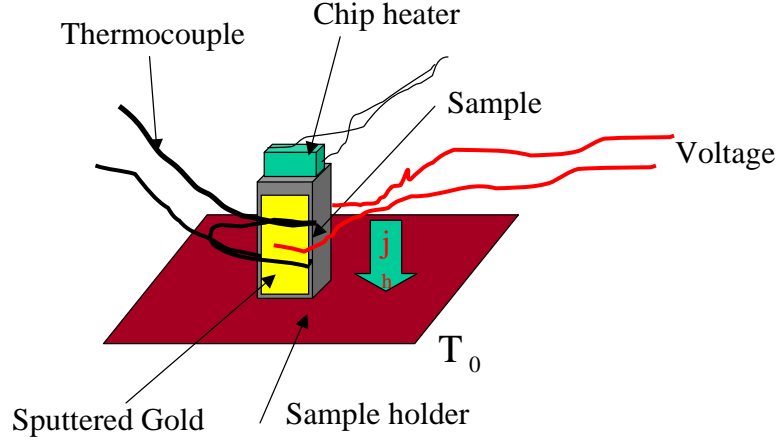


Figure 3.5.: Setup for the thermal conductivity measurements in electrical field performed for TbMnO_3 (see Chp. 7). The same setup was used for the measurement of the electrical polarization shown in Fig. 7.21.

3.4. Figure of Merit

The thermoelectric figure of merit ZT is calculated from thermal conductivity, thermopower, and resistivity of the sample via (see Sec. 2.3)

$$ZT = \frac{S^2 T}{\kappa \rho}. \quad (3.6)$$

Usually the thermal conductivity and the thermopower are measured simultaneously in one setup, whereas the resistivity is measured in a different setup and in most cases on a different sample. This enlarges the experimental error, which can be estimated as follows: The different quantities are calculated by

$$\begin{aligned} S &= \frac{U_{\text{TP}}}{U_{\text{TC}}} \cdot S_{\text{TC}} \cdot \frac{l_{\text{TC}}}{l_{\text{TP}}} \\ \kappa &= \frac{U_{\text{H}} I_{\text{H}}}{U_{\text{TC}}} \cdot \frac{l_{\text{TC}}}{A_{\text{TP}}} \cdot S_{\text{TC}} \\ \rho &= \frac{U_{\text{R}}}{I_{\text{R}}} \cdot \frac{A_{\text{R}}}{l_{\text{R}}}. \end{aligned} \quad (3.7)$$

From Eqs. 3.6 and 3.7 it follows

$$ZT = \frac{U_{\text{TP}}^2 S_{\text{TC}} l_{\text{TC}} I_{\text{R}} l_{\text{R}} A_{\text{TP}}}{U_{\text{TC}} A_{\text{R}} l_{\text{TP}}^2 U_{\text{R}} U_{\text{H}} I_{\text{H}}}. \quad (3.8)$$

We assume an error of 10% for all geometric quantities, and an error of 5% for S_{TC} , and neglect the errors of the voltage and current measurements. Error propagation gives an error of $\Delta ZT/ZT \approx 25\%$. If the thermocouples are mounted on the thermopower wires, it follows $l_{\text{TC}} = l$, which reduces the error to $\approx 20\%$. A more precise determination of the thermoelectric figure of merit is possible with a setup which directly measures ZT , see e.g. Ref. [65].

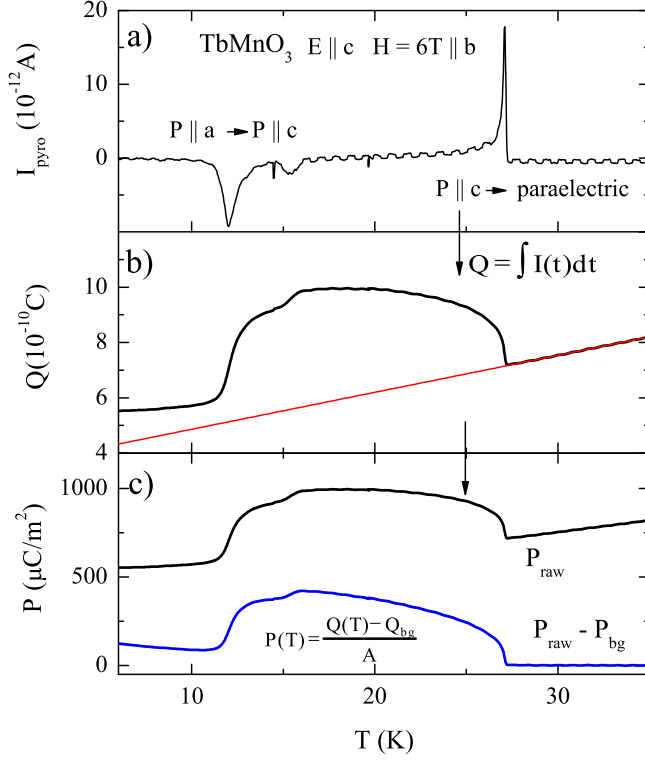


Figure 3.6.: Data analysis for the electrical polarization. a) Measured pyrocurrent b) charge Q obtained by integrating the pyrocurrent over time. c) Electrical polarization P , with and without background subtraction.

3.5. Electrical Polarization and κ in an Electrical Field

In Chp. 7 the thermal conductivity of TbMnO_3 measured under application of electrical fields will be presented. The used setup is shown in Fig. 3.5. An electrical field $E = U/d$ is obtained by applying a voltage U on two capacitor plates with a distance d . As capacitor plates gold was sputtered on two opposite surfaces of the sample. To avoid shortcuts with the sample holder and the thermocouples, a small margin was left. The resistivities between the capacitor plates and sample holder, thermocouple, and heater were checked and were not detectable. In principle the gold surfaces cause a thermal shortcut, which could cause an error for the κ measurement. However, the gold surfaces are very thin and a comparison with a previous measurement yielded identical results. During the experiment voltages up to 1000 V were applied.

The same setup was used to determine the electrical polarization. Herefore, the pyroelectric current was measured by using a Keithley 6517A electrometer in the current mode. From the pyroelectric current, the electrical polarization is calculated via

$$P = \frac{Q}{A} = \frac{\int I(t) dt}{A}. \quad (3.9)$$

For the integration over the time it is necessary to save also the time in the result file. The data analysis will be explained in more detail on an example curve: a measurement of the polarization of TbMnO_3 along the c axis with $H = 6 \text{ T} \parallel b$. In this configuration a polarization should be present for $T_{\text{FE}}(10 \text{ K}) < T < T_c(35 \text{ K})$ [14]. Fig. 3.6 a) shows the measured pyrocurrent, which is already averaged over 5 points. Note that the measured currents are extremely small ($\approx 10^{-11} \text{ A}$). This makes these measurements very sensitive to any kind of external influences. Usually the measurements could not be performed, if persons were in the

3. Experimental

	A	L
Graphite, M1&M2	$0.6 \times 0.74 = 0.44 \text{ mm}^2$	5 mm
Graphite, M3	$1.5 \times 0.9 = 1.4 \text{ mm}^2$	5 mm
Electrolytic iron, thin sample	$0.2 \times 0.6 = 0.12 \text{ mm}^2$	5.2 mm
Electrolytic iron, thick sample	$\phi = 6.37 \text{ mm} \quad A = 32 \text{ mm}^2$	11.6 mm

Table 3.2.: Sample dimensions of the used reference samples. The "thick sample" was directly cut from the cylinder formed rod, the other samples were cut to cuboids.

laboratory. The measured signal is superposed by a periodic signal, which was present all the time. The source of this signal could not be identified. Panel b) shows the signal after the integration over the time t , which gives the charge Q . A problem is the occurrence of an offset of I_{pyro} which leads to an additional linear term in Q . Under the assumption that for $T > 35 \text{ K}$ no polarization is present, this linear contribution is estimated by a linear fit as shown and subtracted. Panel c) finally shows the calculated polarization P , with and without the offset correction. The assumption of a time-independent offset is not perfectly fulfilled, since a residual signal of P remains below $T = 10 \text{ K}$. The problem of a changing offset was always present, especially for measurements in a poling field⁴. In this case, it took usually several hours until a stable current was obtained.

3.6. Check of the Thermocouple Calibration

The used thermocouples were recalibrated as discussed in detail in Ref. [57]. The calibration was checked by measurements of reference samples. The sample sizes of the used specimens are listed in Tab. 3.2. Here, the geometric error is much smaller than usual, because long samples which large distances between the thermocouple ends could be used, and the material properties (e.g. hardness) allow a precise cutting. In Ref. [57] the measurement of graphite yield only a fair agreement of the measured thermal conductivity with the reference values. One reason is that the reference thermal conductivity of the graphite reference sample has to be corrected based on the resistivity and the density of the individual sample, which was not taken into account in Ref. [57]. In Ref. [66] relations for the corrections are given. For the used sample the values $d_0 = 1719 \text{ kg/m}^3$ and $\rho_0 = 1.2446 \Omega\text{m}$ were measured. Fig. 3.7a shows the reference values, the corrected reference values, and three measurements with the Chromel-Au+0.07%Fe thermocouples. Fig. 3.7b shows the ratio $\kappa_{\text{meas}}/\kappa_{\text{ref}}$, with the corrected reference values taken. The measurements M1 and M2 suffer from low-temperature thermal shortcuts, because copper wires were used as heater wires (these are the measurements presented in Ref. [57]). Therefore K. Kordonis repeated this measurement with the appropriate use of manganin heater wires. The resulting curve (solid symbols) is in a good agreement with the reference value ($\kappa_{\text{meas}}/\kappa_{\text{ref}} < \approx 5\%$ in the whole temperature range). As a further check, a second sample was measured, electrolytic iron [67]. Here, the reference thermal conductivity also has to be corrected with respect to the residual resistivity which was estimated⁵ as

⁴Usually P is measured by cooling the sample under the application of a polling field to avoid domain formature.

⁵This was done by measuring the residual resistivity ratio and calculating ρ_0 according to Ref. [67] to avoid geometric errors.

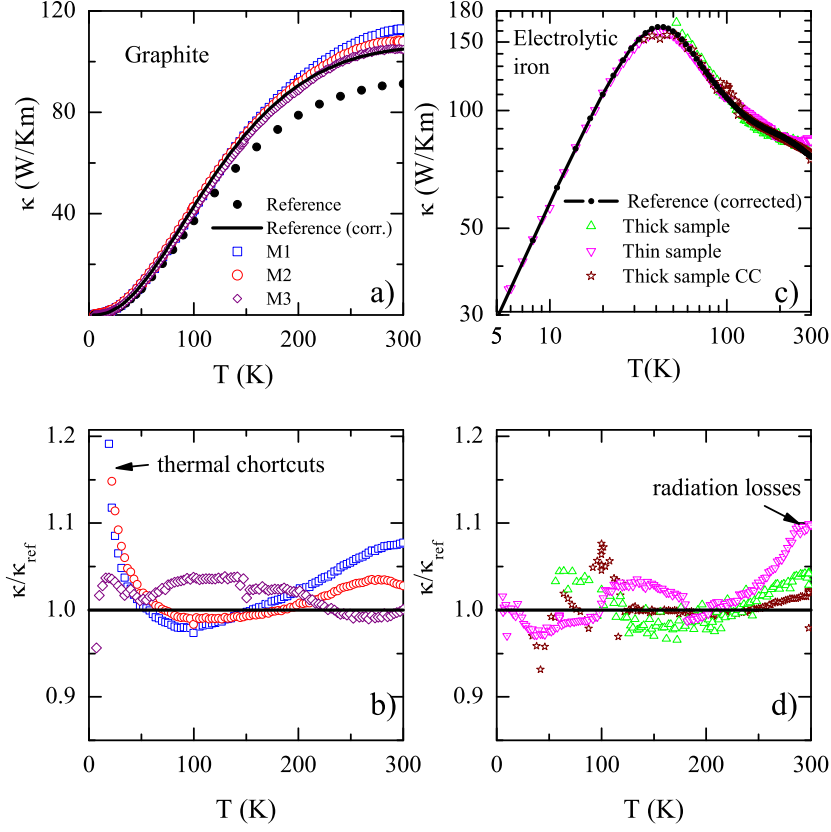


Figure 3.7.: Thermal conductivity κ of reference samples. a) κ of graphite: Reference values, corrected reference values and three sets of measurements using Chromel-Au+0.07%Fe thermocouples b) Ratio $\kappa_{\text{meas}}/\kappa_{\text{ref}}$ for the measurements of graphite. c) κ of electrolytic iron. The reference values of κ , two sets of measurements with Chromel-Au+0.07%Fe thermocouples and one set with a Constantan-Chromel thermocouple are shown. d) Ratio $\kappa_{\text{meas}}/\kappa_{\text{ref}}$ for the measurements of electrolytic iron.

$\rho_0 = 4.249 \cdot 10^{-9} \Omega\text{m}$. In comparison to graphite, the correction is only small and only affects the low-temperature range. Fig. 3.7c shows the corrected reference curve, and two sets of measurements taken with Chromel-Au+0.07%Fe thermocouples performed with two samples. The first sample ("thin sample") had a small cross section (see tab Tab. 3.2), which allowed the measurement down to 6 K. This measurement shows a good agreement between 6 K and ≈ 200 K ($\kappa_{\text{meas}}/\kappa_{\text{ref}} \lesssim 5\%$). However, at higher temperatures an upturn of the measured curve occurs, which is due to radiation losses. Therefore a second sample was cut with a large cross section ("thick sample"), which gives a good agreement at high temperatures. For lower temperatures this measurements does not give good results, because the temperature gradients were too small. Combining the two sets of measurements again an error below $\approx 5\%$ is estimated.

The Constantan-Chromel thermocouple was only tested with the thick electrolytic iron sample, which gives a good agreement down to 50 K. Because these thermocouples are used for measurements at higher temperatures, the agreement is satisfactory.

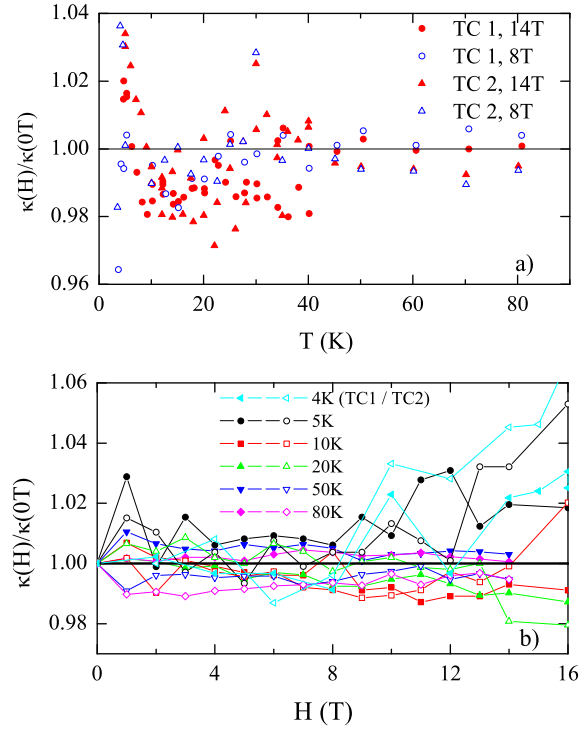


Figure 3.8.: Test measurements of quartz samples to check the correct field calibration of the Chromel-Au+0.07%Fe thermocouples. Two different thermocouples (TC) were used. a) $\kappa(H)/\kappa(0)$ vs. T . b) $\kappa(H)/\kappa(0)$ vs. H .

3.6.1. Magnetic Field Dependence

To check the magnetic-field dependence of the thermocouple calibration, thermal conductivity measurements of a quartz-glass sample was performed. Quartz is a purely phononic heat conductor, and therefore shows a negligible magnetic field-dependence. A further advantage is that the thermal conductivity at low temperatures has very low absolute values, and shows no pronounced temperature dependence. This ensures that no heating of the samples with respect to the sample holder occurs.

Fig. 3.8 shows the results of these measurements. Panel a) shows the results from temperature dependent measurements. The ratio $\kappa(H)/\kappa(0T)$ is shown for 8 T and 14 T for two different thermocouples. The field dependence is below $\approx 4\%$ in the whole investigated temperature range. In panel b) measurements with fixed temperatures are shown. Except for 5 K and 3 K the measured field dependence is below 2%. For 5 K and 3 K and $H > 10$ T it increases to $\approx 6\%$, which is rather small, but one has to keep this error in mind for low temperatures / high fields.

For the Constantan-Chromel thermocouples the field dependence was not checked, since it is almost negligible at higher temperatures, and these thermocouples were not used for low-temperature field-dependent measurements.

4. Thermal Conductivity in $R_2\text{CuO}_4$

La_2CuO_4 is well known as parent compound for high-temperature superconductors, which is an intense field of research since more than twenty years [1, 68]. La_2CuO_4 becomes superconducting by hole doping, which can be done by e.g. Sr doping. It was discovered only a short time later, that another class of superconductors exists, based on the compounds $R_2\text{CuO}_4$, where the La is replaced by rare earth $R = \text{Pr, Nd, Sm, Eu}$ [69, 70]¹. In contrast to La_2CuO_4 , superconductivity is created by electron doping here, e.g. with Ce. The similarities and differences in the mechanisms of superconductivity between these two classes of high-temperature superconductors puzzle the researchers up to now, and the coupling mechanism is not yet understood. Apart from becoming superconductors upon doping, the undoped mother compounds also show a lot of other interesting physics [71, 72]. Although La_2CuO_4 and the $R_2\text{CuO}_4$ compounds crystallize in different structures, the physics in both compounds is dominated by the CuO_2 square lattice, realizing a two-dimensional spin-system with a large exchange constant J , which makes these compounds to ideal model systems to investigate two-dimensional physics. In contrast to La_2CuO_4 , most of the $R_2\text{CuO}_4$ compounds contain a second magnetic subsystem formed by the R ions, which rises a lot of new properties, caused by the additional interactions between the Cu and R magnetic moments, and by the R - R interactions itself.

One aspect of such a low-dimensional spin-structure is the question, whether magnetic heat transport plays an important role. This is discussed for many compounds, and several publications investigate this question for La_2CuO_4 [6–8, 11]. For the rare-earth cuprates, however, there was no systematic investigation of κ up to now.

In this chapter I will first give a brief overview of low-dimensional spin systems, where magnetic heat transport was observed. Then I will discuss the structural and magnetic properties of the investigated $R_2\text{CuO}_4$ compounds. After a more detailed view on the available literature of thermal conductivity data of the cuprates, I will present measurements of κ_{ab} for $R = \text{Pr, Nd, Sm, Eu, and Gd}$ and of κ_c for $R = \text{Pr and Gd}$ in zero field from 5...300 K. The question, if a magnetic contribution to the heat transport is present, will be discussed. In the second part the focus will be on the low-temperature data and the influence of magnetic fields. Parts of the results presented in this chapter have been published in Refs. [57, 73, 74].

4.1. Heat Transport by Magnetic Excitations

For insulators, only one low-temperature phononic peak of the thermal conductivity κ is expected, see Sec. 2.1.2. In contrast, various low-dimensional spin systems show an unusual thermal conductivity κ with a double-peak structure for a heat flow along the low-dimensional direction (or directions in 2D) as a function of temperature. There is growing evidence that this anomalous behavior arises from magnetic excitations contributing to the heat transport. The most clear experimental evidence is found in the spin-ladder compounds, where a double-peak

¹ Gd_2CuO_4 does not become superconducting [70].

structure with a huge high-temperature maximum of κ is present for a heat current parallel to the ladder direction, but absent for a heat current perpendicular to the ladders [3, 4]. For one-dimensional spin-chain systems the experimental results are less clear. For the spin-chain compounds SrCuO_2 and Sr_2CuO_3 Sologubenko *et al.* find a sizeable extra contribution to κ along the chain direction, which is missing in the other directions [75]. In the spin-Peierls compound CuGeO_3 κ along the chain direction has two low-temperature maxima and one of them was attributed to a magnetic contribution in Ref. [76]. However, this interpretation is questionable, because a similar double peak is also present in κ perpendicular to the chain direction [5, 27]. In the Haldane-chain ($S = 1$) System AgVP_2S_6 , a magnetic contribution plays a role, too [77], but the absolute values are much smaller than in the $S = 1/2$ systems. Recently, a magnetic contribution to heat transport was discovered in the Haldane-spin system Y_2BaNiO_5 [78]. The results in 1D systems raise the question whether a sizeable heat current due to magnetic excitations is also present in two-dimensional magnets. This was discussed for the low-temperature thermal conductivity of $\text{K}_2\text{V}_3\text{O}_8$ and Nd_2CuO_4 [10, 79, 80]. As already mentioned, the latter is one of the insulating parent compounds of high-temperature superconductors containing CuO_2 planes, which represent the perhaps most studied two-dimensional antiferromagnets so far [71]. Whereas the studies on Nd_2CuO_4 (Refs. [10, 80]) mainly concern the magnetism of the Nd^{3+} moments, the influence of the Cu^{2+} moments on κ is present at higher temperature. In the layered perovskite La_2CuO_4 , the thermal conductivity κ_{ab} for a heat current along the CuO_2 planes exhibits a pronounced double-peak structure with a low-temperature maximum around 25 K and a second one around 250 K. In contrast, the thermal conductivity κ_c perpendicular to the CuO_2 planes has only one low-temperature peak [6–8, 11]. These findings have been interpreted in terms of an additional heat transport parallel to the CuO_2 planes due to magnetic excitations. However, a double-peak structure can also be explained by phonons only. Any additional scattering mechanism which acts in a narrow temperature range suppresses κ in that temperature window and as a result κ may exhibit two peaks. For example, in $\text{SrCu}_2(\text{BO}_3)_2$ a double-peak structure is caused by resonant scattering of acoustic phonons by magnetic excitations [27, 28]. Such a mechanism does not apply for La_2CuO_4 . However, La_2CuO_4 has a structural instability with low-lying optical phonon branches, which could also serve as scatterers for the acoustic phonons. Such an explanation has been proposed by Cohn *et al.* for the heat transport data of $\text{YBaCuO}_{6+\delta}$, which show a similar temperature dependence of κ_{ab} as La_2CuO_4 [81]. M. Hofmann *et al.* investigated κ_{ab} of $\text{Sr}_2\text{CuO}_2\text{Cl}_2$, which is almost isostructural to La_2CuO_4 , but shows no structural instability [27, 82]. A second high-temperature maximum in κ_{ab} was taken as evidence for the second peak of the in-plane heat conductivity being caused by magnetic excitations. Basing on this observation it was suggested that a pronounced magnetic contribution to the thermal conductivity is a common feature of the layered cuprates. However, the high-temperature peak of κ_{ab} of La_2CuO_4 is significantly larger and its low-temperature peak is much smaller than the corresponding peaks observed in $\text{Sr}_2\text{CuO}_2\text{Cl}_2$. These quantitative differences could arise from the absence or presence of a structural instability and/or weak charge carrier doping in the different samples. These findings motivated the systematic study of κ_{ab} on single crystals of $R_2\text{CuO}_4$ with different rare earths R .

4.2. Structural and Magnetic Properties of $R_2\text{CuO}_4$

		$a \times b \times c$ (mm ³)	T_N (K)	Θ_D (K)	v_s (m/s)	P (10^{-43}s^3)	D (10^{-18}s)	U ($10^{-31}\text{s}^2/\text{K}$)	u
La_2CuO_4 <i>ab</i>	(Ref. 6)		316			21	26	22	4.4
La_2CuO_4 <i>ab</i>	(Ref. 11)		323			1.5	11.8	23	5.3
La_2CuO_4 <i>ab</i>	(Ref. 11)		313			23.8	4.6	14.1	7
La_2CuO_4 <i>ab</i>	(Ref. 7)		308	385 [83]	5200 [84]	25.8	26.2	15.3	4.4
La_2CuO_4 <i>c</i>	(Ref. 6)		316			15.4	14.6	17.3	6.4
La_2CuO_4 <i>c</i>	(Ref. 11)		325			1.9	15.1	18.8	5.5
$\text{La}_2\text{CuO}_{4+\delta}$		$0.6 \times 3 \times 2.5$		245					
Pr_2CuO_4 <i>ab</i>		$1.7 \times 1.6 \times 1.4$	250	361 [85]	6000 [86]	7.1	1	8.5	5.8
Pr_2CuO_4 <i>c</i>						10.3	2.0	13.0	5
Nd_2CuO_4 <i>ab</i>		$2 \times 1 \times 0.3$				5	10.7	11.0	4.9
Nd_2CuO_4 <i>ab</i>	(Ref. 80)		275	319 [85]	5900 [86]	0.27	11.1	9.6	4
Sm_2CuO_4 <i>ab</i>		$3.2 \times 3.7 \times 0.4$		353 [85]	5900	1.2	16.5	21.2	5.2
Eu_2CuO_4 <i>ab</i>		$2.6 \times 2 \times 0.3$							
Gd_2CuO_4 <i>ab</i>	A	$2 \times 0.7 \times 1.1$	285			11	17.5	2.4	5
Gd_2CuO_4 <i>c</i>	A			350	5900	7.6	40.1	3.5	3.1
Gd_2CuO_4 <i>ab</i>	B	$1.6 \times 0.9 \times 0.4$	290			8.3	10.6	2.6	5

Table 4.1.: Sample sizes, Néel temperatures T_N (see text and the respective references). P , D , U and u are fit parameters for the fits of the phononic contribution of κ . P and D describe the scattering on point defects and planar defects, respectively, whereas U and u model Umklapp scattering (for details see Sec. 2.1.2). If available, the Debye temperatures Θ_D and sound velocities v_s are taken from literature², otherwise similar values have been used for the fits.

4.2. Structural and Magnetic Properties of $R_2\text{CuO}_4$

A common feature of La_2CuO_4 and $R_2\text{CuO}_4$, with $R = \text{Pr}, \text{Nd}, \text{Sm}, \text{Eu}$, and Gd is the layered structure with planes consisting of a CuO_2 square lattice. These planes are a good realization of a two-dimensional antiferromagnetic $S = \frac{1}{2}$ Heisenberg square lattice. Bi-magnon Raman scattering [87] yields exchange constants J between $\approx 1200 - 1400$ K for $T = 300$ K given in Table 4.2. Here, only room-temperature values are listed because temperature-dependent values are not available for all samples. Note that these values are slightly larger than the low-temperature data, obtained by bi-magnon-plus-phonon absorption from infrared spectroscopy for La_2CuO_4 and $\text{Sr}_2\text{CuO}_2\text{Cl}_2$ [88, 89]. These values have been used in Refs. [27, 57, 82].

Finite inter-plane couplings J_\perp cause three-dimensional antiferromagnetic ordering with Néel temperatures $T_N \approx 250 \dots 320$ K (see Tab. 4.1 and 4.2). In general, the ordering temperature is determined by the ratio of the inter- and the intra-plane coupling. However, crystal quality and the oxygen stoichiometry strongly influence T_N , too. For example, very small amounts δ of excess oxygen drastically suppress T_N of $\text{La}_2\text{CuO}_{4+\delta}$ [90]. Apart from the magnetic Cu subsystem, the compounds with magnetic rare earth ions R contain another magnetic subsystem. In all these compounds the behavior of the Cu subsystem is very similar. However, the details of the magnetic structure are determined by the competition between the different couplings (Cu-Cu, R - R , R -Cu). The main consequences to the magnetic properties are as follows:

- The two spin lattices allow various magnetic structures, with different relative orien-

²Here, the longitudinal sound velocities have been used. The value of the sound velocity is, however, irrelevant for the used high-temperature extrapolations of the Debye fits. This is easily seen by neglecting L in Eq. 2.5: A change of the sound velocity just rescales the pre-factors P , D , and U .

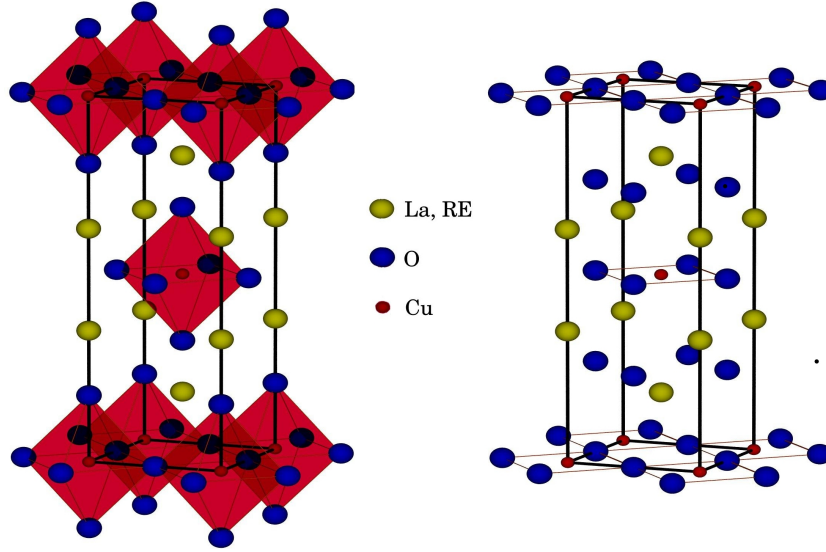


Figure 4.1.: Crystal structure of the $R_2\text{CuO}_4$ compounds. Left: The T Phase, which is realized for La_2CuO_4 . Here, the Cu ions are surrounded by oxygen octahedra. Right: The T' phase for $R = \text{Pr}, \text{Nd}, \text{Sm}, \text{Eu}, \text{and Gd}$. Here, the Cu ions are surrounded by oxygen plaquettes, but have no apex oxygens.

tions of the spins. In the case of Nd_2CuO_4 there are temperature-dependent transitions between different magnetic structures.

- For $R = \text{Sm}$ and Gd the R -sublattice orders antiferromagnetically itself for low temperatures ($T \lesssim 7 \text{ K}$). For $R = \text{Nd}$ a peak observed in the specific heat at $\approx 1.5 \text{ K}$ is due to a Schottky contribution, see Sec. 4.2.2.
- The spin-wave spectrum is more complex, the R spins cause additional branches.

In the following sections these effects will be discussed. For a review of the $R_2\text{CuO}_4$ compounds see Ref. [72].

4.2.1. Crystal Structure

La_2CuO_4 crystallizes in the so-called T-phase structure (also called K_2NiF_4 structure type), see left panel of Fig. 4.1. The CuO_4 plaquettes of the planes and the apex oxygen ions form CuO_6 octahedra. At high temperatures La_2CuO_4 is in the high-temperature tetragonal phase (HTT phase). At 530 K a structural phase transition takes place [91], where the octahedra tilt, leading to the low-temperature orthorhombic phase (LTO), which is stable down to lowest temperatures. Due to the octahedron tilt the point bisecting the nearest neighbor Cu-Cu distance is no longer a center of inversion symmetry giving rise to a Dzyaloshinski-Moriya (DM) type interaction. $\text{Sr}_2\text{CuO}_2\text{Cl}_2$ is almost isostructural to La_2CuO_4 with the La^{3+} ions being substituted by Sr^{2+} and the apex O^{2-} by Cl^- ions. In $\text{Sr}_2\text{CuO}_2\text{Cl}_2$ the HTT phase is stable down to the lowest temperature and due to inversion symmetry no DM exchange and consequently no spin canting occurs. The $R_2\text{CuO}_4$ compounds crystallize in the tetragonal so-called T'-structure (right panel of Fig. 4.1). While the T structure may be viewed as a stacking

R	J [K]	T_N^{Cu} [K]		T_N^R [K]		4f GS
La	1465	250 – 324	[11, 71, 72]	–		1S
Pr	1243	250 – 280	[92–95]	–		3H_4
Nd	1248	250 – 277	[80, 94–103]	$^{-1}$		$^4I_{9/2}$
Sm	1300	280	[104]	4.9 – 6.0	[85, 105–108]	$^6H_{5/2}$
Eu	1300	265	[109]	–		7F_0
Gd	1292	285 – 295	[73, 108, 110–113]	6.4 – 7.5	[106, 108, 111, 112, 114]	$^8S_{7/2}$
$\text{Sr}_2\text{CuO}_2\text{Cl}_2$	1220	245	[71, 72, 89]	–		–

Table 4.2.: Exchange constants J at 300 K (Ref. [87]), Néel temperatures for various crystals from the literature, magnetic ground state (for a free atom).

of one CuO_2 layer followed by two LaO (or SrCl) layers, the stacking of the T' structure is one CuO_2 layer followed by a layer of R^{3+} ions, a layer of O^{2-} ions, and finally another layer of R^{3+} ions. Consequently, there are no apex oxygen ions present in the T' structure and the basic building blocks are CuO_4 plaquettes instead of the CuO_6 octahedra of the T structure. For $R = \text{Pr}$, Nd , and Sm the T' structure is stable over the entire temperature range. Eu_2CuO_4 and Gd_2CuO_4 show structural instabilities, which will be discussed in Sec. 4.2.3.

4.2.2. Cu Magnetism in $R_2\text{CuO}_4$ for $R = \text{Pr}$, Nd , Sm , Eu , and Gd

The antiferromagnetic ordering of the Cu^{2+} spins is confirmed by neutron diffraction for $R = \text{Pr}$, Nd , Sm , Eu , and Gd . In Tab. 4.2 the Néel temperatures taken from various references are listed. The transition temperatures range from $T_N^{\text{Cu}} \approx 245 - 295$ K. Details of the magnetic structure differ depending on R . For Pr_2CuO_4 a non-collinear ordering of the Cu^{2+} spins is observed. In this type of ordering the spins are aligned in the planes, and the orientation of the spins in the planes alternates along the $[100]$ and $[010]$ direction, moving along the c axis. Further an induced Pr ordering arises, when the temperature is lowered. However, there is no antiferromagnetic transition of the Pr 4f spins, they order with the same propagation vector as Cu [94]. In contrast, the magnetic structure for $R = \text{Nd}$ is more complex. Two transitions of the magnetic structure at $T = 75$ and 30 K are found, where the magnetic structure switches between different noncollinear structures[94]. Below 1.5 K an increase of the Nd 4f moment was observed [99]. A peak in the specific heat at the same temperature was attributed to an antiferromagnetic transition of Nd driven by the Nd - Nd exchange interaction [106]. However, as pointed out in Refs. [115, 116], the Nd moments do not order, but are polarized by the Cu ordering. The peak in the specific heat can be attributed to a Schottky anomaly due to the Nd level splitting. It follows that the Nd moment continuously gets larger if the temperature is lowered, as for Pr . The noncollinear spin structure in Nd_2CuO_4 can be changed by applying a magnetic field. For $H \parallel [100]$ a spin-flop transition at $H_c = 4.5$ T turns the magnetic structure into a collinear state [117].

For Sm_2CuO_4 the spin structure is collinear with no reorientation transitions of the Cu^{2+} spins. However, a Néel transition of the R ions is observed at 5.9 K, which will be discussed in detail in Sec. 4.2.4. Eu_2CuO_4 is the first compound of the series, where a structural distortion

¹The observed transition in the specific heat at 1.5 K discussed in Ref. [106] turned out to be a Schottky peak, see Sec. 4.2.4 and 4.6.2.

occurs, see Sec. 4.2.3. In Eu_2CuO_4 , the $4f$ moments of the Eu^{3+} ion have a $4f^6$ configuration leading to a nonmagnetic $J = 0$ ground state, and the Eu magnetism is dominated by a van Vleck contribution. Consequently, there is no $4f$ moment, and the magnetic structure is determined by the Cu solely [118]. In Ref. [109] the authors proposed two possible magnetic structures, a collinear and a non-collinear one. For $R = \text{Gd}$ the structural distortion gets stronger, and leads to a complex magnetic behavior of the Cu subsystem, see also Sec. 4.2.3. Further, as will be discussed in Sec. 4.2.4, as for $R = \text{Sm}$, a low-temperature Néel ordering of the Gd moments occurs.

4.2.3. Structural Distortions and Magnetism for $R = \text{Gd}, \text{Eu}$

In Eu_2CuO_4 and Gd_2CuO_4 structural phase transitions are observed with transition temperatures of 170 K and 685 K, respectively [119, 120]. The structural changes can be described by an alternating rotation of the CuO_4 plaquettes around the c axis. The rotation angles amount to 2.3° at 20 K for $R = \text{Eu}$ and to 5.2° at 300 K for $R = \text{Gd}$ [119, 120]. The occurrence of the phase transition is interpreted as a consequence of an increasing mismatch of different bond lengths which develops with decreasing size of the R^{3+} ions. These structural transitions transform the T' structure into an orthorhombic structure. However, these crystals are usually strongly twinned with respect to the a and the b axes.

Because of the distorted phase at low temperatures, weak ferromagnetism caused by the DM interaction, is possible. Weak ferromagnetism means, that a collective canting of the Cu^{2+} spins leads to a finite macroscopic magnetic moment.

In Gd_2CuO_4 weak ferromagnetism is established, and was investigated by several groups [112, 121–126]. Below $T_N^{\text{Cu}} \approx 287$ K a spontaneous magnetic moment arises. The measured moment is mainly caused by the Gd $4f$ moments, which are polarized by the canted Cu spins (for the data of our crystals see Fig. 4.7). In principle, one would expect that the weak ferromagnetic moment remains down to lowest temperatures. However, the interactions with the Cu sublattice leads to a more complex behavior. If the temperature is lowered, the magnetic moment monotonously increases, but suddenly disappears at $T_c = 20$ K. This was interpreted as a disappearance of the weak ferromagnetism by Ref. [121]. The authors find by magnetization measurements, that the weak ferromagnetism between T_N^{Gd} and T_c is restored in small in-plane magnetic fields $\gtrsim 0.4$ T. The Néel ordering of Gd at 6.5 K will be discussed in the next section.

For Eu_2CuO_4 weak ferromagnetism was not seen in Ref. [118], but as pointed out in Ref. [127] occurrence of weak ferromagnetism is in principle possible, and depends on the sample preparation, e.g. on the used crucibles. For our sample, however, no weak ferromagnetic moment is observed, the magnetic susceptibility shows no anomalies in the relevant temperature range (see Sec. 4.4). The observed anomaly at T_N^{Cu} in Ref. [127] requires an already distorted structure at $T_N^{\text{Cu}} \approx 240$ K, which is above the observed phase transition temperature [120]. A possible reason to explain this contradiction is that the sample in Ref. [127] is already distorted at T_N^{Cu} , what seems reasonable, because the investigated sample is not pure Eu_2CuO_4 , but contains a small amount of Gd, which may drive the structural transition to a higher temperature.

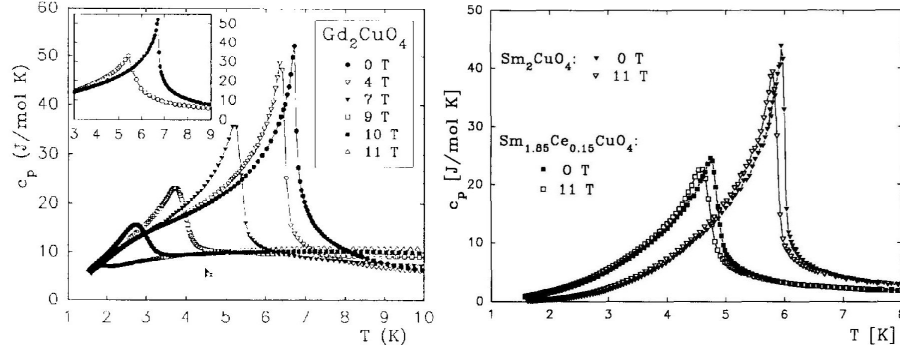


Figure 4.2.: Left: Specific heat of Gd_2CuO_4 taken from Ref. [128]. For $H = 0$ T a peak at $T_N^{\text{Gd}} = 6.5$ K can be attributed to a Néel transition of the Gd moments. T_N^{Gd} is strongly suppressed by large magnetic fields. Right: Specific heat of Sm_2CuO_4 taken from Ref. [129]. For zero field a similar peak as for Gd_2CuO_4 is observed, which can be attributed to $T_N^{\text{Sm}} = 5.9$ K. In contrast to Gd_2CuO_4 , a magnetic field of 11 T has only a small effect to the transition temperature.

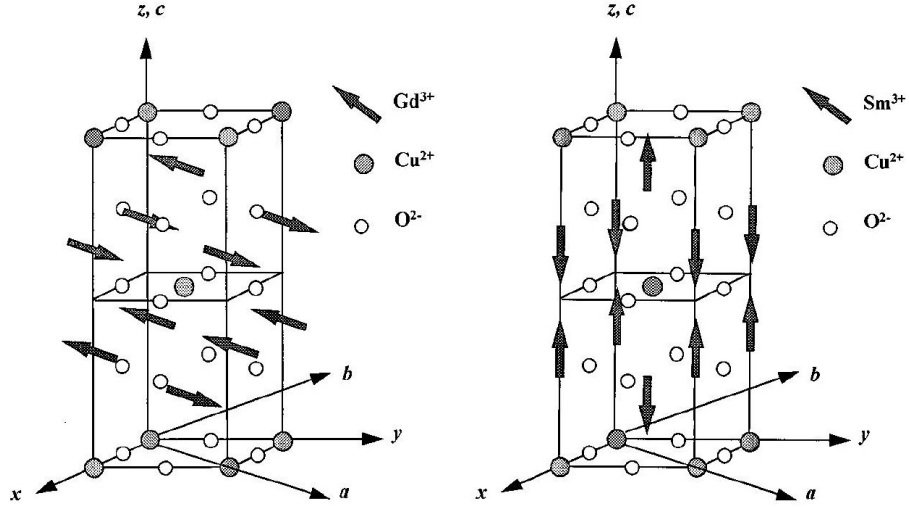


Figure 4.3.: Magnetic structure of $R_2\text{CuO}_4$ with $R=\text{Sm}, \text{Gd}$. The R moments are ferromagnetically aligned in the planes, and antiferromagnetically ordered along the c direction. The propagation vector of the R ordering is $k = (0, 0, 0)$, in contrast to the $(\frac{1}{2}, \frac{1}{2}, 0)$ ordering of Cu. For $R=\text{Gd}$ the spins are oriented along the $[110]$ direction, for $R=\text{Sm}$ along $[001]$. The graphs are taken from Ref. [130].

4.2.4. Néel Ordering of the R -Moments at low Temperatures

At low temperatures antiferromagnetic Néel ordering of the R moments occurs for $R = \text{Gd}$ and Sm . Here, the ordering of the $4f$ moments is a symmetry breaking phase transition, which is different to e.g. Pr_2CuO_4 , where the ordering of the R moments is induced by the Cu ordering. The transition is driven by the R - R exchange interaction. The Néel temperatures are 6.5 K for Gd, and 5.9 K for Sm, for references see Tab. 4.2. Specific heat data, see Fig. 4.2, clearly show that a phase transition occurs. The propagation vector of the ordering is $\mathbf{k} = (0, 0, 0)$. This might be confusing, since this is a ferromagnetic wave vector. The reason is that there are two spins in each unit cell with opposite signs. Their moments cancel each other. Even if the Néel temperatures are almost the same, the nature of the ordering is different for the two compounds. Gd_2CuO_4 is a so-called easy-plane antiferromagnet, whereas Sm_2CuO_4 is an easy-axis antiferromagnet. In Gd_2CuO_4 the R spins form ferromagnetic planes parallel to the CuO_2 planes, which are ordered antiferromagnetically along the c direction and are aligned along the $[110]$ direction, see Fig. 4.3a and Refs. [130, 131]. The corresponding magnetic point group changes from mmm to $mm'm$. This means that for a mirror symmetry operation along the (orthorhombic) b axis the time has to be reversed, too. This is not the case for the other directions³. In Sm_2CuO_4 the magnetic structure looks similar, with the difference that the spins are oriented along the $[001]$ direction, Fig. 4.3b. Here, the magnetic point group denotes $m'm'm'$. If a magnetic field is applied, for $R = \text{Gd}$ the antiferromagnetic transition is almost suppressed by a field of 11 T, whereas for $R = \text{Sm}$ the shift of the transition temperature is only about 100 mK, see the specific heat data in Fig. 4.2 (Refs. [128, 129]). The origin of the different behavior is based on the different orbital states (see Tab. 4.2). Gd_2CuO_4 has a vanishing orbital moment which causes only a weak coupling to the crystal field. The competition of different weak anisotropy interactions causes the observed spin orientation. If an external magnetic field $H > H_c$ is applied, the Zeeman energy leads to a destruction of the antiferromagnetic order. This is the spin-flip transition, and above H_c all Gd spins are ferromagnetically aligned. At 1.5 K magnetization measurements give $H_c = 11$ T [130, 131]. Now, the strong suppression of T_N^{Gd} can be understood, the value of $H_c = 11$ T corresponds to $T_N^{\text{Gd}}(11 \text{ T}) \approx 1.5$ K in the temperature-dependent measurement of the specific heat.

In Sm_2CuO_4 the strong orbital moment causes a large single-ion anisotropy, which on the one hand leads to the orientation of the Sm spins along the c direction, on the other hand explains the observed weak magnetic-field dependence. For a phenomenological description of the R ordering in Gd_2CuO_4 and Sm_2CuO_4 see e.g. Ref. [130].

4.2.5. Spin Waves

Collective excitations of an ordered antiferromagnet are called spin waves. Because of the two magnetic subsystems in $R_2\text{CuO}_4$ different branches are expected for Cu and R . The spin-wave spectrum has been studied experimentally and theoretically for $R = \text{Nd}$ and Pr . The main findings are several low-energy branches, which are associated with the Nd moments ($E < 1$ meV), whereas the Cu branches have higher energies ($E > 5$ meV). It is important to notice that the spin-wave differs in the different magnetic phases. Sachidanandam *et al.* proposed a model for the spin-wave spectrum in Nd_2CuO_4 . One prediction is a low-energy

³Note that a spin does not change its sign in a mirror operation, if the direction of the spin is parallel to the normal vector of the plane. If the spin is oriented parallel to the plane, the sign changes. A simple picture for this can be drawn by representing the spin as small circuit currents, and mirror these currents.

acoustic mode, with a very small gap. This gap can be closed by experimentally accessible magnetic fields. Petitgrand *et al.* investigated experimentally and theoretically mainly the spin-wave spectrum of Pr_2CuO_4 [132] with similar results.

For the other rare-earth cuprates there are to my knowledge no investigations concerning the spin-wave excitations. The main reason is the difficulty of neutron-scattering experiments, because of the large neutron absorption cross section of these elements.

4.3. Thermal Conductivity of $R_2\text{CuO}_4$: Literature Data

The first observation of an unusual temperature dependence of the thermal conductivity κ in cuprates was published by Morelli *et al.* in 1989 [133]. These authors observed a strong increase of thermal conductivity with increasing temperature after a minimum at about 30 K, and attributed this feature to unusual phonon scattering. The first systematic investigation including in- and out-of-plane data was published by Nakamura *et al.* in 1991 [6]. In this paper the thermal conductivity of $\text{La}_{2-x}\text{Sr}_x\text{CuO}_4$ was investigated for different crystallographic directions on single crystals for various Sr-doping levels. Figure 4.4 shows this data. The most surprising feature of these curves is the occurrence of a double-peak structure of κ for the ab direction (left panel), which is missing for a heat current along the c direction. Nakamura *et al.* already suggested the possibility of a magnetic contribution within the ab planes, which was denied by Morelli *et al.* [133]. As already mentioned in the introduction, the interpretation in terms of a magnetic origin was further questioned by Cohn *et al.* [81]. These authors investigated the in-plane thermal conductivity of $\text{YBa}_2\text{Cu}_3\text{O}_{7-x}$, also showing a double peak structure, and proposed an explanation based on phonon scattering by optical phonons. Since then several publications which address the thermal conductivity of La_2CuO_4 single crystals have been published [7, 8, 11]. In Ref. [7] the authors systematically investigated the influence of Zn and Sr doping for small doping levels. Another focus in the literature is the low-temperature phononic contribution to investigate e.g. superconductivity and stripe phases. In this respect, mainly doped crystals have been measured [11, 134–142].

Compared to the broad database for La_2CuO_4 , literature data of $R_2\text{CuO}_4$ are scarce. For Pr_2CuO_4 , Inyushkin *et al.* [143] published in-plane data, but the high-temperature dependence of κ is not discussed in this publication. Sologubenko *et al.* published data of Zn-doped Pr_2CuO_4 polycrystals. Sun *et al.* investigated the in-plane and out-of-plane thermal conductivity of $\text{Pr}_{1.3}\text{La}_{0.7}\text{CuO}_4$ for $0.3 \leq T \leq 300$ K [139, 144]. In the first paper the focus is the influence of Ce doping, whereas in the second paper magnetic-field dependent measurements at low temperatures are presented. Further literature data is available for Nd_2CuO_4 [10, 80]. In these publications the authors focus on the low-temperature thermal conductivity and the influence of magnetic fields (see next section). However, the paper of Jin *et al.* shows the in-plane thermal conductivity of Nd_2CuO_4 up to room-temperature. To my knowledge, no literature data are available for $R = \text{Sm}$, Eu , and Gd as well as for out-of-plane thermal conductivity data for all $R_2\text{CuO}_4$ compounds.

4.3.1. Thermal conductivity by Nd Spin Waves in Nd_2CuO_4 ?

In Ref. [80] Jin *et al.* investigated the in-plane thermal conductivity of Nd_2CuO_4 down to 2 K in magnetic fields applied along different in-plane directions. Fig. 4.5 shows the κ_{ab} vs. field data of these authors. For the magnetic field applied along the [100] direction and a temperature of 10 K, κ_{ab} first decreases, up to a field $H_c = 4.5$ T, and then increases again.

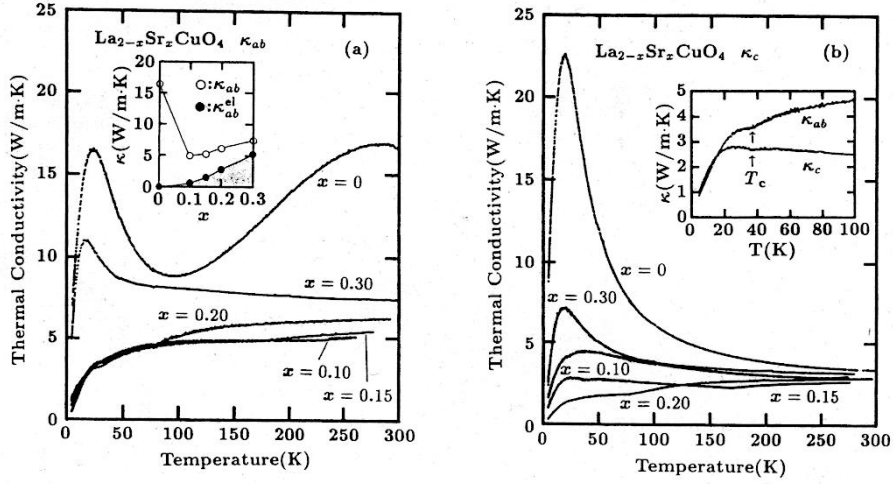


Figure 4.4.: Thermal conductivity data κ_{ab} (left panel) and κ_c (right panel) for $\text{La}_{2-x}\text{Sr}_x\text{CuO}_4$ taken from Ref. [6]. For $x = 0$, a broad maximum is observed in κ_{ab} at $T \approx 290$ K which is absent for κ_c . For Sr doping κ is strongly suppressed.

This increase gets stronger at lower temperatures, and is attributed to a magnetic contribution to κ_{ab} by thermal Nd spin waves. We will call this a "magnon" contribution, to distinct this kind of magnetic thermal conductivity from the high-temperature magnetic contribution which will be discussed in Sec. 4.5.4. The decrease is attributed to phonon-magnon scattering, and the authors estimate the magnon contribution to κ_{ab} by subtracting a linear fit of the low-field thermal conductivity, as depicted in the figure. In this picture the magnetic contribution is only present in a magnetic field, which is attributed to a small spin-wave gap, which is closed at the critical field H_c , coincident with a spin-flop transition. The authors develop a phenomenological model based on the calculated spin-wave dispersion from Ref. [132].

Li *et al.* performed a similar investigation, however, they present κ_{ab} from 10 K down to 50 mK and applied the magnetic field along the a and the c direction [10]. Below ≈ 0.5 K the thermal transport becomes ballistic and the heat carrying excitations are only scattered by the crystal boundaries. The authors argue that below 500 mK the thermal conductivity in zero field is purely phononic due to the spin-wave gap. In a magnetic field of 10 T, $H \parallel ab$, a drastic enhancement of κ is observed. The possible magnon contribution is extracted via $\kappa_{\text{mag}} = \kappa_{ab}(10 \text{ T} \parallel a) - \kappa_{ab}(0 \text{ T})$. The extracted magnon contribution is shown in Fig. 4.6. A closer inspection yields a $T^{2.6}$ dependence of the phononic part due to specular scattering [145], and a T^3 dependence of the magnetic contribution, what allows a distinction of both contributions to κ_{ab} . For higher temperatures the authors conclude from the field dependence of κ with respect to the direction of the magnetic field that both magnons and phonons scatter strongly on each other.

The interpretation of the unusual field dependences in terms of magnon contributions / magnon-phonon scattering used in Refs. [10, 80] was questioned by Sun *et al.* [144]. These authors observed magnetic-field dependences at low temperatures in $\text{Pr}_{1.3}\text{La}_{0.7}\text{CuO}_4$ samples, for measurements along the a and the c axis with magnetic fields applied along different di-

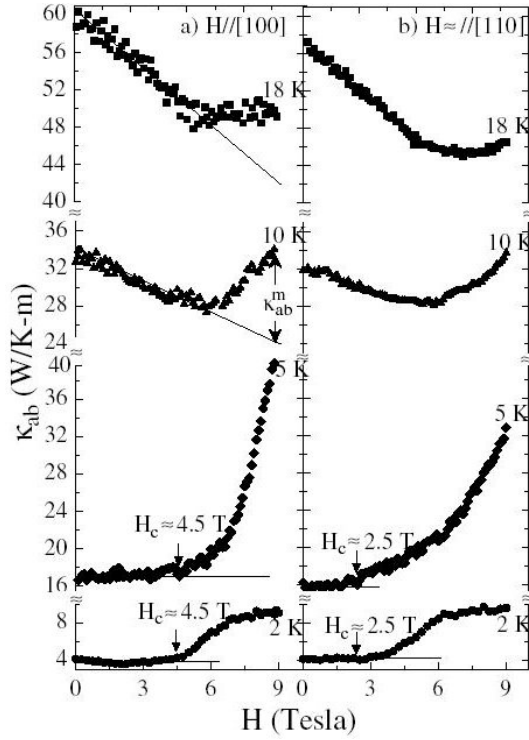


Figure 4.5.: Magnetic field dependent in-plane thermal conductivity of Nd_2CuO_4 at fixed temperatures from 2 to 18 K taken from Ref. [80]. In panel a) H is applied along the [100] direction, in panel b) along [110]. The lines are estimated phononic contributions assuming phonon-magnon scattering linearly suppressing κ vs H . In Ref. [80] the difference of the measured κ_{ab} and the lines (above $H_c = 4.5$ T) is attributed to a magnon contribution to κ_{ab} by spin waves.

rections. The authors argue that because of the dilution of the Pr moments the magnon contribution should be negligible. A further argument against a magnon contribution comes from the comparison of the temperature of the field H_{\min} , where the field-dependent measurements show the minimum with the spin-flop field H_{sf} taken from Ref. [146]. Jin *et al.* attributed the minima in $\kappa(H)$ to the spin-flop transition, which should give a similar temperature dependence of H_{\min} and H_{sf} . Sun *et al.* further argue, that the minimum of κ is caused by resonant scattering process on free $S = 1/2$ spin moments.

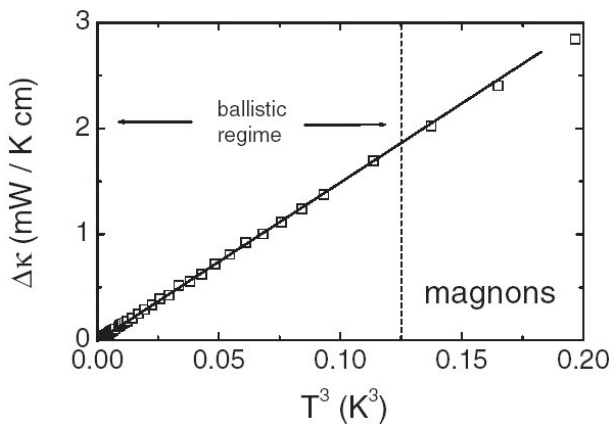


Figure 4.6.: $\kappa_{\text{mag}} = \kappa_{ab}(10 \text{ T} \parallel ab) - \kappa_{ab}(0 \text{ T})$ vs. T^3 for Nd_2CuO_4 from Ref. [10]. The authors attribute the observed T^3 dependence to 3D magnons and argue, that the magnon contribution can be distinguished from the phononic contribution ($\equiv \kappa(0 \text{ T})$), which has a $T^{2.6}$ temperature dependence.

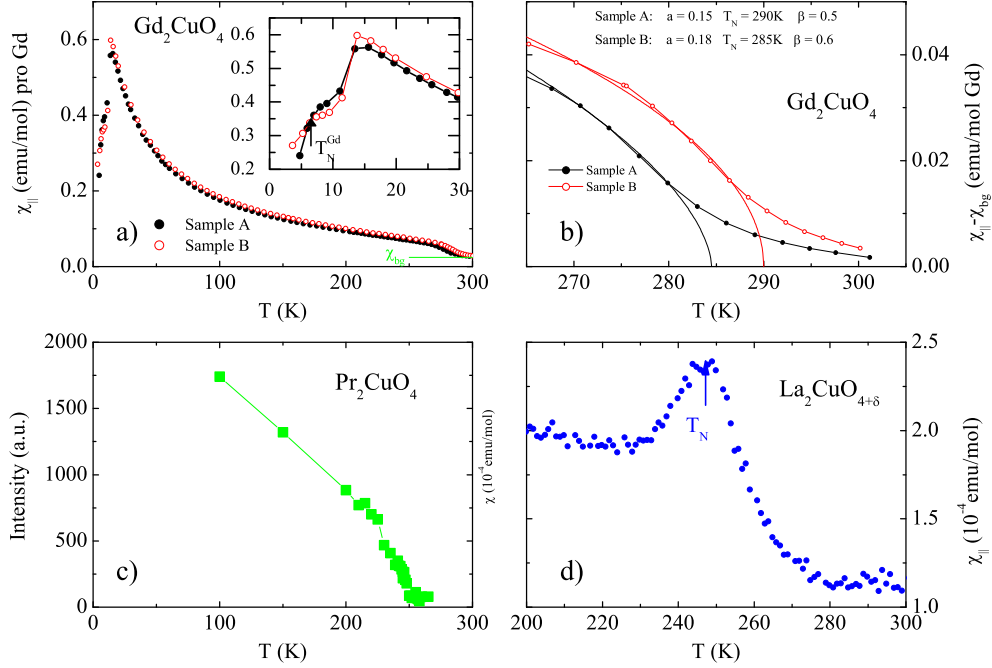


Figure 4.7.: a) Susceptibility for two Gd_2CuO_4 crystals [147]. There are three anomalies, at $T_N^{\text{Gd}} \approx 6.5$ K, 20 K, and $T_N^{\text{Cu}} \approx 290$ K. Inset: The same data up to 30 K. b) Susceptibility of Gd_2CuO_4 around T_N^{Cu} and fits of the weak ferromagnetic moment (lines). c) Neutron scattering intensity of the magnetic $(\frac{1}{2}, \frac{1}{2}, 0)$ reflection of Pr_2CuO_4 [148]. d) Susceptibility of the $\text{La}_2\text{CuO}_{4+\delta}$ crystal. The Néel temperature is at the peak position [149].

4.4. Samples

The $R_2\text{CuO}_4$ single crystals have been grown by S. Barilo from the Institute of Solid State & Semiconductor Physics in Minsk. They were grown in Pt crucibles by the top-seeded solution method as described in Ref. [152]. The La_2CuO_4 crystal is from F. Nakamura, Department of Quantum Matter, ADSM, Hiroshima University. It is grown by a traveling-solvent floating-zone method.

All crystals have been oriented using a Laue camera and cut into rectangular pieces. Sample sizes are listed in Table 4.1. The accuracy of the orientation with respect to the crystal axes is about 2° . Since the Sm_2CuO_4 crystal has approximately the shape of a cuboid, it has not been cut. Here, the misalignment with respect to the c axis amounts to $\simeq 10^\circ$. The shape of Pr_2CuO_4 and Gd_2CuO_4 allowed measurements of κ_c with a heat current j_H parallel to the c axis, i.e. perpendicular to the CuO_2 planes, and of κ_{ab} with j_H within the CuO_2 planes. For $R = \text{Nd}$, Sm , and Eu , we could only measure κ_{ab} , because these crystals were very thin with lengths of less 0.4 mm parallel to the c axis. For $R = \text{Pr}$, Nd , and Gd we measured κ_{ab} with j_H parallel to the a' axis of the HTT phase, which has an angle of $\simeq 45^\circ$ with respect to the orthorhombic a and b axes. For $R = \text{Eu}$ and Sm j_H had an arbitrary orientation with respect to the a and b axes. Therefore the magnetic field direction in the latter compounds was also in an arbitrary in-plane direction for the measurements with $H \neq 0$ T.

The finite DM interaction for $R = \text{La}$ and Gd causes a weak ferromagnetic moment, which

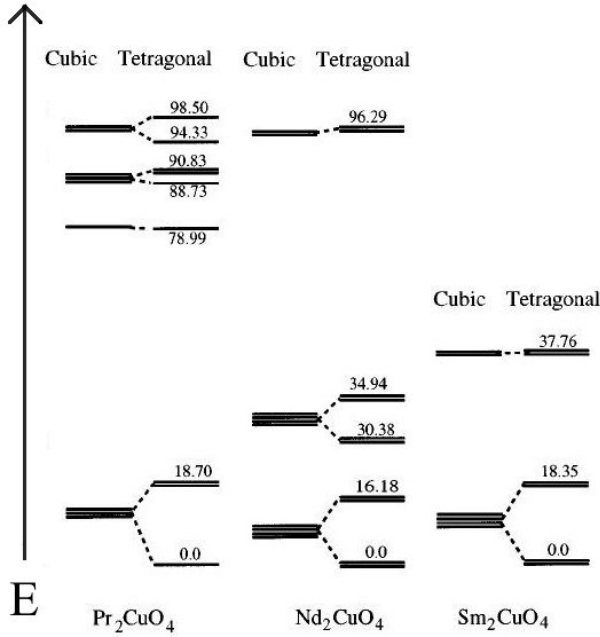


Figure 4.8.: $4f$ level scheme for Pr_2CuO_4 , Nd_2CuO_4 , and Sm_2CuO_4 , taken from Ref. [150]. Energies are given in meV. The level schemes are shown for the tetragonal crystal field. The cubic level scheme is obtained by setting the non-cubic part of the crystal field to zero.

allows an easy determination of the Néel temperatures T_N by measurements of the magnetic susceptibility χ . For Gd_2CuO_4 , J. Baier and H. Roth performed measurements of $\chi(H||ab)$ on two different crystals (labeled Sample A and Sample B) in a SQUID-magnetometer (Cryogenics). The curves are measured in a magnetic field of 50 mT with increasing temperature after cooling the samples in the field (field cooled, FC). Fig. 4.7a shows the measured susceptibility for both crystals. The low-temperature behavior is complex as discussed in Sec. 4.2.3. At $T \approx 290$ K one can see the spontaneous increase of χ with decreasing temperature which is caused by the weak ferromagnetic moment. Panel b) of Fig. 4.7 shows this temperature range in more detail. To determine T_N^{Cu} , the data are fitted by

$$\chi(T) = a \left(1 - \frac{T}{T_c}\right)^\beta + \chi_0, \quad (4.1)$$

what describes a ferromagnetic moment near the transition for $T < T_c$ [16]. The background contribution is estimated as $\chi_0 = 0.025$ emu/mole and is mainly due to the paramagnetic signal of the Gd $4f$ moments⁴. The fits yields the values of T_N listed in Tab. 4.1⁵, the other fit parameters are listed in Fig. 4.7. The value $T_N \simeq 288$ K is in agreement with the highest values reported for Gd_2CuO_4 [123, 153].

For $R = \text{Pr}$, Nd , Sm , and Eu susceptibility measurements were performed by M. Kriener in a vibrating sample magnetometer (VSM). The results of these measurements are shown in Fig. 4.9. The susceptibilities were also calculated using the CFT Mathematica package[36] (see Sec. 2.4 for details). The crystal field parameters were taken from Refs. [150, 154, 155]. The theoretical results were compared to calculations from Ref. [150]. These authors calculated the susceptibility for $R = \text{Pr}$, Nd , and Sm , based on the crystal field splitting of the $4f$

⁴We use a temperature independent background contribution χ_0 , since the weak temperature dependence of χ_0 has no influence on T_N .

⁵These values are slightly smaller than in Ref. [73], since there the background contribution χ_0 was neglected. However, the difference of the estimated T_N is very small.

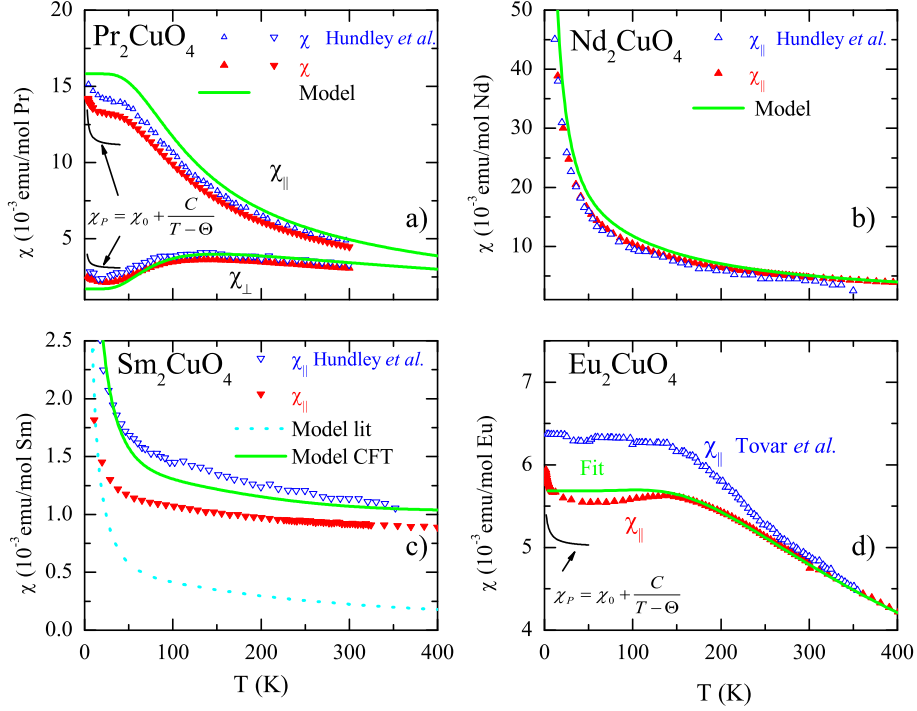


Figure 4.9.: Magnetic susceptibility of $R_2\text{CuO}_4$ with $R = \text{Pr}, \text{Nd}, \text{Sm},$ and Eu . Shown are data measured by M. Kriener in a VSM in FC configuration in 50 mT (open symbols) and literature data (close symbols) taken from Refs. [85, 118]. Lines for $R = \text{Pr}, \text{Nd},$ and Sm : Our calculations of χ . Dotted line for Sm_2CuO_4 : Calculation from Ref. [150]. Line for Eu_2CuO_4 : Fit according to Ref. [151], see text.

multiplet. This calculation is restricted to the Hund's rule J ground state multiplet, whereas our calculation includes all multiplets. Fig. 4.8 shows the calculated splitting of the $(2J + 1)$ -fold degenerate ground state. Here, the level schemes in the tetragonal and cubic crystal field are shown⁶. The results of our calculations are plotted as solid lines in Fig. 4.7.

Fig. 4.7a shows the data of Pr_2CuO_4 . Here, $\chi_{||}$ with $H \parallel a$ and χ_{\perp} with $H \parallel c$ were measured (closed symbols). For comparison data obtained by Hundley *et al.* [85] are also shown (open symbols) and are in very good agreement with our data. The susceptibility is strongly anisotropic. The calculated susceptibility $\chi_{||}$ is somewhat too high, but gives a good description of the data, taking into account, that the calculation is based on the experimentally obtained crystal field energies, with no additional fit parameters. Panel b) presents the results of $\chi_{||}$ for Nd_2CuO_4 . The agreement with the literature and the calculation is also good. Our calculated susceptibilities for $R = \text{Pr}$ and Nd are in good agreement with the results from Ref. [150]. For Sm_2CuO_4 (panel c) $\chi_{||}$ was measured. Here the data are smaller than the data taken from the literature. This may be partly caused by a misalignment of the sample (see Sec. 4.4), since χ_{\perp} is smaller in Sm_2CuO_4 [85]. Our calculation gives a good description of the data, in contrast to the calculation taken from Ref. [150]. The reason herefore is an additional van Vleck contribution to $\chi_{||}$ due to level mixing with the $J = 7/2$ excited state [150]. This

⁶According to Ref. [150], the tetragonal crystal field is a unique linear combination of cubic and non-cubic elements. It follows, that the cubic components can be obtained by switching off the noncubic elements.

effect is negligible for $R = \text{Pr}$ and Nd , where the excited states have much higher energies. In Eu_2CuO_4 (panel d) the van Vleck term of Eu^{3+} dominates. The data agree qualitatively with the literature [118]. However, the low-temperature data are too small, and there is an unexpected minimum at $T \approx 50$ K. The increase at lowest temperatures can be attributed to paramagnetic impurities, but the reason for the minimum is not clear, and has most likely an experimental reason. At present, the $4f^6$ Hamiltonian is not implemented in the CFT Mathematica package[36], so another approach is used. In Eu_2CuO_4 (Fig. 4.7d) the susceptibility is also highly anisotropic due to the tetragonal crystal field. M. Hücker performed a detailed analysis of the anisotropic van Vleck magnetism of Eu^{3+} in a tetragonal crystal field [151]. The Eu^{3+} van Vleck susceptibility is determined by three parameters, the crystal field parameter $B_{20}^{J=1}$, and the level splitting of the 7F_0 ground multiplet to the higher J multiplets 7F_0 (splitting E_1) and 7F_2 (splitting $E_2 = 3E_1$). A fit by Eq. 8.7 from Ref. [151] yields the values $B_{20}^{J=1} = -39$ K and $E_1 = 590$ K, and gives a good description of the data⁷.

For $\text{La}_2\text{CuO}_{4+\delta}$, T_N^{Cu} can easily be determined by the maximum of the susceptibility [156]. H. Hartmann measured the susceptibility χ_\perp in a VSM, in a magnetic field of 0.1 T in a FC configuration. Panel d) of Fig. 4.7 shows the data and we obtain $T_N = 245$ K, which is comparatively low ($T_N(\delta = 0) \approx 325$ K [11]). This suppression is due to a significant amount of excess oxygen, which the samples adopt automatically if they are stored in air. Usually $\text{La}_2\text{CuO}_{4+\delta}$ samples are annealed in vacuum to obtain a good stoichiometry ($\delta \approx 0$), but here the purpose was to measure a sample with a low T_N , and the sample was not annealed. Because of phase separation effects, the Néel temperature is not sufficient to determine the oxygen content, this will be discussed in Sec. 4.5.1. The determination of T_N from $\chi(T)$ does neither work in the undistorted samples with $R = \text{Pr}$, Nd , and Sm , since there is no weak ferromagnetism nor for $R = \text{Eu}$, where the structural transition takes place below T_N . According to Ref. [80] there is a slope change of χ_{ab} at T_N in Nd_2CuO_4 . However, we could not reproduce such a feature in χ_{ab} of our crystal. For Pr_2CuO_4 , D. Senff determined $T_N \simeq 250$ K at the Laboratoire Leon Brillouin, Saclay by neutron diffraction, see Fig. 4.7c. This value is well below the maximum values up to $T_N \simeq 280$ K reported for this compound (see Tab. 4.2).

Unfortunately, the Nd_2CuO_4 crystal is too small for neutron diffraction and this method cannot be applied for $R = \text{Eu}$ and Sm because of the large neutron absorption cross section of these elements.

4.4.1. Contributions by Paramagnetic Impurities

At low temperatures an additional contribution due to paramagnetic impurities is possible. In the following we will estimate the impurity contents of our samples, because paramagnetic impurities can play an important role for the thermal conductivity. If the intrinsic susceptibility becomes temperature independent for $T \rightarrow 0$, an additional Curie-like behavior of the susceptibility can be observed. This is the case for Pr_2CuO_4 and Eu_2CuO_4 , see Fig. 4.9. Here the Curie contribution can be obtained by fitting the low-temperature susceptibility by

$$\chi_P(T) = \chi_0 + C/(T - \Theta), \quad (4.2)$$

where χ_0 is the temperature-independent contribution, C the Curie constant and Θ the Curie-Weiss temperature. These fits were performed up to 25 K, and the results are listed in Tab. 4.3.

⁷In Ref. [151] the values $E_1 = 545$ K and $B_{20}^{J=1} = -165$ K were obtained for Sr doped $\text{La}_{1.8}\text{Eu}_{0.2}\text{CuO}_4$ (which has a different structure).

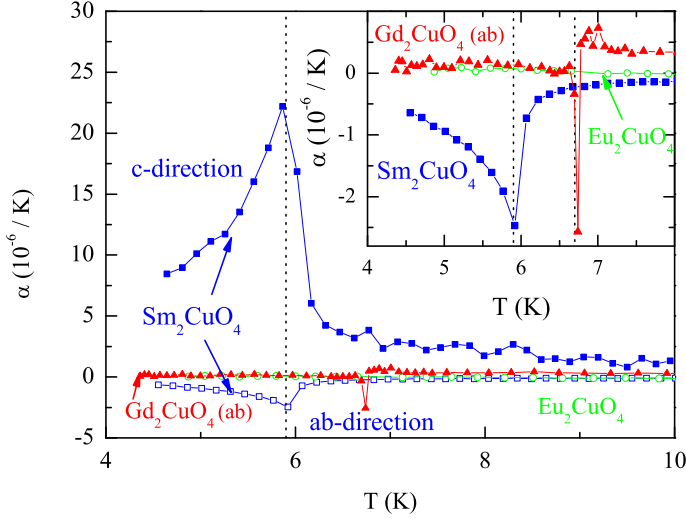


Figure 4.10.: Thermal expansion of $R_2\text{CuO}_4$ with $R = \text{Sm}, \text{Eu}, \text{and Gd}$. For $R = \text{Sm}$ α_{ab} (\square) and α_c (\blacksquare) show large anomalies at T_N^{Sm} , whereas the anomaly in α_{ab} for T_N^{Gd} (\blacktriangle) is much smaller (see Inset). For $R = \text{Eu}$ (\circ) no anomalies are observed [157, 158].

		$\chi(T)$				$M(H)$			
	H	C $10^{-3} \frac{\text{emuK}}{\text{mole}}$	χ_0 $10^{-3} \frac{\text{emu}}{\text{mole}}$	Θ K	n 10^{-3}	χ_0 $10^{-3} \frac{\text{emu}}{\text{mole}}$	g	n 10^{-3}	C $10^{-3} \frac{\text{emuK}}{\text{mole}}$
Pr_2CuO_4	ab	11.0	26	-0.76	2.9	11.0	2.0	0.40	1.6
Pr_2CuO_4	c	5.0	4.0	-0.38	1.3				
Eu_2CuO_4	ab	3.2	11.0	2.1	0.9				
Sm_2CuO_4	ab								
$\text{Sr}_2\text{CuO}_2\text{Cl}_2$	ab	1.24		-4.6	0.3	3.6	2.0	0.9	3.4
$\text{Sr}_2\text{CuO}_2\text{Cl}_2$	ab	6.95		0.0	0.2				
							3.0	0.6	5.0

Table 4.3.: Parameters for the low-temperature paramagnetic susceptibility for $R_2\text{CuO}_4$ with $R = \text{Pr}, \text{Sm}, \text{and Eu}$; and $\text{Sr}_2\text{CuO}_2\text{Cl}_2$. The left side of the table shows the values extracted from the temperature-dependent susceptibility measurements (Fig. 4.9); the right side the values estimated by the magnetization curves (Fig. 4.11). If no other values is listed, a g factor of 2 was used for the estimations. The values for $\text{Sr}_2\text{CuO}_2\text{Cl}_2$ are taken from Ref. [146].

The accuracy of the determination of C is limited, because the assumption of a constant χ_0 is not perfectly fulfilled. The g factor of the impurities seems to be anisotropic, from $g_{\parallel}/g_{\perp} = \sqrt{C_{\parallel}/C_{\perp}}$ it follows an anisotropy of $1.3 \dots 1.5$. An other way to estimate the paramagnetic contribution, is to analyze the magnetization at low temperatures. Fig. 4.11 shows the magnetization curves at $\approx 2 \text{ K}$ up to 14 T for Eu_2CuO_4 and Sm_2CuO_4 . In Eu_2CuO_4 , see the upper panel, $M(T)$ is almost linear, since the paramagnetic Eu contribution dominates. The paramagnetic impurity contribution M_P is extracted by a linear fit $M_{\text{Eu}} = \chi_0 * H + M_0$ for high magnetic fields, which is subtracted from the data. The total magnetization data are scaled by a factor of 50. The resulting curve is fitted by a Brillouin function

$$M(H) = NgJ\mu_B B_J(x) \quad \text{and} \quad x = gJm_B H/k_B T. \quad (4.3)$$

$N = n \cdot N_A$ is the amount, J the total momentum and g the g factor of the paramagnetic moments. The size of the Curie constant makes it unlikely that the Curie contribution is

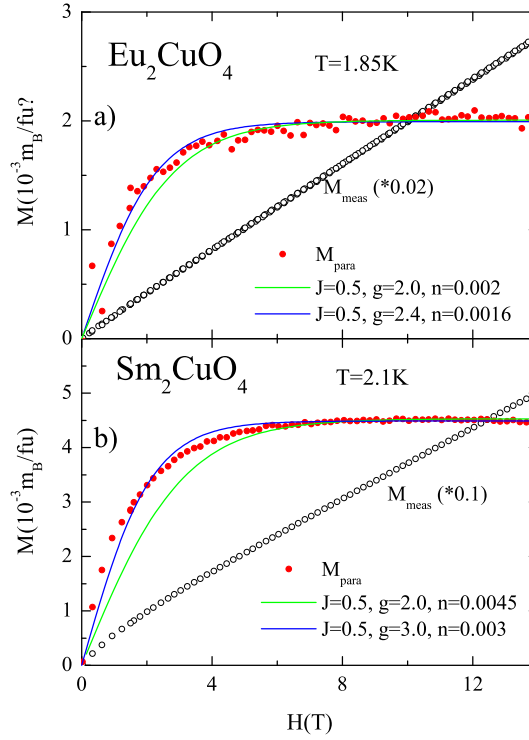


Figure 4.11.: a): Magnetization of Eu_2CuO_4 . The paramagnetic contribution is extracted by subtracting a linear high-field fit. Lines are calculated magnetization curves according to Eq. 5.6. b): The same for Sm_2CuO_4 .

caused by foreign atoms. Further in Ref. [144] χ_P showed an annealing dependence, which is not expected if it is caused by foreign atoms. In this paper an amount $n \approx 1\%$ of free $S = 1/2$ moments is estimated. Because C is of the same order of magnitude for Pr_2CuO_4 , $Pr_{1.3}La_{0.7}CuO_4$, $Sr_2CuO_2Cl_2$, and Eu_2CuO_4 , the most likely origin of χ_P is the occurrence of nearly free Cu^{2+} moments due to crystal imperfections or impurity phase inclusions, yielding $J = 1/2$. This explanation was proposed in $Sr_2CuO_2Cl_2$ [146], where similar values of C were observed. The g factor is also not known, so it was either set to 2.0 or fitted. The fits are shown as solid lines in Fig. 4.11. The description of the data is good, with slightly better fits if g is fitted, too. However, one has to keep in mind the large "background" from the R moments, which makes it likely that M_P has a large uncertainty. Therefore the value for the g factor should not be taken to literally. For Eu_2CuO_4 the difference of the Curie constant obtained from $M(H)$ and $\chi(T)$ is considerably large (a factor of two), which is due to the uncertainty of the background estimation for both cases.

4.4.2. Thermal Expansion

To check, if the antiferromagnetic Néel transitions of the Sm and Gd moments are present and to determine the Néel temperatures, the zero-field thermal expansion was measured by M. Kriener. Fig. 4.10 shows the low-temperature data. In the main panel α_{ab} and α_c for Sm_2CuO_4 are shown. In Sm_2CuO_4 for both directions a large peak is seen at $T_N = 5.9K$,

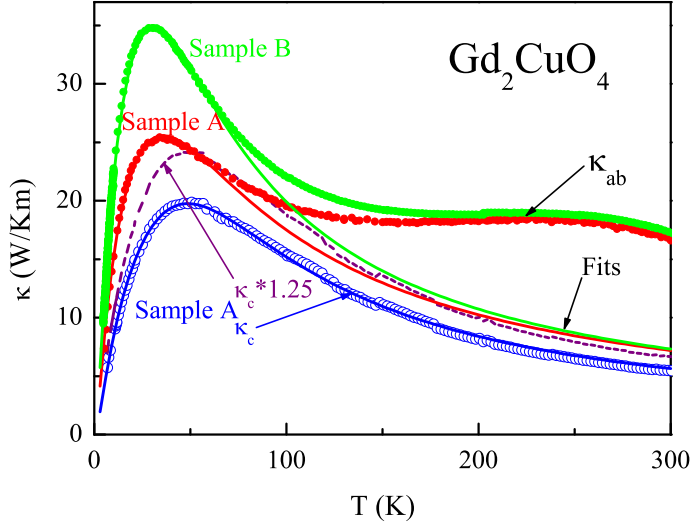


Figure 4.12.: In-plane (κ_c) and out-of-plane (κ_{ab}) thermal conductivity of Gd_2CuO_4 . κ_{ab} was measured on two different crystals. Solid lines are fits by the Debye model and the dashed line is κ_c multiplied by a factor of 1.25 (see text) [57, 73, 74].

which is typical for a second-order phase transition. In comparison to α_c , the anomalies of α_{ab} are much smaller in Sm_2CuO_4 , and plotted enlarged in the inset of Fig. 4.10. For Gd_2CuO_4 a small anomaly is seen at $T_N \approx 6.7$ K, which shows that the Néel transition is present.

The thermal expansion of Eu_2CuO_4 was measured as a reference by J. Baier. Here, the lattice contribution is dominant, which is much smaller than the effects caused by the Néel transition. Unfortunately no information about the structural phase transition could be obtained in this measurement, because the used dilatometer does not work well for temperatures higher than ≈ 150 K.

4.5. Experimental Results: Zero Field

4.5.1. Gd_2CuO_4 and Pr_2CuO_4

Fig. 4.12 shows the thermal conductivity of Gd_2CuO_4 measured on two different crystals. Sample A allowed to measure κ_{ab} and κ_c , whereas Sample B was too thin to measure κ_c . In Fig. 4.13 we display κ_{ab} and κ_c of Pr_2CuO_4 . Apart from differences around the low-temperature maximum, which is very sensitive to the sample quality, the data agree well to the previously reported κ_{ab} of Pr_2CuO_4 [143]. For both compounds κ_c follows the typical temperature dependence of the thermal conductivity of acoustic phonons. As shown by the solid lines, κ_c can be reasonably well described within a Debye model. The fits are done using Eqs. 2.5 and 2.6, see Sec. 2.1.2 and the corresponding fit parameters are given in Table 4.1.

In both crystals κ_{ab} exceeds κ_c over the entire temperature range. The low-temperature maxima of κ_{ab} and κ_c for Gd_2CuO_4 are slightly shifted in temperature. The most striking anisotropy is, however, the additional, broad maximum of κ_{ab} around 250 K. Although the low-temperature maxima of κ_{ab} strongly differ for the two crystals with $R = \text{Gd}$ indicating differences in the crystal quality, the magnitudes of their high-temperature maxima are almost identical. In Pr_2CuO_4 κ_{ab} also shows an additional high-temperature maximum, but its magnitude is less pronounced (see section 4.5.4).

The double-peak structures of κ_{ab} cannot be modeled by the usual Debye model, but it is possible to describe the low-temperature maxima up to about 50 K. Comparing the corresponding fit parameters of κ_{ab} and κ_c (see Tab. 4.1), the largest differences are found for

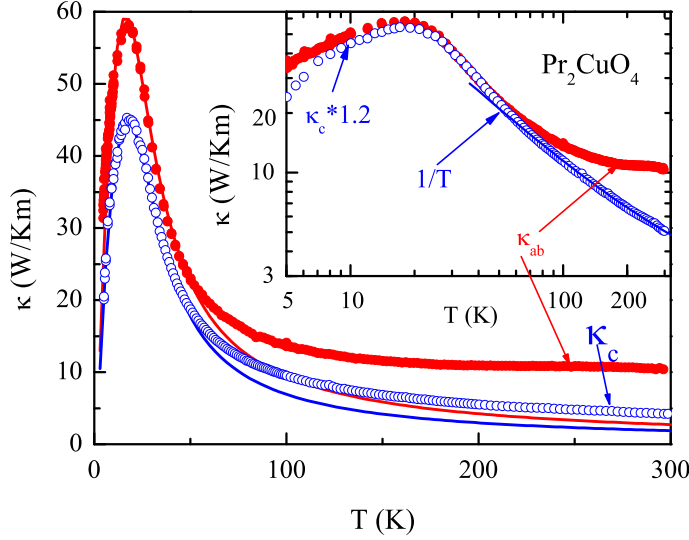


Figure 4.13.: In-plane (κ_c) and out-of-plane (κ_{ab}) thermal conductivity of Pr_2CuO_4 . Lines are fits by the Debye model (see text). Inset: The same data on double-logarithmic scales with κ_c multiplied by a factor of 1.2. The temperature dependences of κ_{ab} and κ_c around the low-temperature maxima are nearly the same. Above about 70 K κ_c follows a $1/T$ behavior (solid line), whereas an anomalous high-temperature upturn is present in κ_{ab} [57, 73, 74].

the parameter D , which is significantly larger for the fits of κ_c than for those of κ_{ab} . This parameter gives the strength of phonon scattering by planar defects and it appears reasonable that due to the layered structure of $R_2\text{CuO}_4$ scattering by planar defects should be more effective for a heat current perpendicular to the planes than for j_H within the planes. Thus the different magnitudes of the low-temperature maxima of κ_c and κ_{ab} can be interpreted as a consequence of the layered structure. The high-temperature maxima of κ_{ab} around 250 K will be discussed in section 4.5.4.

4.5.2. Nd_2CuO_4 , Sm_2CuO_4 , and Eu_2CuO_4

In Fig. 4.14 the in-plane thermal conductivities κ_{ab} of Nd_2CuO_4 , Sm_2CuO_4 , and Eu_2CuO_4 are shown. The data of $R = \text{Nd}$ and Sm are very similar to each other and also to those of $R = \text{Pr}$ and Gd . In all crystals κ_{ab} exhibits a well defined low-temperature peak around 20 K and an additional broad maximum around 250 K. For $R = \text{Nd}$ similar results have been obtained by Jin *et al.* [80], but κ_{ab} of our crystal is systematically lower in the entire temperature range (see inset of Fig. 4.14). For Eu_2CuO_4 , the low-temperature peak of κ_{ab} is almost completely suppressed. As described above, for $R = \text{Eu}$ a structural transition takes place at around 170 K. The suppression of the low-temperature peak is most probably a consequence of this structural instability, which prevents a strong increase of the phonon mean free path at low temperatures. In contrast, however, the high-temperature maximum of κ_{ab} is hardly affected by this structural transition. The high-temperature maximum for Eu_2CuO_4 is even more pronounced than for the structurally stable crystals with $R = \text{Nd}$ and Sm .

4.5.3. $\text{La}_2\text{CuO}_{4+\delta}$

In contrast to the rare earth cuprates, La_2CuO_4 can be easily doped by a significant amount of oxygen. For small oxygen doping levels, the main effect is a suppression of T_N^{Cu} already for very small amounts of oxygen [159, 160]. For higher oxygen doping levels, however, the phase

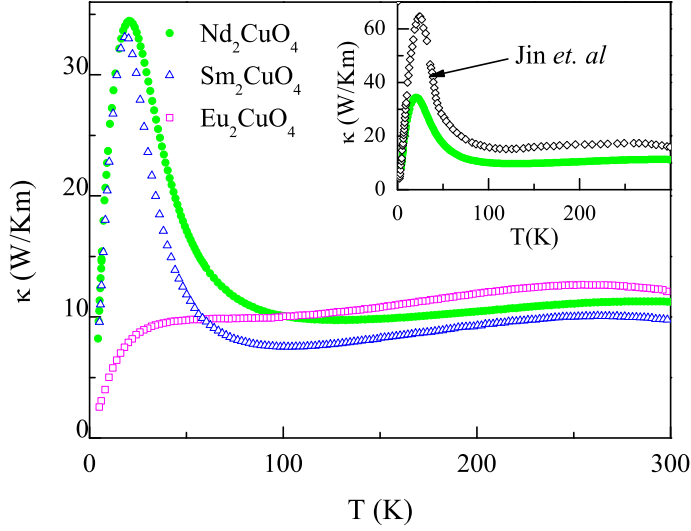


Figure 4.14.: In-plane thermal conductivity of Nd_2CuO_4 , Sm_2CuO_4 , and Eu_2CuO_4 . For $R = \text{Eu}$ the low-temperature maximum is suppressed [57, 73]. The inset compares κ_{ab} (●) of our Nd_2CuO_4 crystal with data (○) from Ref. [80].

diagram turns out to be very complex. This is because of a phase separation in oxygen-rich and oxygen-poor regions [72, 161] occurs. Temperature-dependent resistivity measurements show various transitions, with a complex doping and temperature dependence [162]. The in-plane electrical conductivity σ_{ab} for our crystal is shown in Fig. 4.15b. Four transitions can be observed in the measurements, which are clearly seen in the derivative of σ_{ab} , Fig. 4.15c. The transition at 35 K is the superconducting transition. The three transitions at high temperatures are labeled T_f , T_m , and T_s in analogy to Ref. [162]. The anomalies at T_f and T_m are hysteretic. These findings agree with the literature data from Ref. [162]. Comparison of the in-plane resistivity with Ref. [162] yields $\delta \approx 0.01$ for our crystal. The temperature of the transition at T_s , was taken as a reference for the comparison.

Fig. 4.15a shows the thermal conductivity results for the ab plane and for the c direction. The qualitative behavior of κ_{ab} is the same as for $\text{La}_2\text{CuO}_{4+\delta}$ with $\delta \approx 0$ (Fig. 4.4), a double-peak structure of κ_{ab} as a function of temperature. However, the absolute values of the low-temperature maximum as well as the high-temperature maximum of κ_{ab} are smaller for our sample. An additional anomaly is observed at $T = 290$ K for κ_{ab} , which is absent for κ_c . We conclude that the anomaly is due to a change of the magnetic contribution to κ_{ab} . A similar feature was observed in [142] and attributed to the Néel temperature. However, this turned out not to be the case [162, 163]. The comparison of κ_{ab} and σ_{ab} clearly shows that the transition in κ_{ab} can be attributed to the transition at T_s , which is much higher than T_N^{Cu} for our crystal, in agreement with Refs. [162, 163].

In contrast to T_s , the other anomalies seen in σ_{ab} do not cause any anomalies in the thermal conductivity.

4.5.4. Discussion: Zero Field

The results of κ_c of Pr_2CuO_4 and Gd_2CuO_4 together with κ_c of La_2CuO_4 (Refs. [6–8, 11]) clearly reveal that, on the one hand, the out-of-plane thermal conductivities of all these compounds of slightly different structures (tetragonal and orthorhombic T', and orthorhombic T) do not exhibit any indications of an anomalous high-temperature behavior. On the other hand, all in-plane conductivities clearly show additional broad high-temperature maxima. The fact that these high-temperature maxima are present in crystals without ($R_2\text{CuO}_4$ with

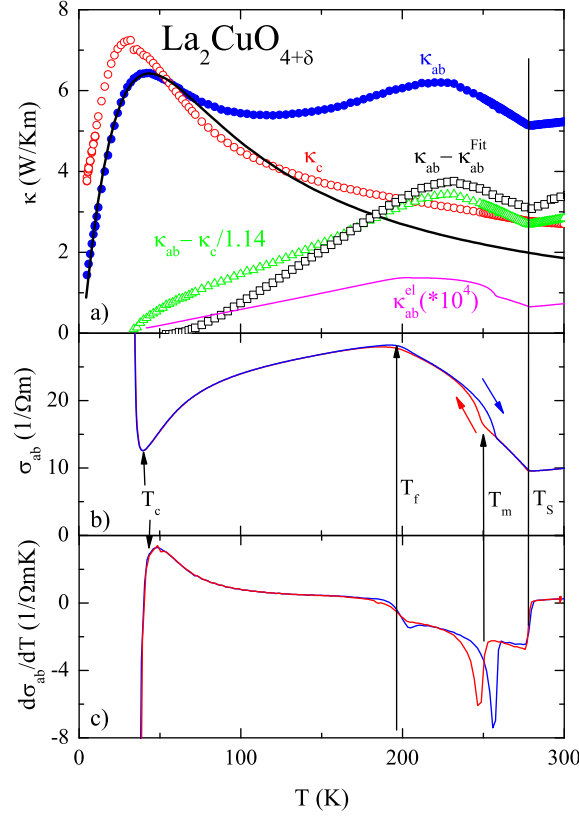


Figure 4.15.: a) Thermal conductivity of $\text{La}_2\text{CuO}_{4+\delta}$ for an in-plane (\bullet) and an out-of-plane (\circ) heat current. The magnetic contribution to κ_{ab} can be estimated by $\kappa_{\text{mag}} = \kappa_{ab} - \kappa_{ab}^{\text{Fit}}$ (\square). For comparison, the difference $\kappa_{ab} - \kappa_c/1.14$ is plotted (\triangle), too. Furthermore, the estimated electronic contribution to κ_{ab} is shown (solid line, scaled by a factor of 10^4). b) In-plane electrical conductivity σ_{ab} of the same crystal. The transition at T_S corresponds to the transition which is seen in κ_{ab} . The transitions at 200 K and 250 K are hysteretic, but are not seen in κ_{ab} . c) Temperature derivative of σ_{ab} .

$R = \text{Pr}, \text{Nd}, \text{Sm}$, and $\text{Sr}_2\text{CuO}_2\text{Cl}_2$) or with (different) structural instabilities (T : $R = \text{La}$; T' : $R = \text{Eu}$ and Gd) unambiguously shows that the anomalous contribution to κ_{ab} does not depend on the existence of structural instabilities. This complements the previous suggestion based on a comparative study of κ of $\text{Sr}_2\text{CuO}_2\text{Cl}_2$ and La_2CuO_4 (Refs. [27, 82]). The most natural explanation for the high-temperature maximum of κ_{ab} is an additional contribution to the heat transport caused by magnetic excitations.

The similar behavior of κ for all $R_2\text{CuO}_4$ confirms that such a magnetic contribution κ_{mag} to the in-plane heat transport is an intrinsic property of the CuO_2 planes. It remains, however, to be clarified what determines the magnitude of κ_{mag} . For a quantitative analysis the in-plane thermal conductivity is considered as the sum of a phononic and a magnetic contribution

$$\kappa_{ab} = \kappa_{\text{ph}} + \kappa_{\text{mag}}, \quad (4.4)$$

which are only weakly coupled to each other. In general, such an Ansatz can be used when the characteristic energy scales for the two contributions are well separated from each other.

For example, this is usually the case for electronic and phononic heat transport since the Fermi temperature is much larger than the Debye temperature, i.e. $T_F \gg \Theta_D$. In the case of $R_2\text{CuO}_4$ it is a priori not clear whether the assumption of weakly coupled phononic and magnetic contributions is fulfilled, since the magnetic coupling J is only about four times as large as Θ_D (see Table 4.1). However, the experimental observation that κ_{ab} shows two characteristic maxima, which are well separated from each other, encourages to use Eq. (4.4).

In order to separate κ_{mag} from κ_{ab} the assumption is made that in the region of the low-temperature peak κ_{mag} is negligibly small. We fit the data for $T < 50$ K (Gd_2CuO_4 : $T < 85$ K) by the Debye model (see Eq. 2.5) and subtract the extrapolation of the fit from the measured data up to room temperature, i.e. $\kappa_{\text{mag}} = \kappa_{ab} - \kappa_{\text{ph}}^{\text{fit}}$. For the fit θ_D , v_s and L are not taken as free fit parameters, but experimentally determined values are used. If no experimental values are available as e.g. for Gd_2CuO_4 , values similar to those obtained in the other compounds (see Table 4.1) were taken. The resulting fits hardly change when the upper boundary of the temperature range is varied by ± 10 K. This analysis is not possible for Eu_2CuO_4 , because the low-temperature maximum is not well-enough pronounced. However, even without a fit rather similar values of κ_{mag} for $R = \text{Nd}$, Sm , and Eu are expected, because the high-temperature data of κ_{ab} are very similar for these crystals (see Fig. 4.14). One can check the applicability of the Debye model to describe the phononic contribution by corresponding fits of κ_c , i.e. the temperature range of the fit is restricted to the low-temperature maxima and then the high-temperature extrapolations of the fits are compared to the measured κ_c . As shown in Figs. 4.12 and 4.13 these fits yield a good description of κ_c for $R = \text{Gd}$ over the entire temperature range, whereas in the case of Pr the high-temperature values of κ_c are slightly underestimated by the fit. This probably arises from the sharper low-temperature peak for $R = \text{Pr}$. Since the low-temperature peaks of κ_{ab} for $R = \text{Pr}$, Nd , and Sm are also rather sharp, one may expect that the corresponding Debye fits will also underestimate the high-temperature values of the phononic contribution of κ_{ab} and consequently the magnetic contributions κ_{mag} may be overestimated to some extent. For the $\text{La}_2\text{CuO}_{4+\delta}$ crystal the low-temperature maximum is small, and a Debye fit may be not so accurate, so the difference $\kappa_{\text{mag}} = \kappa_{ab} - \kappa_c/1.14$ is also plotted, with basically the same result, see Fig. 4.15.

The upper panel of Fig. 4.16 gives a comparison of the resulting κ_{mag} of all our $R_2\text{CuO}_4$ crystals, the previous result of $\text{Sr}_2\text{CuO}_2\text{Cl}_2$ (Ref. [82]), and κ_{mag} obtained from an analysis of κ_{ab} measured on Nd_2CuO_4 (Ref. [80]). For comparison, κ_{mag} obtained from the literature data of various La_2CuO_4 crystals [6, 7, 11] are also shown. Obviously, the temperature dependence of κ_{mag} is very similar for all crystals, but the magnitude of the broad maximum varies between about 7 and 10 W/Km for our $\text{Sr}_2\text{CuO}_2\text{Cl}_2$ and $R_2\text{CuO}_4$ crystals and from about 12 to 25 W/Km for the various crystals from literature with $R = \text{La}$ and Nd [6, 7, 11, 80]. Although these differences are not too large, it is unlikely that they simply arise from the experimental uncertainty in the quantitative determination of κ_{mag} .

Because the magnetic properties are rather similar for the different crystals, one expects that the different κ_{mag} mainly arise from differences in the scattering of the magnetic excitations. Possible scattering mechanisms are scattering between magnetic excitations and scattering by defects, phonons, and charge carriers. One may suspect that scattering between magnetic excitations, comparable e.g. to phonon-phonon Umklapp scattering, plays the most important role with respect to the temperature dependence of κ_{mag} . A deeper analysis of this scattering requires a detailed theoretical model for the dynamics of magnetic excitations, but even without such a model one may conclude that the similar magnetic properties naturally explain the similar temperature dependences of κ_{mag} of the different compounds.

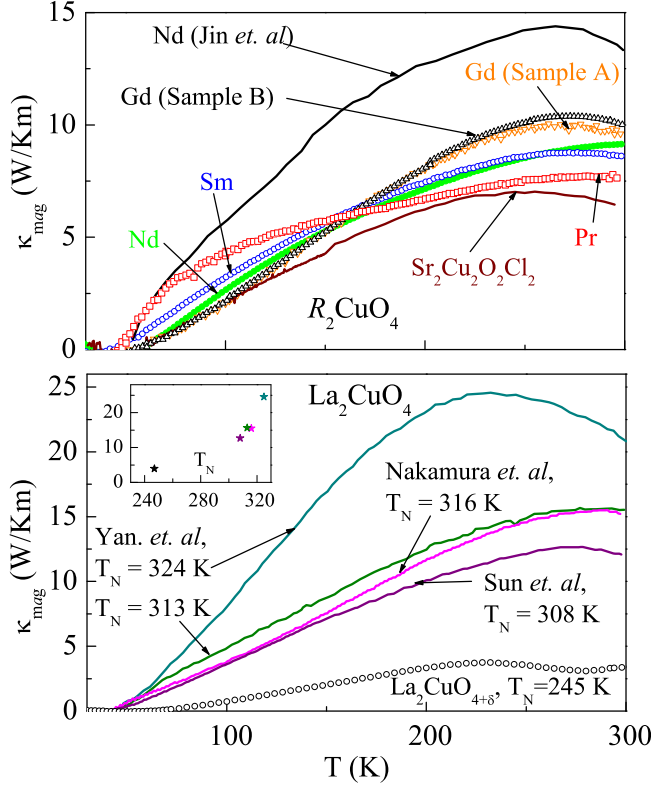


Figure 4.16.: Magnetic contributions to the in-plane thermal conductivity, calculated via $\kappa_{\text{mag}} = \kappa_{ab} - \kappa_{\text{ph}}$, where κ_{ph} is determined by a Debye fit of the low-temperature maximum. Upper panel: Values calculated from the measurements of κ_{ab} of $R_2\text{CuO}_4$ and from the data from Ref. [80]. Lower panel: The same analysis for various data of $\text{La}_2\text{CuO}_{4+\delta}$ taken from Ref. [6, 7, 11] and of our crystal with $T_N = 245$ K. Inset: The maximum of the calculated κ_{mag} vs. the Néel temperature for $\text{La}_2\text{CuO}_{4+\delta}$ [57, 73].

The influence of defects and charge carriers on the thermal conductivity has been investigated in Zn- and Sr-doped La_2CuO_4 [7, 8]. It has been found that Sr doping suppresses κ_{mag} much stronger than Zn doping and κ_{mag} vanishes almost completely above about 1% Sr. For both dopants the magnetic system is diluted, either by replacing magnetic Cu^{2+} by nonmagnetic Zn^{2+} ions or by the formation of Zhang-Rice singlets due to the introduced holes. However, the mobility of the holes strongly enhances the effect of charge-carrier doping, what is also reflected in a much stronger suppression of T_N by Sr doping as compared to Zn doping [164]. As shown in the lower panel of Fig. 4.16, the magnitude of κ_{mag} for the various nominally undoped La_2CuO_4 crystals varies by about a factor of two. Since it is known that $\text{La}_2\text{CuO}_{4+\delta}$ is likely to have some excess oxygen, the maximum of κ_{mag} is plotted as a function of T_N , which is very sensitive to small amounts of δ (Inset of Fig. 4.16). The observed correlation between the magnitude of κ_{mag} and T_N is a clear indication that the different magnitudes of κ_{mag} arise from small amounts of charge carriers in the different crystals [11].

One may suspect that the higher values of κ_{mag} of $R_2\text{CuO}_4$ with $R = \text{La}$ and Nd from Refs. [6, 7, 11, 80] in comparison to our crystals could result from a weak charge carrier doping in our crystals. The rather low $T_N \simeq 250$ K of our Pr_2CuO_4 crystal compared to the T_N values up to $\simeq 280$ K reported in literature [93, 94, 165] supports this view. However, this argumentation can neither explain the low κ_{mag} of our Gd_2CuO_4 with a large $T_N \simeq 292$ K nor does it hold for $\text{Sr}_2\text{CuO}_2\text{Cl}_2$, which is commonly believed to be very stable with respect to charge carrier doping. Unfortunately, not much is known about possible variations of the oxygen content in $R_2\text{CuO}_4$. Irrespective of the question of the exact oxygen stoichiometry, our finding that κ_{mag} is very similar in crystals with and without structural instabilities leads to the conclusion that scattering by phonons seems to play a minor role for the magnetic heat

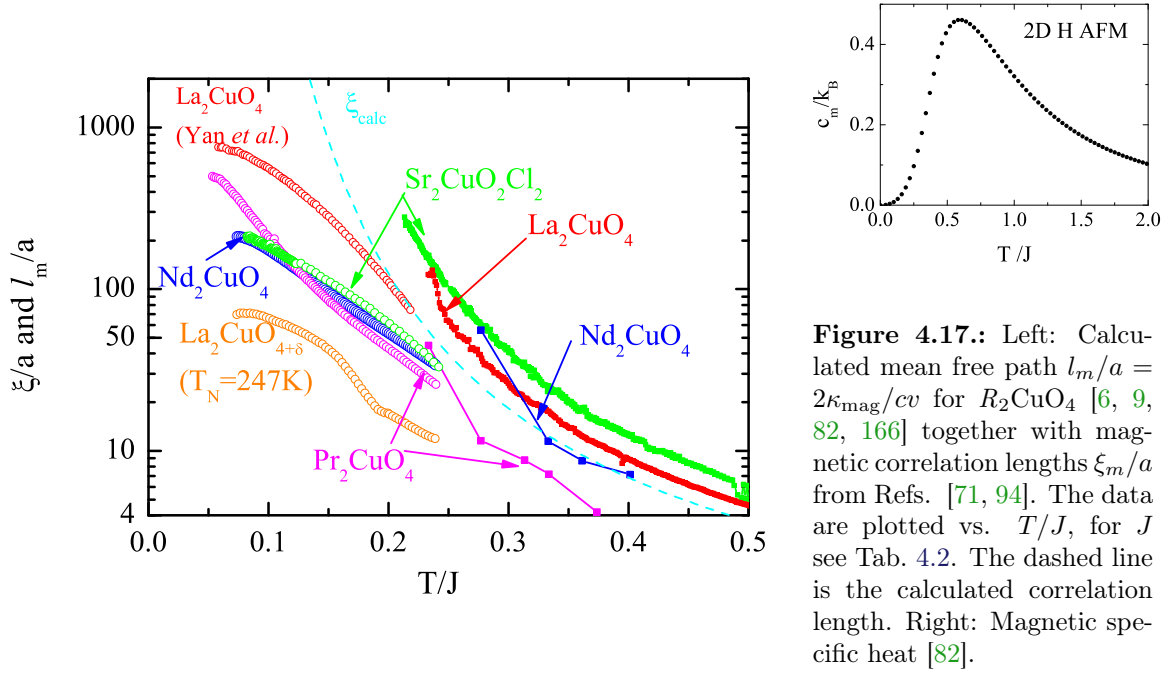


Figure 4.17.: Left: Calculated mean free path $l_m/a = 2\kappa_{\text{mag}}/cv$ for $R_2\text{CuO}_4$ [6, 9, 82, 166] together with magnetic correlation lengths ξ_m/a from Refs. [71, 94]. The data are plotted vs. T/J , for J see Tab. 4.2. The dashed line is the calculated correlation length. Right: Magnetic specific heat [82].

transport in the CuO_2 planes. This is most clearly seen in Eu_2CuO_4 where the phononic low-temperature peak of Eu_2CuO_4 is strongly suppressed by a structural instability whereas its magnetic high-temperature maximum is hardly affected.

4.5.5. Mean Free Path and Magnetic Correlation Length

To check, whether the magnitude of the estimated magnetic contribution is reasonable, we consider Eq. 2.1 applied for the 2D spin lattice:

$$\kappa_{\text{mag}} = \frac{1}{2} c_m v_m \ell_m. \quad (4.5)$$

The magnetic specific heat c_m is calculated by an extrapolation of the high-temperature series for the partition sum, see Ref. [82]. In Fig. 4.17 the result of this calculation is shown. c_m shows a maximum $c_{\text{max}} = 0.4613 N k_B$ at $T_{\text{max}} = 0.5956 J$, which is located at about 800 K for the large exchange constants in the cuprates, and therefore far above the temperature range in which κ was investigated. The group velocity

$$v_m = \sqrt{8} S Z_c k_B J a / \hbar \quad (4.6)$$

is calculated via spin-wave theory [57, 82]. Here, a is the lattice constant (in the tetragonal notation) and Z_c the so-called Oguchi correction [167]. The calculated values are in the range $v_m \approx 1.1 \cdot 1.2 \times 10^5 \text{ m/s}$. The fact that these values are much larger in comparison to the sound velocity, results from $J \gg \Theta_D$. Eq. 4.6 may be used to calculate $\ell_m(T)$ by using the estimated κ_{mag} . Fig. 4.17 shows the calculated mean free path for $R_2\text{CuO}_4$, with $R = \text{La}, \text{Pr}, \text{Nd}$, and for $\text{Sr}_2\text{CuO}_2\text{Cl}_2$. At room temperature ($T/J = 0.2 \dots 0.3$) ℓ_m/a ranges between 16 for the $\text{La}_2\text{CuO}_{4+\delta}$ crystal and 100 for La_2CuO_4 from Ref. [11]. This is much smaller than the values observed in 1D systems [3, 4, 75]. Lowering the temperature, ℓ_m strongly increases. Below $T/J \approx 0.07$ ($\approx 100 \text{ K}$) ℓ_m cannot be determined because the experimental uncertainty

of κ_{mag} becomes too large. The temperature dependence of ℓ_m explains, why the maximum in κ_{mag} is observed at a much lower temperature than the maximum in c_m , since the decrease of ℓ_m with increasing temperature overcompensates the increase of c_m .

To obtain more insight, the mean free path ℓ_m/a can be compared to the magnetic correlation length ξ_m , determined by neutron diffraction. In an ideal 2D AFM $\xi_m = \infty$ only holds for $T = 0$. For finite temperatures excited magnons will lower ξ_m . In the quasi 2D system of the cuprates ξ_m is still large above T_N , because T_N is mainly determined by the interplane interaction, and much smaller than J . Note that this also explains why no anomalies are observed in c_m and κ_{mag} [168] at T_N . At T_N , ξ_m diverges, and below T_N , $\xi_m = \infty$ is realized. Fig. 4.17 shows the magnetic correlation length $\xi_m(T)$ taken from the Refs. [71, 95]. $\xi_m(T)$ is still large above room temperature, but then strongly decreases. In principle the $\xi_m(T)$ curves for the different compounds should scale to one curve. One reason, that this is not the case is the large uncertainty of the experimental $\xi_m(T)$. From the comparison of ℓ_m and ξ_m one can see that $\ell_m < \xi_m$ holds, which is expected for an ordered state since ξ_m should conventionally give an upper boundary for ℓ_m . For a comparison to the intrinsic two-dimensional correlation length, we show a calculation of $\xi_m(T)$ given by [72]

$$\frac{\xi_m(T)}{a} = 0.5061 \exp(1.12J/T) \left(1 - 0.4464 \frac{T}{J}\right). \quad (4.7)$$

This calculation systematically underestimates the measured $\xi_m(T)$ above T_N , but describes the temperature dependence very well. The calculated value $\xi_m(T)$ is almost exactly equal to the value of ℓ/a for La_2CuO_4 at room temperature ($x \approx 0.2$). From the exponential temperature dependence of $\xi_m(T)$ the relation $\ell(T) \ll \xi_m(T)$ holds for all temperatures below room temperature. In this sense, the heat transport in the cuprates is rather conventional.

4.5.6. Comparison to 1D systems

In this section we will compare our results concerning the magnetic heat transport in a $S = 1/2$ square lattice with 1D systems. In 1D chains with $S = 1$ (Haldane chain) the dispersion is gapped, leading to a temperature-dependent group velocity. This is a disadvantage, because the group velocity is needed for the calculation of the mean free path. Therefore we will follow the idea worked out in Ref. [78], and calculate the energy diffusion constants $D_E(T) = \kappa_m(T)/c_m(T)a^2$. Here, only the calculated magnetic specific heat is needed, which is available in high accuracy. The constant a is the spin-spin distance and is used to get dimensionless scales by plotting $D_E\hbar/J$ vs. T/J . Fig. 4.18 shows $D_E\hbar/J$ vs. T/J for the spin 1/2 chains Sr_2CuO_3 , SrCuO_2 , and $\text{BaCu}_2\text{Si}_2\text{O}_7$ (from Refs. [75, 169]) and for the spin 1 chains AgVP_2S_6 and Y_2BaNiO_5 (from Refs. [77, 78]). The principle shape of the curves is different depending on S : For $S = 1/2$, an increase of $D_E(T)$ with decreasing temperature and a saturation at low temperatures is observed. In contrast, for $S = 1$ the values of $D_E(T)$ are much lower and show a maximum. The dotted lines (1D) and the dashed line (2D) are theoretical estimations calculated via

$$a^2 D_E(T) = \frac{1}{d} v_m(T) \xi_m(T) \quad (4.8)$$

using Eq. 2.1. Here, calculations of the correlation length $\xi_m(T)$ are used, which is the expected upper limit for $\ell(T)$ (see Ref. [78] for details). The calculations lead to a power-law behavior for $S = 1/2$ and a curve showing a maximum for $S = 1$. The principle shape of these curves is the same as observed in the experimental data of the $S = 1/2$ and $S = 1$ chains. However,

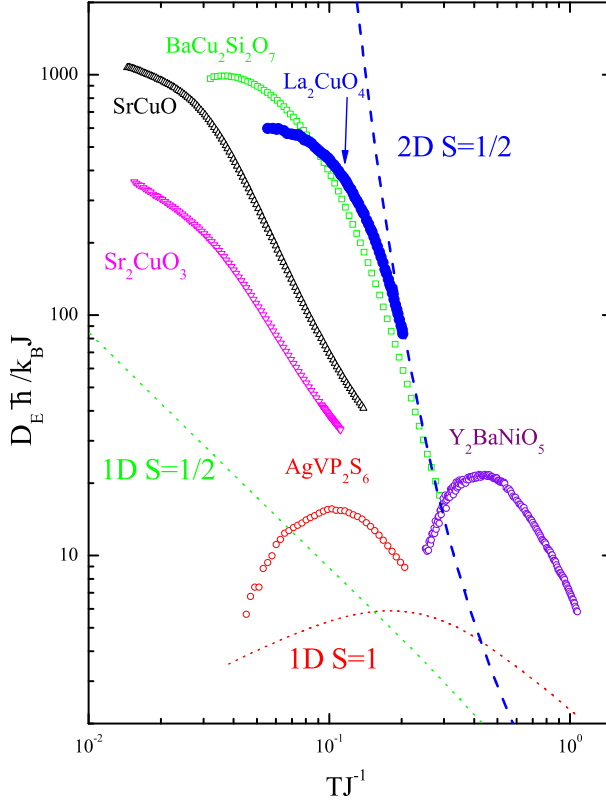


Figure 4.18.: The energy diffusion constant $D_E(T)$, as calculated from the thermal conductivity for various low-dimensional spin systems. The diffusion constants for the 1D chains are taken from Ref. [78], and are calculated from thermal conductivity data from Refs. [75, 77, 78, 169]. For La_2CuO_4 D_E was calculated as described in the text. The dotted lines (1D) and the dashed line (2D) are theoretical values calculated via $D_E = v_m \xi_m / da^2$.

the experimental energy diffusion constants show much higher values, than those calculated by Eq. 4.8. This clearly shows that the heat transport in 1D systems is anomalous.

To calculate $D_E(T)$ for the 2D cuprates, we use the estimated κ_{mag} of La_2CuO_4 from Ref. [11], since these data show the highest magnetic contribution. The same specific heat calculation as shown in the previous section is used. The resulting energy diffusion constant increases with decreasing temperature and saturates at low temperatures (closed circles). This result is very similar to the spin 1/2 chains. For the determination of $D_E(T)$ the same calculations as in the previous section are used. The temperature dependence of $D_E(T)$ is, however, very different to the 1D systems, since it diverges exponentially. The calculated values of $D_E(T)$ (dashed line) are equal to the experimental $D_E(T)$ at $T/J = 0.22$. For lower temperatures, $D_E(T)$ increases much faster than the experimental values of $D_E(T)$. This is exactly the same observation as already obtained from the comparison of the mean free path and the correlation length: The thermal transport in the 2D lattice is rather conventional, in contrast to an unconventional behavior of the 1D systems. The unusual experimental observation of the magnetic heat transport in 2D is therefore just a consequence of two facts: First, the exchange constant J is very large, which causes a considerable contribution to κ . Second, the exchange constant J is much larger than the Debye temperature, which allows the observation of κ_{mag} , since it can be distinguished from the phononic contribution.

4.6. Magnetic-Field Dependence of κ

In this section, magnetic-field dependent measurements of κ are presented. For some of the measurements the temperature range was extended to ≈ 3 K. Except for Pr_2CuO_4 the zero-

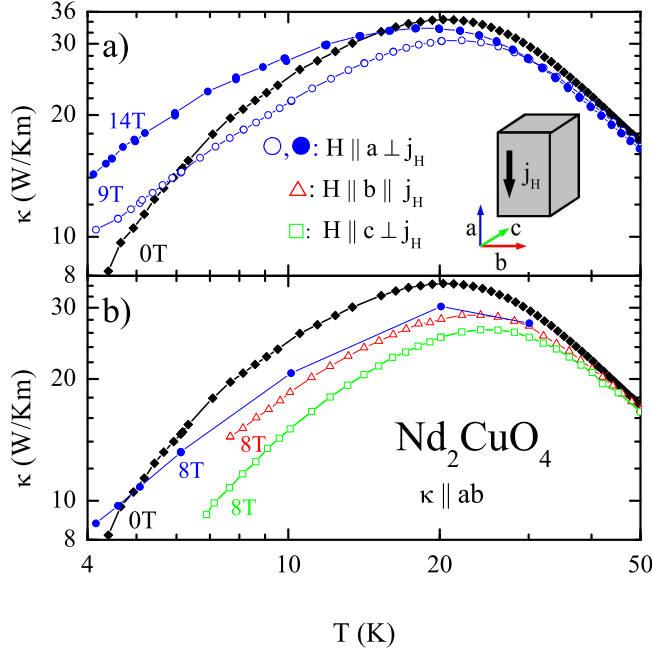


Figure 4.19.: κ vs. temperature for Nd_2CuO_4 in various magnetic fields along all three crystallographic axes. a): Zero field (\blacklozenge), $H \parallel a \perp j_H$ (\circ, \bullet). b): Zero field (\blacklozenge), $H \parallel a \perp j_H$ (\bullet), $H \parallel b \parallel j_H$ (\triangle), $H \parallel c \perp j_H$ (\square). All curves were measured with the same setup. The sketch points up the alignments of the heat current and the magnetic fields [57, 73].

field data are the same as already shown in the previous section. Again, the different compounds are discussed consecutively. All measurements have been done with the magnetic field perpendicular to the heat flow, except for Nd_2CuO_4 , where also other configurations were measured.

Nd_2CuO_4

Fig. 4.19 shows the thermal conductivity of Nd_2CuO_4 in various magnetic fields. The measurements were first performed with $H \parallel a \perp j_H$ in fields up to 14 T. Then the same setup was measured in a 8 T transverse-field cryostat. Unfortunately, during these measurements the cooling stage did not work properly⁸, and the lowest achievable temperature was 4.5 K for $H \parallel a$, and even higher for the transverse-field measurements. For $H = 9 \text{ T} \parallel a$, κ_{ab} is suppressed by 10% at the maximum. Lowering the temperature, the suppression reduces and the field dependence changes sign at $T \approx 6 \text{ K}$. At 14 T the suppression at the maximum is weaker and the sign change the field dependence shifts up to 14 K. The relative increase of κ_{ab} with respect to the zero-field measurement increases up to about 60% at 5 K. For the field along the b and c axis, the thermal conductivity is monotonously suppressed by a field of 8 T, for $H \parallel b$ by about 20% and for $H \parallel c$ by about 30% at the maximum. Further, these maxima shift slightly to higher temperatures. The curves for 8 T, $H \parallel a$ and $H \parallel b$ are qualitatively similar, but differ by about 10% at 10 K. This can be partly caused by the misalignment in the transverse-field measurements. According to Chp. 3, this misalignment can be up to $\approx 20^\circ$ for the used setup (without Hall probe). If the magnetic field is misaligned, one can calculate via

$$\kappa_\alpha(H) = \sqrt{\kappa_a(H||a)^2 \cos^2 \alpha + \kappa_c(H||c)^2 \sin^2 \alpha} \quad (4.9)$$

⁸This problem occurred with a newly setup probe, and was later solved by improving the thermal anchoring of the copper wires to the cooling stage, see Ref. [57].

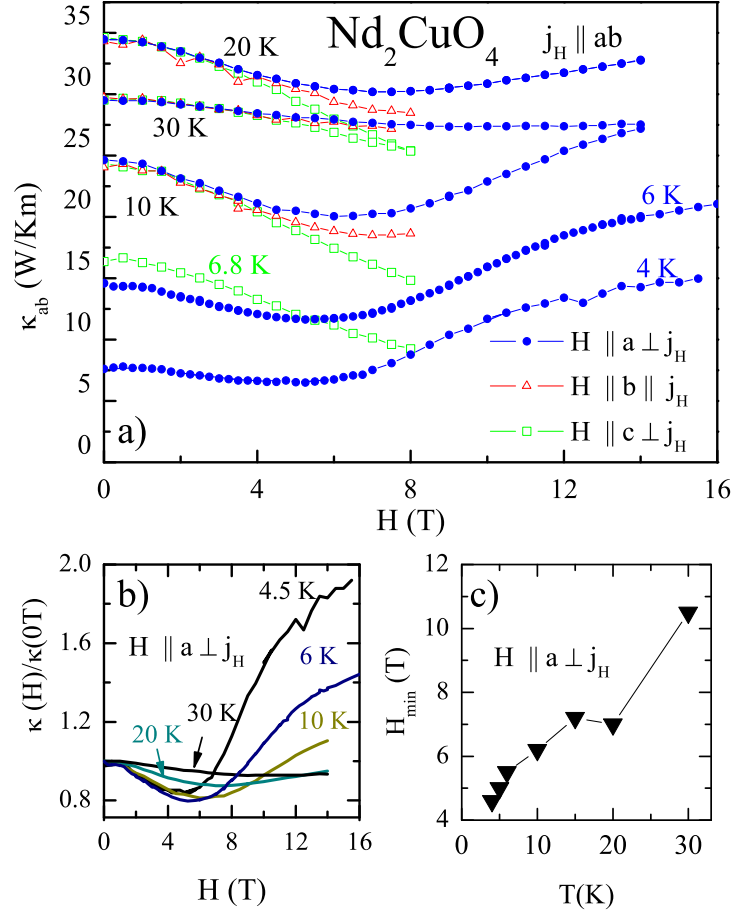


Figure 4.20.: a): κ vs. magnetic field for Nd_2CuO_4 . For $T = 10$ K, 20 K, and 30 K the field was applied along all crystallographic axes; $H \parallel a \perp j_H$ (\bullet), $H \parallel b \parallel j_H$ (\triangle), $H \parallel c \perp j_H$ (\square). b) $\kappa(H)/\kappa(0T)$ vs. H . c) H_{\min} vs. T . (\blacktriangledown)

for the thermal conductivity measured with an angle α of the magnetic field with respect to the a plane. If the probe is not aligned perfectly in the transverse-field cryostat it follows that $\kappa(H \parallel b)$ may be lowered due to the admixture of a $\kappa(H \parallel c)$ component; as well the measured κ_c increases due to a κ_a component. For this reason we do not discuss the small difference between both in-plane directions.

Field-dependent measurements with constant temperatures are presented in Fig. 4.20. For $\kappa_a(H \parallel a)$ almost the same principal behavior is observed at all measured temperatures below 30 K. The thermal conductivity first decreases, up to a field H_{\min} , and then strongly increases again with further increasing magnetic field. For 6 K and 4 K an onset of a saturation at about 12 T is indicated, however this is not clear from the available field range. For $\kappa_{ab}(H \parallel b)$ at 20 K and 10 K an onset of a minimum is visible in the data, however the maximum field of 8 T is too small to observe a possible increase. In contrast, κ_{ab} behaves differently for $H \parallel c$, and monotonously decreases up to 8 T, and no indication for a saturation is seen.

Fig. 4.20b shows the normalized thermal conductivity $\kappa(H)/\kappa(0T)$. The minimum of $\kappa_a(H)$ monotonously shifts to higher fields at higher temperatures and broadens. H_{\min} vs. T is shown

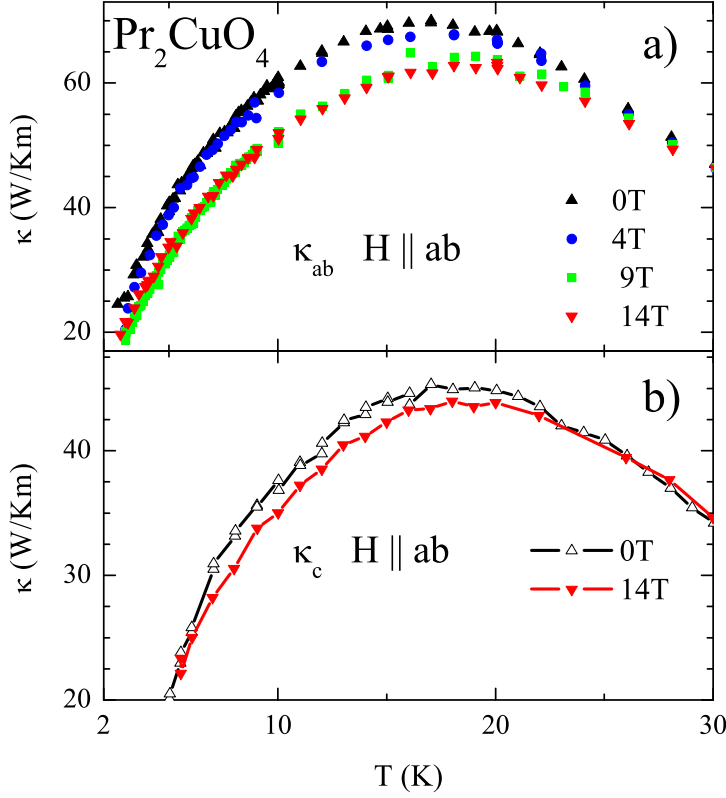


Figure 4.21.: a) κ_{ab} vs. T for Pr_2CuO_4 in 0 T (\blacktriangle), 4 T (\bullet), 9 T (\blacksquare), and 14 T (\blacktriangledown) with the field applied along the in-plane direction. b) κ_c for $H = 0$ T (\triangle) and $H = 14$ T (\triangledown) with the same field direction.

in Fig. 4.20c, and H_{\min} increases roughly linearly with temperature. A detailed discussion and a comparison with literature data will follow in Sec. 4.6.2.

Pr_2CuO_4

In Fig. 4.21a the in-plane thermal conductivity of Pr_2CuO_4 is shown⁹ in 0, 4, 9, and 14 T. For a field of 4 T there is almost no effect, but for $H = 9$ and 14 T the thermal conductivity is suppressed by the field below $T \approx 25$ K. The magnetic-field dependence is much smaller than in Nd_2CuO_4 ; about 10% at the maximum. In Fig. 4.22a the magnetic-field dependent measurements at fixed temperatures are shown. At 10 K, the κ vs. H curve first decreases and then stays constant above about 12 T. For lower temperatures a minimum occurs which shifts slightly to lower fields for lower T . In comparison to Nd_2CuO_4 (Fig. 4.22b), the magnetic-field dependence is weaker. Particularly the strong increase observed in Nd_2CuO_4 at higher fields is missing in Pr_2CuO_4 . In the paper of Jin *et al.* [80] the authors claim, that they see the same behavior for κ of Pr_2CuO_4 and for Nd_2CuO_4 . However, no data are shown¹⁰. Fig. 4.22b shows κ_c with $H \parallel a$. Here, κ is weakly suppressed by a field of 14 T. The effect is only 5% at the maximum of κ_c , which is close to the experimental resolution for the field-dependence of κ and will therefore not be discussed further.

⁹The low-temperature maximum has a slightly higher absolute value as the data presented in Fig. 4.13, which is due to the experimental uncertainty. The data presented here were measured in a different setup as the data used for the zero-field analysis.

¹⁰The same authors published a preprint, containing a field dependent curve for Pr_2CuO_4 at 2 K and $H \parallel a$, which shows a strong increase of κ [170]. Since no systematic data are available, however, a comparison is not possible.

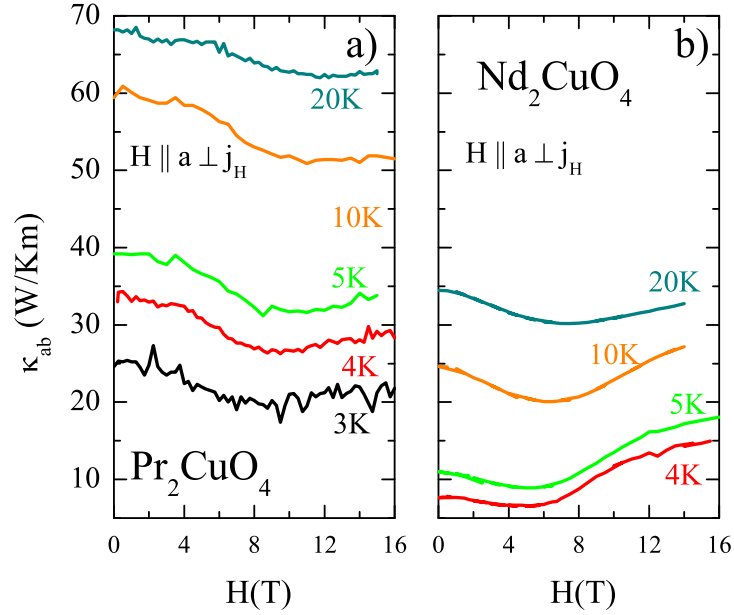


Figure 4.22.: a): κ vs. magnetic field for Pr_2CuO_4 at fixed temperatures. b): κ vs. magnetic field for Nd_2CuO_4 (for comparison).

Sm_2CuO_4

Fig. 4.23a presents the thermal conductivity of Sm_2CuO_4 from 3 K to 300 K in magnetic fields of 0 and 14 T. At 6 K a kink is observed, which can be attributed to the Néel transition of the Sm moments. Such an additional small suppression of κ at low temperatures is known from other antiferromagnets [171]. In a magnetic field of 14 T the Néel transition is only shifted by ≈ 300 mK to lower temperatures (see Sec. 4.2.4). This is consistent with the thermal conductivity data, where the dip shifts slightly in a field of 14 T. Except this small anomaly, there is no magnetic-field dependence in the whole temperature range within the experimental uncertainty. The field independence at low temperatures for magnetic fields between 0 T and 14 T is verified by measurements at constant temperatures (see inset of Fig. 4.23).

Gd_2CuO_4

In Fig. 4.24 the temperature-dependent measurements of the thermal conductivity of Gd_2CuO_4 in magnetic fields of 0 T and 14 T (c direction: 9 T) are presented. For the c direction there is no detectable magnetic-field dependence above ≈ 25 K. For the in-plane direction the low-temperature maximum is suppressed by about 6% in both samples. A surprising new finding is, that the field dependence of κ_{ab} remains visible up to high temperatures, a feature which is found in both Gd_2CuO_4 samples. We will discuss this aspect later in comparison with the other samples.

Next, we consider the low-temperature behavior of κ . Fig. 4.26 shows the temperature-dependent measurements of κ_{ab} and κ_c in magnetic fields. For $H = 0$ T a small change of the slope is visible in κ_{ab} at T_N^{Gd} , similar to that observed in Sm_2CuO_4 . Applying a magnetic field of 4 T, the kink is still visible, but for higher fields no anomaly is identifiable in the κ vs. T

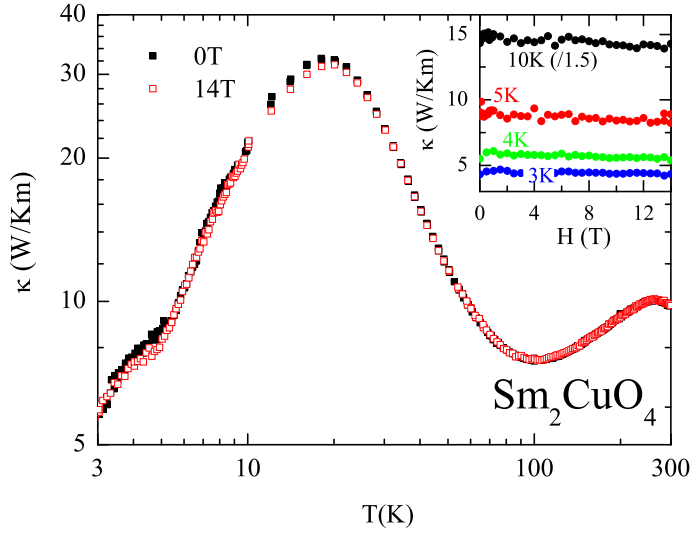


Figure 4.23.: Thermal conductivity of Sm_2CuO_4 in magnetic fields of 0 T and 14 T. Inset: Magnetic-field dependent measurements at 3 K, 4 K, 5 K, and 10 K. The latter curve is divided by a factor of 1.5.

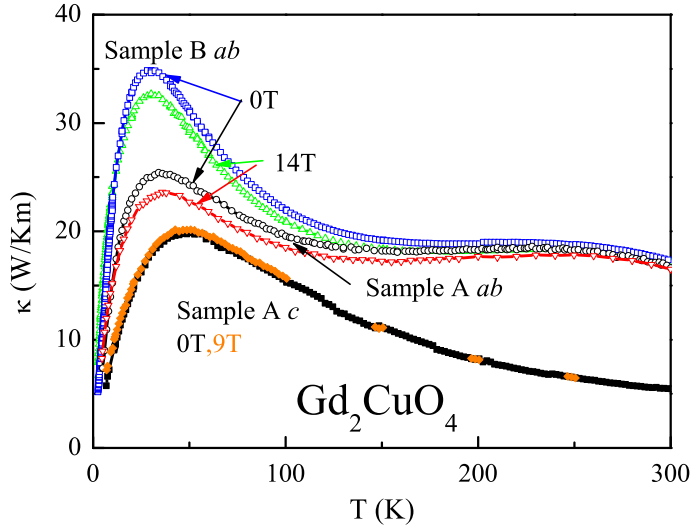


Figure 4.24.: κ vs. temperature in different magnetic fields for Gd_2CuO_4 . κ_{ab} is shown for both samples in fields of 0 T and 14 T. κ_c was measured in fields of 0 T and 9 T. Here, the field independence at higher temperatures was only checked at three different temperatures.

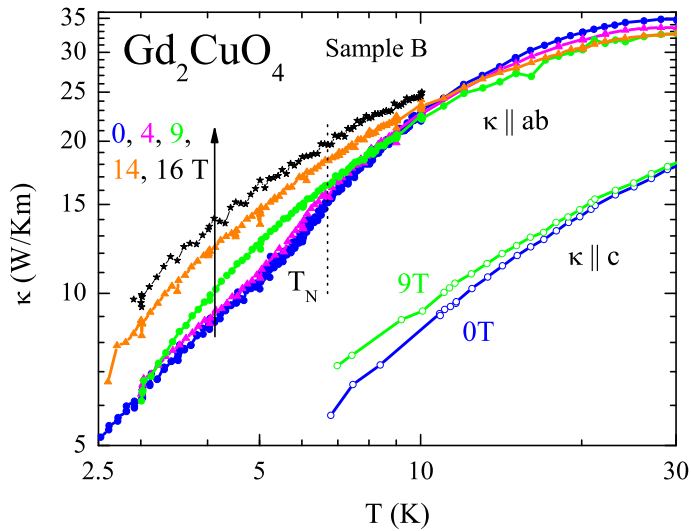


Figure 4.25.: κ vs. temperature in different magnetic fields for Gd_2CuO_4 . For κ_{ab} several fields between 0 T and 16 T were applied. κ_c was measured in 0 T and 9 T.

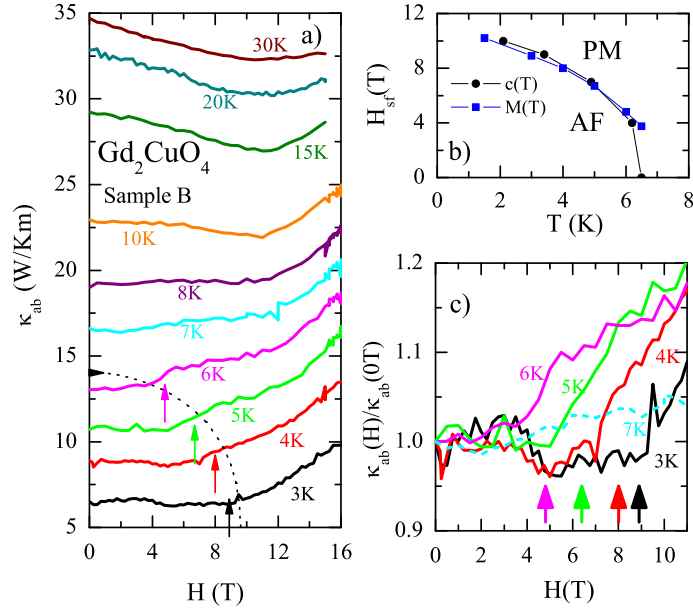


Figure 4.26.: a): κ of Gd_2CuO_4 vs. magnetic field at fixed temperatures. The arrows indicate the spin-flip field H_{sf} . b) H-T phase diagram of the Gd Néel transition as derived from magnetization (■) from Ref. [131] and specific heat (●) from Ref. [128]. c) $\kappa(H)/\kappa(0\text{ T})$ vs. T. for Gd_2CuO_4 . Arrows point to the spin-flip field determined from the magnetization (see panel b).

curves. In contrast to Sm_2CuO_4 , the Néel-transition is suppressed drastically in Gd_2CuO_4 by magnetic fields, as shown in Sec. 4.2.4. Fig 4.26b shows the field-dependent Néel-temperature extracted from the specific heat and magnetization data of Refs. [129] and [131], respectively. The curvature of the phase boundary explains that the kink in κ does not shift much for 4 T. Fig. 4.26a shows the measurements of κ_{ab} vs. field. Here, the Néel transition is seen as small slope changes. The corresponding spin-flip fields from Ref. [131] are plotted as arrows. In Fig. 4.26c, normalized $\kappa(H)/\kappa(0)$ curves are shown. The dip in the temperature-dependent zero-field curve is caused by scattering of phonons by spin-waves. The κ vs. H curves are almost field independent below the spin-flip field. Because of the small anisotropy, the spin-flop field in Gd_2CuO_4 is below 1 T at all temperatures[172]. It follows, that for all investigated fields the CF anisotropy plays no role. For small fields the Gd moments are aligned almost perpendicular to the applied field. With increasing field, the moments cant towards the field direction, until a full alignment is reached at the spin-flip field of $H_{sf} = 11\text{ T}$. Because in the canted phase the moments can precess around the axis of the external field, gapless spin-wave excitations are possible. This is the reason why the suppression of the thermal conductivity in the AFM phase does not change with field. Above the spin-flip field, an energy gap of the spin-wave excitations opens, which becomes larger with increasing field. This presumably explains, why the thermal conductivity increases above T_{sf} . The increase of the gap freezes out this scattering channel. Considering the field dependence at higher temperature, the data resemble to the Nd_2CuO_4 curves. A magnetic field causes a minimum in κ vs. H . In contrast to Nd_2CuO_4 and Pr_2CuO_4 , a field H_{min} can only be determined for $T \geq 10\text{ K}$.

The total field dependence is large, at 3 K κ increases by about 50% between 9 T and 14 T.

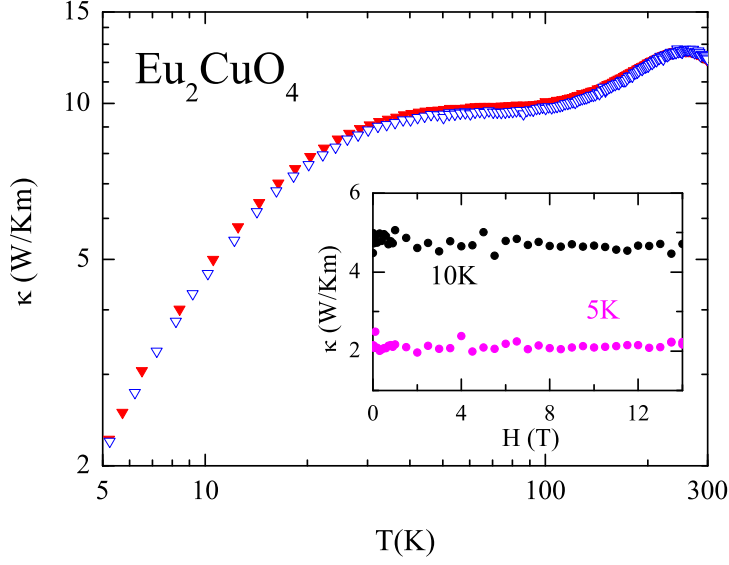


Figure 4.27.: Thermal conductivity of Eu_2CuO_4 in magnetic fields of 0 T and 14 T. Inset: Magnetic field-dependent measurements at 5 K and 10 K.

For κ_c in $H \leq 9$ T, the field dependence appears to be less pronounced (see Fig. 4.24), but a quantitative comparison of the anisotropy would require higher-field data.

Eu_2CuO_4

Fig. 4.27 shows κ_{ab} of Eu_2CuO_4 in magnetic fields of 0 T and 14 T. At low temperatures no significant field dependence is observed, which is confirmed by measurements of κ vs. H at 5 K and 10 K. A closer inspection of the field dependence shows, however, that a small field dependence is present up to high temperatures, what will be discussed in the following section.

4.6.1. Magnetic Field Dependence at High Temperatures

To analyze the field dependence at high temperatures in more detail, Fig. 4.28 shows the ratio $\kappa(14\text{T})/\kappa(0\text{T})$ for $R = \text{Pr}, \text{Sm}, \text{Eu}$ and Gd . As shown in Fig. 4.24, a considerably large field dependence is present up to room temperatures for $R = \text{Gd}$ and a weaker one for $R = \text{Eu}$. For $R = \text{Pr}$ and Sm , no field dependence¹¹ is observed above 50 K. Because κ_c does not change in a field for Gd_2CuO_4 above $T \approx 30$ K (see Fig. 4.24), we conclude that it is the magnetic contribution which is field dependent. In Gd_2CuO_4 , $\kappa(14\text{T})/\kappa(0\text{T})$ reaches the value 1 at about 300 K, which is close to the Néel transition. This makes it likely that the field dependence is only present in the Néel ordered state. The difference to T_N may be caused by the experimental uncertainty of the field-dependent measurements¹². The disappearance of the field dependence in Eu_2CuO_4 could be either attributed to the structural phase transition or to the Néel transition, since we do not know these transition temperatures for our sample. Because in Gd_2CuO_4 both, the Néel ordered state and the distorted structure are present when the field dependence arises, and no effect is observed in the undistorted compounds, we suspect that both, the distorted structure and the Néel ordered state are related to the magnetic-field dependence of κ_{ab} .

¹¹For Nd_2CuO_4 , the magnetic-field dependence was only measured up to 60 K. However, in Ref. [80] no field dependence was detectable between $T \approx 80$ K and room temperature.

¹²For $R = \text{Pr}$ and Sm the deviation of $\kappa(14\text{T})/\kappa(0\text{T})$ from 1 is about 0.5%, whereas $\kappa(14\text{T})/\kappa(0\text{T})$ of Gd_2CuO_4 has to be scaled by about 1% to become 1 at T_N^{Cu} .

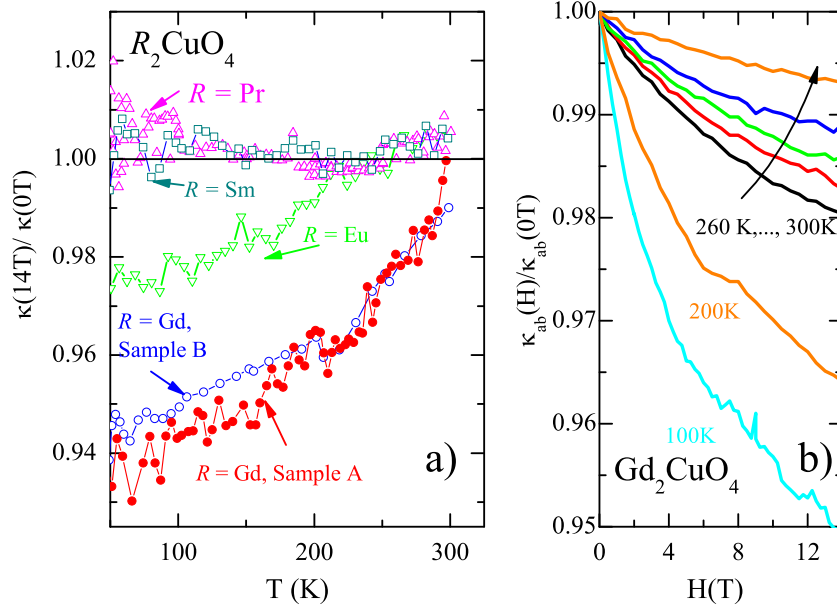


Figure 4.28.: a): $\kappa(14\text{T})/\kappa(0\text{T})$ for $R_2\text{CuO}_4$ with $R = \text{Pr}$ (\triangle), Sm (\square), Eu (∇), and Gd (\circ, \bullet) as a function of T . Whereas for Sm and Pr no field dependence is observed to higher temperatures, a small field dependence remains visible up to 200 K for $R = \text{Eu}$ and up to ≈ 300 K for $R = \text{Gd}$. For the latter, the temperature dependence is exactly the same for both samples. b): $\kappa_{ab}(H)/\kappa_{ab}(T)$ vs. H of Gd_2CuO_4 at high temperatures.

The reason for these field dependences is unclear. The effect of domains can be ruled out, since the WF moment is saturated at much lower fields in Gd_2CuO_4 [126].

4.6.2. Discussion: Low-temperature Magnetic-Field Dependence of κ

In this section, we will compare our results to the literature data. Furthermore we will analyze the different methods used in Refs. [10, 80] to extract a possible magnon contribution to κ of Nd_2CuO_4 . We will apply the same analysis to our data and compare the different results. Finally, we will discuss other possible mechanisms to explain the observed magnetic-field dependences.

Comparison with the Literature Data

Fig. 4.29a shows selected results of κ_{ab} of Nd_2CuO_4 in combination with data taken from the literature. Jin *et al.* measured κ_{ab} down to ≈ 2 K in fields of 0 and 9 T|| a . They do not specify the relative field direction with respect to the heat flow. Their data are plotted as dashed lines. Li *et al.* performed measurements of κ_{ab} down to 50 mK in zero field and with a magnetic field of 10 T along the a and c direction, applied perpendicular to the heat flow (solid lines) [10]. The absolute value of the thermal conductivity at low temperatures strongly depends on the sample quality. At 5 K the absolute value of κ is 11 W/Km for our crystal, 5.1 W/Km for the sample from Li *et al.*, and 15 W/Km for the sample from Jin *et al.*, what means that the quality of our samples lies between the ones used in Refs. [10, 80].

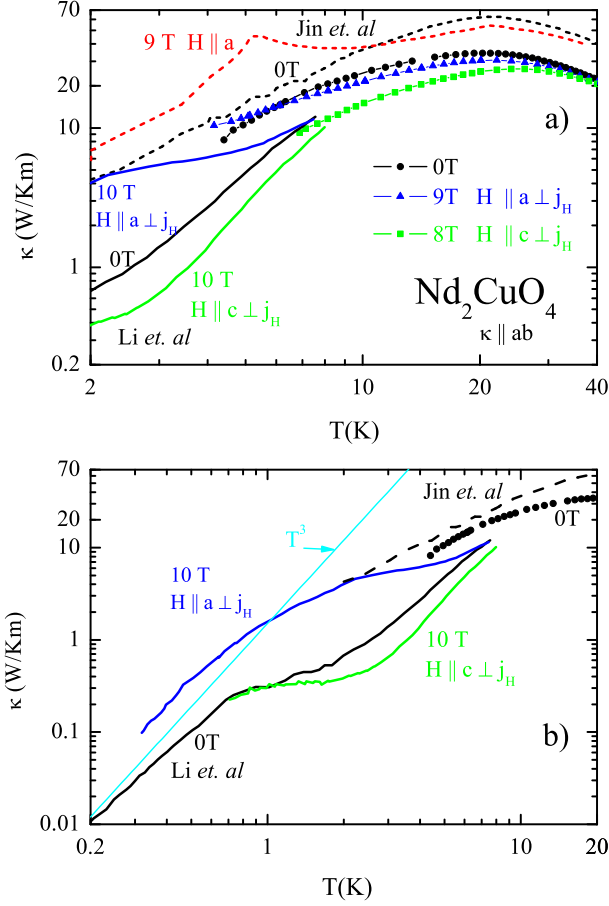


Figure 4.29.: a) Thermal conductivity of Nd_2CuO_4 in zero field (\bullet), $H = 9\text{ T} \parallel a \perp j_H$ (\blacktriangle), and $H = 8\text{ T} \parallel c \perp j_H$ (\blacksquare) in combination with literature data from Ref. [80] (dashed lines) and Ref. [10] (solid lines) [57, 73]. b) The data of Li *et al.* shown to lower temperatures, and zero field data of our measurements and from Jin *et al.*. The line is a low-temperature estimation of κ , see text.

As in our sample, a sign change of the magnetic-field dependence is present in the data of Jin *et al.* at $\approx 10\text{ K}$. The data of Li *et al.* are only shown up to 8 K , however a sign change of the field dependence is suggested by the temperature dependences of the curves. The change from a strong enhancement of κ_{ab} for $H \parallel ab$ at low temperatures to a weak suppression at higher temperatures seems to be a general feature of Nd_2CuO_4 . However, the strength and temperature dependence of these effects is strongly sample dependent. In the interpretation of Jin *et al.*, this feature is caused by the competition of magnon-phonon scattering and a sizeable magnon contribution: At lower temperatures the suppression due to magnon-phonon scattering is overcompensated by the magnon contribution, whereas at higher temperatures κ_{mag} is too small, and only the effect of magnon-phonon scattering is seen (see Fig. 4.5).

The observed sharp dip at 5 K in the data of Jin *et al.* is neither reproduced in the sample of Li *et al.* nor in our sample. From our measurement we cannot exclude, that this effect is just shifted to a lower temperature. Li *et al.* do not observe such a feature down to 50 mK , but since the absolute values of their data are much lower, one cannot rule out that the effect

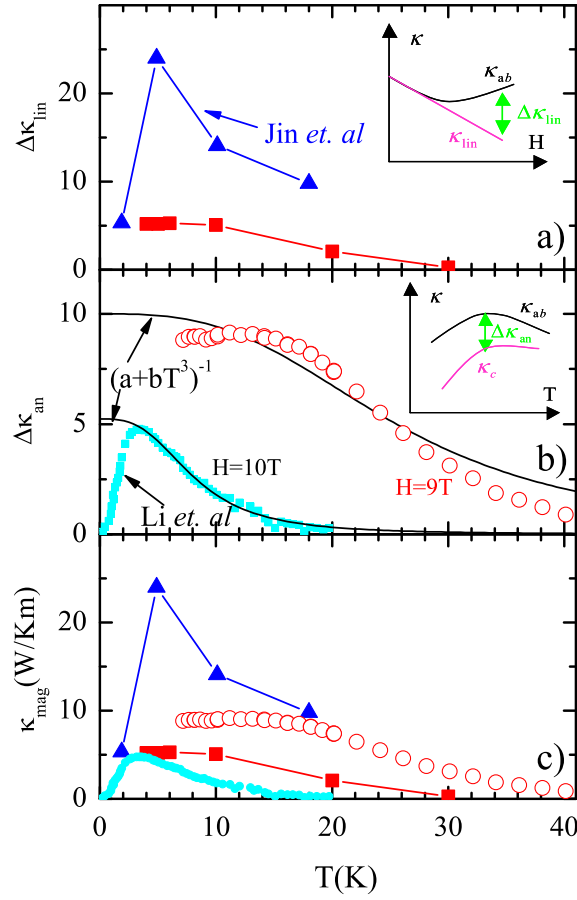


Figure 4.30.: a) $\kappa_{\text{mag}}^{\text{lin}} = \kappa(H \parallel) - \kappa(H \parallel)_{\text{lin}}$ from Ref. [80] and for our data. b) $\kappa_{\text{mag}}^{\text{an}} = \kappa(H \parallel) - \kappa(H \perp)$ from Ref. [10] ($H_{\perp} = H_{\parallel} = 10$ T) and for our crystal ($H_{\perp} = 8$ T, $H_{\parallel} = 9$ T). Lines are fits as indicated. The insets sketch how the different $\Delta\kappa$ were determined. c) Compilation of a) and b). The huge sensitivity of the proposed magnon contribution κ_{mag} on both, the method of its determination and the different samples, is evident.

is just smeared out.

Estimation of a possible Magnon Contribution

Jin *et al.* estimated the possible magnon contribution to κ by linear fitting $\kappa_{ab}(H)$ for low fields and subtracting the fits from the data ($\Delta\kappa_{\text{lin}}$, see Fig. 4.5a. Performing this analysis for our data, a much smaller $\Delta\kappa_{\text{lin}}$ is obtained. The reason for this deviation can be seen in the magnetic-field dependent measurements (Fig. 4.19): The data for $H \parallel a$ are already larger than for $H \parallel c$ below H_{min} , leading to an overestimation of the phononic contribution. This is not contradictory to the proposed model, since the magnon branch could be already thermally populated at these temperatures, even if the spin gap is not fully closed. However, this shows that this kind of estimation of a possible magnon contribution is not very accurate, particularly at higher temperatures.

Fig. 4.29b shows the data of Li *et al.* above ≈ 200 mK.¹³ An enhancement of κ_{ab} for a magnetic field applied along the ab plane, and a suppression of κ_{ab} for $H \parallel c$ is observed above ≈ 1 K. At low temperature the suppression of κ_c vanishes. The data analysis of Li *et al.* is as follows: As discussed in Sec. 4.3.1 the enhancement of κ for $H \parallel a$ is attributed to a magnon contribution and the suppression of κ for $H \parallel c$ to scattering of phonons by magnons. Assuming that the suppression of κ is caused by an isotropic phonon-magnon scattering, it follows that

$$\Delta\kappa_{an} = \kappa_{ab}(H \parallel ab) - \kappa_{ab}(H \parallel c). \quad (4.10)$$

For their data below 0.5 K, Li *et al.* estimate $\Delta\kappa_{an}$ by the difference

$$\Delta\kappa_{an}^{LT} = \kappa_{ab}(H \parallel ab) - \kappa_{ab}(0T), \quad (4.11)$$

arguing that the field dependence for $H \parallel c$ vanishes below 1 K. The resulting $\Delta\kappa_{an}$ is plotted in Fig. 4.29b and shows a maximum at ≈ 3 K. To describe the temperature dependence of $\Delta\kappa_{an}$, the following model is introduced. Based on the assumption that the specific heat of the heat-carrying magnons is nearly saturated at the temperature of the maximum, the decrease above 3 K is attributed to the magnon scattering rate Γ_m , which is written as a sum of boundary scattering and magnon-phonon scattering:

$$\Gamma_m = \Gamma_0 + \Gamma_P. \quad (4.12)$$

The first term gives a constant and the latter one is written as $\Gamma_P = A_P T^3$. The fit of the data of Li *et al.* yields the values $\Gamma_0 = 0.2$ and $A_P = 3.7 \cdot 10^{-4}$. The interpretation is that above 3 K the magnon contribution is strongly suppressed by the phonons, which are populated by the conventional T^3 dependence of acoustic phonons. Fig. 4.29b shows $\Delta\kappa_{an}$ calculated by Eq. 4.10 for our data¹⁴, and a fit by Eq. 4.12. The calculated $\Delta\kappa_{an}$ is much larger for our sample. The comparison of the different $\Delta\kappa_{an}$ raises the following questions, if we follow the argumentation of Li *et al.*:

- A broad maximum occurs at ≈ 11 K, which is about 4 times higher in temperature than the maximum observed by Li *et al.*. Li *et al.* argue that the maximum of $\Delta\kappa_{an}$ at 3 K exactly corresponds to the averaged optical magnon energy of $k_B T^* = 0.25$ meV = 3 K. However, our result yields a four times higher value of T^* .
- The fit of our data gives a fair description of $\Delta\kappa_{an}$ and yields the values $\Gamma_0 = 0.1$ and $\Gamma_P = 6.0 \cdot 10^{-6}$. The first value is a factor of two smaller in our sample. According to Li *et al.* the characteristic sample length is given by $l_0 = 2\sqrt{A/\pi} = 0.24$ mm for their sample. The value Γ_0 should be proportional to l_0 . For our sample the same estimation gives a larger value of $l_0 = 0.6$ mm. Therefore the different values for the boundary scattering are consistent with the respective sample sizes.
- Γ_P is much smaller in our sample, which would yield a much less effective phonon-magnon scattering for our sample. This is not expected, because magnon-phonon scattering should be an intrinsic property only depending on the population of the phonon spectrum.

¹³The data of Li *et al.* are measured down to 50 mK. However, the digitalization of the data was not possible at the lowest temperatures.

¹⁴Since a 9 T curve is not available for $H \parallel c$, the 8 T curve was extrapolated to 9 T. This is appropriate, because of the almost linear behavior of κ vs. field for this field direction.

A further argument of Li *et al.* towards a magnon contribution to κ is based on power-law fits of the thermal conductivity at low temperatures. Herefore the low-temperature estimation of κ (Eq. 2.3) is used with $l = 2\sqrt{A/\pi}$. Li *et al.* argue that κ in zero field is purely phononic below $T \approx 0.4$ K. They observe a $T^{2.6}$ dependence of $\kappa(0\text{T})$ and a T^3 dependence of $\Delta\kappa_{an}$. The different exponents are taken as an argument that $\kappa(0\text{T})$ is of phononic origin, since a $T^{2.6}$ dependence of a phononic κ is known to occur due to specular scattering.¹⁵ A second argument comes from the sound velocity $v = 3500$ m/s estimated from Eq. 2.3, since it is of the order of the experimentally determined values.¹⁶ However, both arguments are questionable. First, $\kappa(10\text{T}||a)$ shows a $T^{2.8}$ dependence¹⁷, what indicates that specular scattering is present for this curve, too. Second, specular scattering *increases* the thermal conductivity, since the mean free path becomes larger than the transverse sample dimensions. Fig. 4.29 shows a low-temperature estimation of κ using a pure T^3 dependence. The averaged sound velocity is calculated by Eq. 2.4, using the experimental values of v , yielding $\bar{v} = 2550$ m/s. The resulting curve is only a factor of two smaller than κ_{ab} with $H = 10\text{ T}||a$. In Ref. [173] an increase by κ of more than a factor of 3 was observed in Al_2O_3 in the same temperature range due to specular scattering. This clearly shows, that the use of l_0 to get an upper limit for κ_{phon} is not possible. Because the extrapolation of the T^3 curve to higher temperature is far above our data and the data of Jin *et al.* (Fig. 4.29b), no further conclusion can be made here.

The uncertainty of the used separation methods is evident from Fig. 4.30c. Here, the different $\Delta\kappa$ from the literature and for our data estimated via the different methods are plotted together. The large spread of the curves shows, that even if the general assumptions would be right, a reliable extraction of a possible magnon contribution is not possible in the considered temperature range.

Phonon-scattering

All the considerations discussed above do not take into account that there may be also other magnetic-field dependent phonon-scattering mechanisms. Resonant scattering processes can drastically influence κ . In Chp. 7 it is shown that phonon scattering by the $4f$ moments causes a strong suppression and large field dependences of κ of NdMnO_3 at low temperatures. This may be important for the field dependence of κ of the $R_2\text{CuO}_4$ samples, too. The magnetic-field dependence of Nd_2CuO_4 with a minimum at about 5 T may be explained by the simplest kind of a resonance, namely resonant scattering on a magnetic doublet (see inset of Fig. 4.31). If the doublet is degenerate, no scattering occurs. If the levels are split by the Zeeman effect and /or exchange splitting, resonant processes become possible (see Sec. 2.1.6 for more details). A resonant scattering process is most effective, if the energy splitting is equal to the frequency of the peak in $\kappa(\omega)$, and becomes weaker for further increasing splitting. At very low temperatures an estimate can be made by[17]

$$\hbar\omega_{\text{max}} = 4k_B T \stackrel{!}{=} \hbar\omega_{\text{res}}, \quad (4.13)$$

¹⁵Specular scattering means reflexion of phonons at the sample boundaries. This increases the mean free path of the phonons. Eq. 2.3 is in principle only valid, if all phonons are scattered diffusely at the sample boundaries. Specular scattering enhances the thermal conductivity and leads to a low-temperature dependence $\kappa \sim T^j$ with $j < 3$ [17, 173].

¹⁶ $v_t = 6050$ m/s, $v_l = 2550$ m/s[86].

¹⁷This value was estimated from the $T^{2.6}$ and T^3 power laws in the relevant temperature range, since the low-temperature data of $\kappa(10\text{T}||a)$ are not available.

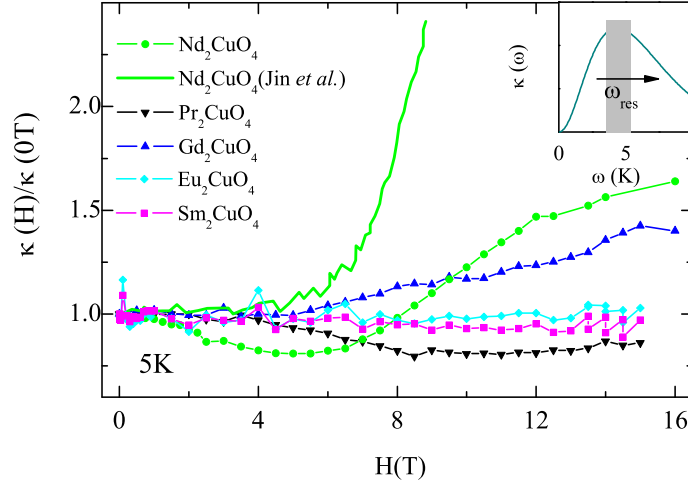


Figure 4.31.: Relative magnetic-field dependence $\kappa(H)/\kappa(0\text{ T})$ vs. H at 5 K for Nd_2CuO_4 , Pr_2CuO_4 , Sm_2CuO_4 , Eu_2CuO_4 , and Gd_2CuO_4 . The inset shows the principle shape of $\kappa(\omega)$ at low temperatures, showing a maximum at $4k_B T$. The shaded area symbolizes a resonant process suppressing κ .

where ω_{\max} is the position of the maximum in the ω dependent thermal conductivity. If the resonance energy is given by the Zeeman splitting we can rewrite Eq. 4.13 a

$$4k_B T \stackrel{!}{=} g\mu_B H_{\min}. \quad (4.14)$$

The same equation can be used to get an rough estimate of the minimum caused in the temperature-dependent measurements. The $4f$ level splitting of the $R_2\text{CuO}_4$ cuprates is well known, see Secs. 2.4 and 4.4. For the magnetic-field dependence of κ only the ground-state multiplet is relevant, since the excited levels are energetically too high to be significantly excited in the relevant temperature range (see Fig. 4.8). In Eu_2CuO_4 and Pr_2CuO_4 , the ground state is a singlet, whereas for Nd_2CuO_4 , Sm_2CuO_4 , and Gd_2CuO_4 a doublet is realized. The doublets can be split by the Cu- R exchange field, as observed in Nd_2CuO_4 [174], and by external magnetic fields. Note that the treatment of the $4f$ moments as free moments for $R = \text{Gd}$ and Sm is only possible above T_N^R . In order to obtain a better comparability, Fig. 4.31 shows the relative magnetic-field dependences $\kappa_{\text{rel}} = \kappa(H)/\kappa(0\text{ T})$ for the different samples at 5 K. From the direct comparison, the conclusion can be drawn, that only for Nd_2CuO_4 and Gd_2CuO_4 larger field dependences of κ are observed. These are two of the three doublet systems, where the ground state splitting could play a role. In Ref. [174] the specific heat of Nd_2CuO_4 was investigated at low temperatures. A Schottky peak is observed in zero field, which can be described with a gap $\Delta_0 \approx 5\text{ K}$. The influence of magnetic fields is strongly anisotropic, for $H \parallel c$ almost no effect is observed up to 4 T, whereas for $H \parallel a$ the anomaly shifts to higher temperatures in fields up to 8 T. This behavior arises from a complex interplay of the external field and internal exchange fields. Unfortunately the specific heat data have not been measured up to the field of 10 T, to allow a direct comparison to the results of Li *et al.*. However, we may assume that the observed anisotropy of the specific heat gives the correct trend for higher fields. Such a behavior could in principle explain the observed behavior of κ observed by Li *et al.*. Herefore, we consider the temperature-dependent

measurements shown in Fig. 4.29b. We assume that a resonant scattering processes causes the dip observed in $\kappa(0\text{T})$ vs T . According to Eq. 4.13, a gap $\Delta_0 \approx 5\text{ K}$ would cause the strongest suppression around 1.3 K, which is close to that experimentally observed. If the magnetic field is applied along the in-plane direction, the dip shifts to higher temperatures, as expected from an increase of the Nd ground-state gap. For $H \parallel c$, the position of the dip remains more or less unchanged, which is consistent to the insensibility of the gap to a field applied along the c direction. In Gd_2CuO_4 we observed an additional field-independent scattering due to spin waves in the Néel ordered state. At higher temperature the field dependence is similar to Nd_2CuO_4 and the same scattering mechanisms may apply. In Sm_2CuO_4 , κ is practically field-independent. However, this can be understood since the large uniaxial anisotropy along the c axis is much stronger than the effect of an external field applied within the planes. Now, we consider the singlet systems. In Pr_2CuO_4 , a small field dependence of κ is observed. Because of the singlet ground state the $4f$ orbitals have no influence to κ at low temperatures. In Chp. 5 it is shown that paramagnetic impurities can also act as resonant scatterers. The impurity levels are also split by the Zeemann effect, if a magnetic field is applied, and are therefore possible resonant scatterers. Here, the scattering strength depends on the impurity amount. In Sec. 4.4.1 we estimated significant impurity amounts in Eu_2CuO_4 , Sm_2CuO_4 , and Pr_2CuO_4 . We may attribute the small observed field dependences for the systems with a singlet ground state to the influence of the paramagnetic impurities. Since for Eu_2CuO_4 no significant field dependences is observed, we conclude that the general influence of these moments is much smaller than the influence of the $4f$ orbitals. The fact that Pr_2CuO_4 has the largest content of impurities (Tab. 4.3) shows that the small field dependence in Pr_2CuO_4 may indeed be caused by scattering by paramagnetic impurities. The small magnetic-field dependences observed in $\text{Pr}_{1.3}\text{La}_{0.7}\text{CuO}_4$ [139] have presumably the same origin.

4.7. Conclusions

In this chapter we presented measurements of the thermal conductivity of $R_2\text{CuO}_4$ with $R = \text{La, Pr, Nd, Sm, Eu, and Gd}$. In the first part the zero-field thermal conductivity was studied in the temperature range $5\text{ K} \leq T \leq 300\text{ K}$ for both, a heat current perpendicular ($R = \text{Pr and Gd}$) and parallel ($R = \text{Pr, Nd, Sm, Eu, and Gd}$) to the CuO_2 planes. The out-of-plane thermal conductivity shows the typical temperature dependence of a purely phononic thermal conductivity with a low-temperature maximum, whose magnitude depends on the crystal quality. In contrast, the in-plane conductivity for all crystal exhibits a pronounced double-peak structure consisting (i) of a low-temperature peak similar to that of the out-of-plane thermal conductivity and (ii) of an anomalous high-temperature contribution with a broad maximum around 250 K. Such an anisotropy between the in-plane and the out-of-plane thermal conductivity is also found in La_2CuO_4 . [6–8, 11] The fact that the double-peak is present in the structurally stable $R_2\text{CuO}_4$ with $R = \text{Pr, Nd, and Sm}$ unambiguously rules out the possibility that the double-peak structure is caused by a structural instability, which is present for $R = \text{La, Eu, and Gd}$. The qualitative anisotropy between the in-plane and the out-of-plane thermal conductivity and the rather similar high-temperature behavior of the out-of-plane thermal conductivity for all the different crystals gives clear evidence that this additional high-temperature contribution arises from a sizeable heat transport by magnetic excitations within the CuO_2 planes. Our analysis yields a magnetic contribution to the in-plane thermal conductivity between about 7 to 25 W/Km depending on the R system. In weakly

doped La_2CuO_4 this magnetic contribution is strongly suppressed showing that scattering of magnetic excitations by mobile charge carriers plays an important role. In contrast, the structural instability does hardly influence the magnetic thermal conductivity indicating that scattering of magnetic excitations by soft or anharmonic phonons plays a minor role. To compare the principle behavior of the thermal conductivity of the 2D square lattice with 1D systems, the energy diffusion constant $D_E(T)$ was calculated for La_2CuO_4 [9] and compared with $D_E(T)$ obtained for 1D chains with $S = 1/2$ and $S = 1$. The heat transport in the 1D systems is anomalously enhanced, since the estimated $D_E(T)$ is much larger than an estimate using the calculated correlation length[78]. In contrast, a rather conventional behavior of the thermal transport in the 2D square lattice is found. The observation of a large magnetic contribution to the heat transport is just a consequence of the large coupling constant J , which causes a sizeable contribution to κ , and the fact that $J \gg \Theta_D$, allowing the distinction of κ_{mag} from the phononic heat conductivity.

A second focus was the influence of magnetic fields on κ . At low temperatures we observed large magnetic-field effects of κ_{ab} in Nd_2CuO_4 and Gd_2CuO_4 , a smaller effect in Pr_2CuO_4 , and no magnetic-field dependences in Sm_2CuO_4 and Eu_2CuO_4 . We showed that resonant scattering by the $4f$ orbitals can in principle consistently describe the observed behavior. This conclusion is in contrast to the magnon heat transport proposed in Refs. [10, 80]. A detailed analysis revealed, that the methods used to extract the possible magnon contributions are affected with large uncertainties, particularly at higher temperatures as done in Ref. [80]. We further showed, that the argumentation used in Ref. [10] is not consistent with our data. Our scenario based on phonon scattering can in principle also explain the findings of Ref. [10]. The observed magnetic-field dependences of κ are much smaller than observed e.g. in NdMnO_3 , where the effect is unambiguously caused by the $4f$ orbitals. Therefore, we conclude that the proposed observation of a magnon contribution to the heat transport is highly questionable.

5. Thermal Conductivity in Cubic Cobaltates

Among transition-metal oxides cobalt compounds are of particular interest due to the possibility of the Co ions to occur in different spin states. LaCoO_3 is one of the most prominent examples, which is in the focus of researchers since several decades [175, 176], and still the nature of the spin-state transition is to be clarified. The spin-state transition is visible in various quantities, like e.g. susceptibility, thermal expansion and specific heat. Recently, it was found that the low-temperature thermal conductivity of LaCoO_3 is also very unusual [9, 33, 57], which was also attributed to the spin-state transition. However, the mechanism responsible for the observed unusual thermal conductivity is not clear. In this chapter a detailed investigation of the thermal conductivity in LaCoO_3 , PrCoO_3 , NdCoO_3 , and EuCoO_3 will be presented. The aim is to develop a consistent picture of the influence of the spin-state transition on the thermal conductivity. The measurements of κ in PrCoO_3 and NdCoO_3 were performed by H. Anapa [177]. Some of the thermal conductivity data have been already shown in Refs. [33, 57, 166].

5.1. The Spin-state Transition in $R\text{CoO}_3$ with $R = \text{La, Pr, Nd, and Eu}$

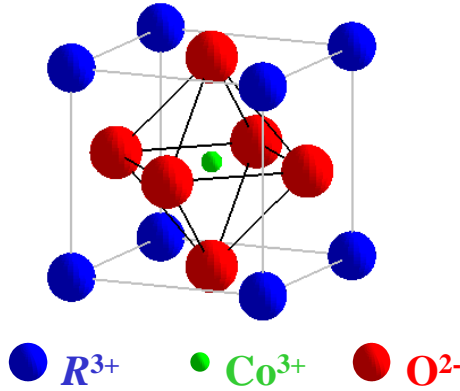


Figure 5.1.: Structure of $R\text{CoO}_3$ in the cubic notation. The Co^{3+} is surrounded by an oxygen octahedron.

The $R\text{CoO}_3$ compounds with $R = \text{La, Pr, Nd, and Eu}$ crystallize in a AMO_3 -type perovskite structure, see Fig. 5.1. LaCoO_3 is slightly rhomboedrally distorted, which is often referred to as pseudo cubic. For the smaller rare-earth ions the type of the distortion changes, and an orthorhombic structure is realized [178–181]. Rare earth ionic radii, lattice constants and volumes of the unit cells (in cubic notation) with the respective references are listed in Tab. 5.2. Resistivity measurements show that all $R\text{CoO}_3$ compounds are insulating below room temperature [177, 182]. For all $R\text{CoO}_3$ the Co^{3+} ion has a $3d^6$ configuration, which is five-fold degenerate for a free ion. In the cubic crystal field these five levels split into

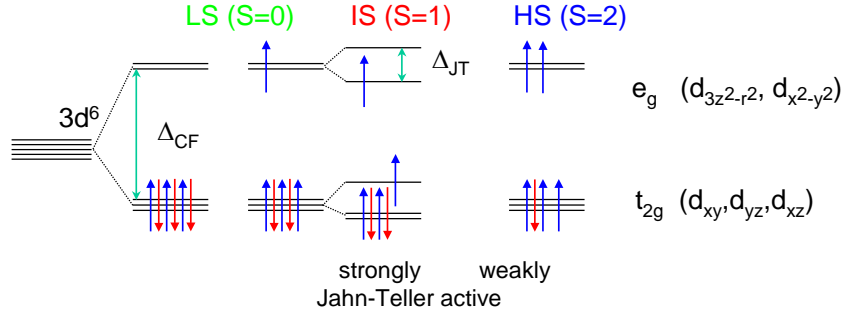


Figure 5.2.: Splitting of the 3d orbitals in a cubic crystal field and possible spin states for a $3d^6$ configuration. Both, the e_g and the t_{2g} levels can be Jahn-Teller active.

the three-fold degenerate t_{2g} and the two-fold degenerate e_g level, where the level spacing denotes Δ_{cf} (see Fig. 5.2) [183]. The e_g levels consist of the $d_{x^2-y^2}$ and $d_{3z^2-r^2}$ orbitals, which directly point to the surrounding oxygen ions. The d_{xy} , d_{xz} , and d_{yz} orbitals of the t_{2g} levels point inbetween the oxygen orbitals, yielding a lower energy for the t_{2g} and a higher energy for the e_g levels. The second important energy scale is the Hunds rule energy J_H [16]. If J_H is the dominant energy scale ($J_H \gg \Delta_{cf}$), the six electrons of the Co^{3+} ion will have parallel spin according to Hunds first rule [16], what leads to the high-spin (HS) state with $S = 2$, see Fig. 5.2. In the other case, $J_H \ll \Delta_{cf}$, the crystal field energy will not allow that electrons occupy the e_g orbitals. Therefore the low-spin (LS) state ($S = 0$) with 6 electrons in the t_{2g} levels is realized [183]. In recent years several authors proposed another possible low-lying spin-state, the so-called intermediate (IS) spin-state with $S = 1$ [184–201]. In LaCoO_3 the unusual situation is realized, that J_H and Δ_{cf} are so close that temperature can induce transitions between different spin states [176]. Fig. 5.3 shows the Co^{3+} susceptibility of LaCoO_3 and EuCoO_3 [202].¹ For LaCoO_3 , at low temperatures, the system is nonmagnetic, and the LS state is realized. The sudden increase of χ for temperatures above ≈ 25 K is due to the thermally driven spin-state transition, where spin states with a magnetic moment get populated. The question, if this spin state is an IS or a HS state, has been widely discussed in the literature, and is still under debate [184–201, 203, 204]. The LS-IS state scenario gives a better description of the thermodynamic properties in an analysis based on a two-level system [12, 205]. This analysis works well with a g factor of ≈ 2.3 , which is much smaller than the g factor recently measured by ESR measurements, $g = 3.5$. Such a high g factor does not allow a description of the susceptibility in a simple LS-IS or LS-HS model, since the calculated susceptibility is much too high. For the description of other thermodynamic properties, like thermal expansion or specific heat, the g factor plays no role. As pointed out in Refs. [13, 204], a way out is the introduction of a spin-orbit coupled HS state (SOcHS). The idea hereby is that the usual assumption of a quenched orbital moment [16] is not valid, and then the $S = 2$ HS state couples with a $\tilde{l} = 1$ orbital moment to an effective moment $\tilde{J} = 1$ [205]. However, the description of the susceptibility only works if a temperature-dependent gap is introduced [178, 205], see Sec. 5.3.2. None of these models gives an unambiguous picture of the spin-state transition in LaCoO_3 . The newest results [13] prefer a SOcHS scenario. Since the IS model gives the best thermodynamic description with a fixed gap (but with the wrong

¹The other contributions to the susceptibility are subtracted, this procedure will be discussed in Sec. 5.3.

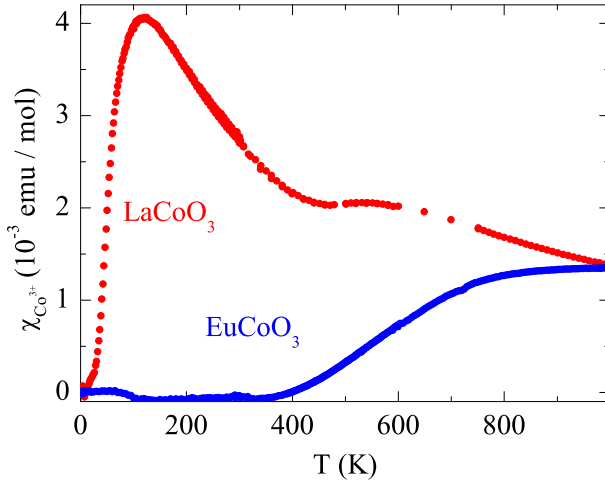


Figure 5.3.: Co^{3+} susceptibility of LaCoO_3 and EuCoO_3 . Background contributions have been subtracted (see Fig. 5.4). [202]

g factor), we will perform the data analysis using both, the IS model with $\Delta_{\text{Co}} = 185 \text{ K}$, $\nu = 1$ and the SOcHS model². The energy gaps are taken from the susceptibility and thermal expansion fits of Ref. [205]. The aim hereby is to keep as many parameters as possible fixed. The spin-orbit coupled HS model will also be analyzed, herefore the temperature-dependent energy gap will be calculated in Sec. 5.3.2.

If La is replaced by the smaller Eu, the LS state is stabilized, which causes a shift of the spin-state transition to much higher temperatures, as seen in the susceptibility data for EuCoO_3 (Fig. 5.3). A detailed investigation of the evolution of the spin-state transition of $\text{La}_{1-x}\text{Eu}_x\text{CoO}_3$ crystals with $0 \leq x \leq 1$ can be found in Refs. [178, 206]. However, these mixed crystals have several disadvantages, in particular in terms of thermal conductivity measurements [177]³. This motivated the growth and investigation of $R\text{CoO}_3$ single crystals with $R = \text{Pr}$ and Nd [205, 207]. In these compounds the spin gap lies inbetween those of LaCoO_3 and EuCoO_3 [205]. For the data analysis of the rare-earth compounds, the IS model will be used with the parameters derived from thermal expansion and susceptibility [205].

5.1.1. Jahn-Teller Effect

The Jahn-Teller effect causes a spontaneous distortion of the crystal symmetry, when the energy gain through lifting the degeneracy of an energy level is bigger than the elastic energy which is needed to distort the crystal [208]. The e_g orbitals split into two singlets, while the center of mass remains unchanged (see Fig. 5.2). It follows that for a high-spin state no Jahn-Teller effect is possible for the e_g orbital, since the energy gain and loss of the two electrons in the e_g orbital exactly cancel each other. The t_{2g} orbital splits into a doublet with the lower energy and a singlet. Here, the energy gain is less than for the e_g orbital, and the Jahn-Teller effect is less effective.

As long as the octahedral distortions fluctuate, one speaks of a dynamical Jahn-Teller effect. The other possibility is that the distorted octahedra form a long-range ordered state, which is called the collective Jahn-Teller effect. The possible influence of the Jahn-Teller effect in LaCoO_3 is discussed in Refs. [9, 12, 197, 201, 209–212].

² ν describes an additional orbital degeneracy, see Refs. [12, 205, 206].

³The mixed compounds are only available as polycrystals. Moreover, the additional effect of the disorder on the R site suppresses κ .

		$A[\text{mm}^2]$	$L[\text{mm}]$
LaCoO ₃	Zo104	0.8×1.5	3.7
LaCoO ₃	Mar5b_07	0.8×1.4	2.6
LaCoO ₃	Mar5a_08	1.4×0.8	3.4
LaCoO ₃	Mar5_09	1.1×0.8	2.3
LaCoO ₃	EKParis	2.3*	4.7
PrCoO ₃		1.0×3.8	2.5
NdCoO ₃		1.7×2.0	2.8
EuCoO ₃		0.3×0.9	2

Table 5.1.: Sample sizes of the investigated $R\text{CoO}_3$ samples. *) The EKParis crystal has a half-moon shaped cross section.

5.2. Samples

All investigated $R\text{CoO}_3$ samples are single crystals grown in a floating-zone furnace. The measurements of the thermal conductivity of LaCoO₃ were performed on five different single crystals. The crystal Zo104 was grown by C. Zobel [33] and was used for several investigations, e.g. thermal expansion, susceptibility, and specific heat measurements. [12, 178, 205, 213] The crystal labeled EKParis was grown by G. Dhallenne (Université Paris Sud). The other three samples were grown by M. Reuther [214], and are labeled as Mar5a_8, Mar5b_07, and Mar5_09. The EuCoO₃ crystal (AR11) was grown by A. Reichl [179], and the PrCoO₃ (MB15) and NdCoO₃ (MB16) crystals by M. Benomar [207].

All measurements have been performed along arbitrary directions. The LaCoO₃ crystals are heavily twinned, so no pronounced direction dependence is expected. The twinning in the rare-earth cobaltates was not investigated. Because of the larger anisotropy twinning may be less important.

5.3. Susceptibility Analysis

Fig. 5.4a shows the measured susceptibilities of $R\text{CoO}_3$ with $R = \text{La}, \text{Pr}, \text{Nd}, \text{and Eu}$. For LaCoO₃ the measured susceptibility contains the background contributions

$$\chi_{\text{bg}} = \chi_{\text{CW}} + \chi_{\text{vV}} + \chi_{\text{dia}}, \quad (5.1)$$

where the first part χ_{CW} is a paramagnetic impurity contribution, and the latter consists of a temperature independent van Vleck contribution χ_{vV} of the Co^{3+} ions and the diamagnetic susceptibility of closed shells χ_{dia} . The paramagnetic low-temperature contribution is comparatively large, which is possibly related to the occurrence of so-called HS polarons [215], as will be discussed later. In EuCoO₃ the van Vleck contribution of the Eu^{3+} ions becomes large and temperature dependent [216], what has to be taken into account in Eq. 5.1. Replacing La by a rare-earth ion, whose ionic radius lies inbetween those of La and Eu, leads to a spin gap inbetween those of LaCoO₃ and EuCoO₃. Complications arise from the $4f$ magnetism, which dominates the measured susceptibility in NdCoO₃ and PrCoO₃ (see Fig. 5.4). However, a separation was successfully done in Ref. [205]. The lower panel shows the Co^{3+} susceptibility, and as expected the onset temperature of the spin-state transition for $R = \text{Pr}$ and Nd lies

R	$\Delta_{\text{Co}}^{\text{IS}}(\chi)$ (K)	$\Delta_{\text{Co}}^{\text{IS}}(\alpha)$ (K)	ν (K)	a_{cubic} (Å)	V_{uc} (Å ³)	r_R (Å)	C ($\frac{\text{emuK}}{\text{mole}}$)
La	185	180	1	3.825 [200]	55.98 [200]	1.160	0.033 [178]
Pr	1100	1200	3	3.788 [45]	54.38 [45]	1.126	0.018
Nd	1400	1750	3	3.775 [52]	53.78 [52]	1.109	
Eu	1900		3	3.750 [178, 179]	52.75 [178, 179]	1.066	0.003 [178]

Table 5.2.: Co^{3+} spin gap Δ_{Co} as derived from susceptibility and thermal expansion in Ref. [205] (with degeneracy ν used for the analysis), cubic lattice constant a , cubic unit cell volume V_{uc} , ionic radii (from Ref. [54]), and Curie constants of the paramagnetic low-temperature contribution (see text).

inbetween those for $R = \text{La}$ and Eu . The analysis of the susceptibility was done in Ref. [205] based on a two-level system which gives the relation

$$\chi_{\text{Co}} = \frac{N_A \mu_B^2 g^2}{3k_B T} \cdot \frac{S(S+1) \cdot \nu(2S+1) \cdot \exp(-\Delta/T)}{1 + \nu(2S+1) \cdot \exp(-\Delta/T)}. \quad (5.2)$$

The model dependent parameters are the g factor, the spin S ($S = 1$ for IS and $S = 2$ for HS), the spin gap Δ , and an additional orbital degeneracy ν , which can be 1 or 3. For the LS-IS and LS-HS model the values are listed in Tab. 5.2. Except for LaCoO_3 only the LS-IS model with $\nu = 1$ has been considered (see Ref. [205]). Note that for a SOcHS model, the formula is the same, if one replaces S by \tilde{J} and sets $\nu = 1$.

5.3.1. CF Analysis of the Susceptibility of PrCoO_3 and NdCoO_3

In principle the susceptibility of the R^{3+} ions in PrCoO_3 and NdCoO_3 can be calculated if the CF parameters are known. No CF investigations are available for these compounds, but as shown in Sec. 2.4 the CF is expected to be very similar in PrNiO_3 and NdGaO_3 . Fig. 5.5 shows the calculated⁴ inverse susceptibilities and magnetization curves for PrCoO_3 and NdCoO_3 using the CF parameters from Refs. [44, 47]. The general temperature and field dependences of the R^{3+} moments are well described by the calculations. In PrCoO_3 , the calculated susceptibility is anisotropic (panel a). The best agreement between data and calculation is given for the b direction. The deviations at low temperatures are due to the paramagnetic impurities, and at high temperatures due to the Co^{3+} susceptibility. Note, that the slopes of the different χ^{-1} curves are nearly identical. This shows that the fit used in Ref. [205] to determine the Co^{3+} susceptibility is a good approximation. Fig. 5.5b shows magnetization curves at 1.8 K. Again, a large anisotropy and a good agreement of the data to the calculated curve for $H \parallel b$ is observed. Fig. 5.5c and d show the results for NdCoO_3 , with basically the same conclusions. Here, the best agreement is given for the calculation with $H \parallel a$.

5.3.2. Spin-State Transition with variable Energy Gap

By using the measured g factor of $g \approx 3.5$ [204] in Eq. 5.2, the description of the susceptibility gets worse. A possible way out is the introduction of an effective interaction between the

⁴The directions are given in the Pbm \bar{n} notation (see Chp. 7).

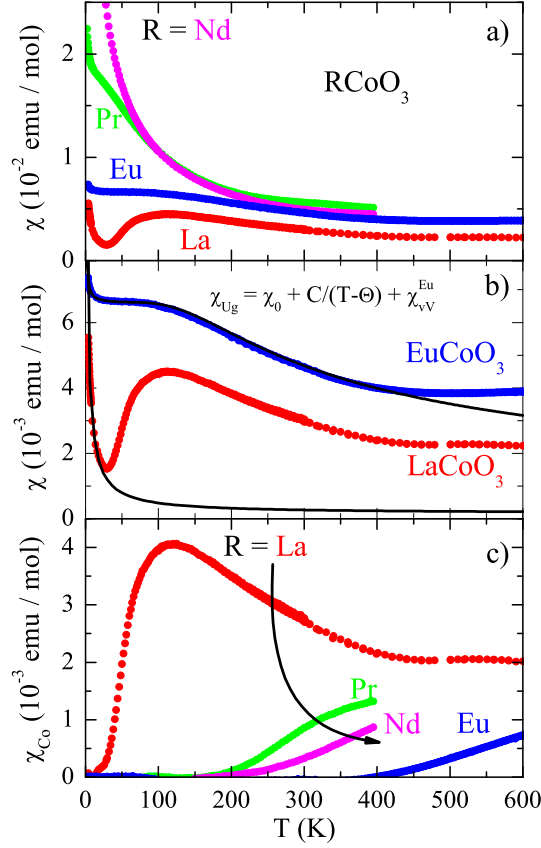


Figure 5.4.: a) Measured susceptibility for $R\text{CoO}_3$ with $R=\text{La}$, Pr , Nd , and Eu . For PrCoO_3 and NdCoO_3 the $4f$ contribution is dominant. b) Estimation of the background contribution to χ . For EuCoO_3 a large Eu van Vleck contribution is present. c) Co^{3+} contributions to the susceptibility. The spin-state transition shifts successively to higher temperatures with decreasing rare earth size. [202, 217]

Co^{3+} sites, what can be described by a temperature-dependent energy gap [178, 205]. The underlying idea is that the population of an excited state hinders the surrounding Co^{3+} ions to get excited, what effectively increases the spin gap Δ_{Co} . The temperature-dependent gap can be calculated by reverting Eq. 5.2, what leads to

$$\Delta_{\text{Co}}(T) = T \ln \left(\frac{N_A g^2 \mu_B^2 S(S+1)}{3k_B T} \frac{\nu(2S+1)}{\chi_{\text{Co}}(T)} - \nu(2S+1) \right). \quad (5.3)$$

Setting $\tilde{J} = \nu = 1$, the temperature-dependent gap shown in Fig. 5.6a is calculated. Note that the gap should get temperature independent at low temperatures, when the distance between excited sites gets large. However, here the gap cannot be determined exactly because of the uncertainty of the background contribution below ≈ 25 K. This model is supported by recent experimental results based on soft x-ray absorption spectroscopy and magnetic circular dichroism, where an energy dependent gap with the same temperature dependence is obtained [13]. In Ref. [205] a combined analysis of the susceptibility and thermal expansion

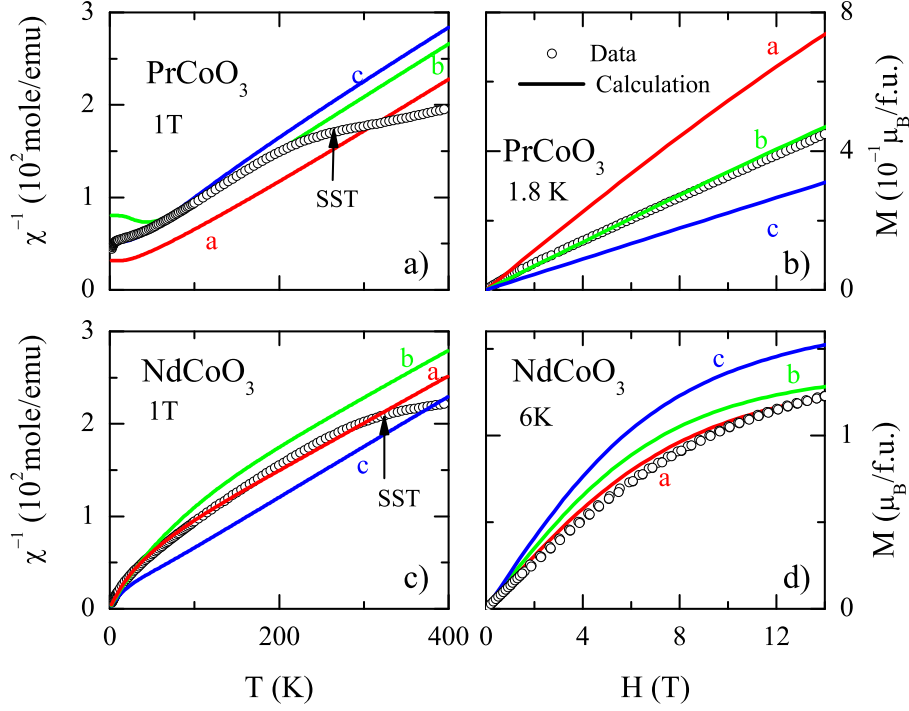


Figure 5.5.: Calculated susceptibilities and magnetization with different field directions using the CF parameters of PrNiO_3 and NdGaO_3 [44, 47] in comparison to the data of PrCoO_3 and NdCoO_3 . The arrows labeled SST show where the Co^{3+} susceptibility starts to contribute due to the spin-state transition.

was performed with the LS-IS model. Using the same Ansatz the formula

$$\alpha_{\text{Co}} = \frac{3d \exp\left(\frac{\Delta(T)}{T}\right) \left(\Delta(T) - T \frac{\partial \Delta(T)}{\partial T}\right)}{\left(3 + \exp\left(\frac{\Delta(T)}{T}\right)\right)^2 T^2} \quad (5.4)$$

is obtained for the additional thermal expansion, if the energy gap is temperature dependent. Using the values of $\Delta(T)$ from Fig. 5.6, the thermal expansion can be calculated. The result is shown in Fig. 5.6b, and is in good agreement with the measured thermal expansion. The value $d = 1.8\%$ is obtained. By scaling the thermal expansion and the susceptibility curves with the scaling procedure from Ref. [205], a scaling factor of 170 emuK/mole is obtained, which is in good agreement with the experimental observation of 180 emuK/mole [205].

5.3.3. Impurity Contribution in LaCoO_3

In this section a detailed analysis of the paramagnetic impurity contribution to the susceptibility will be given, with the purpose to analyze the influence of these impurities to the thermal conductivity. Therefore the magnetization measurements were performed on the identical samples which were used for the thermal conductivity measurements.

The paramagnetic impurity content can be determined either by temperature-dependent susceptibility measurements or from the magnetic-field dependent magnetization at low tem-

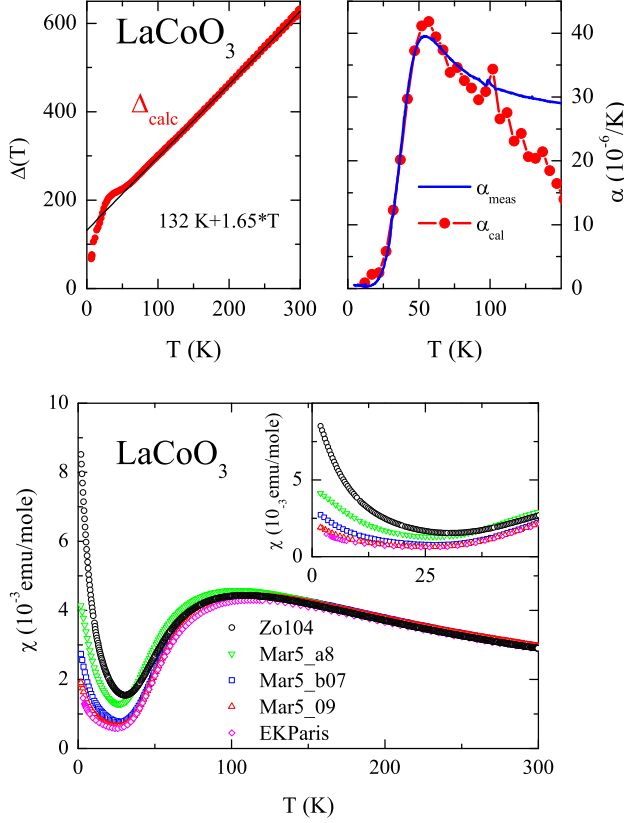


Figure 5.6.: a) Temperature-dependent energy gap Δ_{Co} for LaCoO_3 (symbols) as calculated from the magnetic susceptibility with $g = 3.5$ and an excited triplet state, see text. The solid line is a linear fit. b) Anomalous thermal expansion caused by the spin-state transition from [205], and calculation with Eq. 5.4 using $\Delta(T)$.

Figure 5.7.: Temperature-dependent magnetic susceptibility measured in a field of 1 T. The low-temperature paramagnetic impurity contribution is strongly sample dependent. [218]

peratures. The magnetization measurements were carried out by H. Hartmann [218] at a fixed temperature of 3 K in a vibrating sample magnetometer (VSM). Because the population of the IS/HS state is negligible at this temperature, the magnetization contains only two contributions:

$$M(H) = M_{\text{para}}(H) + M_0(H), \quad (5.5)$$

where M_{para} is the paramagnetic impurity contribution, and $M_0(H)$ is the background. $M_0(H)$ consists of the diamagnetic contribution of the core electrons and the paramagnetic van Vleck susceptibility of the Co^{3+} electrons, and gives a simple linear contribution $M_0(H) = \chi_0 * H$. The paramagnetic part $M_{\text{para}}(H)$ is usually described by

$$M_{\text{para}}(H) = NgJ\mu_B B_J(x) \quad \text{with} \quad x = gJ\mu_B H/k_B T \quad (5.6)$$

and the so-called Brillouin function $B_J(x)$ [16]. Here, N denotes the number of the paramagnetic moments with spin J . Fig. 5.8 shows the magnetization curves at 3 K for the sample Zo104. The linear part of $M(H)$ is obtained by a fit for $H > 12$ T, and the subtraction yields the curves for the paramagnetic contribution in Fig. 5.8 (dashed line). The calculation of $M(H)$ with Eq. 5.6 does reproduce the field dependence only qualitatively. If the fit range is restricted to low fields ($H \leq 0.1$ T), a value $J = 5$ is obtained (with $g = 2$). This fit leads to a good description of the initial slope of $M(H)$. The two fit parameters of the linear fit give the values of M_{sat} and χ_0 listed in Tab. 5.3. The paramagnetic part of the susceptibility from

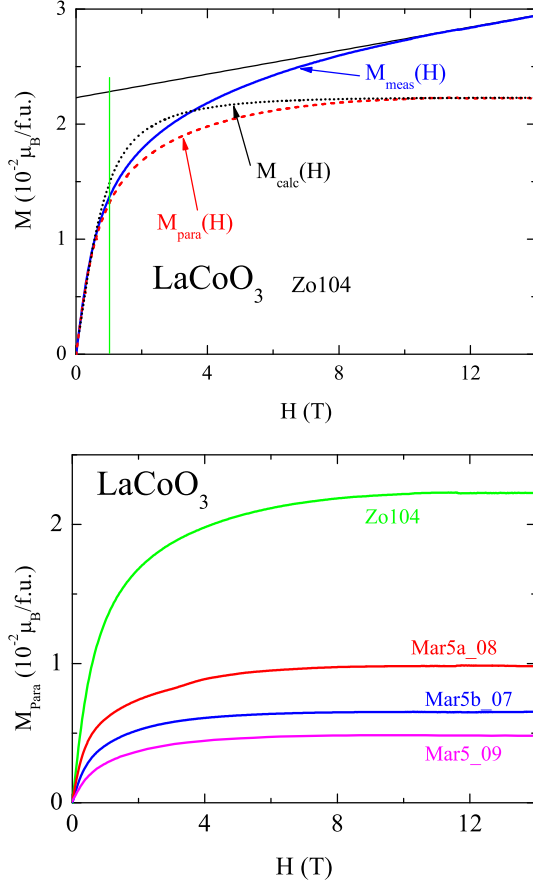


Figure 5.8.: Magnetization curve for LaCoO_3 at 3 K. The contribution of the paramagnetic impurities is estimated by subtracting a linear contribution estimated by a high-field fit (see text). The calculated Brillouin function does not describe the data very well. The vertical line indicates the field of 1 T, which was used for the temperature-dependent measurements.

Figure 5.9.: Paramagnetic contribution to the magnetization $M(H)$ of LaCoO_3 at 3 K for different samples. The linear contribution to $M(H)$ has been estimated by high field fits, and subtracted from the data.

the temperature-dependent measurements can be determined by fitting the low-temperature range by⁵

$$\chi(T) = \chi_0 + C/(T - \Theta). \quad (5.7)$$

The estimation of C from the temperature-dependent susceptibility requires measurements at the low-field limit, since the paramagnetic impurity part is suppressed in higher fields. $\chi(T)$ was measured for all samples in a magnetic field of 1 T (see Fig. 5.7). The magnetization measurements (Fig. 5.8) show that $M(H)$ is beyond the linear behavior at 1 T. However, for large x the Brillouin function $B_J(x)$ goes to 1 and Eq. 5.6 can be replaced by

$$M(\mu_B H \gg k_B T) = N g J \mu_B. \quad (5.8)$$

It follows that the saturation magnetization is proportional to N and can therefore be used as a measure of the impurity content.

A magnetization measurement is not available for the EKParis sample. For this sample $M_{\text{imp}}^{\text{sat}}$ was estimated from the temperature-dependent susceptibility, which was measured in a field of 1 T in all samples. Herefore the fact is used, that the shape of all magnetization curves is almost identical in all samples. It follows that the magnetization at 1 T determined from the temperature-dependent measurement can be extrapolated to the saturation magnetization via

$$\tilde{M}_{\text{imp}}^{\text{sat}} = [\chi(3 \text{ K}, 1 \text{ T}) - \overline{\chi_0}] \cdot \overline{M(14 \text{ T})/M(1 \text{ T})}. \quad (5.9)$$

⁵A more reliable estimation of C can be achieved by determining χ_0 from the high-field slope of $M(T)$.

5. Thermal Conductivity in Cubic Cobaltates

Specimen	$\chi(3\text{K})$ $10^{-3}(\frac{\text{emu}}{\text{mole}})$	$M_{\text{imp}}^{\text{sat}}$ $(10^{-3}\frac{\mu_B}{\text{f.u.}})$	χ_0 $(10^{-4}\frac{\text{emu}}{\text{mole}})$	$M_{\text{para}}^{14\text{T}}/M_{\text{para}}^{1\text{T}}$	$\tilde{M}_{\text{imp}}^{\text{sat}}$ $(10^{-3}\frac{\mu_B}{\text{f.u.}})$	$\Delta\tilde{M}_{\text{imp}}^{\text{sat}}$ $10^{-3}\frac{\mu_B}{\text{f.u.}}$
Zo104	7.6	22.3	2.6	1.7	21.7	0.6
Mar5b_07	2.5	6.5	1.7	1.62	6.6	0.1
Mar5a_08	3.9	9.8	4.1	1.51	10.9	1.1
Mar5_09	1.7	4.8	1.9	1.85	4.4	0.4
EKParis	1.5				3.6	

Table 5.3.: Parameters for the estimation of the impurity contribution for the different LaCoO_3 samples, see text.

Here, $\overline{M(14\text{T})}/\overline{M(1\text{T})} = 1.7$ and $\overline{\chi_0} = 2.6 \cdot 10^{-4} \text{emu/mole}$ are averaged over the four samples, where magnetization measurements were available. The application of Eq. 5.9 to these four samples yields values which only slightly deviate from the measured $M_{\text{imp}}^{\text{sat}}$ (see Tab. 5.3). This ensures, that a confident value of $M_{\text{imp}}^{\text{sat}}$ is obtained for the sample EKParis with Eq. 5.9.

In Ref. [215] the authors investigated the influence of so-called high-spin polarons with $S = 10 \dots 16$ for slightly Sr-doped $\text{La}_{1-x}\text{Sr}_x\text{CoO}_3$ crystals ($x \leq 0.01$). This analysis is performed by the use of Eq. 5.6. The idea is that the divalent Sr^{2+} ions nominally cause the same amount of Co^{4+} ions, and that these magnetic ions induce a spin-state transition of the neighboring Co^{3+} ions from LS to IS or HS states. These sites then couple to a high-spin polaron with $S = 10 \dots 16$. The samples investigated here were Sr free, however, if the samples contain additional oxygen, the same effect may be achieved. An indication hereof is that the value of J obtained by the Brillouin fits ranges from $J = 5 \dots 9.5$, if the criteria is to fit the initial slope of the $M(T)$ curves. This is consistent with Ref. [215], because J decreases for a smaller Sr content, and the amount of additional oxygen is presumably very small. The question remains, why the measured magnetization deviates from a Brillouin function. A possible explanation is another kind of magnetic defects contributing significantly to $M(H)$. Moreover, interactions between the magnetic moments can explain such a behavior. In the next chapter the thermopower of the LaCoO_3 crystals will be investigated. The sign of the thermopower gives an information about the sign of the dominant charge carriers. Interestingly, only two of the samples show a positive thermopower at room temperature, Mar5b_07 and Mar5_09. These are the samples, which have the smallest values of $P_{\text{imp}}^{\text{sat}}$.

The concept of magnetic polarons explains the considerably high paramagnetic contribution to $M(H)$ in LaCoO_3 . The induction of surrounding ions into the HS/IS state gets less favorable, if the spin gap is increased. As a consequence, the paramagnetic contribution should weaken with increasing energy gap. Therefore we expect a successively decreasing Curie constant for $R\text{CoO}_3$ with $R = \text{Pr}, \text{Nd}, \text{and Eu}$. In EuCoO_3 the Curie constant is indeed about an order of magnitude smaller, than in LaCoO_3 . For $R = \text{Pr}$ the estimation of the paramagnetic contribution is shown in Fig. 5.10a. Because of the non-magnetic ground state of the Pr^{3+} ion (see Sec. 5.3.1), a Curie fit with Eq. 5.7 is possible. χ_0 is the temperature independent sum of the van Vleck contributions of Co^{3+} and Pr^{3+} . The fit yields the values $\chi_0 = 0.017 \text{emu/mole}$, $\Theta = -0.73 \text{K}$ and $C_{\text{imp}} = 0.015 \text{emu/moleK}$. The pure PrCoO_3 susceptibility obtained by subtracting the impurity contribution is shown as solid line. The inset shows the magnetization of PrCoO_3 at 1.8 K. Here, the impurity contribution is estimated as in LaCoO_3 by subtracting a high-field linear fit, and analyzing the residual magnetization by Eq. 5.6. The resulting impurity magnetization is much smaller than the magnetization of the Pr^{3+} ions (note the

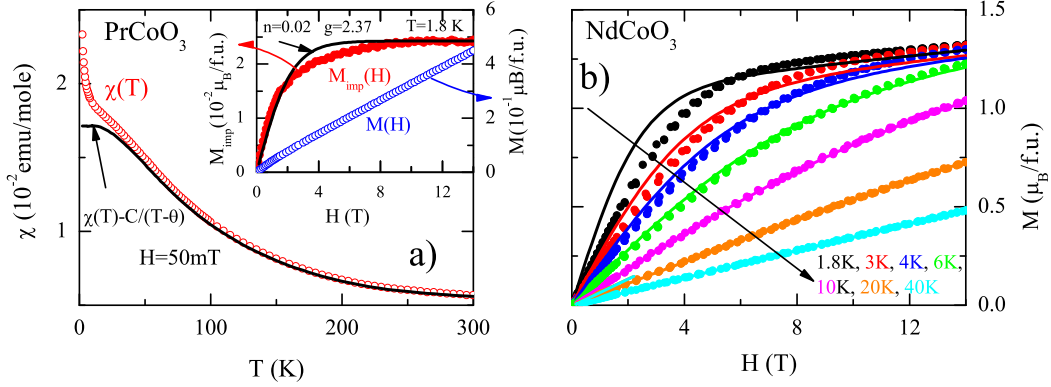


Figure 5.10.: a) Susceptibility of PrCoO_3 and calculated Pr^{3+} contribution by subtraction of the low-temperature Curie term caused by paramagnetic impurities. Inset: Magnetization at 1.8 K and extracted impurity contribution. Note the different scales. b) Low-temperature magnetization measurements of NdCoO_3 at various temperatures. Lines are calculated according to Eq. 5.6 taking into account a linear van Vleck contribution.

different scales). The best fit using $J = 0.5$ for a two-level impurity system yields the values $n_{\text{imp}} = 0.02$ and $g_{\text{imp}} = 2.37$. The resulting $C = 0.019 \text{ emu/moleK}$ is in good agreement with the result from the analysis of the temperature dependent measurement. The value of C lies inbetween those of LaCoO_3 and EuCoO_3 , which shows indeed the correlation between spin gap and paramagnetic impurities.

For $R = \text{Nd}$, Fig. 5.10b, the ground state of the Nd^{3+} ion is a Kramer's doublet (see Sec. 5.3.1). The magnetization at low temperatures is determined by the Nd contribution, consistent of a Brillouin and a van Vleck term. The magnetization curves have been fitted⁶ by Eq. 5.6 and an additional term $M_{\text{Nd}}^{\text{V}} = 1.5 \cdot 10^{-6} H \mu_B/\text{f.u.}$, estimated from a high-field fit at 1.8 K. The other values used are $J = 0.5$, $n_{\text{Nd}} = 1$ and the g_{Nd} factor is the only adjustable parameter. The resulting g factor is almost constant between 1.8 K and 40 K, ($2.12 \leq g \leq 2.19$), yielding an average value $g = 2.15$. Note that the absolute values of the magnetization is much larger than the impurity contributions determined for the other compounds. A determination of the impurity Curie constant C is therefore not possible for NdCoO_3 .

5.4. Results

5.4.1. LaCoO_3

In Fig. 5.11 the thermal conductivity of LaCoO_3 is shown (sample Zo104). [57] At first glance κ seems to be consistent with usual phononic heat transport (see Sec. 2). However, a closer inspection of the data reveals several anomalous features. The thermal conductivity above about 100 K is anomalously small and its temperature dependence is very unusual, since above 150 K the thermal conductivity slightly increases with increasing temperature. The small absolute values cannot be attributed to strong defect scattering, since conventional defect scattering does not vanish below 100 K so that κ would not increase and show a maximum

⁶The deviations at low temperatures are likely to be caused by fluctuations of the Nd ordering, which occurs at 1.2 K [219].

Specimen	T_{\max} (K)	κ_{\max} (W/Km)	$\kappa(300\text{ K})$ (W/Km)	$S(300\text{ K})$ $\mu\text{V/K}$
Zo104	28	10	2.2	-700
Mar5b_07	28	20	3.5	1000
Mar5a_08	32	8	4.4	-600
Mar5_09	25	34	3.3	1000
EKParis	29	27	4.4	-300
PrCoO ₃	26	26	3.0	-400
NdCoO ₃	23	53	4.8	-400
EuCoO ₃	19	266	8.1	-500

Table 5.4.: $R\text{CoO}_3$: Low-temperature maxima and room-temperature values of thermal conductivity κ and thermopower S .

below 100 K. Therefore, the small κ and its unusual temperature dependence indicate that an unusual, additional scattering mechanism is active above about 25 K. It is, in principle, possible that low-lying optical phonons cause resonant scattering of acoustic phonons and therefore suppress the heat current in a certain temperature range. A softening of optical phonon branches has been observed in Ref. [220]. However, in LaAlO_3 , having the same structure, has a conventional thermal conductivity [22]. It is unlikely that the unusual thermal conductivity is an intrinsic feature of the phonon modes of LaCoO_3 .

Another source of additional phonon scattering could be the spin-state transition. The idea is that the thermal population of the excited spin state causes additional disorder due to the random distribution of the populated sites. To motivate this picture, the Co^{3+} susceptibility of LaCoO_3 is plotted in Fig. 5.11 (right scale). The temperature-dependent spin-state transition implies an increasing lattice disorder above 25 K, and therefore an additional suppression of the thermal conductivity. The disorder and thus the suppression of κ is most pronounced for an equal number of LS and IS (HS) ions. For an energy gap $\Delta \simeq 185\text{ K}$ between the LS and IS/HS states an equal occupation of LS and IS ions is expected around $T \simeq 165\text{ K}$. Therefore the strong reduction of κ above 25 K, its small absolute values and the weak minimum around 150 K can arise from temperature-induced LS-IS/HS disorder.

If a magnetic field of 14 T is applied, the thermal conductivity is significantly changed below 50 K. That is not expected for a conventional phononic heat transport, since phonons are not expected to be field dependent. Furthermore, the energy gap Δ_{Co} is too large to be affected by a magnetic field in a significant way. Moreover, the field dependence remains below 5 K, where practically all Co^{3+} sites are in the LS state. This suggests that another scattering mechanism is present at low temperatures, which is magnetic-field dependent.

5.4.2. $R\text{CoO}_3$ with $R = \text{La, Pr, Nd, and Eu}$

As shown in Sec. 5.1, the spin-state transition shifts to higher temperature if La is replaced by smaller R ions. This should have an influence on the thermal conductivity, if the picture depicted above is valid. Fig. 5.12 shows the thermal conductivity in zero field for $R\text{CoO}_3$ with $R = \text{La, Pr, Nd, and Eu}$. [57, 221]. First, the compound with the smallest ion Eu will

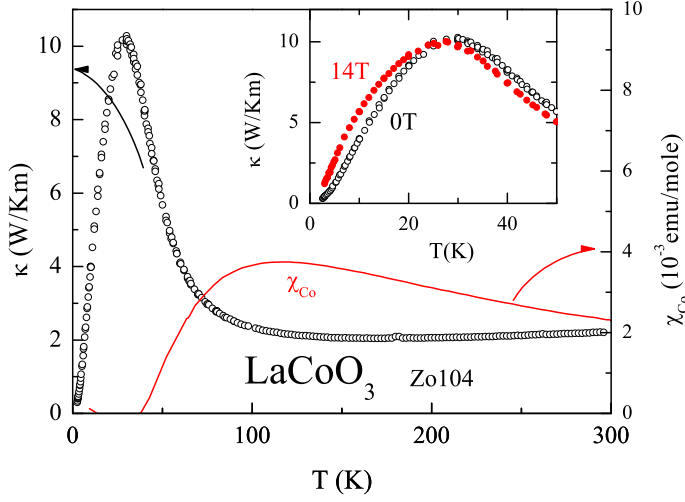


Figure 5.11.: Left scale: Thermal conductivity of LaCoO_3 . Right scale: Co^{3+} susceptibility of LaCoO_3 . Inset: Thermal conductivity of LaCoO_3 for $T < 50$ K in magnetic fields of 0 T and 14 T.

be discussed. In contrast to LaCoO_3 , the thermal conductivity shows comparatively large absolute values, and a general temperature dependence as expected for a purely phononic heat conductor. This is confirmed by a Debye fit according to Eq. 2.5. The fit parameters are listed in Tab. 5.5. The low-temperature maximum reaches a value of 250 W/Km at 18 K, which is about an order of magnitude larger than for LaCoO_3 . In NdCoO_3 , κ is lowered in the whole temperature range in comparison to EuCoO_3 , but still consistent with a conventional phononic picture. At the onset temperature of the spin-state transition (see Fig. 5.4) a slight change of the curvature to a steeper slope is visible. In contrast to NdCoO_3 , PrCoO_3 shows an unusual temperature dependence of κ , which reminds of κ of LaCoO_3 . The low-temperature peak decreases very strongly with increasing temperature. Between 50 K and 200 K, κ is more or less temperature independent with a low absolute value $\kappa \approx 3.5$ W/Km. Because the Co^{3+} spin gap is too large to account for this anomaly, another explanation is needed for this behavior. As will be discussed in detail in Sec. 5.4.10, multiplet transitions of the $4f$ orbitals can cause the additional scattering. Above 200 K, κ starts to decrease again, with a comparatively sudden slope change. According to the susceptibility measurements (Fig. 5.4) this is the temperature range where the higher spin state becomes excited. This is a further hint that the same scattering mechanism is present here, which suppresses κ in LaCoO_3 above 25 K.

Comparing all curves, it is clearly seen that the thermal conductivity is monotonously suppressed with increasing rare earth size in the whole temperature range (not taking into account the additional effect for $R=\text{Pr}$). This systematic trend at low temperatures cannot directly be attributed to the additional disorder scattering caused by the spin-state transition, because here the population of the excited spin states is negligible. If the suppression of κ due to the spin-state transition would be the only difference between LaCoO_3 and EuCoO_3 , one would expect that the thermal conductivity should not be affected below ≈ 25 K. This contradicts the experimental observation. In principle, this finding could arise from a different sample quality. However, there is no indication for a significantly better crystal quality in EuCoO_3 than in LaCoO_3 . Furthermore, the low-temperature behavior of LaCoO_3 is unusual. This is confirmed by the shown Debye fit, which is obtained by keeping all parameters fixed at the values obtained for EuCoO_3 , and adjusting the factor P for the point defect scattering to obtain the height of the low-temperature maximum. This gives a hint that usual point defect

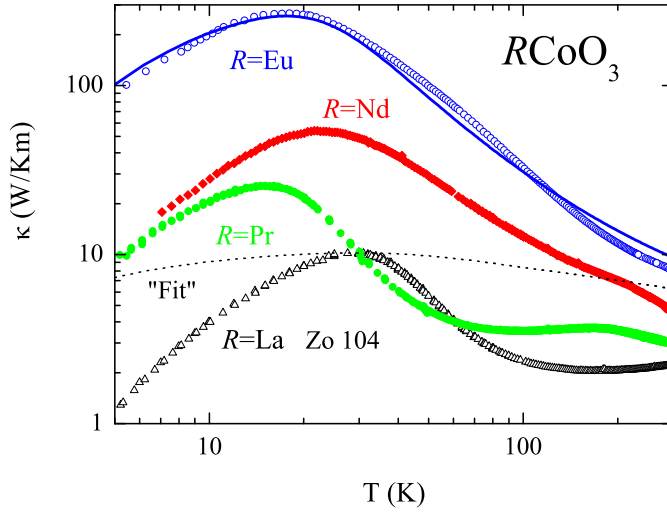


Figure 5.12.: Thermal conductivity of $R\text{CoO}_3$ with $R = \text{La}, \text{Pr}, \text{Nd},$ and Eu . For EuCoO_3 a Debye fit is shown (solid line). For LaCoO_3 a Debye fit is shown with the same parameters, but a larger point-defect scattering rate P .

scattering is not the only source of the strong suppression of the low-temperature thermal conductivity, since P is the only adjustable parameter which is effective in this temperature region.⁷

5.4.3. $R\text{CoO}_3$: Comparison to the Literature

To my knowledge, only Yan *et al.* have published low-temperature thermal conductivity data of undoped $R\text{CoO}_3$ compounds with $R = \text{La}, \text{Pr},$ and Nd [9]. These results are shown in Fig. 5.13. Above ≈ 50 K these data show the same qualitative and quantitative behavior like our samples. The broad minima for $R = \text{La}$ and Pr are present, showing that these are intrinsic features of the compounds. Differences occur in the heights of the low-temperature maxima, ranging from only 10% for $R = \text{Pr}$ up to a factor of 2 for $R = \text{Nd}$ and of 5 for LaCoO_3 . Such differences generally reflect different sample qualities. It follows that the height of the low-temperature peak does not follow such a systematic behavior like in our samples. However, above 100 K there is the same monotonous decrease of κ with the ionic size of the rare earth. Furthermore, all absolute values are well below the data from our EuCoO_3 crystal.

In Ref. [222, 223] the thermal conductivity of LaCoO_3 was investigated above room temperature. Here, the interpretation becomes even more difficult. The Debye approximation is no longer valid, and electronic scattering mechanisms and electronic contributions get relevant. Furthermore, additional effects like excitonic or radiative heat transport may play a role [223].

5.4.4. LaCoO_3 : Low Temperatures

In this section we present a detailed study of the zero-field thermal conductivity of LaCoO_3 for five crystals. Furthermore the influence of magnetic fields up to 14 T (in some cases 16 T) was investigated for all samples. The motivation was to study the unusual low-temperature- and field dependence of κ . In particular, the detailed analysis of the magnetic susceptibility allows to correlate the influence of the sample-dependent content of paramagnetic impurities to κ . For the samples Zo104 and MAR5b_07 the measurement range was extended down to ≈ 300 mK with the new setup for the Heliox ^3He insert (see Sec. 3.2.2).

⁷It is possible to get a much better fit by using a very small value of L for the sample size, $L \approx 1 \cdot 10^{-5}$ [57].

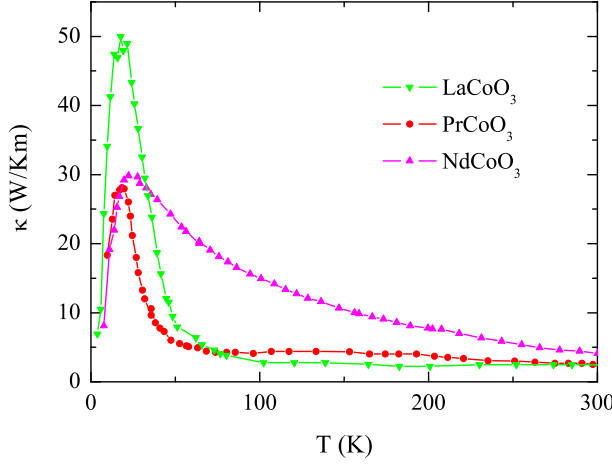


Figure 5.13.: Thermal conductivity data for LaCoO_3 , PrCoO_3 , and NdCoO_3 taken from Ref. [9].

In order to analyze the whole temperature range, these data are plotted together with the measurements performed in the conventional setup. In Fig. 5.14a the results for the sample Zo104 are shown.⁸ In zero field, the temperature dependence follows a T^2 dependence below ≈ 10 K. In a magnetic field of 14 T the thermal conductivity is strongly enhanced below ≈ 20 K up to almost a factor of 3 at ≈ 2.5 K. By further lowering the temperature, the field dependence becomes smaller and vanishes around 600 mK. In field, the slope of κ shows a T^3 behavior below 1 K. However, the temperature window is too small to unambiguously confirm a power-law behavior. In Fig. 5.14b the data for crystal Mar5b_07 are shown. The most striking feature is the occurrence of a pronounced dip in zero field around 2 K, which contrasts the T^2 dependence of specimen Zo104. For the fields of 6 T and 10 T, κ is strongly enhanced below ≈ 5 K, with almost no difference between these two curves. At 14 T, κ suddenly decreases again, and shows the same temperature dependence as specimen Zo104. The 14 T curve crosses the zero-field curve at 1 K, and with decreasing temperature κ decreases much stronger than κ in zero field.

Fig. 5.15 shows the thermal conductivity vs. magnetic field for the sample Mar5b_07. For a better comparison, all values are normalized to the zero field values. At 3 K, κ first increases, reaches a maximum at 9 T, and then decreases again. Above 13 T, κ is almost field independent up to 16 T. By lowering the temperature the maximum shifts to lower fields and strongly increases. At 1.85 K the thermal conductivity is enhanced by a factor of 8 at 8 T in comparison to the zero-field value.⁹ At 330 mK, the maximum is much smaller, and κ at higher fields is smaller than in zero field.

From the onset of a T^3 behavior for 14 T below 1.5 K one may suspect that the temperature region is reached, where only boundary scattering is effective. However, two observations contradict this interpretation: On the one hand, the boundary scattering gives an upper limit of κ , meaning that all other κ values should be below the 14 T curve, which is obviously not the case in sample Mar5b_07. Furthermore, the estimation of L from Eq. 2.3 yields a value of $L = 2.5 \cdot 10^{-5}$ m, which is much smaller than the real sample dimension. The non-monotonous complex field dependence in sample Mar5_07 clearly shows that defect scattering

However, the physical meaning of such a fit is questionable.

⁸For sample Zo104, the 0 T and 14 T curves could only be measured above ≈ 500 mK. The strong increase of the thermometer resistance of the used Cernox thermometers restricted the measurement range. For sample Mar5b_07, RuO thermometers were used. Here, all measurements extend to 300 mK (see Sec. 3.2.2).

⁹The ^3He measurements have been only measured up to 14 T.

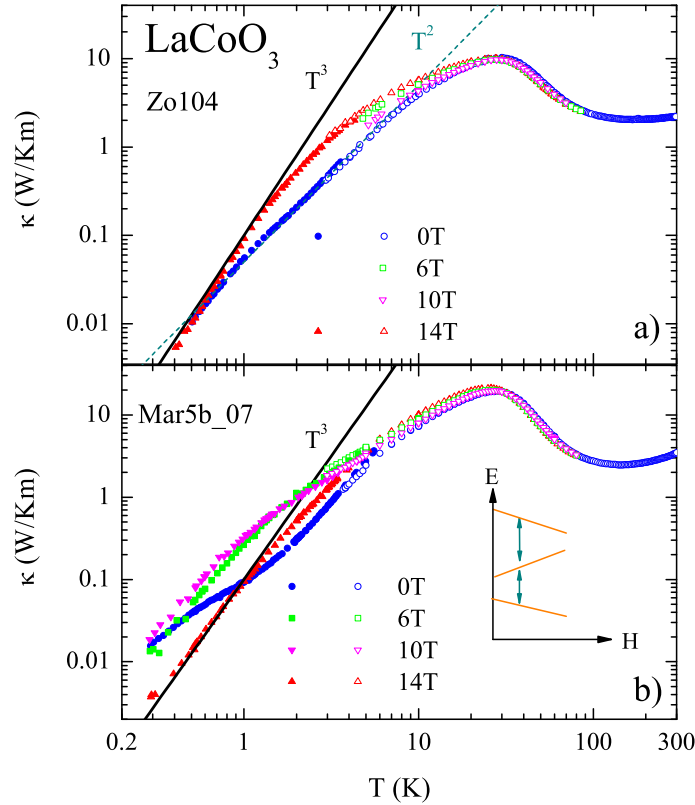


Figure 5.14.: a) κ of LaCoO_3 down to ≈ 400 mK in fields of 0 T and 14 T for sample Zo104. The ^3He measurements were performed up to ≈ 8 K and are shown together with the high-temperature data to cover the whole temperature range. The lines show power laws with different exponents. b) The same measurements for sample Mar5b_07.

is not sufficient to explain the data. The dip observed in $\kappa(0\text{ T})$ in sample Mar5b_07 is typical for a resonant scattering process [5, 27]. It is well known that paramagnetic impurities can cause such resonant scattering processes at low temperatures leading to complex temperature and field dependences of κ (see e.g. Sec. 2.1.6) [26, 29, 224].

The simplest case of one resonance can only explain a minimum in κ vs. H , but not a maximum (see Sec. 2.1.6). This leads to the conclusion that at least two resonances are responsible for the suppression of κ . This is supported by regarding the field-dependent thermal conductivity at 3 K in sample Mar5b_07. The sudden stop of the decrease of κ at ≈ 13 T suggests that here a second resonance occurs (since the first resonance is already seen in the zero-field curve). With this knowledge, the following scenario can be proposed: At zero field one resonance causes a dip in κ at 2 K. This resonance shifts to higher energies in magnetic fields, what explains the increase of κ for low fields and low temperatures. A second resonance belongs to a transition initially having an energy which is too high to lead to significant scattering. This gap becomes smaller at high fields leading to the maximum and sudden decrease of κ . A possible level scheme causing such a behavior is shown in Fig. 5.14b. Since, we do not know the level scheme for the impurities in LaCoO_3 , this scenario should not be taken too literally. In the next section the other samples will be considered, to see if a

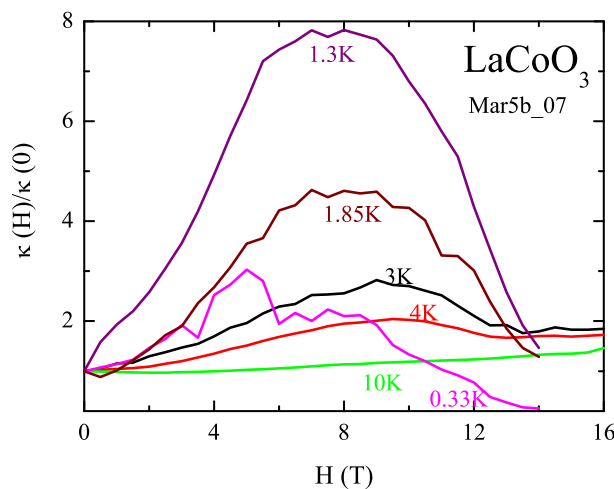


Figure 5.15.: κ vs. H for LaCoO_3 , sample Mar5b_07, down to 0.33 K. The data down to 3 K are measured with the conventional setup, whereas for the lower temperatures the ^3He insert was used.

consistent picture can be drawn.

5.4.5. LaCoO_3 : Field Dependence of κ

Fig. 5.16 shows the field-dependent measurements for four samples at fixed temperatures between 3 K and 50 K. Some general features can be seen:

- At the highest temperatures, $\kappa(H)$ weakly decreases with increasing magnetic field.
- At low temperatures and below 8 T, $\kappa(H)$ increases approximately linearly. The slope of $\kappa(H)$ increases with decreasing temperature, and is different for the different samples.
- For two of the samples the additional effect of a suppression of κ for $T < 3$ K and $H > 8$ T occurs, the specimens Mar5b_07 and Mar5_09. These are the only two specimens, which have a positive thermopower at room temperature (see Tab. 5.4; the thermopower measurements of LaCoO_3 will be presented in Chp. 6).

In the temperature-dependent measurements, see Fig. 5.17, the additional resonance leads to a more complex structure for the samples Mar5b_07 and Mar5_09. This provides a further hint that at least two resonances are responsible for the suppression of κ . One, which becomes weaker in magnetic fields, and a second one, which is only present in the samples Mar5b_07 and Mar5_09.

5.4.6. LaCoO_3 : Comparison Zero Field

In this section, all zero-field measurements of κ of LaCoO_3 will be compared. Fig. 5.18 shows κ vs. T for all samples in the temperature range of $3 \leq T \leq 300$ K.¹⁰ First, we will regard κ at higher temperatures. All samples show the broad minimum with $T_{\min} = 120 \dots 190$ K. This seems to be a large range, however, one has to keep in mind that the position of such a broad minimum is shifted easily by e.g. differences of the tail of the low-temperature maximum. The large differences at room temperature are surprising, in particular the low values for sample Zo104. Geometry errors and radiation losses may be responsible for the differences between

¹⁰The sample EKParis was only measured above 5 K.

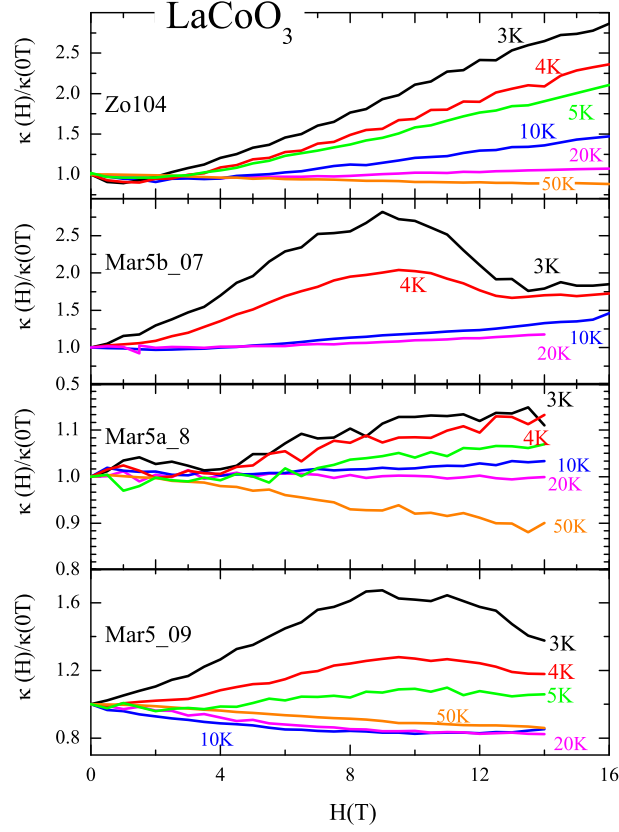


Figure 5.16.: Thermal conductivity of LaCoO_3 vs. magnetic field for various samples down to 3 K. The data are shown normalized to the zero-field value. Note the different scales of the y axes.

most of the samples (see Sec. 3.2.1), but the reason for the low values of sample Zo104 remains unclear.

At low temperatures a strong sample dependence of κ is observed. The height of the low-temperature peak varies from 8 to 34 W/Km, and the position shifts between 24 and 34 K, see Tab. 5.4. Interestingly, below ≈ 20 K all samples grown in cologne show nearly the same temperature dependence, whereas sample EKParis has a steeper slope, which could be related to either the used constituents, or details of the growing method. As discussed above, the suppression of κ at low temperatures is most likely largely determined by resonant scattering on paramagnetic impurity levels. Therefore the height of the low-temperature peak should correlate with the estimated paramagnetic impurity level P_{imp} . In a simple approach we neglect all other scattering mechanisms at T_{max} and get

$$\kappa_{\text{max}} \sim \frac{1}{\tau_{\text{res}}} \sim \frac{1}{P_{\text{imp}}}. \quad (5.10)$$

In the inset of Fig. 5.18, κ_{max} is plotted vs. P_{imp} . A fit by Eq. 5.10 describes the general trend quite well. The question may arise, why the field dependences do not correlate in the same way with P_{imp} . The explanation is that the conventional defect scattering is different for the different samples. To illustrate this, Fig. 5.19 shows a sketch of the frequency dependent

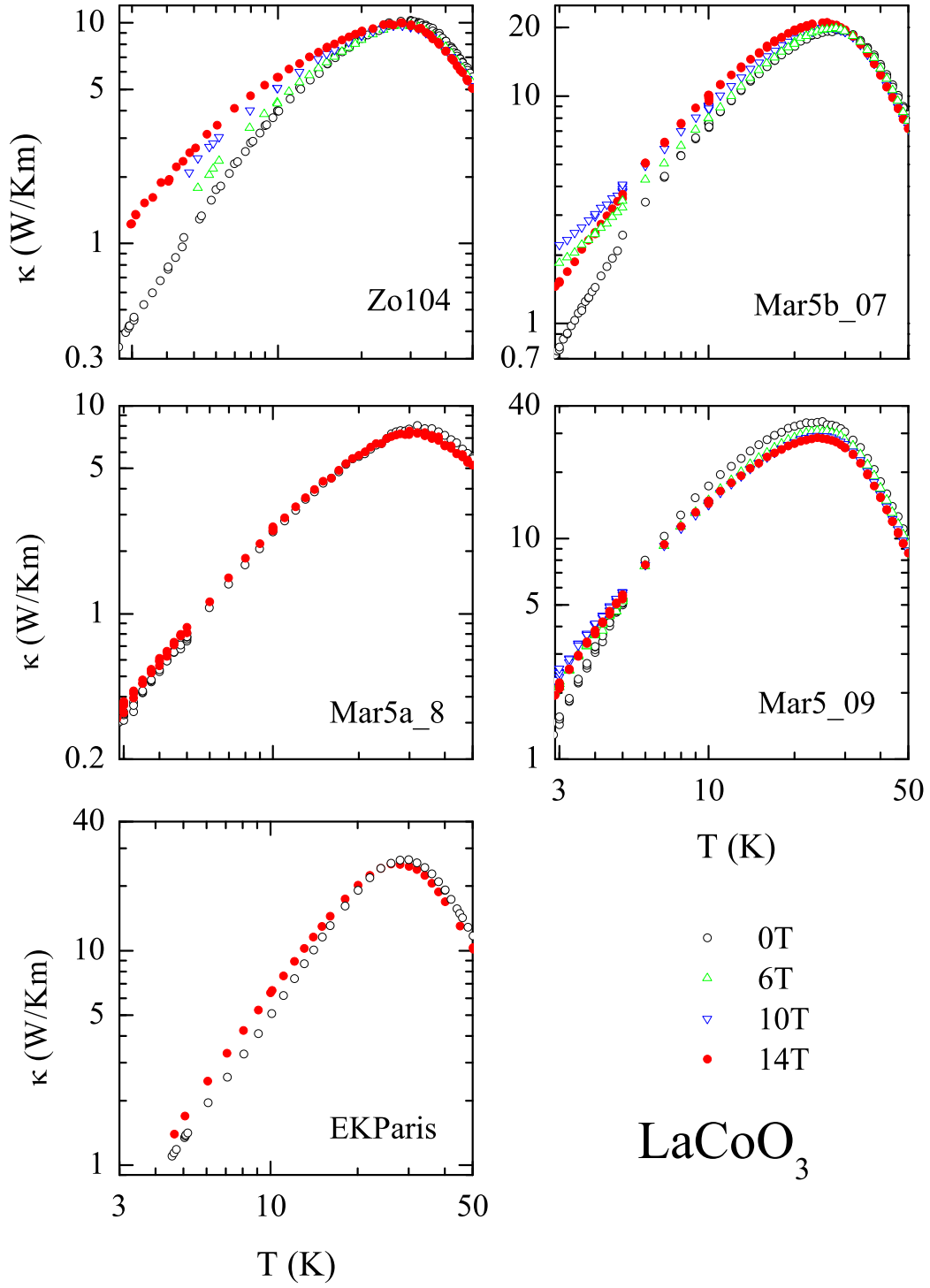


Figure 5.17.: κ vs. T for all LaCoO_3 samples in various magnetic fields. For the samples Mar5a_8 and EKParis, only 0 T and 14 T values are shown, because the field dependence is small and approximately linear with field.

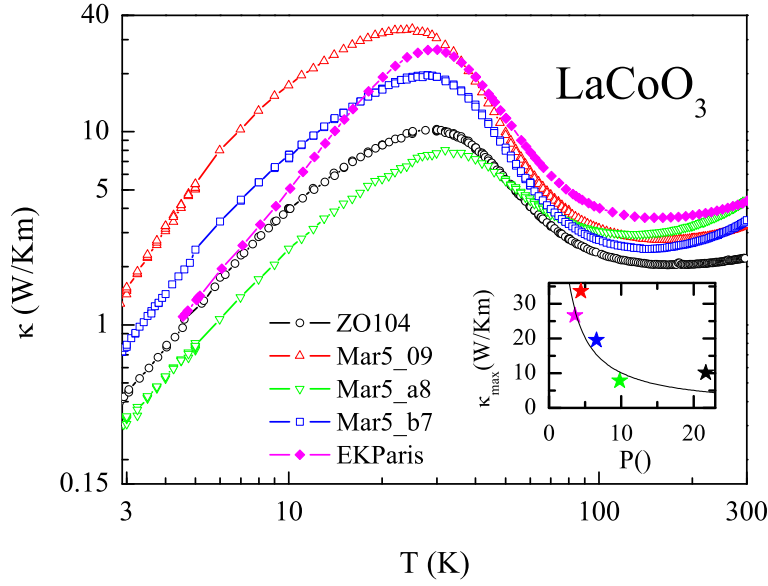


Figure 5.18.: κ of LaCoO_3 for all investigated samples. Inset: Maximum thermal conductivity κ_{max} vs. paramagnetic impurity content P_{imp} . The line is a fit according to Eq. 5.10

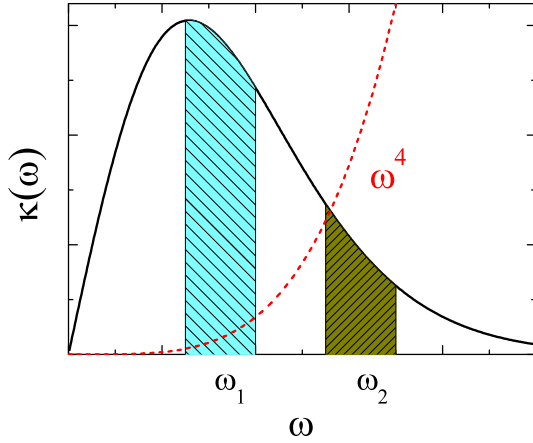


Figure 5.19.: Solid line: Sketch of the frequency dependent thermal conductivity at low temperatures. Dashed line: ω^4 dependence of point defect scattering. The shaded areas symbolize regions, where a resonance suppresses $\kappa(\omega)$.

thermal conductivity. Defect scattering mainly suppresses $\kappa(\omega)$ at high frequencies with a ω^4 dependence (dotted line). If we assume that a field-dependent resonance acts in the left shaded area, it will have a strong influence on κ . This suppression is not so much influenced by the defect scattering, since ω is too low. On the other hand, if a field-dependent resonance acts in the right shaded area, it is less effective, since this part of the frequency spectrum of κ is suppressed anyway by point defect scattering. The influence of the conventional defect scattering is supported by the fact that the two samples with the smallest field dependences, Mar5a_8 and EKParis, are those where κ_{max} lies below the fit according to Eq. 5.10.

5.4.7. LaCoO_3 : Influence of the Spin-State Transition on κ

Because the sample Mar5_09 has a low content of paramagnetic impurities, and the highest low-temperature peak of κ , the data of this sample will be used for the further analysis. This has the advantage that the effects caused by the spin-state transition can be better separated from the low-temperature scattering processes. We will perform the analysis for the LS/IS model with a fixed gap of 185 K and for the SOcHS scenario.

Before the data will be analyzed more quantitatively, the low absolute value of κ at high

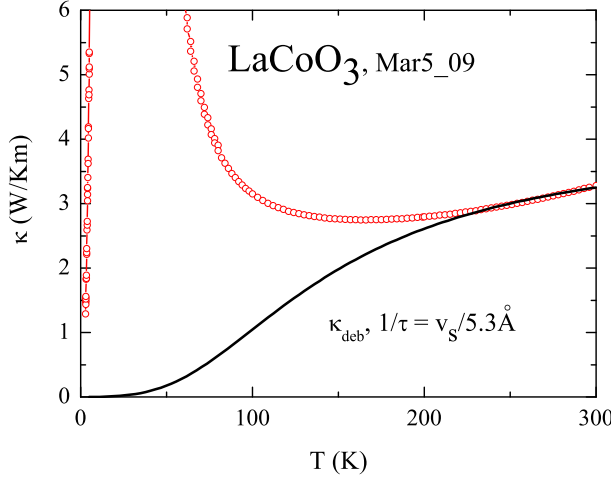


Figure 5.20.: Thermal conductivity of LaCoO_3 (Sample Mar5_09) and Debye thermal conductivity with $l = l_{\min} = 5.3 \text{ \AA}$.

temperature has to be addressed. As shown in Sec. 2.1.5, the Debye approximation (Eq. 2.5) is not a good approximation anymore, if the mean free path is of the order of the lattice constant. Applying the Ansatz from Cahill *et al.* [25] (Eq. 2.9), we calculate a value $\kappa_{\min} = 1.2 \text{ W/Km}$, summing over all three branches with the averaged sound velocity $v_s = 3900 \text{ m/s}$ from Ref. [225] and the volume density $n = 9.1 \cdot 10^{22} / \text{cm}^3$. The calculated κ_{\min} is about a factor 3 smaller than the observed $\kappa(300 \text{ K})$. This is close to the usual underestimation of this model of a factor of two [25], which shows that limiting effects have to be taken into account.

Because the data will be modeled by Eq. 2.5, an estimate has to be made when limiting effects will play a role in this model. Therefore we calculate $\kappa = \frac{1}{3}cvl_{\min}$ where l_{\min} is a constant. If the assumption is made that κ already reaches a minimum value, l_{\min} can be calculated by taking the room temperature value of κ , which yields a value of $l_{\min} = 5.3 \text{ \AA}$. The resulting temperature-dependent curve, calculated according to Eq. 2.5, is plotted together with κ for LaCoO_3 in Fig. 5.20. From the comparison of the temperature dependence, the conclusion can be drawn that limiting effects are significant above 200 K, and may extend to ever lower temperatures. Therefore the following analysis gets worse for temperatures above 150 K.

As discussed in Sec. 5.4.1, the additional disorder caused by the spin-state transition can in principle explain the suppression of the thermal conductivity, what will be discussed more quantitatively now.

For the analysis EuCoO_3 is taken as a reference compound, with the assumption that almost all additional scattering in LaCoO_3 for $T \gtrsim 50 \text{ K}$ is due to the spin-state transition. To illustrate the principle idea, Fig. 5.21 shows the thermal resistivity $w = 1/\kappa$ for LaCoO_3 and EuCoO_3 . Assuming that the additional thermal resistance at high temperatures is totally determined by the disorder scattering induced by the spin-state transition, one may write:

$$\tau_{\text{dis}} \propto w_{\text{dis}} \propto w_{\text{La}} - w_{\text{Eu}}. \quad (5.11)$$

This is of course a very crude estimation, since it totally neglects the ω dependence of κ . However, from the temperature dependence of w_{dis} it is seen that the scattering significantly changes above 35 K. The steep increase of w_{dis} below 35 K can be attributed to the various low-temperature scattering processes which have been discussed in Sec. 5.4.4. The assumption that these scattering processes vanish for higher temperatures is supported by the temperature dependence of $w(T)$ below 35 K.

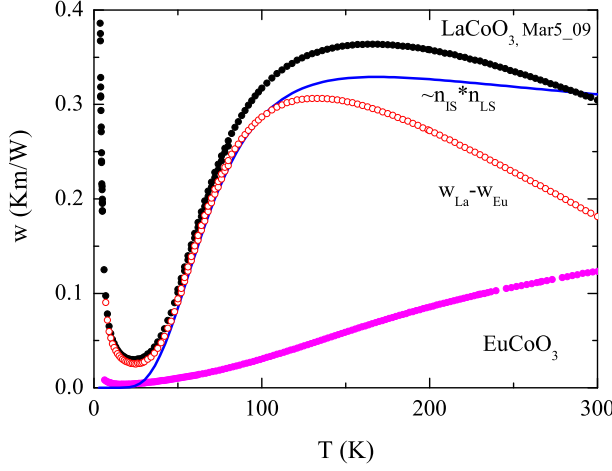


Figure 5.21.: Thermal resistances W for LaCoO_3 and EuCoO_3 and the difference $w_{\text{La}} - w_{\text{Eu}}$. The solid line is the product of the populations of the LS and IS state, scaled on $w_{\text{La}} - w_{\text{Eu}}$.

A successful approach to describe the thermal conductivity in disordered mixed alloys, is the so-called Nordheim-rule [226], which tells that the additional scattering is proportional to $x(x - 1)$, where x is the number fraction of one of the constituents. For the disorder caused by the population of the IS/HS states this reads:

$$\tau_{\text{dis}} \sim n_{\text{IS/HS}} \cdot n_{\text{LS}} \sim \frac{t \exp(-\Delta_{\text{Co}}/T)}{(1 + t \exp(-\Delta_{\text{Co}}/T))^2}, \quad (5.12)$$

where t is the total degeneracy of the excited level. Fig 5.22 shows the calculated curves for τ_{dis} in the LS-IS scenario, with $\Delta_{\text{Co}} = 185 \text{ K}$ taken from the susceptibility analysis [205]. The temperature dependence of w_{dis} is described well in a temperature range from $\approx 40 \dots 150 \text{ K}$. This finding gives a strong indication that the thermal conductivity is indeed suppressed by the spin-state transition.

A better data analysis should include the ω dependence of κ , what can be done in the following way: The scattering rate

$$\frac{1}{\tau_{\text{Eu}}} = \frac{1}{\tau_{\text{bd}}} + \frac{1}{\tau_{\text{pt}}} + \frac{1}{\tau_{\text{um}}} \quad (5.13)$$

is calculated by fitting the thermal conductivity of the reference compound EuCoO_3 (for the fit parameters see Tab. 5.5). Here, $\theta_D = 600 \text{ K}$ and $v_s = 3900 \text{ m/s}$ are the literature values for LaCoO_3 [188, 225]. With these values the fit already shown in Fig. 5.12 is obtained. Next, we assume that the thermal conductivity of LaCoO_3 is determined by the scattering rate

$$\frac{1}{\tau_{\text{La}}} = \frac{1}{\tau_{\text{bd}}} + \frac{1}{\tau_{\text{bd}}} + \frac{1}{\tau_{\text{um}}} + \frac{1}{\tau_{\text{dis}}} \quad (5.14)$$

with

$$\frac{1}{\tau_{\text{dis}}} = C(T) \cdot \omega^4, \quad (5.15)$$

where the conventional scattering rates are not changed.¹¹ Using the parameters obtained by the fit of EuCoO_3 we can calculate $C(T)$ by determining the $1/\tau_{\text{dis}}(T)$ which is necessary to

¹¹This assumes the ω^4 dependence of point defect scatterers. In principle, other ω dependences are possible.

A analysis performed with ω^2 and ω^0 is shown in the appendix (Fig. A.25)

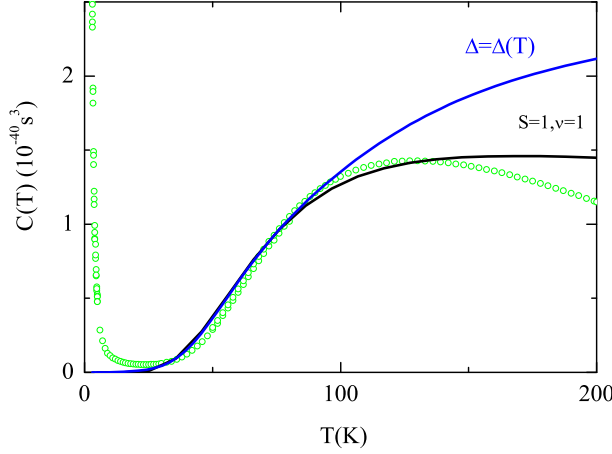


Figure 5.22.: Estimated scattering rates $C(T)$ for LaCoO_3 according to Eq. 5.16. The calculation with Eq. 5.12 are shown as solid lines.

describe the LaCoO_3 data. The resulting $C(T)$ starts to increase at about 40 K and shows a maximum at $T \approx 130$ K. Next, we calculate the temperature-dependent prefactor $C(T)$. We assume

$$C(T) = C_0 \cdot n_{\text{LS}} \cdot n_{\text{IS/HS}}, \quad (5.16)$$

where C_0 is a temperature independent prefactor describing the scattering strength. The resulting curves for $C(T)$ calculated for $\Delta_{Co} = 185$ K and $\nu = 1$ in the LS-IS scenario, and the SOcHS scenario are shown as lines in Fig. 5.22. The only adjustable parameter is the constant C_0 , which was fitted in a range from 30 K to 150 K. With the LS-IS model a good agreement of measured and calculated scattering rate is obtained up to 150 K. The deviation for $T \gtrsim 150$ K should not be taken into account, because here limiting effects start to play a role. The second fit is obtained by the SOcHS model, here the temperature-dependent energy gap was used in Eq. 5.12. The calculated curves for the LS/IS and the SOcHS scenario are nearly identical below 100 K. Above the calculated values of the SOcHS model give larger values than for the IS model.

We conclude that the calculated scattering rate which is necessary to model the thermal conductivity for LaCoO_3 , with EuCoO_3 as a reference compound, can be described assuming a ω^4 dependence of the scattering term. The temperature-dependent prefactor can be modeled by a two-level system for the spin-state transition for both, either the LS-IS or SOcHS model.

		Δ (K)	P (10^{-43} s^3)	$C_{m=4}$ (10^{-40} s^3)	l_{\min} (Å)
Fig. 5.12	EuCoO_3		3.7		0
	LaCoO_3		300		0
Fig. 5.23	LaCoO_3	185	23.6	5.3	0/2.3
	LaCoO_3	$\Delta(T)$	28.6	12	0/1.5

Table 5.5.: Fit parameters for the Debye fits of LaCoO_3 shown in Fig. 5.23. The other parameters are taken from EuCoO_3 and the same for all fits: $U = 4.9 \cdot 10^{-31} \text{ s}^2/\text{K}$, and $u = 7.6$.

As shown above, an additional scattering rate τ_{diss} according to Eq. 5.12 is strongly supported by comparing the temperature dependence to the estimated scattering rates using

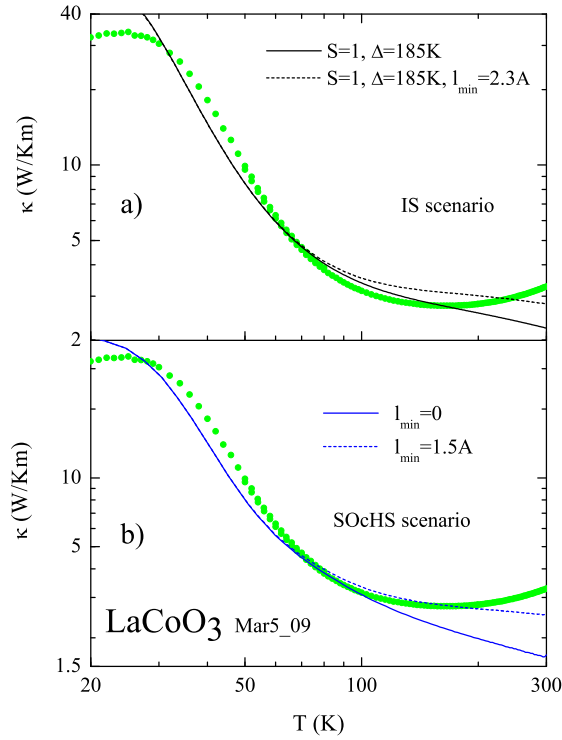


Figure 5.23.: Modelation of κ for LaCoO_3 in the extended Debye model. a) Fits obtained by the LS-IS model with fixed energy gap. b) Fits with the temperature-dependent energy gap from the SOcHS model.

EuCoO_3 as a reference. In the following, this knowledge will be used to describe the thermal conductivity of LaCoO_3 with an additional scattering rate τ_{diss} . Again, we restrict our analysis to temperatures above ≈ 35 K, and keep most of the parameters fixed by the Debye fit of EuCoO_3 . However, we will also fit the prefactor P of the point-defect scattering, since the number of point defects of course varies in different crystals, and the effect on the thermal conductivity is not negligible above 35 K. However, there are only two free parameters for the fits, P and C_0 . Again, the results will be presented for the LS-IS as well as for the SOcHS model. Fig. 5.23a shows κ of specimen Mar5_09 on double-logarithmic scales. The fit for the LS-IS is shown as a solid line, and gives a good description of the data from 30...200 K. The deviation at high temperatures can be explained by the very small mean free path, and the mentioned limiting of κ . A simple way is to limit the frequency-dependent scattering rate $1/\tau$ to a value v_s/l_{min} , as discussed in Sec. 2.1.5. This way is different to the estimation used above, since it also takes into account the frequency dependence of κ . l_{min} was adapted without changing the other parameters. The calculated κ including l_{min} is shown as dashed line in Fig. 5.23a. In Fig. 5.23b the results using the SOcHS scenario are shown. Both models describe the thermal conductivity well over a large temperature range. The difference of the resulting curves is very small, and none of the models is preferred by the thermal conductivity measurements.

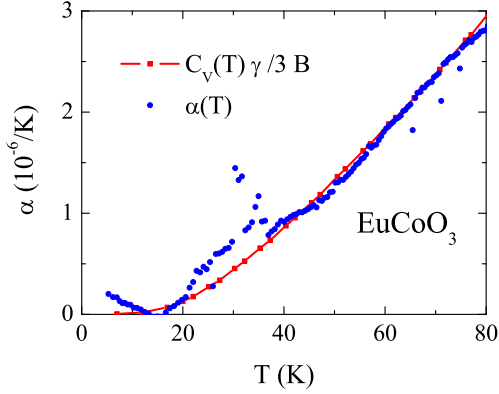


Figure 5.24.: Scaling of thermal expansion and specific heat of EuCoO_3 with Eq. 5.21. The used parameters are: $V_{\text{uc}} = 52.75 \text{ \AA}^3$, $\gamma = 2.3$ and $B = 230 \text{ GPa}$. [205, 228]

Scattering Strength

The anomalous temperature dependence of κ can be understood by the scattering caused by the spin-state transition. However, the question remains if the scattering strength can be analyzed in a quantitative way. Therefore we assume that the scattering is caused by the volume differences of the Co^{3+} ions in different spin states. Such an analysis was successfully done for mixed semiconductor alloys of the Form $A_x B_{1-x}$ in Ref. [227]. The scattering rate by point defects is given in Ref. [24]:

$$\frac{1}{\tau_P} = \frac{a^3 \Gamma}{4\pi v_s^3} \cdot \omega^4 \equiv C_0^{\text{calc}} \cdot \omega^4, \quad (5.17)$$

where a denotes the lattice constant and v_s the sound velocity. For Γ we write

$$\Gamma = x(x-1) \left[(\Delta M/M)^2 + 2 \left(\frac{\Delta B}{B} - 6.4\gamma \frac{\Delta R}{R} \right)^2 \right] \quad (5.18)$$

following the notation of Ref. [227]. Here, $\Delta M/M$, $\Delta B/B$, and $\Delta R/R$ denote the relative differences of the mass, the bulk modulus, and the radii of the different pure compounds A and B . In our case this corresponds to LaCoO_3 in the LS or in a hypothetical pure IS/HS state. The bulk modulus is defined as

$$B = -V \frac{\partial V}{\partial p}. \quad (5.19)$$

The constant γ is the Grüneisen parameter defined by

$$\gamma = -\frac{\partial(\ln \omega_D)}{\partial(\ln V)}, \quad (5.20)$$

which is a measure of the lattice anharmonicity. In the semiconductor mixed alloy of Ref. [227] values of $\gamma = 0.25 \dots 0.5$ are obtained. In LaCoO_3 the thermal expansion is mainly due to the spin-state transition. Therefore we use EuCoO_3 as a reference. The Grüneisen parameter can be obtained by scaling the thermal expansion and the specific heat using the data of Ref. [205] and

$$\alpha = \frac{\gamma c_V}{3B}. \quad (5.21)$$

We do not know the bulk modulus B of EuCoO_3 and therefore use the value of $B = 230 \text{ GPa}$ of NdCoO_3 from Ref. [228]. Fig. 5.24 shows the thermal expansion and the scaled specific

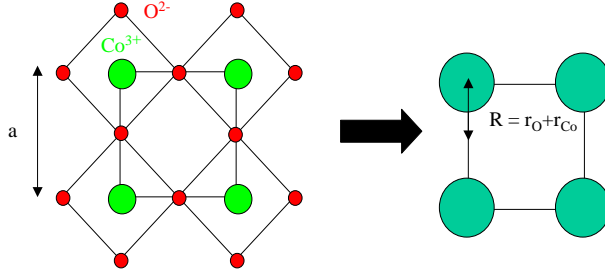


Figure 5.25.: Geometry used for the estimation of $\Delta R/R$ in LaCoO_3 .

heat. The curves can be scaled by the value $\gamma = 2.3$. $\Delta M/M$ plays no role in our case. The temperature dependence of the bulk modulus of LaCoO_3 ($B = 122 \text{ GPa}$ [228]) was investigated in Ref. [225]. Between 5 and 200 K a relative change of approximately 20% is observed. At 200 K the population of the HS/IS state is of the order of 50%, yielding a value $\Delta B/B \approx 0.4$. This term can be neglected, since the resulting values of the $\Delta R/R$ term will be much larger.

Next, we turn to the question, how $\Delta R/R$ is calculated. The principle idea is sketched in Fig. 5.25. We neglect the La ions, since they are irrelevant for the disorder scattering. The CoO_6 octahedra are treated as "balls". This leads to a simple cubic lattice with $a = 3.82 \text{ \AA}$. The "ionic" radius is given by the Co-O bond length in this treatment. The ionic radii of the Co^{3+} ions in the different spin states, taken from Ref. [54], are 0.545 \AA for the LS, and 0.61 \AA for the HS state¹². To obtain the relative length change of the bond length, we use the oxygen bond length of 1.35 \AA , yielding the values listed in Tab. 5.6. In Ref. [229] a value of 0.56 \AA for the IS radius has been derived. The ionic radii from Ref. [54] are derived from real bond length of Co^{3+} systems in the LS or HS system. In contrast, the value for the IS state is based on a model calculation for LaCoO_3 , since no system with an unambiguous IS of Co^{3+} state is known. This means that the value of 0.56 \AA cannot directly be compared to the HS/IS radii of Ref. [54]. Therefore we show for comparison also results obtained by the simple assumption $r_{\text{IS}} = (r_{\text{LS}} + r_{\text{HS}})/2 = 0.578 \text{ \AA}$. In Tab. 5.6 the resulting values of $\Delta R/R$ are listed.

Another way to treat the problem, is to regard the virtual change of the cubic lattice constant if all spins are excited in the higher spin state. This value is given by the parameter d resulting from the susceptibility / thermal expansion scaling analysis in Ref. [205]. In Tab. 5.6 the values of d for both scenarios are listed. The value for the IS scenario is taken from Ref. [205], the value for the SOcHS scenario was derived in Sec. 5.3.2.

From the prefactor C_0^{calc} for the scattering rate from the thermal conductivity fits we calculate γ . We obtain values between $13 \dots 43$, depending on the model and the term used for $\Delta R/R$. These values are larger than the estimated value for EuCoO_3 , but of the right order of magnitude. The exact value is very sensitive to the used parameters and the details of the model, since some of the parameters are quadratic or cubic in Eqs. 5.18 and 5.17. Therefore we will not discuss the differences of the different estimations. Yan. *et al.* [9] who measured the thermal conductivity of LaCoO_3 , PrCoO_3 , and NdCoO_3 and attributed the suppression of κ in LaCoO_3 to the spin-state transition. They suggested that the dynamical Jahn-Teller fluctuations strongly enhance the scattering strength. The proposed idea is that fluctuating octahedra distortions provide much more effective scatterers, than static ones. Such an explanation has been proposed by the same authors to explain the thermal conductivity in manganates. Our data show, that there is no need to involve the dynamics. The static scat-

¹²The ionic radii listed in Ref. [54] are calculated from Co-O bond lengths by subtracting the O bond length $r_0 = 1.45 \text{ \AA}$.

model	r_{IS} Å	$l_{\text{Co}^{\text{LS}}-\text{O}}$ Å	$l_{\text{Co}^{\text{HS/IS}}-\text{O}}$ Å	long	$\Delta l/l$ %	γ_l^{fit}	d %	γ_d^{fit}	C_0^{fit} 10^{-40}s^3
LS-IS	0.56	1.895	1.91		0.8	37	0.7	43	5.3
LS-IS	0.578	1.895	1.928		1.7	16			
SOcHS		1.895	1.96		3.4	13	1.8	25	12

Table 5.6.: Parameters for the estimation of the scattering strength caused by volume differences of the Co^{3+} ions.

tering caused by the volume changes of the Co^{3+} ions is sufficient to explain the suppression of κ . A possible way to resolve this issue, is to investigate a related system with only static disorder. A system which is promising for this purpose is LaAlO_3 , which has the same crystal structure. In Ref. [22] it was shown that LaAlO_3 has a conventional high-temperature dependence of κ , which large absolute values, comparatively to LaAlO_3 . The ionic radius of Al^{3+} is $r = 0.535\text{\AA}$. As dopands one could use Ga, with a ionic radius of $r = 0.62\text{\AA}$. This is very similar to the ionic radii of Co^{3+} in the different spin states. However, of course here the mass difference of the different dopands plays a role.

5.4.8. $R\text{CoO}_3$ with $R=\text{Pr}$, Nd , and Eu : Low Temperatures

In Fig. 5.26 field-dependent measurements of κ for EuCoO_3 , PrCoO_3 , and NdCoO_3 are presented. The principle behavior is the same for all three samples: the low-temperature maximum is monotonously suppressed with increasing magnetic field. The largest effect is observed in NdCoO_3 , here at $T_{\text{max}} = 24\text{ K}$ and 14 T κ is reduced by 37%. For PrCoO_3 the suppression is smaller, 25% at $T_{\text{max}} = 15\text{ K}$. For EuCoO_3 the reduction amounts only to 5%, which is close to the experimental uncertainty for the measurements in magnetic field. Several mechanisms could play a role for the field dependence of κ . First, resonant scattering by paramagnetic impurities may also apply here. In LaCoO_3 , κ always is enhanced for low temperatures and low fields, whereas κ is always suppressed in the other $R\text{CoO}_3$ compounds. In contrast to LaCoO_3 , here also the $4f$ orbitals of the rare-earth ions are present. This may lead to an additional field-dependent scattering in NdCoO_3 , where the ground-state doublet splits in the magnetic field.

In Sec. 5.3.3 we argued that the paramagnetic impurity content systematically decreases with the smaller rare-earth ions. The reason herefore is presumably that induced spin-state transitions (polarons) are less likely, if the spin gap increases. The intrinsic spin-state transition cannot be responsible for the systematic increase of κ with R at low temperatures, since no thermal population is present. From the correspondence of the increase of κ and C_{imp} with R the influence of paramagnetic impurities seems indeed to dominate the phonon scattering at low temperatures. This is a further hint that the defect-induced magnetic polarons are a general feature of these compounds.

5.4.9. PrCoO_3 and NdCoO_3 : Influence of the Spin-State Transition on κ

To analyze κ of PrCoO_3 and NdCoO_3 , the same procedure as for LaCoO_3 was used to obtain the temperature-dependent prefactor $C(T)$ for the additional scattering (see Sec. 5.4.7). In Fig. 5.27a, $C(T)$ for NdCoO_3 is shown. The absolute values are of course smaller than for

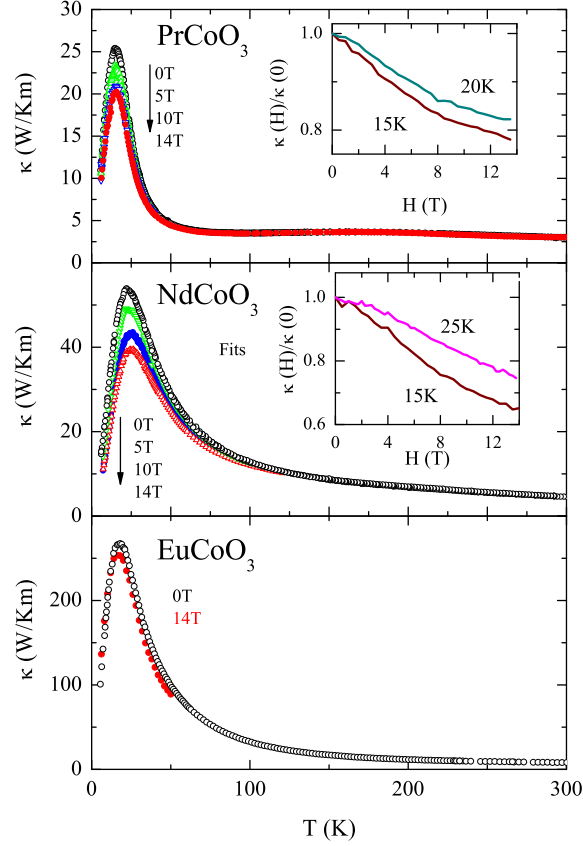


Figure 5.26.: Thermal conductivity of $R\text{CoO}_3$ as a function of temperature in different magnetic fields. The insets show field-dependent measurements at fixed temperatures.

LaCoO_3 , because κ is larger. $C(T)$ increases for $T > 20$ K, reaches a plateau around 150 K, but then increases again above 230 K. The reason for the second increase is likely to be the onset of the spin-state transition. To show this, we use again Eq. 5.12 to calculate the contribution of the scattering which is produced by the spin-state transition, using the LS-IS model. Here, we only change the energy gap Δ , and leave the prefactor C_0 the same as in LaCoO_3 . It turns out that the value of the energy gap is crucial. For the calculation, the value $\Delta_{\text{Co}} = 1750$ K from thermal expansion is taken. If the resulting scattering rate is subtracted from the measured scattering rate, the additional increase disappears completely. This clearly indicates that the increase of $C(T)$ above 200 K is indeed caused by the spin-state transition. Using the prefactor of $C(T)$ obtained from the SOcHS model¹³ for LaCoO_3 , the result is basically the same, if the energy gap is slightly shifted to 1900 K.

Regarding PrCoO_3 , a peak at 80 K is observed, which is caused by an additional effect, as will be discussed in Sec. 5.4.10. For further increasing T , again a saturation of $C(T)$ is observed. Here, the values of the spin gap determined from susceptibility and thermal expansion only differ by about 100 K. By subtracting the calculated $C(T)$ with the energy gap determined from χ , a smooth curve is obtained, which is approximately linear with T . Of

¹³Note, that here no temperature-dependent gap has to be used, since the amount of excited spins states is still small, and the interactions leading to the temperature-dependent gap may be neglected.

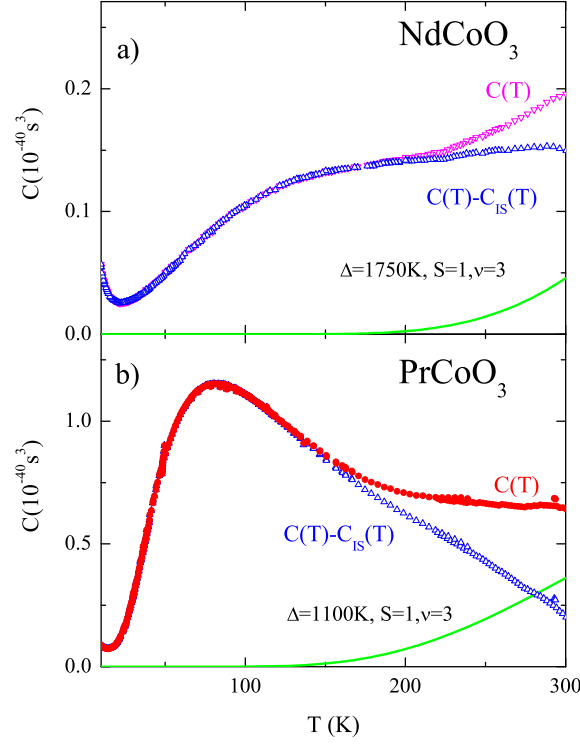


Figure 5.27.: a) Calculated scattering rates for NdCoO_3 (closed symbols), together with the scattering rate estimated by Eq. 5.12 (line), and the difference of both (open symbols). b) The same for PrCoO_3 .

course, the residual scattering rate is not known, but again the change of the curvature is at the temperature where the spin-state transition develops. Using C_0 from the SOcHS model, the different prefactor of $C(T)$ would give the same results with an energy gap of 1400 K, which is still reasonable. The fact that for all compounds only the energy gap is changed, and the prefactor for the scattering strength is the same, is clear evidence that the spin-state transition suppresses κ of PrCoO_3 and NdCoO_3 in the same way as in LaCoO_3 .

5.4.10. Resonant Scattering in PrCoO_3

In PrCoO_3 an additional scattering mechanism must be present below 200 K, since in the relevant temperature range the Co^{3+} IS/HS spin states are not significantly populated. The origin for an additional scattering channel is most probably scattering by the $4f$ orbitals. The effect of $4f$ orbitals to the thermal conductivity is known e.g. from rare earth garnets [230], where an additional suppression of κ was observed. The idea is again based on resonant scattering processes: A phonon is absorbed by causing a transition between different multiplet levels of an $4f$ multiplet, and then re-emitted in an arbitrary direction (see Sec. 2.1.6), causing additional thermal resistance. A mechanism based on random ionic volume changes as proposed for LaCoO_3 seems not likely because the $4f$ orbitals are inner shells. As discussed in Sec. 2.4, the $^3\text{H}_4$ multiplet of the Pr^{3+} ions splits into 9 singlets in the orthorhombic CF. To my knowledge there are no experimental investigations of the $4f$ CF splitting for PrCoO_3 and NdCoO_3 .

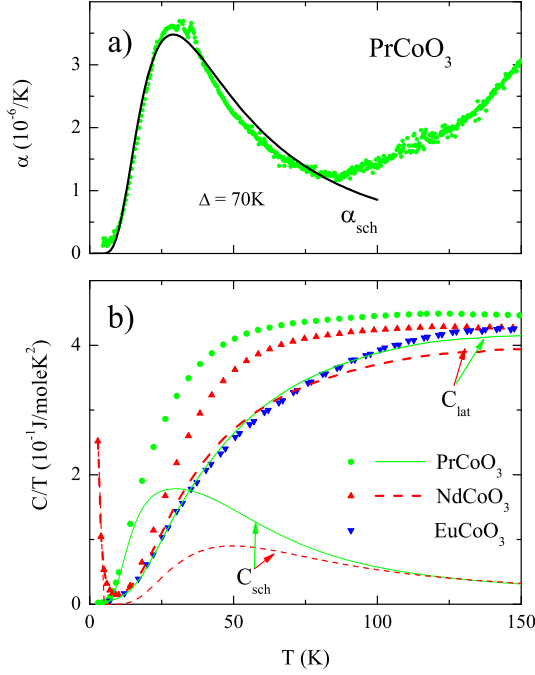


Figure 5.28.: a) Low-temperature thermal expansion of PrCoO_3 , with estimated Schottky contribution. b) Specific heat of PrCoO_3 , NdCoO_3 , and EuCoO_3 , shown as C/T . Lines are estimated Schottky- and lattice contributions, see text.

From the analysis of the susceptibility measurements (see Sec. 5.3.1) we know that the CF parameters of NdGaO_3 and PrNiO_3 are good approximations for NdCoO_3 and PrCoO_3 . The energy splitting to the first excited $4f$ level in PrCoO_3 can be obtained by the analysis of the low-temperature thermal expansion. Fig. 5.28a shows the zero-field thermal expansion α [205]. α shows a maximum at 30 K, which can be attributed to a Schottky contribution. The calculated¹⁴ Schottky contribution of a two-level system with non-degenerate levels yields an energy gap $\Delta = 70$ K which is slightly lower than the value observed in PrNiO_3 [44].

Further evidence for the correctness of this approach comes from the specific heat. Fig. 5.28b shows C/T for PrCoO_3 , NdCoO_3 , and EuCoO_3 , from Ref. [205]. In EuCoO_3 , C/T has the lowest values, which are purely phononic at low temperatures. Above ≈ 100 K a contribution of the first excited multiplet appears. The additional specific heat for $R = \text{Pr}$ and Nd is due to the Schottky contribution of the $4f$ orbitals. The low-temperature increase of C/T in NdCoO_3 below ≈ 10 K is due to fluctuations, which are precursors of a Néel ordering of the Nd moments at $T = 1.2$ K [219]. The Schottky contribution to C/T was calculated with the CF parameters of PrNiO_3 and NdGaO_3 (see Sec. 5.3.1). Since we know the energy of the first excited level of PrCoO_3 from the thermal expansion, we corrected this energy.

Fig. 5.29a shows the thermal conductivity of PrCoO_3 together with the thermal expansion. To model the data, Eq. 2.11 is used to calculate the scattering rate for a direct resonant process. For the fits the Debye temperature, sound velocity and sample length are kept fixed, whereas P , U , and u are adjusted to fit the data. The fits have been restricted to $T \geq 20$ K, since at low temperatures other processes may be relevant, as discussed in the previous sections. The fit parameters are listed in the caption of Fig. 5.29. For the partition sum, the energy levels up to E_4 have been taken into account. In a first attempt, resonant scattering between the ground state level $E_0 = 0$ and $E_1 = 70$ K is considered, yielding the fit labeled F01.

¹⁴For details of the calculation of the splitting of a Schottky contribution to the thermal expansion see Sec. 7.4.2.

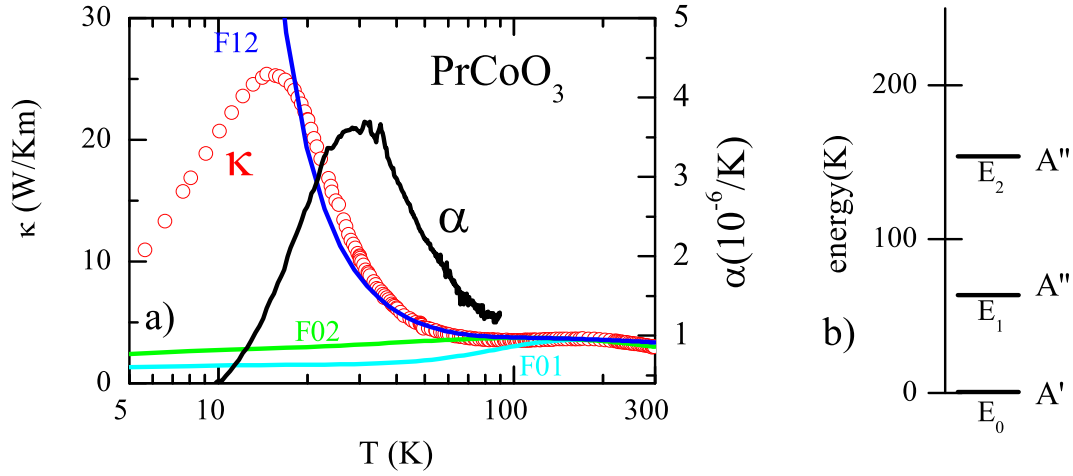


Figure 5.29.: a) Thermal conductivity and thermal expansion of PrCoO_3 . Lines are calculated thermal conductivities assuming different resonant scattering processes. The Debye fit parameters used are: $\Theta_D = 600$ K, $v_s = 3900$ m/s, $P = 5 \cdot 10^{-43} \text{ s}^3$, $U = 4.85 \cdot 10^{-18} \text{ s}^2/\text{K}$. The energy levels used were $E_1 = 70$ K, $E_2 = 151$ K, $E_3 = 174$ K. The prefactors of the resonant scattering rates are $R_{C01} = 3.1 \cdot 10^{-40} \text{ s}^3$, $R_{C02} = 7 \cdot 10^{-40} \text{ s}^3$ and $R_{C12} = 3.8 \cdot 10^{-40} \text{ s}^3$. b) Symmetry of the energy levels [44]

This fit does not describe the data at all, the scattering strength C needed to describe the high-temperature behavior totally suppresses the low-temperatures maximum. Basically the same result is achieved by considering the process $E_0 \rightarrow E_2$ (F02).

A good description of the data is obtained by considering the process $E_1 \rightarrow E_2$ solely (F12). This seems surprising, but is consistent with the observation that the maximum of the Schottky contribution of α is at a much lower temperature than the minimum of κ . The transition $E_1 \rightarrow E_2$ seems to be the dominant scattering channel of the phonons in PrCoO_3 . To understand this, we have to consider the symmetry of the relevant levels. These are taken from Ref. [44] and are shown in Fig. 5.29b. Because of the low-symmetry point group C_s the states have only two different symmetries, A' and A'' [231]. The levels E_2 and E_3 have both the symmetry A'' , but the ground state the symmetry A' . This explains, why only the scattering process between E_2 and E_3 is relevant.

5.5. Conclusions

The thermal conductivity of $R\text{CoO}_3$, with $R = \text{La}, \text{Pr}, \text{Nd}, \text{and Eu}$ was measured. LaCoO_3 shows an unconventional thermal conductivity in the whole temperature range, which is caused by the spin-state transition of Co^{3+} . At low temperatures, a maximum with an unusual temperature and magnetic-field dependence is observed. The low-temperature behavior of the thermal conductivity was systematically investigated on five different samples. We showed that non-intrinsic strong scattering processes caused by paramagnetic impurity levels governs the heat transport in this temperature range. The measured thermal conductivity could be correlated to the paramagnetic impurity content of the samples obtained via magnetization measurements. The effectiveness of these processes may be enhanced due to the formation of

magnetic polarons. Concerning the whole $R\text{CoO}_3$ series, we observed a systematic increase of the thermal conductivity from $R = \text{La}$ to Eu . At low temperatures, this observation cannot directly be attributed to the spin-state transition. The analysis of the thermal conductivity in combination with susceptibility measurements suggests a scenario, where magnetic polarons significantly scatter phonons at low temperatures. Because the polaron formation becomes less likely when the spin gap is increased, the systematic increase of the thermal conductivity from La to Eu results.

Above $T \approx 30 \text{ K}$, a strong suppression of the thermal conductivity is observed in all samples. The resulting very low absolute value of the thermal conductivity up to room temperature is an intrinsic feature of the thermal conductivity of LaCoO_3 . We showed that this unusual behavior of the heat transport is a consequence of the spin-state transition. The Co^{3+} ion has a larger ionic radius in the thermally activated IS/HS state than in the LS ground state. The random distribution of the LS and IS/HS states causes an additional lattice disorder which strongly suppresses the thermal conductivity. To check this scenario also quantitatively, we estimated the additional scattering-rate due to the spin-state transition. Herefore we used EuCoO_3 as a reference compound, where the influence of the spin-state transition is negligible below room temperature. We were able to describe the temperature dependence of the additional phonon scattering by a model based on the Nordheim rule. Such a model was successfully used in the literature to describe the thermal conductivity of mixed semiconductor alloys. Our model works with the LS-IS scenario with a spin gap of 185 K estimated by susceptibility measurements [12] as well as with the recently proposed model based on a spin-orbit coupled high-spin state [13]. In PrCoO_3 and NdCoO_3 , the spin-state transition shifts gradually to higher temperatures. In PrCoO_3 , an additional scattering mechanism could be identified, which is attributed to resonant scattering by the $4f$ orbitals of Pr^{3+} .

Despite the additional effect in PrCoO_3 , we could show that the spin-state transition influences the thermal conductivity at high temperatures in PrCoO_3 and NdCoO_3 in the same way as in LaCoO_3 . The change of the scattering rates due to the spin-state transition could be modeled using the parameters estimated from LaCoO_3 . This is clear evidence that the spin-state transition indeed causes the suppression of the thermal conductivity due to the additional disorder. We explored the scattering mechanism in detail and quantitatively investigated the scattering strength for LaCoO_3 . Our results show, that the static volume changes of the Co^{3+} ions caused by the spin-state transition are sufficient to explain the observed behavior of the thermal conductivity. This is in contrast to the scenerio proposed in Ref. [9], which proposes that dynamical fluctuations are responsible for the strong suppression of the thermal conductivity.

6. Thermal Conductivity, Thermopower, and Figure of Merit of $\text{La}_{1-x}\text{Sr}_x\text{CoO}_3$ and $\text{La}_{0.75-x}\text{Eu}_{0.25}\text{Sr}_x\text{CoO}_3$

In this chapter measurements of the thermal conductivity and the thermopower of $\text{La}_{1-x}\text{Sr}_x\text{CoO}_3$ with $0 \leq x \leq 0.3$ and $\text{La}_{0.75-x}\text{Eu}_{0.25}\text{Sr}_x\text{CoO}_3$ with $0 \leq x \leq 0.4$ will be presented. From these results and the electrical resistivity the thermoelectric figure of merit will be calculated, which is of interest for the applicability for thermoelectric devices. The zero-field measurements for $\text{La}_{1-x}\text{Sr}_x\text{CoO}_3$ are partly from C. Zobel [33], the measurements of the thermal conductivity and the thermopower of $\text{La}_{0.75-x}\text{Eu}_{0.25}\text{Sr}_x\text{CoO}_3$ were performed by H. Anapa [177]. The resistivity measurements were carried out by C. Zobel and C. Hanebeck [33, 232]. The experimental methods used in this section are described in the Secs. 3.2, 3.3, and 3.4. The main results of this chapter have been published in Ref. [166].

6.1. Introduction

In Sec. 5.1 the thermally driven spin-state transition in LaCoO_3 was discussed [12, 176, 185, 189, 190, 205, 233, 234]. During the last years cobaltates with layered CoO structures have also become subject of intense studies. [203, 235–242] It has been proposed that various of these compounds would also show temperature-dependent spin-state transitions of the Co^{3+} and/or Co^{2+} ions, but an unambiguous proof of such spin-state transitions is still missing (see e. g. Ref. [203]).

Recently, the observation of superconductivity in $\text{Na}_x\text{CoO}_2 \cdot y\text{H}_2\text{O}$ has attracted much attention. [243] The water-free parent compound Na_xCoO_2 became prominent some years ago already in a different context. [244] It was found that Na_xCoO_2 with $x = 0.6$ has a metallic electrical conductivity σ , but a low thermal conductivity κ and, in addition, a large thermopower S . The combination of large σ , small κ , and large S values is a precondition for effective thermoelectric cooling. The performance of thermoelectric devices depends on the so-called thermoelectric figure of merit $Z = S^2/\kappa\rho$ where $\rho = 1/\sigma$ denotes the electrical resistivity. For an effective cooling, ZT values (T is the absolute temperature) of order unity should be reached and are found for instance in Bi-based alloys, some thin-film devices or quantum dot superlattices. [245, 246] For comparison, typical metals have much smaller ZT values of order 10^{-4} . In this respect it was quite surprising that Na_xCoO_2 has $ZT \simeq 0.03$ for $150\text{ K} \leq T \leq 300\text{ K}$. The enhanced figure of merit of Na_xCoO_2 mainly arises from an enhanced thermopower. [247] Based on a study of the magnetic-field dependence $S(H)$ of Na_xCoO_2 it has been argued that the spin entropy is the likely source for the large thermopower. [248]

A large thermopower occurs also in $\text{La}_{1-x}\text{Sr}_x\text{CoO}_3$. [249] This motivated the study of the transport properties of this series in order to determine experimentally the ZT values and their dependence on temperature and doping. Another motivation for this study was that the previous results do not give a consistent picture of the transport properties. For example,

x	δ	x	δ
0	0.005	0.125	-0.006
0.002	0.003	0.15	-0.017
0.01	0.002	0.18	0.000
0.04	-0.001	0.25	-0.025
0.08	0.000	0.3	-0.004

Table 6.1.: Oxygen content δ of the $\text{La}_{1-x}\text{Sr}_x\text{CoO}_{3+\delta}$ crystals determined by thermogravimetric analysis. [166, 253]

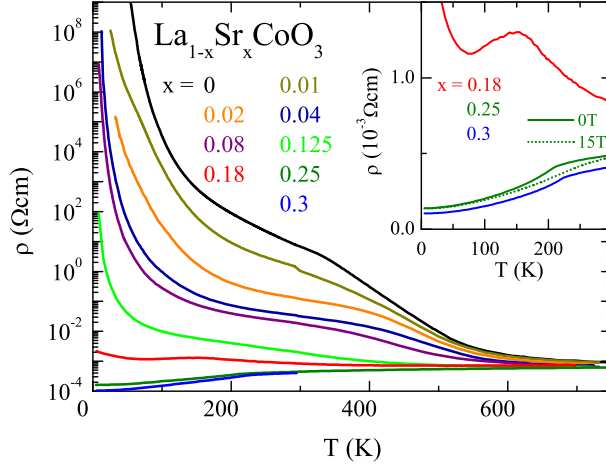
from various anomalous features in the temperature dependences of S , ρ , and the magnetic susceptibility χ a complex phase diagram was proposed for the $\text{La}_{1-x}\text{Sr}_x\text{CoO}_3$ system. [249] It has, however, been argued that the occurrence of some of these anomalous features depends on the preparation technique of the polycrystals. [250] In fact, the phase diagram derived from $\rho(T)$ and $\chi(T)$ measured on $\text{La}_{1-x}\text{Sr}_x\text{CoO}_3$ single crystals [205, 213, 251] is much less complex than the previous one [249]. Moreover, the temperature dependences of S for undoped LaCoO_3 reported in Refs. [176] and [252] are contradictory. For $T > 400$ K both reports find a positive thermopower of order $+50 \mu\text{V/K}$, which slightly increases with decreasing temperature. For $T < 400$ K, however, a further increase of S with a maximum of about $+1200 \mu\text{V/K}$ around 100 K is found in Ref. [176], whereas a sign change of S and a decrease to about $-400 \mu\text{V/K}$ for $T \simeq 200$ K is reported in Ref. [252]. The thermal conductivity of the $\text{La}_{1-x}\text{Sr}_x\text{CoO}_3$ system has to my knowledge not yet been studied at all.

6.2. Samples

The single crystals of $\text{La}_{1-x}\text{Sr}_x\text{CoO}_3$ with $x > 0$ used in this study have been grown by a floating-zone technique in an image furnace by C. Zobel [33]. For further details of the sample characterization by X-ray diffraction, magnetization, and resistivity measurements see also Refs. [12, 178, 205, 205, 213, 213, 254] For discussion of the thermal conductivity of undoped LaCoO_3 see Chp. 5. The thermopower for LaCoO_3 was measured on the same five specimens used for the thermal conductivity measurements. As a reference for the thermal conductivity of the undoped LaCoO_3 the specimen ZO104 is used¹. The $\text{La}_{0.75-x}\text{Eu}_{0.25}\text{Sr}_x\text{CoO}_3$ samples, with $x = 0, 0.1, 0.2, 0.3$, and 0.4 , are polycrystals prepared by a standard solid-state reaction by A. Reichl, see Ref. [179]. For further details of the characterization of these samples see also Ref. [232].

The nominal valence of the Co ions does not only depend on the Sr content, but also on the oxygen concentration, i. e. the amount n of charge carriers in $\text{La}_{1-x}\text{Sr}_x\text{CoO}_{3+\delta}$ is given by $n = x + 2\delta$. Positive (negative) values of n mean hole (electron) doping and formally an amount n of the Co^{3+} ions is transformed into Co^{4+} (Co^{2+}). In the case of hole doping this formal description must not be taken literally, because due to the high oxidation state of Co^{4+} the holes are likely to enter the oxygen $2p$ states. Note that depending on the spin states of the various Co ions hole and electron doping may be strongly different with respect to charge transport due to the so-called spin-blockade effect [255, 256]. Because of the high oxidation state of Co^{4+} , one may suspect that with increasing Sr concentration the amount of oxygen vacancies also increases, i. e. an increasing x could be partially compensated by a decreasing δ . In order to check this the oxygen content of the entire series $\text{La}_{1-x}\text{Sr}_x\text{CoO}_{3+\delta}$

¹This crystal was grown at the same time like the rest of the $\text{La}_{1-x}\text{Sr}_x\text{CoO}_3$ series.

**Figure 6.1.:**

Resistivity of $\text{La}_{1-x}\text{Sr}_x\text{CoO}_3$ for $0 \leq x \leq 0.3$. For consecutive doping an insulator-metal transition occurs for $x \approx 0.18$ [213, 260]. Inset: Resistivity of $\text{La}_{1-x}\text{Sr}_x\text{CoO}_3$ for $x \geq 0.18$ below 300 K. Here, the ferromagnetic order is seen at 157, 209, and 227 K for $x = 0.18$, 0.25, and 0.3, respectively [205, 213]. For $x = 0.25$ the resistivity is also shown in a magnetic field of 15 T (Dotted line) [261].

was determined by thermogravimetric analysis (TGA/SDTA851, Mettler-Toledo). Pieces of about 50 mg of the single crystals have been ground and heated up to 900°C in a reducing atmosphere (N_2 with 5% H_2) in order to decompose $\text{La}_{1-x}\text{Sr}_x\text{CoO}_{3+\delta}$ into La_2O_3 , SrO and elementary Co . [257–259] The value of δ is then calculated from the measured weight loss. The reproducibility of this method was tested by repeatedly measuring amounts of about 50 mg from the same badge of a LaCoO_3 polycrystal. The different results agree to each other within ± 0.01 , which is comparable to the uncertainty of the same and alternative methods of oxygen-content determination in cobaltates. [257–259] A scatter of ± 0.01 is also present in the determined oxygen contents of the $\text{La}_{1-x}\text{Sr}_x\text{CoO}_{3+\delta}$ crystals (see Table 6.1). A linear fit of $\delta(x)$ yields a weak decrease $d\delta/dx = -0.05$. The analysis reveals a 10% reduction of the charge-carrier content with respect to the Sr content. We do not calculate $n = x + 2\delta$ for each crystal individually, because the scatter of δ would correspond to a scatter of the charge carrier content of ± 0.02 , which can be excluded for the studied crystals from the measurements of the magnetization and resistivity (see Ref. [205, 213]). Both quantities vary monotonously as a function of x for $0 \leq x \leq 0.3$. Thus the scatter of n between samples with neighboring x is much smaller than their difference Δx , which amounts e.g. to only 0.01 for the lowest concentrations. This conclusion is also confirmed by the data presented in this chapter. The only exception is the thermopower of nominally undoped LaCoO_3 , which will be discussed in more detail below.

6.3. Experimental Results

6.4. $\text{La}_{1-x}\text{Sr}_x\text{CoO}_3$

6.4.1. Resistivity

The temperature and doping dependent resistivity of LaCoO_3 is shown in Fig. 6.1 [260]. Undoped LaCoO_3 is an insulator². With increasing Sr doping, the resistivity drastically de-

²The additional transition above room-temperature is discussed in Refs. [33, 213], and not the scope of this investigation.

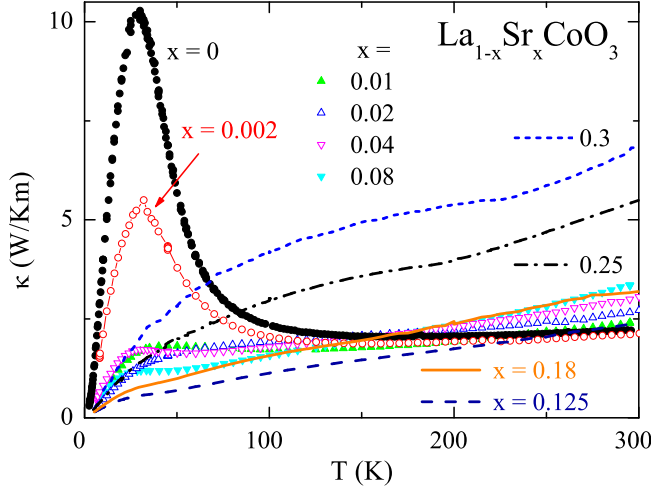


Figure 6.2.: Thermal conductivity of LaCoO_3 as a function of temperature for different doping x . [33, 166, 262]

creases, and an insulator-metal (IM) transition occurs at $x \approx 0.18$. For the metallic samples ferromagnetic order is observed, [205, 213] which causes an anomaly in the resistivity at the ferromagnetic transition temperature T_c . The lowered resistivity in the ferromagnetic state can be explained by the double-exchange interaction, hopping between neighboring ferromagnetically aligned sites lowers the energy of the system and increases the conductivity. If a magnetic field is applied, the ferromagnetic state is stabilized, the consequence is that the transition shifts to a higher temperature and smears out, as seen in the inset of Fig. 6.1. The magnetic field is most effective around the transition temperature, see Sec. 6.4.3.

6.4.2. Thermal Conductivity

Fig. 6.2 shows the thermal conductivity of $\text{La}_{1-x}\text{Sr}_x\text{CoO}_3$. For $x = 0$ the data for the crystal ZO104 are shown. In Chp. 2 the thermal conductivity of insulators was discussed. The main results was that an T^3 dependence of κ for $T \rightarrow 0$ K is expected. At intermediate temperatures a maximum of κ occurs, and at high temperatures κ follows roughly a $1/T$ dependence.

As discussed in detail in Chp. 5, the thermal conductivity of LaCoO_3 is quite unusual. The main result is that strong additional scattering due to the spin-state transition suppresses κ in the whole temperature range investigated. The thermal conductivity of the crystal with $x = 0.002$ is similar to that of pure LaCoO_3 , but the low-temperature maximum of κ is already strongly suppressed. For higher Sr doping this maximum is almost completely absent and κ increases continuously with increasing temperature. The room temperature values of κ lie between 2 and 3 W/Km for all crystals with $x \leq 0.18$. We attribute the drastic suppression of κ at low temperatures to a Sr-induced disorder, which hinders a strong increase of ℓ for $T \rightarrow 0$ K. Probably this disorder does not solely arise from the bare difference between La^{3+} and Sr^{2+} ions. From magnetization measurements it is found that for $x \leq 0.01$ so-called magnetic polarons with high spin values ($S = 10 - 16$) are formed, [215] see Sec. 5.3.3.

Due to such a polaron formation the disorder is strongly enhanced for the lowest Sr concentrations, whereas for larger x the polarons start to overlap and the enhancement becomes less effective. Samples with $x > 0.18$ show metallic conductivity and ferromagnetic order at low temperatures, see Inset of Fig. 6.1. In this concentration range one expects that magnetic polarons become much less important. However, the low-temperature peak of κ remains absent, since the Sr concentration is so large that the bare doping-induced lattice disorder

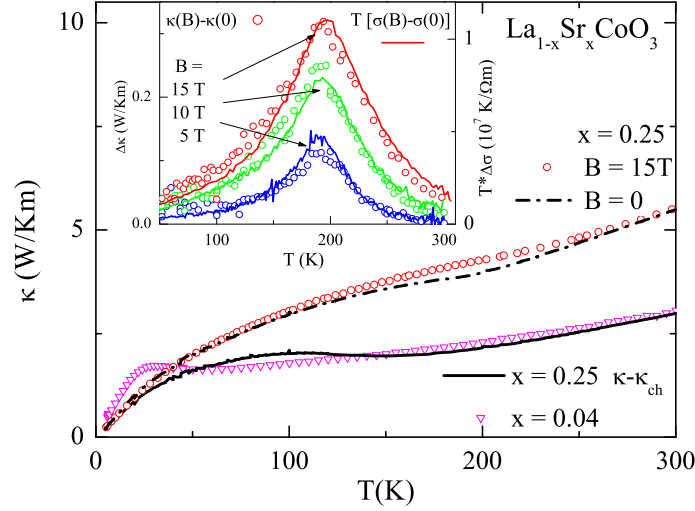


Figure 6.3.: Thermal conductivity κ of $\text{La}_{1-x}\text{Sr}_x\text{CoO}_3$ with $x = 0.25$ as a function of temperature measured in 15 T (\circ) and in zero magnetic field ($-\cdot-$). The solid line is the phononic contribution κ_{ph} of the $x = 0.25$ crystal, which is obtained by $\kappa_{ph} = \kappa(B) - LT\sigma(B)$ using the electrical conductivity σ and the Lorenz number L . For comparison κ of the $x = 0.04$ sample (∇) is also depicted. The Inset shows the magnetic-field dependences $\Delta\kappa(B) = \kappa(B) - \kappa(B = 0)$ (\circ , left y scale) and $T\Delta\sigma(B) = T[\sigma(B) - \sigma(B = 0)]$ ($—$, right y scale) for $B = 5, 10$, and 15 T, respectively. The value of the Lorenz number is obtained from the field- and temperature-independent scaling factor between both quantities, i.e. via $L = \Delta\kappa(B) / [T\Delta\sigma(B)] = 2.9 \cdot 10^{-8} \text{ V}^2/\text{K}^2$. [33, 166, 262]

is sufficient to suppress the low-temperature peak. Moreover, the Sr doping induces mobile charge carriers, which serve as additional scatterers for the phonons.

The mobile charge carriers for larger x are expected to transport heat, too. The total thermal conductivity therefore consists of a phononic contribution and a contribution of mobile charge carriers, i.e. $\kappa = \kappa_{ph} + \kappa_{ch}$. Usually, κ_{ch} can be estimated by the Wiedemann-Franz law, which relates κ_{ch} to the electrical conductivity according to $\kappa_{ch} \simeq L_0 \sigma T$. Here, $L_0 = 2.44 \cdot 10^{-8} \text{ V}^2/\text{K}^2$ denotes the Sommerfeld value of the Lorenz number. From the room temperature values of ρ $\kappa_{ch}(300 \text{ K}) \simeq 0.4, 0.9, 1.6$ and 2.7 W/Km is estimated for $x = 0.125, 0.18, 0.25$ and 0.3 , respectively, and $\kappa_{ch} \ll \kappa$ for smaller x . Additional heat conduction by charge carriers is therefore relevant for metallic $\text{La}_{1-x}\text{Sr}_x\text{CoO}_3$ only and explains why the crystals with $x \geq 0.25$ have significantly larger $\kappa(T)$ values for $T > 100 \text{ K}$ than the insulating samples with $x < 0.18$. For $x = 0.25$ and 0.3 anomalies of κ occur around 200 K and 230 K , respectively, i.e. close to the respective ferromagnetic ordering temperatures $T_c = 209, 227 \text{ K}$. [205, 213]. Below T_c , κ increases and we attribute this to the decrease of ρ below T_c , [205, 213] which leads to a corresponding increase of κ_{ch} . Since the charge transport close to T_c depends on a magnetic field in $\text{La}_{1-x}\text{Sr}_x\text{CoO}_3$, [263] one may analyze κ_{ch} for $x = 0.25$ in more detail by comparing the magnetic-field dependences of κ and $\sigma = 1/\rho$ (Fig. 6.3). An increase of κ with increasing field is found, that is most pronounced around 200 K where the strongest magnetic-field induced suppression of ρ is observed, too, see Fig. 6.1 [263]. Under the reasonable assumption of a negligible field dependence of κ_{ph} we obtain $\Delta\kappa(T, B) = \kappa(T, B) - \kappa(T, 0) = \kappa_{ch}(T, B) - \kappa_{ch}(T, 0)$, and the Lorenz number is given

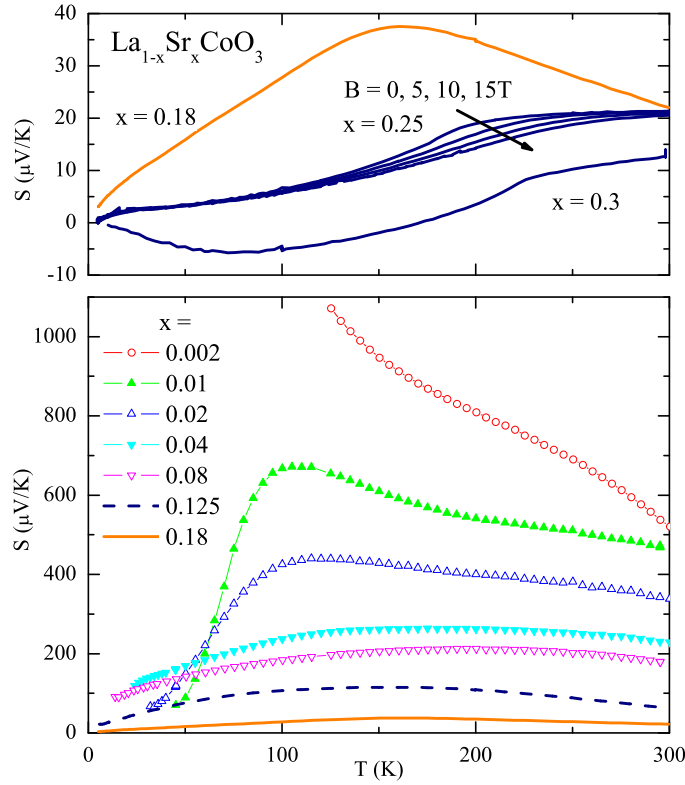


Figure 6.4.: Thermopower S of $\text{La}_{1-x}\text{Sr}_x\text{CoO}_3$ as a function of temperature for different doping $x > 0$. For $x = 0.25$ $S(T)$ is also shown for different magnetic fields. [33, 166, 264]

by the relation $L = \Delta\kappa(T, B) / T\Delta\sigma(T, B)$ with $\Delta\sigma(T, B) = \sigma(T, B) - \sigma(T, 0)$. As shown in the inset of Fig. 6.3 the scaling relation between $\Delta\kappa$ and $T\Delta\sigma(T, B)$ is well fulfilled over the entire temperature and magnetic-field range studied here. From this scaling the value $L = 2.9 \cdot 10^{-8} \text{ V}^2/\text{K}^2$ is estimated, which is about 20% larger than L_0 . The phononic thermal conductivity for $x = 0.25$ is then obtained by $\kappa_{ph} = \kappa(B) - LT\sigma(B)$ and found to agree well with those of the low-doped samples.

6.4.3. Thermopower

The thermopower measurements of the $\text{La}_{1-x}\text{Sr}_x\text{CoO}_3$ series for $x > 0$ are presented in Fig. 6.4. For the crystal with the lowest Sr content $x = 0.002$ a large positive thermopower which increases with decreasing temperature is found. We could not determine S for highly insulating crystals with $\rho \gtrsim 10^9 \Omega\text{cm}$ as it is the case for this crystal below about 100 K. With increasing Sr content S systematically decreases and for $0.01 \leq x \leq 0.18$ all $S(T)$ curves show maxima which become less pronounced and slightly shift towards higher temperature. Note that additional anomalies observed in the temperature dependence $S(T)$ of polycrystalline $\text{La}_{1-x}\text{Sr}_x\text{CoO}_3$ (Ref. [249]) are not reproduced by the single-crystal data. Such a difference has already been observed in magnetization data, and gives further evidence that these additional anomalies are not an intrinsic feature of $\text{La}_{1-x}\text{Sr}_x\text{CoO}_3$. For the metallic samples with $x \geq 0.25$ $S(T)$ varies only weakly with temperature between 300 K and T_c . Around T_c

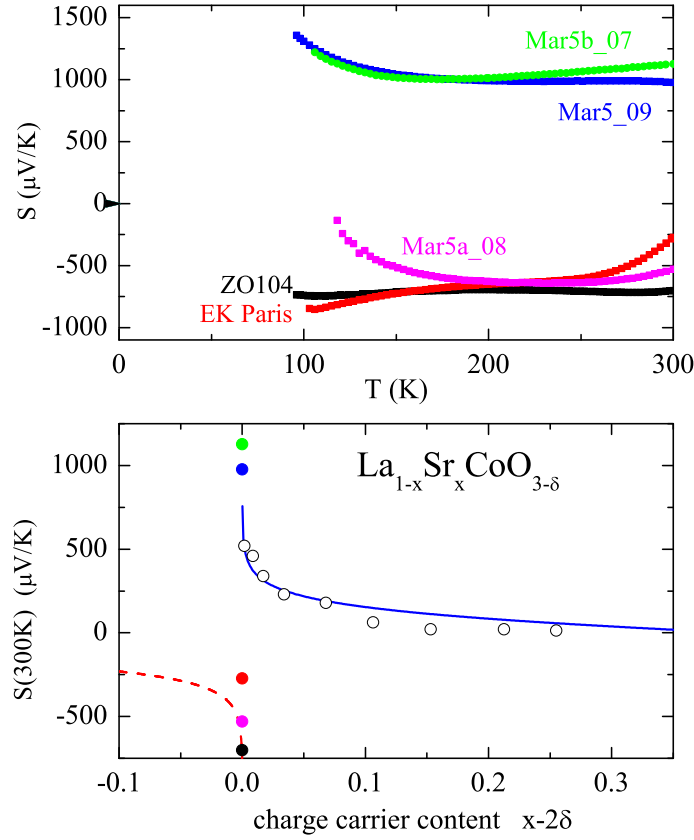


Figure 6.5.: Top: Thermopower S as a function of temperature for 5 different crystals of nominally undoped LaCoO_3 . Bottom: Room-temperature values $S(300\text{K})$ as a function of the charge carrier concentration $n = x + 2\delta$ for Sr-doped (\circ) and pure (\bullet) LaCoO_3 . The lines are calculated via Eq. (6.1). [33, 166, 265]

a sharp kink occurs and S strongly decreases. For $x = 0.3$ there is even a sign change and S becomes negative for $T < 170\text{K}$. The sensitivity of S to the magnetic ordering indicates that a considerable contribution of S arises from magnetic entropy. Therefore, one may also expect a pronounced magnetic-field dependence $S(B)$ as has been pointed out recently. [248] As shown in Fig. 6.4 indeed a strong magnetic-field induced suppression of S is found, that is most pronounced around T_c . This arises from the fact that the magnetic entropy may be strongly reduced by available magnetic-field strengths only around T_c . For higher temperatures thermal disorder becomes too large ($k_B T \gg g\mu_B B$) and for $T \ll T_c$ the magnetic entropy is already frozen by the magnetic exchange coupling.

At high enough temperatures the thermopower is expected to be determined by the so-called Heikes formula (see e.g. Ref. [266]). This general expression has been refined for the case of doped cobaltates in Ref. [267] to

$$S = -\frac{k_B}{e} \left[\ln \left(\frac{n}{1-n} \right) + \ln \left(\frac{g_3}{g_4} \right) \right]. \quad (6.1)$$

Here, n denotes the content of Co^{4+} ions and g_3 (g_4) is the number of possible configurations of the Co^{3+} (Co^{4+}) ions, which is, in general, given by the product of orbital and spin degeneracy.

If different spin states of the $\text{Co}^{3+/4+}$ ions are close enough in energy, the number of possible configurations may further increase. [267]

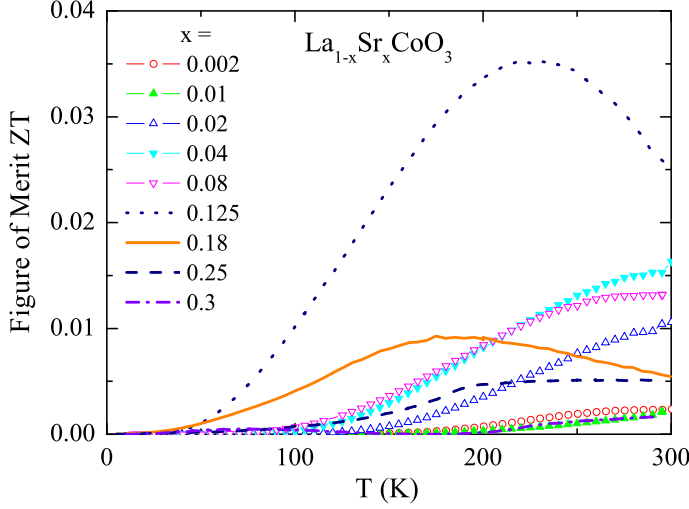


Figure 6.6.: Figure of merit of $\text{La}_{1-x}\text{Sr}_x\text{CoO}_3$ as a function of temperature for different doping x .

In the lower panel of Fig. 6.4.3 the room-temperature values of S for $\text{La}_{1-x}\text{Sr}_x\text{CoO}_3$ are shown (open symbols, $x > 0$) as a function of the charge carrier content $n = 0.9 \cdot x$ as determined by thermogravimetric analysis (see Sec. 6.2). A fit of the experimental data via Eq. 6.1 with the ratio g_3/g_4 as the only fit parameter yields $g_3/g_4 \simeq 1.8$. The saturation magnetization of the samples showing ferromagnetic order ($x > 0.18$) is best described by assuming an $S = 1/2$ low-spin state for Co^{4+} and an $S = 1$ intermediate-spin state for Co^{3+} . [205, 213] For this combination of spin states a ratio $g_3/g_4 = 3/2$ is expected, which is independent from the possible orbital degeneracies $\nu = 1$ or 3 as long as both, the Co^{4+} LS and Co^{3+} IS state have the same ν . If one assumes that the energy of the Co^{3+} LS state is close to that of the Co^{3+} IS state, the ratio increases to $g_3/g_4 = 2$ and $5/3$ for $\nu = 1$ and 3 , respectively. For all of these cases the experimental data are reasonably well described by Eq. 6.1. However, this does not exclude other spin-state combinations, since Eq. 6.1 is derived for the high-temperature limit, whereas in Fig. 6.4 the room-temperature values of S are considered and at least for the samples with $x < 0.25$ the $S(T)$ curves have a more or less pronounced negative slope at 300 K. Thus, it is possible that for higher temperatures a larger g_3/g_4 ratio would be obtained in the fit. In addition, there are also other combinations of spin states yielding g_3/g_4 ratios close to 1.8, but these are not supported by the measured saturation magnetization. Despite these uncertainties we interpret the doping dependence of $S(300 \text{ K})$ as further evidence for the $\text{Co}_{LS}^{4+}/\text{Co}_{IS}^{3+}$ combination suggested from the magnetization and resistivity data. [213]

According to Eq. 6.1 the thermopower is expected to diverge for a vanishing hole content, i. e., when the nominally undoped LaCoO_3 is approached. For electron doping one may still apply Eq. 6.1, but with a positive sign and g_4 for the degeneracy of Co^{2+} . The dashed line in Fig. 6.4 is calculated for $g_4 = 4$ as expected for Co^{2+} in a HS state. A large negative thermopower has been observed recently in electron-doped $\text{La}_{1-x}\text{Ce}_x\text{CoO}_3$. [255] For nominally undoped LaCoO_3 , a different sign of S for different crystals is found. This is shown in the upper panel of Fig. 6.4. Although these crystals have been grown under the same conditions, either a large negative or a large positive thermopower can be obtained. We suspect that this extreme sensitivity of S results from weak deviations in the oxygen content of $\text{LaCoO}_{3+\delta}$, which cause small concentrations 2δ of hole or electron doping depending on the sign of δ .

Already extremely small values of $|\delta| < 0.002$, which are well below the accuracy of oxygen determination in cobaltates, would be sufficient to explain the observed thermopower values with $|S| > 500 \mu\text{V/K}$ in $\text{LaCoO}_{3+\delta}$. We also suspect that there are weak inhomogeneities of the oxygen content in each sample, which can strongly influence the sign and also the temperature dependence of the measured thermopower. Most probably, this is also the reason for the contradictory results for $S(T)$ obtained in Refs. [176, 252]. It should be mentioned that this extreme sensitivity $S(\delta)$ is expected only for the (almost) undoped LaCoO_3 , whereas for samples with a finite Sr content the drastic influence of such small variations of δ rapidly decreases with increasing x .

6.4.4. Figure of Merit

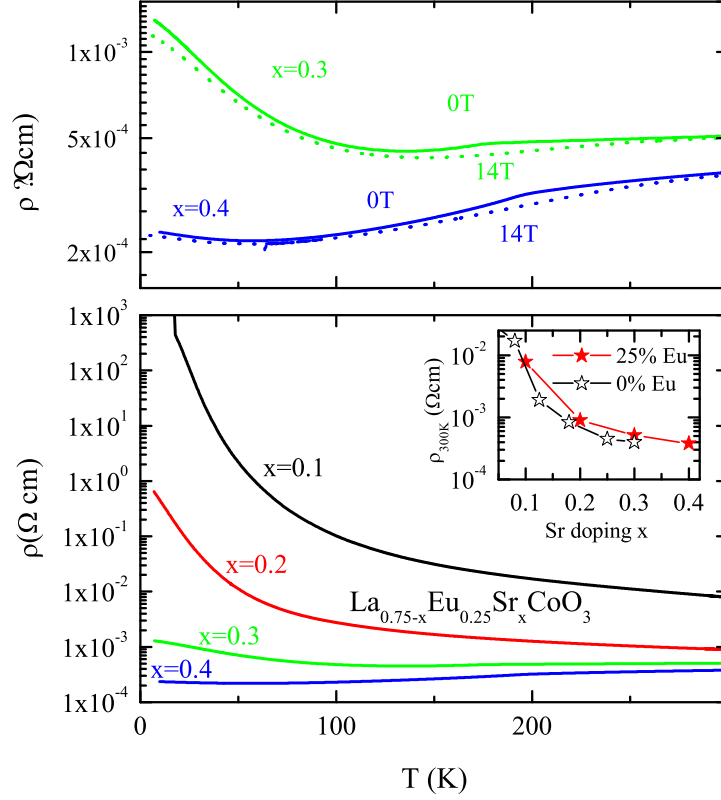
In Fig. 6.6 the thermoelectric figure of merit of $\text{La}_{1-x}\text{Sr}_x\text{CoO}_3$ is presented. Since the thermal conductivity for all x is rather low, one precondition for large ZT values is already fulfilled for the entire $\text{La}_{1-x}\text{Sr}_x\text{CoO}_3$ series. The very low-doped samples show in addition very large thermopower values, but their resistivities are also large and thus prevent large ZT values. Small resistivities are obtained for large x , but these samples also have smaller thermopower values. Thus the optimum figure of merit is obtained in the intermediate doping range. A maximum $ZT \simeq 0.035$ around 225 K is found for $x = 0.125$, which is as large as the value observed in Na_xCoO_2 . [244] These values are among the largest observed in transition metal oxides so far, but are still too small for technical applications. This raises the question, how an improvement of ZT is possible. One possibility, additional substitution of La by Eu, will be discussed in the next section.

6.5. $\text{La}_{0.75-x}\text{Eu}_{0.25}\text{Sr}_x\text{CoO}_3$

A way to tune the physical properties of the $\text{La}_{1-x}\text{Sr}_x\text{CoO}_3$ system is doping with Eu, which is isovalent to La and so does not change the nominal valence of the system. The main effect is chemical pressure due to the smaller Eu ion size. [54] The Sr-free series $\text{La}_{1-x}\text{Eu}_x\text{CoO}_3$ has been investigated by resistivity and susceptibility measurements in the whole doping range $0 \leq x \leq 100$. [178, 179, 206] The measurements of the magnetic susceptibility reveal that the spin gap to the IS/HS state increases from $\Delta_{Co} \approx 188 \text{ K}$ for LaCoO_3 to $\Delta_{Co} > 1900 \text{ K}$ for EuCoO_3 . [178, 206] For $\text{La}_{0.75}\text{Eu}_{0.25}\text{CoO}_3$, the spin gap is determined as $\Delta_{Co} \approx 440 \text{ K}$, more than twice as large as in LaCoO_3 . [178, 206] The influence of Sr doping was investigated on samples of the series $\text{La}_{0.75-x}\text{Eu}_{0.25}\text{Sr}_x\text{CoO}_3$ with $x = 0.1, 0.2, 0.3$, and 0.4 (see Ref. [179]). As already mentioned, these samples are polycrystalline, in contrast to the $\text{La}_{1-x}\text{Sr}_x\text{CoO}_3$ samples. The lower panel of Fig. 6.7 shows the zero field resistivities [271]. As for $\text{La}_{1-x}\text{Sr}_x\text{CoO}_3$, increasing Sr doping causes an insulator-metal transition. In contrast to $\text{La}_{1-x}\text{Sr}_x\text{CoO}_3$, the absolute values of the resistivity are higher for the same doping level³, and a higher doping level is required to induce the IM transition. [232]

As shown in the previous section, the large values of ZT are mainly due to the increased spin entropy which causes a large thermopower. In the Eu-doped samples the spin gap is larger. As a consequence, a higher doping level is required in $\text{La}_{0.75-x}\text{Eu}_{0.25}\text{Sr}_x\text{CoO}_3$ in comparison to $\text{La}_{1-x}\text{Sr}_x\text{CoO}_3$ to obtain the same population of the LS- IS/HS states and therefore the

³A quantitative comparison is difficult for two reasons: There are no crystals available with the same doping in both series. [232]. Further polycrystals are compared with single crystals.

**Figure 6.7.:**

Lower panel: Resistivity of $\text{La}_{0.75-x}\text{Eu}_{0.25}\text{Sr}_x\text{CoO}_3$ for $0.1 \leq x \leq 0.4$. For consecutive doping an insulator-metal transition occurs for $x \approx 0.3$ [268]. Upper panel: resistivity for $x = 0.3$ and $x = 0.4$ in magnetic fields of 0 and 14 T. Inset: room temperature values of ρ vs. Sr doping x for $\text{La}_{1-x}\text{Sr}_x\text{CoO}_3$ and $\text{La}_{0.75-x}\text{Eu}_{0.25}\text{Sr}_x\text{CoO}_3$.

same entropy at a given temperature. It follows, that the enhancement of the thermopower is shifted to a higher Sr doping x for Eu doped samples. This could increase the figure of merit and motivated to determine ZT

Fig. 6.9 shows the thermal conductivity data [270] for $\text{La}_{0.75-x}\text{Eu}_{0.25}\text{Sr}_x\text{CoO}_3$ with $x = 0 \dots 0.4$. For $x = 0$ the thermal conductivity is almost identical to LaCoO_3 , which seems surprising, since the disorder introduced by the Eu should suppress the thermal conductivity. This shows, that the suppression of the low-temperature maximum of $\text{La}_{1-x}\text{Sr}_x\text{CoO}_3$ for higher doping levels mainly arises from scattering by charge carriers. With Sr doping, the low-temperature maximum is suppressed as in $\text{La}_{1-x}\text{Sr}_x\text{CoO}_3$, and the thermal conductivity monotonously increases with temperature. The absolute values of the lattice contribution at room temperature, calculated by the Sommerfeld value L_0 , denote 2.2, 3.8, 3.4, and 1.5 W/Km for $0.1 \leq x \leq 0.4$. Performing the same scaling procedure as for $\text{La}_{1-x}\text{Sr}_x\text{CoO}_3$ for the field dependent thermal conductivity curves (see Ref. [177]), one gets $L = 2.0 \cdot 10^{-8} \text{ V}^2/\text{K}^2$. In contrast to LaCoO_3 , where the estimated L is $\approx 20\%$ higher than L_0 , here L is about 20% lower. The inset of Fig. 6.9 shows the electronic contribution to the thermal conductivity, calculated with the value of L from the scaling analysis. However, the estimated room temperature lattice contributions do not show a systematic behavior, [177] which may be related

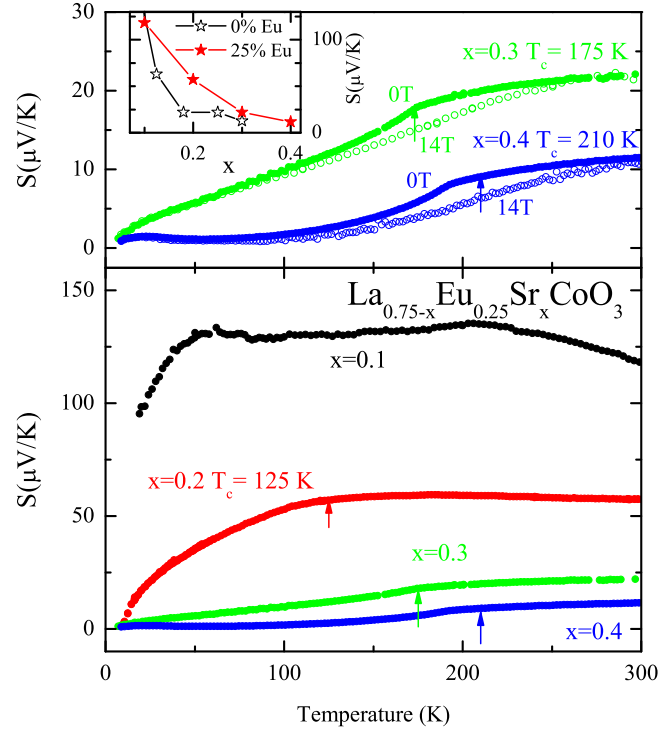


Figure 6.8.: Lower Panel: Thermopower of $\text{La}_{0.75-x}\text{Eu}_{0.25}\text{Sr}_x\text{CoO}_3$ for $0.1 \leq x \leq 0.4$. Upper panel: Thermopower of $\text{La}_{0.75-x}\text{Eu}_{0.25}\text{Sr}_x\text{CoO}_3$ for $x = 0.3$ and $x = 0.4$ in magnetic fields of 0 and 14 T. Arrows mark the ferromagnetic transition temperature. Inset: Room temperature values of the thermopower vs. Sr doping x for $\text{La}_{1-x}\text{Sr}_x\text{CoO}_3$ and $\text{La}_{0.75-x}\text{Eu}_{0.25}\text{Sr}_x\text{CoO}_3$. [269]

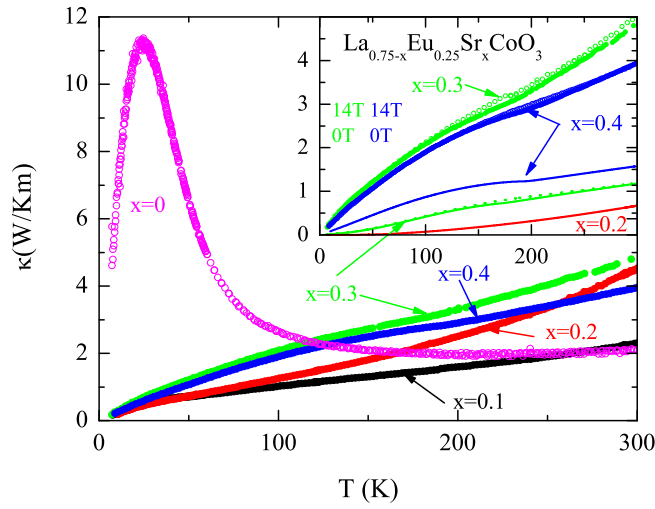


Figure 6.9.: Thermal conductivity of $\text{La}_{0.75-x}\text{Eu}_{0.25}\text{Sr}_x\text{CoO}_3$ for $0.1 \leq x \leq 0.4$. Inset: thermal conductivity for $x = 0.3$ and 0.4 in magnetic fields of 0 and 14 T (Symbols). Lines are electronic contributions to κ calculated by the Wiedemann-Franz law with $L = 2.0 \cdot 10^{-8} \text{ V}^2/\text{K}^2$. [270]

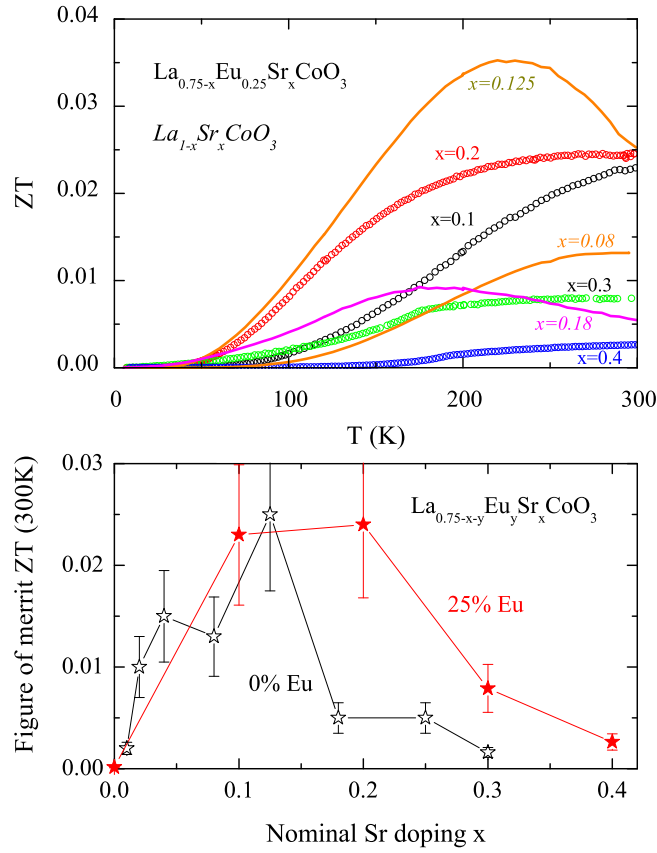


Figure 6.10.: Upper Panel: Figure of Merit of $\text{La}_{0.75-x}\text{Eu}_{0.25}\text{Sr}_x\text{CoO}_3$ for $0.1 \leq x \leq 0.4$ (Symbols). For Comparison the curves for $\text{La}_{1-x}\text{Sr}_x\text{CoO}_3$ with $x = 0.08, 0.125$, and 0.18 are shown (lines). Lower Panel: Room temperature values of ZT for $\text{La}_{1-x}\text{Sr}_x\text{CoO}_3$ and $\text{La}_{0.75-x}\text{Eu}_{0.25}\text{Sr}_x\text{CoO}_3$ vs. Sr doping level x . Errorbars are drawn assuming a relative error of 30%.

to the polycrystal nature of the crystals, and does not allow a more detailed analysis. However, the absolute values of the lattice contribution are of the same order of magnitude as for $\text{La}_{1-x}\text{Sr}_x\text{CoO}_3$ ($\approx 2.5 \text{ W/Km}$).

Fig. 6.8 shows the thermopower. In the lower panel the zero field data are shown. The general findings are the same as for $\text{La}_{1-x}\text{Sr}_x\text{CoO}_3$, a large positive thermopower which is strongly suppressed for the higher doping levels. The inset shows the room-temperature values vs. Sr doping x for both series, the Eu doped crystals have indeed a higher thermopower at the same Sr doping level. The upper panel of Fig. 6.8 shows the thermopower for $x = 0.3$ and $x = 0.4$, which show the same behavior as $\text{La}_{1-x}\text{Sr}_x\text{CoO}_3$ with $x = 0.25$ and $x = 0.3$, taking into account the differences in T_c . Consequently, the explanation for the anomaly at T_c of the ferromagnetic transition and the field dependence is the same as for e.g. $\text{La}_{0.75}\text{Sr}_{0.25}\text{CoO}_3$, see e.g. Sec. 6.4.1. [232]

Calculating the thermoelectric figure of merit, we find the results shown in Fig. 6.10, together with some results from the $\text{La}_{1-x}\text{Sr}_x\text{CoO}_3$ crystals for comparison. The main result is that ZT does not change significantly with Eu doping. The absolute value at the maximum is smaller,

$ZT = 0.02$ at 300 K instead of $x = 0.025$ at 250 K. However, it is likely that the maximum values of ZT is achieved for x inbetween 0.1 and 0.2, and approximately the same as observed in LaCoO_3 . Here one has to keep in mind, that the uncertainty of ZT is comparatively high, since it is calculated from three independent measurements (In Sec. 3.4 a relative error of $\approx 20 \dots 25\%$ was derived). In order to get an better estimate of the doping dependence of ZT , the room temperature values vs. doping level x are shown in the lower panel of Fig. 6.10. The figure shows that the maximum of ZT is shifted to a higher doping level, but does not significantly change the absolute value at room temperature.

6.6. Conclusions

We have presented a systematic study of the thermal conductivity and the thermopower of a series of single crystals of $\text{La}_{1-x}\text{Sr}_x\text{CoO}_{3+\delta}$. The thermal conductivity is strongly suppressed for the entire doping range. In pure LaCoO_3 this suppression most probably arises from local lattice distortions due to a temperature-induced spin-state transition of the Co^{3+} ions. For small finite x , a spin-state transition of the Co^{3+} ions may be induced by the neighboring magnetic Co^{4+} ions, and so-called high-spin polarons can be formed, which also cause lattice disorder. For larger x this effect becomes less important, and scattering of phonons by mobile charge carriers plays the main role for the suppression of the thermal conductivity. This conclusion can be drawn, since in Sr-free $\text{La}_{1-x}\text{Eu}_x\text{CoO}_3$ the low-temperature peak is still present. The static disorder caused by the different ion sizes of La and Sr seems to play a minor role. For finite doping a large, positive thermopower, which strongly depends on temperature and doping, is found. The room temperature values of the thermopower follow a doping dependence that is expected from a modified Heikes formula, [267] if an intermediate-spin state for Co^{3+} and a low-spin state for Co^{4+} is assumed as it is suggested from magnetization and resistivity data. [213] In nominally undoped LaCoO_3 for different crystals either a large positive or a large negative thermopower is observed. This is likely a consequence of weak deviations ($|\delta| < 0.002$) from the nominal oxygen content causing small amounts of hole or electron doping. Most probably, a weak oxygen off-stoichiometry is also the reason for the contradictory results of the thermopower reported for LaCoO_3 previously. [176, 252] For the crystal with $x = 0.25$ both, the thermal conductivity and the thermopower show a significant magnetic-field dependence in the temperature range around the ferromagnetic ordering temperature. The field dependence of the thermal conductivity can be traced back to a field-dependent charge carrier contribution to the heat current, and the field dependence of the thermopower indicates that it contains a sizeable contribution arising from magnetic entropy. From the resistivity ρ , the thermopower S and the thermal conductivity κ the thermoelectric figure of merit $Z = S^2 / \kappa \rho$ was calculated, which strongly depends on both, doping and temperature. A maximum of $ZT \simeq 0.035$ is obtained for $x = 0.125$ and $200 \text{ K} \leq T \leq 250 \text{ K}$. This value is large, but yet too small for technical applications. Additional Eu increases the resistivity and the thermopower at a given Sr doping level, what shifts the maximum of ZT to a higher doping level. However, within the experimental error no change in the maximum value of ZT is observed.

7. Thermal Conductivity of Orthorhombic Manganites

The search for magnetoelectric materials, with the possibility to induce magnetic ordering by electric fields and vice versa, has increased the interest in so-called multiferroic materials, in which magnetic and ferroelectric ordering phenomena coexist [14]. The orthorhombic rare earth manganites of the form $RMnO_3$ are of particular interest in this focus, since for $R = \text{Gd}$, Tb , and Dy a ferroelectric phase develops in a magnetically ordered phase. These compounds show complex magnetic structures driven by frustration effects, and there are indications that the ferroelectric order is driven by the complex magnetic ordering phenomena. In this chapter a brief introduction into the $RMnO_3$ series will be given. Then the results of the thermal conductivity measurements on NdMnO_3 , GdMnO_3 , and TbMnO_3 will be presented. We will compare our results to recent literature of Zhou *et al.* [272]. These authors proposed a general scenario to explain the thermal conductivity in the orthorhombic manganates. By a detailed analysis of the thermal conductivity of NdMnO_3 and TbMnO_3 in combination with results from thermal expansion we will show that the explanation given in Ref. [272] *et al.* may be doubted.

7.1. Orthorhombic $RMnO_3$ Perovskites

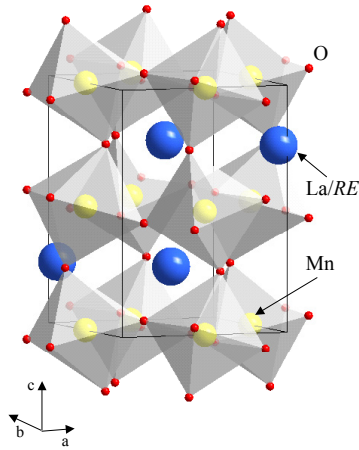


Figure 7.1.: Structure of $RMnO_3$. The Perovskite structure has an orthorhombic distortion of the GdFeO_3 type, which increases with decreasing rare earth size. The degree of this distortion can be characterized by the averaged Mn-O-Mn bond angle.

The mother compound of the $RMnO_3$ series, LaMnO_3 , crystallizes in an orthorhombic crystal structure. The orthorhombic unit cell has the symmetry Pbnm ¹. With respect to the cubic perovskite structure, the distortion is of the GdFeO_3 type. It arises from the fact that the La-O bond length is "too small" in comparison to the Mn-O bond length. The GdFeO_3 distortion is characterized by a tilting of the MnO_6 octahedra, where b is the tilting axis, and a

¹In the Pbnm notation the a axis is the smallest, and the c axis the longest axis. An alternative notation is the space group Pnma , with the transformations: $\text{Pbnm} \rightarrow \text{Pnma}$: $a \rightarrow b$, $b \rightarrow c$, and $c \rightarrow a$.

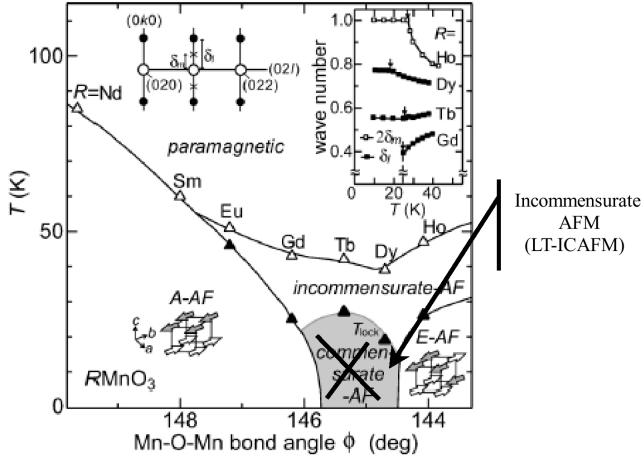


Figure 7.2.: Phase diagram of $RMnO_3$ as a function of the planar Mn-O-Mn bond angle, which characterizes the $GdFeO_3$ type distortion. For the smaller distortions an A-type antiferromagnet is realized. The Néel temperature is successively suppressed with decreasing Mn-O-Mn bond angle. For $R = Gd, Tb$, and Dy complex magnetic structures are realized. Taken from Refs. [15, 273, 274].

rotation around the c axis, see Fig. 7.1. The electronic structure of $LaMnO_3$ is determined by the five-fold degenerate $3d$ orbitals, which split up in the (locally) cubic crystal field into the energetically lower t_{2g} orbital (three-fold degenerate) and the energetically higher e_g orbital (two-fold degenerate). The spin state is fully determined by the dominating Hund's rule energy, leading to a $t_{2g}^4 e_g^1$ configuration. This means that one electron occupies the e_g orbital leading to a Jahn-Teller distortion. In $LaMnO_3$, a Jahn-Teller ordered state is realized below $T_{JT} \approx 750$ K [275]. The Jahn-Teller ordering is of the d type [276], which means that the elongation axes of the octahedra alternate within the ab plane, and a ferro-type ordering is present along the c axis.

If La is replaced by smaller rare earth ions, the $GdFeO_3$ distortion increases, which can be characterized by the Mn-O-Mn bond angle. For the smaller rare earth the ordered Jahn-Teller state is stabilized, and T_{JT} increases, up to ≈ 1500 K [277–279] (not shown). Fig. 7.2 shows the Mn-O-Mn T phase diagram of $RMnO_3$ with $R = Nd, \dots, Ho$.

At low temperatures, the orbital ordering leads to an A type antiferromagnetic ordering of Mn below $T_N^{Mn} \approx 140$ K in $LaMnO_3$. This type of ordering is characterized by a ferromagnetic ordering within the ab planes, and an antiferromagnetic ordering along the c axis [280–282]. The Hamiltonian of the magnetic system denotes

$$\mathcal{H} = \sum_{i,j} J_{ij}(S_i S_j) - \Lambda \sum_i S_i^z{}^2. \quad (7.1)$$

Here, J_{ij} are the coupling constants. The nearest neighbor (NN) couplings can be grouped into the ferromagnetic nearest-neighbor coupling J_{NN}^{FM} in the ab plane with the coordination number $z = 4$ and the antiferromagnetic coupling constant J_{NN}^{AFM} along the c direction with $z = 2$. The second term of Eq. 7.1 takes the single-ion anisotropy into account [283]. Note, that the summation in Eq. 7.1 counts every bond twice, what has to be considered when the absolute values of the different J are discussed. By applying spin-wave theory the values $J_{NN}^{FM} = -9.6$ K and $J_{NN}^{AFM} = 6.7$ K are obtained in Ref. [284]. From these values a mean-field

	J_{NN}^{FM}	J_{NN}^{AFM}	$J_{NNN}^{AFM}/J_{NN}^{FM}$	Λ	T_N^{calc} (K)	Θ^{calc} (K)	T_N^{exp} (K)
LaMnO ₃ [284]	−0.83 meV −9.6 K	0.58 meV 6.7 K		0.17 meV 1.8 K	207	100	140 [55]
LaMnO ₃ [286]	−0.84 meV −9.7 K	0.61 meV 7 K		0.15 meV 1.8 K	211	99	140 [55]
PrMnO ₃ [39]	−0.56 meV −6.5 K	0.6 meV 7 K		0.08 meV 0.9 K	160	48	100 [55]
TbMnO ₃ [39]	−0.15 meV −1.7 K	0.5 meV 5.8 K		0.13 meV 1.5 K	74	18.6	42 [287]
TbMnO ₃ [285]	−0.14 meV −1.6 K	0.58 meV 6.6 K	80%	0.14 meV 1.6 K	78	27	42 [287]

Table 7.1.: Exchange fields of various $RMnO_3$ compounds, single-ion anisotropy Λ , mean-field values for T_N and Θ , frustration, T_N from experiment. Note that the different authors use different definitions of J and Λ . The values have been converted to the Hamiltonian Eq. 7.1, which is the convention used in Ref. [284]

calculation [32, 284] yields

$$T_N^N = \frac{2}{3}S(S+1) \sum_i z_i |J_i| = \frac{2}{3}S(S+1)(4J_{NN}^{FE} + 2J_{NN}^{FE}) \quad (7.2)$$

$$\Theta = \frac{2}{3}S(S+1) \sum_i z_i J_i \quad (7.3)$$

for the Néel and the Curie-Weiss temperature. In Tab. 7.1 I compare the values of T_N and Θ , calculated via Eqs. 7.1 and 7.3 from the exchange constants determined by inelastic neutron scattering [39, 284–286] to the experimentally determined T_N . The calculated Néel temperature for LaMnO₃ overestimates the measured T_N by $\approx 40\%$. The mean-field calculation describes the suppression of T_N , which shows that the main reason for the suppression is the weakening of the exchange constant J_{NN}^{FM} within the planes. The overestimation of T_N by the MF calculation is similar for all compounds.

The spin-orbit coupling causes a Dzyaloshinski-Moriya type interaction. The consequence is a canting of the spins along the c direction causing a weak ferromagnetic (WF) moment in the AFM ordered state. In LaMnO₃ and PrMnO₃ values of $M_0 \approx 0.1 \mu B$ of the WF moment have been determined in the literature [55, 288].

Furthermore, a larger distortion suppresses the NN antiferromagnetic exchange interaction, whereas the NNN ferromagnetic exchange interaction remains more or less constant, which destabilizes the A type ferromagnetic ordering. The resulting frustration leads to complex order phenomena for $R = Gd, Tb$ and Dy [14, 206, 274, 289–296].

Starting with $R = Dy$, $RMnO_3$ can also crystallize in a hexagonal structure. For $R = Er, \dots, Lu$ only the hexagonal structure is realized by the usual growth methods. However, recently the orthorhombic manganites with $R = Er, \dots, Lu$ have also been prepared [297] by high-pressure synthesis. This method is based on the fact that the perovskite structure is more dense than the hexagonal structure and therefore favorable under high pressure. In the perovskite $RMnO_3$ compounds with $R = Ho \dots Lu$ an E type antiferromagnetic ordering is stabilized at low temperatures, with $T_N \approx 40$ K. Note that the complex order phenomena in GdMnO₃, TbMnO₃, and DyMnO₃ are located in the region of the phase diagram, where

	$a[\text{mm}]$	$b[\text{mm}]$	$c[\text{mm}]$
NdMnO ₃	1.5	1.8	1.2
GdMnO ₃	1.7	2.0	1.45
TbMnO ₃ A	2.00	1.1	1.5
TbMnO ₃ B	2.00	1.6	0.14

Table 7.2.: Sample sizes of the investigated $RMnO_3$ samples.

neither the A-type nor the E-type antiferromagnetism can be stabilized.

7.2. Samples

All samples were grown in a floating-solvent image furnace by A.M. Balbashov (see e.g. Ref. [298]). The samples have been oriented by a Laue camera, and have been cut into convenient forms. Samples sizes are listed in Tab. 7.2. The NdMnO₃ sample was oriented and cut into a cuboid by D. Meier (see Ref. [287]). The same specimen was used for the zero-field thermal expansion measurements [287], and all measurements presented in this section. The GdMnO₃ sample was already cut, and had only an approximate cuboid-formed shape. This sample is the same specimen used for the thermal expansion measurements in Refs. [273, 287, 291]. For the measurements of TbMnO₃ two samples were used. Sample A broke into pieces while performing a measurement with a magnetic field of 11 T along the c axis. Such a destruction of the samples in the same magnetic field direction was also observed in thermal expansion measurements [287], and is presumably caused by large torque forces acting on the sample. Therefore another sample was oriented and cut, and used for the rest of the measurements. The results were reproducible very well for the measurements at low temperatures and in magnetic fields. Small samples dependences occurred for $H = 0$ below 10 K (see Sec. A.1). Because of the small cross section of sample B, the measurements at higher temperatures had non-negligible radiation losses. These measurements had to be corrected, as shown in Sec. A.1. For the temperature-dependent measurements the geometric error was slightly corrected by scaling the curves, if measurements with different setups are shown, to get a consistent data set. The corrections amount to only a few percent. As a reference the measurements of sample A were taken.

7.3. Thermal Conductivity of $RMnO_3$: Overview

Recently, Zhou *et al.* [272, 297] published thermal conductivity data of orthorhombic $RMnO_3$ manganites². The authors present zero-field data for $R = \text{La, Gd, Tb, Dy, Eu, Y, and Lu}$, which are shown in Fig. 7.3a. Zhou *et al.* argue that TbMnO₃ and DyMnO₃ show a "glassy-like" thermal conductivity, whereas the other compounds are phonon-like. The latter argument is based on the high-temperature slope of the thermal conductivity [297]: Whereas a decreasing behavior of κ with decreasing temperature is observed above $T \approx 100$ K for $R = \text{Tb and Dy}$, κ increases for the other $RMnO_3$ compounds. The unusual temperature dependence of κ for

²Ref. [297] focuses on the hexagonal manganites. Here, the situation is completely different, since other mechanisms, like "rattling" of Mn ions may play a role. The data for the orthorhombic Perovskites LuMnO₃ and YMnO₃ shown in Ref. [297] are the same as in Ref. [272].

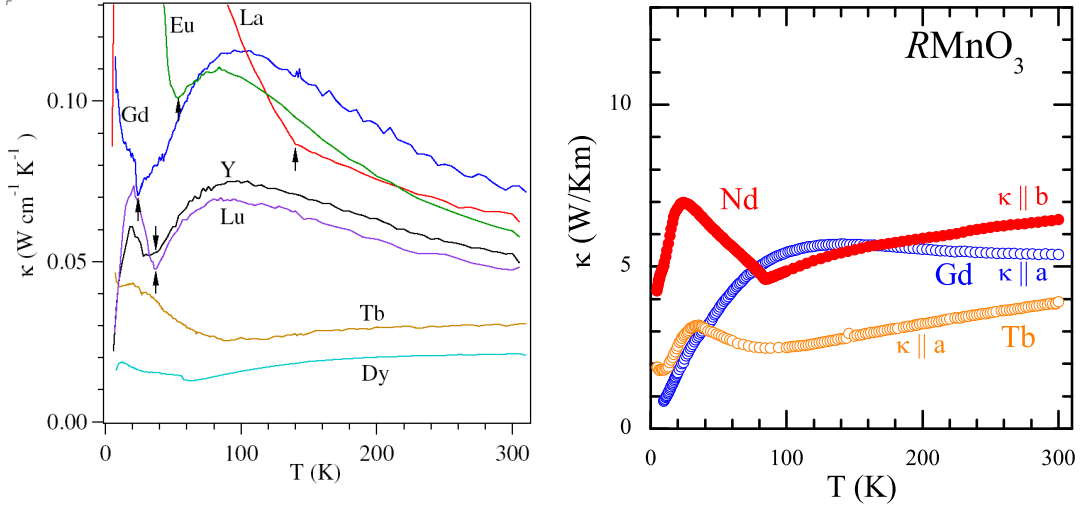


Figure 7.3.: a) Literature data of κ in RMnO_3 with $R = \text{La, Gd, Tb, Dy, Eu, Y, and Lu}$ from Ref. [272]. b) Our zero-field results of the thermal conductivity of NdMnO_3 , TbMnO_3 , and GdMnO_3 . Note that the scale is the same as in a).

$R = \text{Tb}$ and Dy is attributed to magnetic-coupling fluctuations due to the unusual ordering phenomena in these compounds.

Fig. 7.3b presents our zero-field data for $R = \text{Nd, Gd, and Tb}$. For TbMnO_3 the data are in good agreement with the literature above ≈ 30 K. In particular, the broad minimum around 100 K seems to be an intrinsic feature of TbMnO_3 . At low temperatures, the literature data have higher values. The sample used in Ref. [272] seems to have less impurity scattering than our sample.

For GdMnO_3 there is no good agreement with the literature data. The room-temperature values are approximately the same. Zhou *et al.* observe an negative slope of κ at higher temperatures, and a broad maximum around 100 K. Further, at T_c a steep increase of κ is observed with decreasing temperature. Our measurements also show an increase of κ when the temperature is lowered. However, this increase is much weaker. We observe a maximum of κ at around 120 K, which is very broad and shows lower absolute values than the data from Ref. [272]. At low temperatures the largest differences occur, since κ in our sample strongly decreases to very low absolute values. The sharp anomaly of κ at T_c is missing. Instead, κ drops to very low absolute values in our sample. This large differences show that in our sample additional phonon-scattering is present. In principle, this can be caused by a poor crystal quality or a large number of cracks. Another explanation could be the observed low-temperature mixed-phase behavior [273, 291]. At present, it is not clear if this is an intrinsic feature of GdMnO_3 . Such effects may lead to the observed large suppression of κ at low temperatures. In NdMnO_3 we observe a decrease of κ with decreasing temperature. This is in contrast to the proposed scenario of Zhou *et al.*, since in NdMnO_3 a conventional A-type antiferromagnetic order is realized. At the Néel temperature a sharp minimum is observed, and κ shows a maximum at around 30 K.

From the results of NdMnO_3 we conclude that the correlation between the high-temperature behavior of κ to the type of the proposed ordering mechanism at low temperatures is not valid

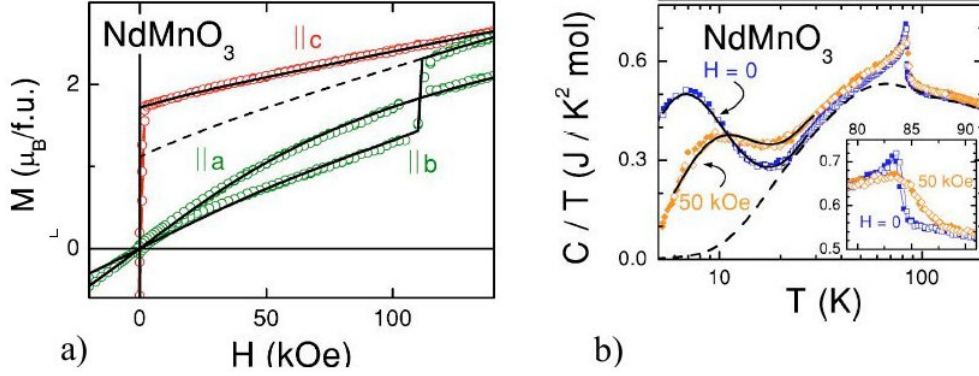


Figure 7.4.: a) Magnetization of NdMnO₃ with $H \parallel a$, b , and c . b) Specific heat of NdMnO₃ in zero field and in $H = 5 \text{ T} \parallel c$. From Ref. [55].

in general. To further resolve this issue, we will perform a detailed analysis of the thermal conductivity of TbMnO₃ and NdMnO₃. Due to a possible non-intrinsic suppression of κ in GdMnO₃, we will not further consider these measurements³.

7.4. NdMnO₃

Before the thermal conductivity of NdMnO₃ will be discussed in more detail, a short introduction into the physical properties of NdMnO₃ will be given. In NdMnO₃, the Néel temperature is shifted to $\approx 88 \text{ K}$ compared to LaMnO₃ with $T_N = 140 \text{ K}$. The Néel transition is observed as a peak in the specific heat [55], see Fig. 7.4b. T_N is hardly changed by a magnetic field of 5 T. The Néel transition also causes large anomalies in thermal-expansion measurements along all crystallographic axes [287], see Fig. 7.5. The sign of the anomaly is positive in α_b and α_c , whereas the anomaly is negative in α_a . The sign of the anomaly in the uniaxial thermal expansion corresponds to the sign of the uniaxial pressure dependence of T_N , what e.g. means that T_N^{Mn} shifts to higher temperatures for uniaxial pressure applied along the b and c axis. The observed behavior for α_a and α_b correlates with the orthorhombic splitting $\epsilon = (b - a)/(a + b)$. Pressure along the a axis decreases the orthorhombic splitting, leading to an increase of the Mn-O-Mn bond angle, and therefore a suppression of T_N . For pressure along the b direction the effect is just the other way around. However, the positive sign of the anomaly of α_c is due to an enhancement of the inter-plane coupling constant $J_{\text{NN}}^{\text{AFM}}$ [273, 287].

As seen in both, specific heat and thermal expansion, an additional low-temperature peak is present below $\approx 30 \text{ K}$, which can be attributed to a Schottky contribution. The $J = 9/2$ ground state multiplet of the $4f$ shell of Nd is split into five doublets in the crystal field (see Sec. 2.4). As shown in Refs. [55, 299] the doublet with the lowest energy further splits by the Nd-Mn exchange interaction. The splitting amounts to $\Delta_0 \approx 20 \text{ K}$. This explains the comparatively low value of Δ_0 , since the next doublet is expected at a much higher energy. The specific heat data [55] and spectroscopic measurements [299] yield values for the zero-field splitting Δ_0 of 21.6 K and 20.0 K, respectively. These values well agree with $\Delta_0 = 19.6 \text{ K}$

³The whole set of measurements of κ in GdMnO₃ is shown in the appendix (Sec. A.2).

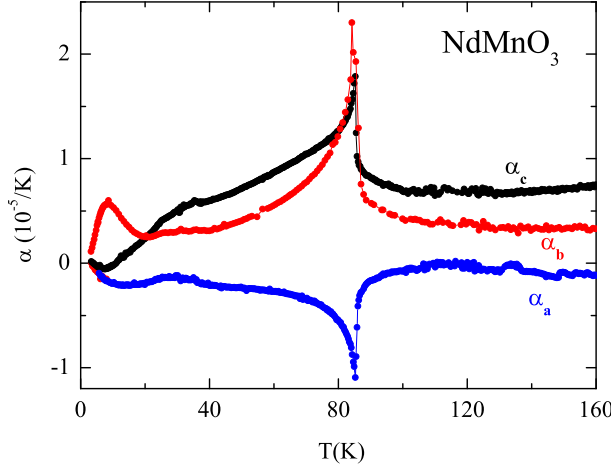


Figure 7.5.: Thermal expansion of NdMnO₃ in zero field. Shown are measurements along the crystal axes *a*, *b*, and *c* [287].

obtained from the zero-field thermal expansion [287]. The Schottky contribution to the specific heat (per site) of a two-level system is given by [205]

$$c_{\text{sch}} = k_B \cdot \frac{\Delta^2}{T^2} \cdot \frac{\tau_1 \tau_2 \exp(-\Delta/T)}{(\tau_1 + \tau_2 \exp(-\Delta/T))^2}, \quad (7.4)$$

where τ_1 and τ_2 are the degeneracies of the levels, and Δ is the energy splitting. It follows that the height of the peak of the specific heat is solely determined by the degeneracies of the two levels. The specific heat data from Ref. [55] are described best with $\tau_1 = \tau_2 = 1$, which is consistent with singlets generated by the splitting of the ground state doublet. From the specific heat (Refs. [55, 300]) it is known that the Schottky peak is strongly field dependent. The energy splitting shifts to higher temperature with increasing field. Hemberger *et al.* determine a value of $\Delta \approx 30$ K in a magnetic field of 5 T.

The magnetization at 5 K is highly anisotropic. For $H \parallel c$, a spontaneous moment of $\approx 1.7\mu_B/\text{f.u.}$ for small H and an increase up to $2.6\mu_B/\text{f.u.}$ at 14 T is observed. For $H \parallel b$, a spin-flop transition occurs at $H \approx 11$ T. The interpretation of the magnetization is difficult, because both Mn and Nd moments contribute, and the Mn-Nd interaction plays an important role, see Sec. 7.4.4 and Ref. [55].

7.4.1. Thermal Conductivity of NdMnO₃: Zero Field

Fig. 7.6 shows the thermal conductivity of NdMnO₃ between 5 K and 300 K measured along the *b* direction (symbols). At 25 K, κ shows a maximum with a relatively low absolute value of 6 W/Km. With increasing temperature, κ decreases until a value of 4.6 W/Km at the Néel temperature $T_N^{\text{Mn}} = 89$ K is reached. At T_N^{Mn} , a sudden change to a positive slope of κ is observed, and above T_N^{Mn} the thermal conductivity monotonously increases up to an absolute value of 6.4 W/Km at room temperature. The correlation between the sharp minimum of κ at T_N^{Mn} is clearly seen by the comparison with the specific heat, which is shown as a solid line. A further small anomaly is observed below 20 K, a small dip which seems to be related to the Schottky contribution in the same temperature range. From Ref. [55] we know that the Schottky peak shifts to a higher temperature in a field of 5 T. Therefore, we will explore the field dependence of the Schottky contribution by thermal-expansion measurements (Secs. 7.4.2 - 7.4.6) before we will proceed with the discussion of the magnetic-field dependent

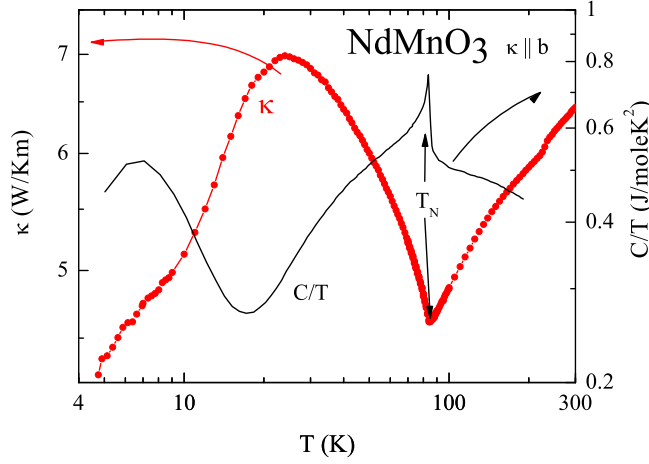


Figure 7.6.: Thermal conductivity and specific heat C/T [55] of NdMnO_3 in zero field.

measurements of κ in Sec. 7.4.9. Furthermore we will analyze the magnetic contribution to the specific heat (Sec. 7.4.7), which will be connected to the κ measurements in Sec. 7.4.8.

7.4.2. Thermal Expansion of NdMnO_3 in Magnetic Fields

For a precise determination of the field dependence of the Schottky contribution and the investigation of the Mn-Nd exchange coupling, field-dependent thermal-expansion measurements were performed. From the zero-field thermal expansion (Fig. 7.5) the b direction seemed to be most promising, since the Schottky contribution is most pronounced along this direction. The thermal expansion α_b was measured with $H \parallel c$ by using a low-temperature dilatometer [61, 301] at temperatures between ≈ 500 mK and 25 K and magnetic fields of 0...14 T. Furthermore, the measurements of α_c with $H \parallel c$ were performed along the c direction with the same setup.

The measurements with the other field directions turned out to be much more difficult. Several runs, with different configurations were performed, which all showed large anomalies, however, were not reproducible. These anomalies turned out to be artefacts due to the large magnetic moment of the samples along the c direction causing a large torque (see e.g. Ref. [287]). Therefore, the thermal expansion along the b direction with $H \parallel b$ was measured by J. Baier in another dilatometer [273]. This probe has the advantage that the sample is fixed by a significantly higher contact pressure than in the low-temperature probe. The measurements in this dilatometer gave reliable results and were performed between 5 K and 25 – 35 K.

Fig. 7.7a shows the thermal expansion α_b of NdMnO_3 in magnetic fields between 0 T and 14 T applied along the c direction. The curve for $H = 0$ is in good agreement with the zero-field data from Fig. 7.5. With increasing magnetic field, the Schottky peak shifts monotonously to higher temperatures, as expected from the specific heat measurements [55, 300]. For the data analysis, Eq. 7.4 is used in combination with the Grüneisen scaling [287, 302], leading to

$$\alpha_{\text{sch}} = \frac{k_B}{V_{\text{uc}}} \frac{\partial \ln(\Delta)}{\partial p} \left(\frac{\Delta}{T} \right)^2 \frac{e^{-\Delta/T}}{(1 + e^{-\Delta/T})^2} \quad (7.5)$$

in the case of two singlets. Here, V_{uc} is the volume of the unit cell (in cubic notation), and $\frac{\partial \ln(\Delta)}{\partial p}$ is the relative pressure dependence of the energy gap Δ . Note that this value can have

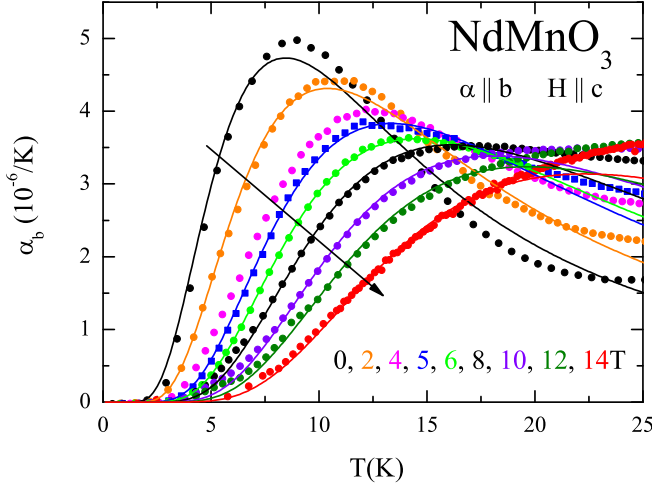


Figure 7.7.: Thermal expansion α_b of NdMnO₃ for $H \parallel c$. The solid lines are calculated Schottky contributions.

a positive or negative sign yielding a Schottky peak with a positive or negative sign. Fig. 7.7b shows the fits performed via Eq. 7.5 for α_b with $H \parallel c$. Here, it turned out that no background subtraction was necessary, since α_b is almost totally determined by α_{sch} in the investigated temperature range.

Fig. 7.8a shows the thermal expansion α_c with $H \parallel c$. Here, the Schottky contribution has a negative sign. For $H = 0$ T the absolute values of α_c are much smaller than for α_b , and the background contribution α_{bg} is no longer negligible. For the analysis it is assumed that α_{bg} is purely phononic and follows a T^3 behavior in the relevant temperature range. The estimation of α_{bg} was done by subtracting a function cT^3 from all curves, and optimizing c to get a good description for all field values. The best results were obtained with $\alpha_{bg} = 1.5 \cdot 10^{-10} T^3 / K^4$, the resulting curve is plotted as a solid line in Fig. 7.8a.

The rest of the analysis was done like for α_b . The resulting fit parameters are listed in Tab. 7.3. Fig. 7.9 shows the derived energy gap and the pressure dependence of the energy gap vs. magnetic field. The values of Δ are in excellent agreement for both measurement directions, and show a linear field dependence.

The pressure dependence of the energy gap $\frac{\partial \ln(\Delta)}{\partial p_i}$, however, shows a different behavior for both measurement directions. For α_b , $\frac{\partial \ln(\Delta)}{\partial p}$ decreases from 4.7%/GPa at 0 T to 3%/GPa at 14 T, whereas for α_c an decrease from -1.2%/GPa at 0 T to -3.6%/GPa at 14 T is observed, very similar to the decrease observed for α_b . Fig. 7.10a shows the temperature-dependent thermal expansion α_b with $H \parallel b$ for magnetic fields up to 8 T. Here, the behavior of the Schottky contribution is totally different to that observed for $H \parallel c$. For small fields ($H \leq 3$ T) no effect is observed within the experimental resolution. For higher fields the peak is suppressed, and disappears completely for $H = 8$ T. The temperature of the maximum only weakly shifts to higher temperature. Because of the decreasing size of the Schottky peak, the uncertainty of the determination of the energy gap increases, as shown by the error bars. For a magnetic field of 10 T applied along the b direction a new anomaly arises with a maximum at 10 K. This peak shifts to higher temperatures with further increasing field, and develops a more complex structure. The new anomaly is caused by the spin-flop transition and can be better analyzed by measurements of the magnetostriction.

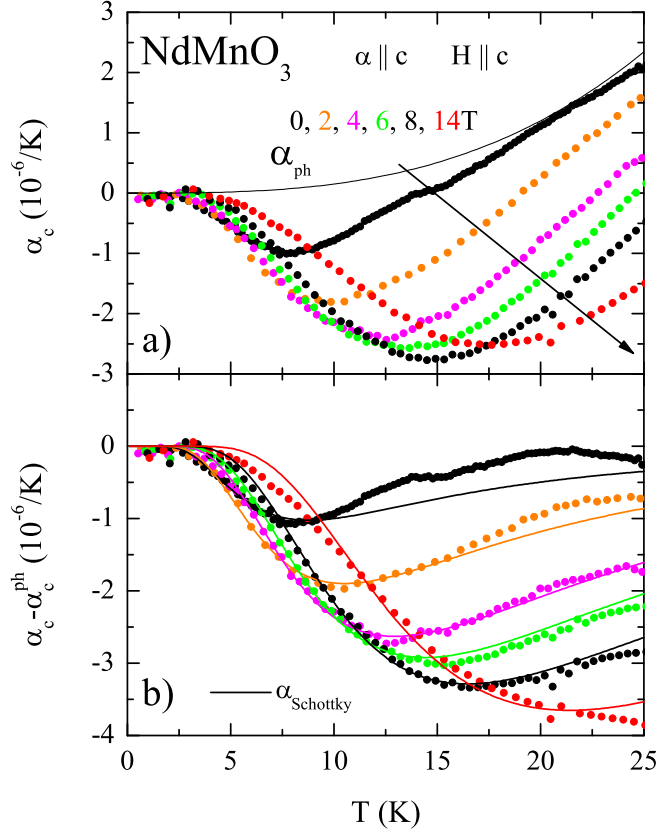


Figure 7.8.: a) Thermal expansion of NdMnO₃ along the c axis for $H \parallel c$. The solid line shows the estimated phononic background contribution. b) Calculated thermal expansion consisting of the sum of the Schottky and the phononic contribution.

7.4.3. Magnetostriction

The additional effects for $H \geq 8$ T can also be nicely seen in magnetostriction measurements. Here, the temperature is kept fixed, and the relative length change of the sample $\Delta L/L$ is measured while the magnetic field is changed with a constant rate of 100 mT/min. The resulting curves for $T = 5, 10, 15$, and 20 K are shown in Fig. 7.11. No hysteresis effects were observed, and therefore only the measurements with increasing field are shown. At 5 K the anomaly is located between 9 and 11 T, which corresponds to the spin-flop transition observed in the magnetization for $H \parallel b$ (see Fig. 7.4). The transition itself shows an unusual structure. There are presumably given by two peaks, a broader one with a negative sign, and a sharp peak with positive sign. The latter peak is located at a slightly higher field, causing an asymmetric shape of the curve. This "double-peak" structure remains present when the temperature is increased. However, the transition field increases faster for the broad peak with the negative sign. This leads to a nearly symmetric structure at 10 K, whereas at 20 K the peak with the positive sign occurs clearly at a lower field value. At 40 K only the peak with the negative sign is visible, and the onset of the downturn of the broader peak. The reason for these additional structures is unclear up to now. We can not exclude that the complex behavior of the magnetostriction is caused by a torque effect, which could be different below

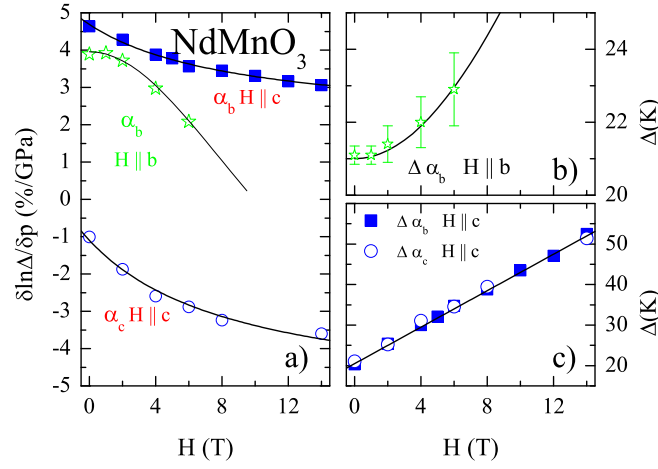


Figure 7.9.: Results of the analysis of the Schottky contribution to α in NdMnO₃. a) Pressure dependence of the energy gap vs. H . b) Energy gap vs. H . Lines are fits, see text.

and above the spin-flop transition.

In order to get a measure of the temperature dependence of the spin-flop transition, in the inset of Fig. 7.11a the peak position of the sharp peak is plotted versus temperature⁴. The observed temperature dependence is unexpected. Conventionally, the spin-flop field decreases with increasing temperature. From the almost linear behavior a zero-temperature spin-flop field of $H_{\text{SF}}^{0\text{T}} = 9.5$ T can be extracted. The spin-flop transition will be treated quantitatively in Sec. 7.4.5

	α_c $H \parallel c$		α_b $H \parallel c$		α_b $H \parallel b$	
H (T)	Δ (K)	$\frac{\partial \ln(\Delta)}{\partial p}$ (%/GPa)	Δ (K)	$\frac{\partial \ln(\Delta)}{\partial p}$ (%/GPa)	Δ (K)	$\frac{\partial \ln(\Delta)}{\partial p}$ (%/GPa)
0	20.3	4.6	21.1	1.0	21.1	3.9
1					21.1	3.9
2	25.4	4.3	25.2	1.9	21.4	3.7
4	30.0	3.9	31.1	2.6	22.0	3.0
5	32.1	3.8				
6	34.8	3.6	34.6	2.9	22.9	2.1
8	38.8	3.5	39.5	3.2		
10	43.5	3.3				
12	47.1	3.2				
14	52.0	3.1	51.4	3.6		

Table 7.3.: Fit-parameters for the Schottky contribution of NdMnO₃.

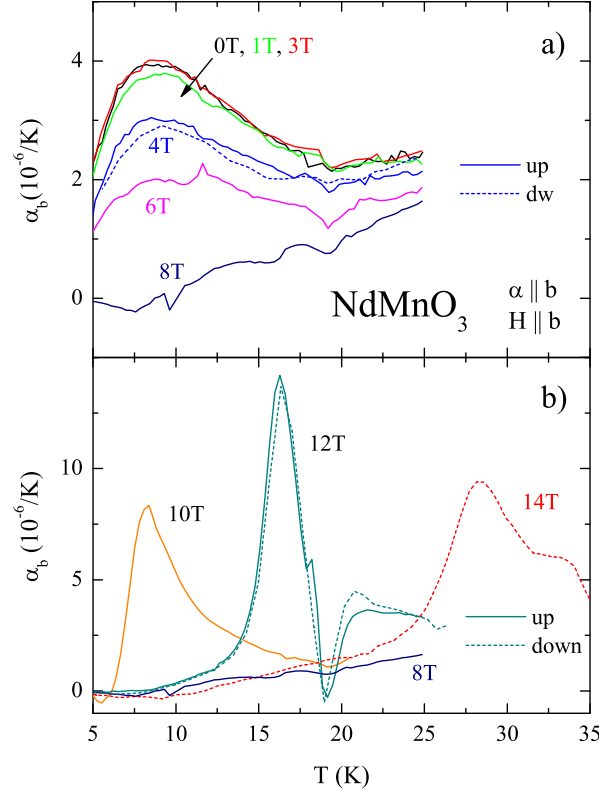


Figure 7.10.: Thermal expansion α_b of NdMnO_3 for $H \parallel b$. Panel a) shows the measurements up to 8 T, panel b) from 8 T to 14 T. For 14 T only a measurement with decreasing field was performed.

7.4.4. Analysis: Thermal Expansion and Susceptibility

In this section a combined analysis of the thermal expansion and of the magnetization measurements at 5 K from Ref. [55] will be presented⁵. The different directions have to be treated differently. The splitting of the Nd ground state doublet is determined by two parameters: The external magnetic field H_i and the exchange interaction $J_i^{\text{Mn-Nd}}$, with $i = a, b, c$. The external field H_i causes a linear term

$$\Delta(H_i) = g_i^{\text{Nd}} H_i \quad (7.6)$$

of the energy splitting⁶. Note, that Eq. 7.6 is only valid if the energy splitting of the ground state doublet is small in comparison to the energy of the first excited doublet ($\Delta_{D2} \approx 200$ K).

To take into account the exchange interaction, usually a mean-field approximation is used. Therefore one approximates Eq. 7.1 by replacing all terms acting on a spin i by a term

$$\mathcal{H}_{\text{MF}} = J \langle S \rangle \mathbf{S}_i, \quad (7.7)$$

⁴The result would hardly change if we define T_{SF} otherwise.

⁵The following calculations are performed in cgs units, with the convention $10^4 \text{ G} = 1 \text{ T}$. Energies will be given in Kelvin, and the magnetization is units of $\mu_B/\text{f.u.}$ (f.u. = formula unit).

⁶We restrict the analysis to the main axes, so only the main axes components of the g tensor are needed. In the following g_i always means the g factor of the ground state Nd doublet for $H \parallel i$.

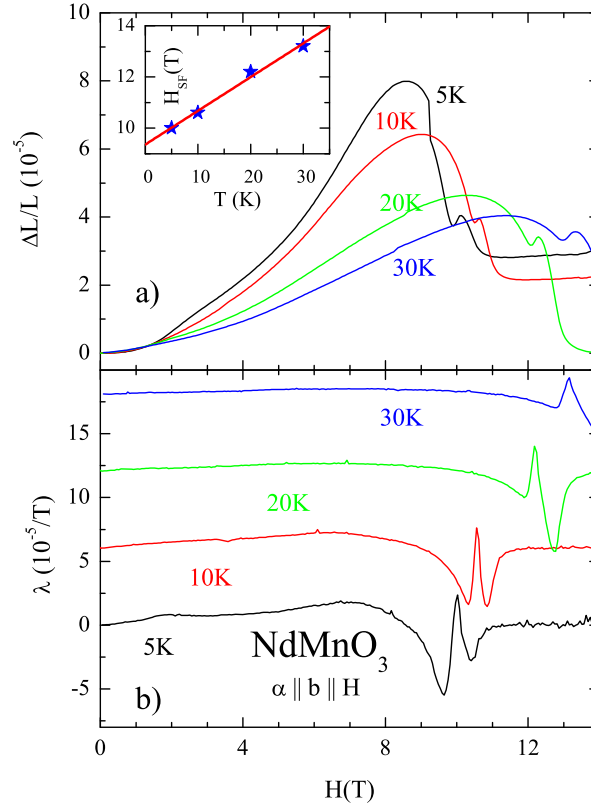


Figure 7.11.: Magnetostriction of NdMnO₃ along the b direction with $H \parallel b$ for $T = 5, 10, 20$, and 30 K. a) Relative length change $\Delta L/L$. b) $\lambda = \partial(\Delta L/L)/\partial H$. Inset: Estimated H_{SF} vs. T with a linear fit.

where $\langle S \rangle$ is the (constant) mean field, written as an expectation value $\langle S \rangle$. In contrast to an external field the exchange interaction only acts on the spin [303]. To simplify the model we introduce, however, an effective exchange field

$$H_c^{\text{ex}} \sim J \langle S \rangle \quad \Rightarrow \quad \mathcal{H} = H_c^{\text{ex}} \cdot g\mu_B(L_z + 2S_z) \quad (7.8)$$

which is treated like an external magnetic field. An external field causes a linear splitting of degenerate energy levels (Zeeman effect). Therefore, the use of an exchange field to model the exchange interaction is only a good approximation, if the exchange interaction has also a linear effect with respect to the magnetic field. The advantage of the use of an exchange field is that the total effective field can be obtained by a vector addition of the different components.

Field Direction $H \parallel b$

Fig. 7.12a illustrates the situation for $H \parallel b$. Here, we restrict the analysis to fields below the spin-flop transition (the spin-flop transition will be analyzed in Sec. 7.4.5). The exchange field along the c direction is proportional to $M_{0,c}^{\text{Mn}} \equiv M_0$ and can be written as

$$H_c^{\text{ex}} = \tilde{c}M_0 = \frac{\Delta_0 k_B}{g_c \mu_B} \quad (7.9)$$

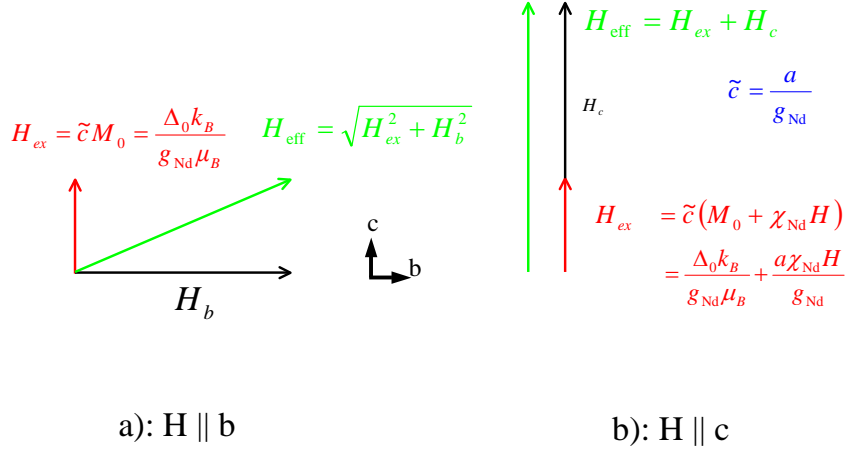


Figure 7.12.: Calculation of the total effective field. a) $H \parallel b$ b) $H \parallel c$.

We assume that the exchange field is not changed by a magnetic field along b . The argument herefore is that the energy gain and loss of the two sublattices of the AFM exactly cancel⁷. It follows that the total effective field is given by

$$H_{\text{eff}} = \sqrt{(H_c^{\text{ex}})^2 + H_b^2}. \quad (7.10)$$

For the calculation of the susceptibility with the CFT Mathematica [36] package the crystal field parameters A_k^m are required⁸. To my knowledge, there are no such investigations available in the literature for NdMnO_3 . However, as shown in Sec. 2.4, the CF is not so much different for different NdAO_3 compounds, and therefore the A_k^m parameters of NdGaO_3 from Ref. [48] will be used. We will refer to this result as the CF calculation.

Since $\vec{M}^{\text{Mn}}(H_b)$ points along the c direction, $M_b(H_b)$ is solely determined by the Nd susceptibility. First H_c^{ex} was determined by adjusting the field $\mathbf{H} = (0, 0, H_c^{\text{ex}})$ to produce the ground state splitting $\Delta_0 \approx 20$ K. This yields $H_c^{\text{ex}} = 12$ T. The magnetization $M_b(H_b)$ was calculated by using the field $\mathbf{H} = (0, H_b, H_c^{\text{ex}})$. The result of this calculation is shown as a dashed line in Fig. 7.13a. The principal behavior of $M_b(H_b)$ is described well. However, the calculated values underestimate the data by a factor ≈ 1.5 in the whole investigated field range. We conclude that the use of the CF parameters from NdGaO_3 gives only a qualitative description of $M_b(H)$. Note, that the use of the magnetization data to adopt the CF parameters is not useful, since we have to deal with 15 CF parameters, and do not know the real level scheme of NdMnO_3 .

$M_b(H)$ is given by the sum of the contribution of the localized spins and a van Vleck contribution. We perform a model calculation similar to that of Ref. [55], where both contributions are treated independently (this analysis will be called TM for thermal expansion /magnetization). In reality, however, both parameters are determined by the same Hamiltonian, Eq. 2.21. The usual Brillouin function [16] describing the magnetization of a doublet in a magnetic field

⁷This is only valid for $T = 0$. Because of $5 \text{ K} \ll T_N$ the parallel susceptibility is negligible.

⁸For the calculation of M the 4 R sites in a unit cell have in principle to be treated separately, see Sec. 2.4. However, it turned out that all sites give the same contribution to M for the regarded cases.

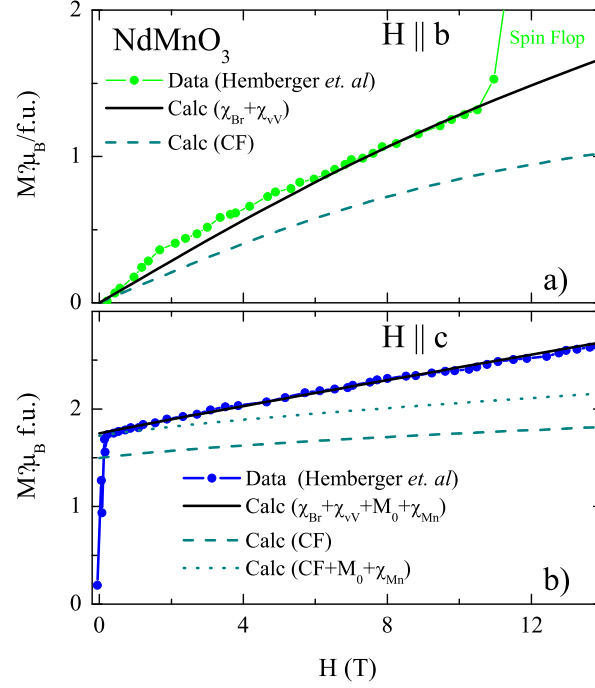


Figure 7.13.: Magnetization $M(H)$ of NdMnO₃ from Ref. [55] and different model calculations, see text. a) $H \parallel b$. b) $H \parallel c$.

can be obtained by starting with the potential

$$\Phi(H) = -k_B T \cosh\left(\frac{\Delta(H)}{2T}\right), \quad (7.11)$$

and calculating

$$M(H) = -\frac{\partial \Phi(H)}{\partial H}. \quad (7.12)$$

To calculate $M_b(H_b)$ one has to use the field-dependent energy gap $\Delta(H_b)$. From Eqs. 7.10 and 7.9 it follows:

$$\Delta(H_b) = \sqrt{\Delta_0^2 + \frac{g_b^2 H_b^2 \mu_B^2}{k_B^2}}. \quad (7.13)$$

The resulting magnetization reads:

$$M_b(H) = \frac{g_b^2 H_b \mu_B \tanh\left(\sqrt{\frac{\Delta_0^2 + g_b^2 H_b^2 \mu_B^2}{k_B^2}} / 2T\right)}{2k_B \sqrt{\Delta_0^2 + \frac{g_b^2 H_b^2 \mu_B^2}{k_B^2}}} + \chi_b^{\text{vV}} \cdot H_b. \quad (7.14)$$

Therefore three parameters determining $M(H)$: Δ_0 , the g factor, and the van Vleck susceptibility χ_b^{vV} . The determination of the parameters is done as follows: First the g factor is fixed by fitting Eq. 7.13 to the $\Delta(H_b)$ curve derived from the thermal expansion data. The result of this fit is shown in Fig. 7.9c and yields the value $g_b = 2.3$. The uncertainty of this fit is rather

$H \parallel b$			$H \parallel c$				
g_b	χ_b^{vV} ($10^{-6}/\text{G}$)		g_c	χ_c^{vV} ($10^{-6}/\text{G}$)	M_0 ($\mu_B/\text{f.u.}$)	χ_{Mn} ($10^{-6}/\text{G}$)	a (10^5G)
TM	TS		1.5	0.0	1.0	6.2	3.0
		1.7	1.7	1.5	0.65	3.6	4.6
			2.0	3.0	0.33	1.4	9.4
		2.3	2.3	4.0	0.10	0.4	28
			2.5	4.5	0.0	0.0	78
CF	2.5	0.62	CF	2.55	1.6	0.2	0.8
			EM	2.2		0.65	2.5
							4.7

Table 7.4.: Parameters for the susceptibility analysis in NdMnO_3 . TM: Combined analysis thermal expansion / magnetization. CF: Analysis using the crystal field program. EM: Analysis using single-site energy minimization.

large because of the large uncertainty of the determination of $\Delta(H_b)$ from the small Schottky peaks in α_b . Performing the fit with the upper and lower boundaries of the error bars of $\Delta(H_b)$ the values $g_b = 1.7$ and $g_b = 2.9$ are obtained. Using Eq. 7.14, χ_b^{vV} is determined by fitting the magnetization data. Fig. 7.13 shows the result for $g_b = 2.3$ which gives a good description of the data. The results for the other g values are not shown since the resulting $M_b(H)$ is nearly the same. In Tab. 7.4 the resulting parameters are listed. From the results of the CF calculation we can also extract a g factor and a van Vleck contribution, also listed in Tab. 7.4. The comparison of both methods shows that the g factor is the same within the resolution of the TM method. The main difference is, that the Schottky contribution calculated with the CF method is about an order of magnitude too small to explain the magnetization. A possible origin of this discrepancy is a lower lying first excited doublet, leading to a larger admixture of the excited states and a higher van Vleck contribution.

Field Direction $H \parallel c$

The determination of $M_c(H)$ is more complex. First, the field-dependent magnetic moment of the Mn ions gives an additional contribution

$$M_{c,\text{Mn}}(H_c) = M_0 + \chi_{\text{Mn}} H_c \quad (7.15)$$

to the magnetization. Second, the field dependence of $M_{c,\text{Mn}}(H)$ leads to a field-dependent exchange field $H_c^{\text{ex}}(H)$. Here, the exchange field and the applied field H_c add, since they point in the same direction. The calculation of $M_{c,\text{Nd}}$ with the CF program is similar to the b direction. The zero field splitting is described by $(0, 0, H_{\text{ex}}^c) = 12 \text{ T}$. If a magnetic field of $H_c = 14 \text{ T}$ is turned on, the calculation gives a gap of 45 K. The difference to the observed gap of 52 K is due to the enhancement of the exchange splitting. This can be included and the field dependence of the energy gap is described by the field

$$\mathbf{H} = (0, 0, 12 \text{ T} + H_c + \tilde{g} H_c) \quad (7.16)$$

with $\tilde{g} = 0.50$. From the resulting Nd magnetization we can determine the Mn contribution with $M_0^{\text{Mn}} = M_c^{\text{meas}}(0T) - M_c^{\text{Nd}} = 0.22$ and $\chi_{\text{Mn}} = \frac{M_0 \cdot \tilde{g}}{14T} = 0.8 \cdot 10^{-6}/\text{G}$. The resulting $M_c(H)$ is shown in Fig. 7.13b. Again, the principle behavior is described correct, but the increase of the calculated magnetization is too small.

Therefore we will also calculate $M_c(H)$ as we have done for $H \parallel b$. The field dependence of the energy gap can be written as

$$\Delta(H_c) = \frac{\mu_B}{k_B} (aM_0 + a\chi_{\text{Mn}}H + g_{\text{Nd}}H) \quad (7.17)$$

where a denotes the Nd-Mn exchange coupling constant, M_0 the weak ferromagnetic moment of the Mn moments in zero field, $\chi_{\text{Mn}}H$ the field-dependent part of the WF moment, and $g_{\text{Nd}} \equiv g_c$ the g factor of Nd along the c direction. The value $a \cdot M_0 = \Delta_0 \frac{k_B}{\mu_B} = 3.1 \cdot 10^5 \text{ G}$ is calculated from Eq. 7.17, using $\Delta_0 = 20.5 \text{ K}$ from the zero-field thermal expansion. From the derivative of Eq. 7.17 and the field dependence of the gap $\Delta(H_c)$ we obtain $a\chi_{\text{Mn}} + g_c = \frac{k_B}{\mu_B} 2.25 \cdot 10^{-4} = 3.35$. The total magnetization along the c direction is calculated via Eq. 7.12 [55], leading to:

$$M_c(H) = M_0 + M_0^{\text{vV}} + \frac{1}{2}g_c \tanh\left(\frac{\Delta(H_c)}{2T}\right) + (\chi_{\text{Mn}} + \chi_c^{\text{vV}})H_c. \quad (7.18)$$

χ_c^{vV} is the van Vleck term of Nd for $H \parallel c$. Using the magnetization data we find:

$$M_b(0) = 1.75 \mu_B / f.u. = M_0 + M_0^{\text{vV}} + \frac{1}{2}g_c \tanh\left(\frac{20.5 \text{ K}}{2 \cdot 5 \text{ K}}\right) \quad (7.19)$$

$$M_b(14\text{T}) = 2.65 \mu_B / f.u. = M_0 + M_0^{\text{vV}} + \frac{1}{2}g_c \tanh\left(\frac{52 \text{ K}}{2 \cdot 5 \text{ K}}\right) + \chi_c^{\text{vV}} \cdot 14\text{T}. \quad (7.20)$$

for the spontaneous magnetization⁹ for $H \rightarrow 0$ and $H = 14 \text{ T}$. The van Vleck contribution is linear in the total effective field and is calculated by

$$\chi^{\text{vV}}(H) = \tilde{v} \left(\frac{a\chi_{\text{Mn}}}{g_c} H_c + H_c \right) \quad (7.21)$$

and

$$M_0^{\text{vV}} = \tilde{v} \frac{\Delta_0 k_B}{\mu_B g_c}. \quad (7.22)$$

The Eqs. 7.19 - 7.22 are fully determined, if one of the parameters a , M_0 , \tilde{v} , χ_{Mn} , or g_{Nd} is known. We take g_c as a free parameter and calculate the other parameters by solving the given equation system. The reasonable range of g_c is limited by two conditions: If g_c is too small, M_0 would become negative, and if g_c is too large χ^{vV} would become negative. The results for the different g_c are listed in Tab. 7.4.

Another starting point to tackle the problem is to consider the single-site energy (referred as EM for energy minimization). In LaMnO₃ and PrMnO₃ the value $M_0 \approx 0.1 \mu_B / f.u.$ is observed [55], which is due to the DM interaction. The DM interaction is presumably almost the same in PrMnO₃ and NdMnO₃. In NdMnO₃, however, one has to take into account that the system can gain additional energy by the splitting of the Nd ground state due to the Nd-Mn exchange interaction. It follows from $J_{\text{Nd-Mn}} \sim M_0$ that a further canting of the

⁹For small fields domain formation occurs. Therefore we take the linear extrapolation of $M_c(H)$, $H > 0.1 \text{ T}$ for $H \rightarrow 0$.

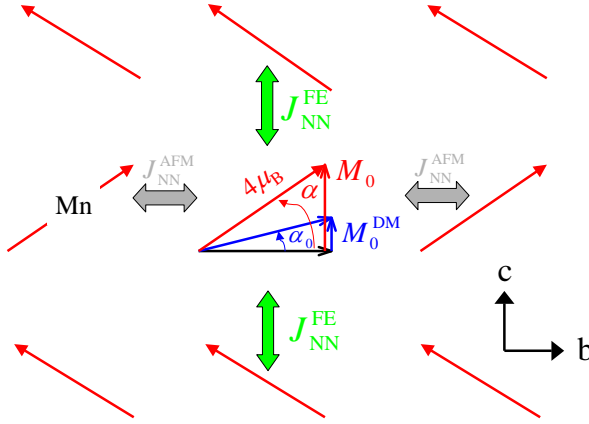


Figure 7.14.: Schematic picture of the Mn spins of NdMnO₃ in the *cb* plane.

Mn spins is favorable. For the calculation the relevant energies will be parameterized by the Mn canting angle α , see Fig. 7.14. Here, only $J_{\text{NN}}^{\text{AFM}}$, the DM interaction, and the single-ion anisotropy are taken into account. The latter term is not known for NdMnO₃, so we take the value $\Lambda = 0.9 \text{ K}$ from PrMnO₃ [304]. However, the result is only slightly influenced by the values of Λ . The energy per Mn site for small angles α is given by

$$E_{\text{ex,DM}}(\alpha) = -E_0 \cos(2\alpha) - 2D \sin(\alpha) - \Lambda[2 \cos(\alpha)]^2 \quad (7.23)$$

with

$$E_0 = 2 \cdot 2 \cdot J\langle S \rangle = 112 \text{ K}. \quad (7.24)$$

Here, we use $\langle S \rangle = S^2 = 4$ and $J_{\text{NN}}^{\text{AFM}} = 7 \text{ K}$ from PrMnO₃ [304]. This is reasonable, since $J_{\text{NN}}^{\text{AFM}}$ does not change much with R (see Tab. 7.1). The first factor 2 takes the coordination number $z = 2$ along the c direction into account. The second factor 2 is needed because of the definition of J in Eq. 7.1. Assuming $M_0 = 0.1 \mu_B$, we can calculate $\alpha = \arctan(0.1/4)$ and D by finding the minimum of Eq. 7.23. via the condition $\partial E(\alpha)/\partial \alpha = 0$. As a result we obtain $D = 5.7 \text{ K}$. In the next step we include the Zeeman energies of the Nd and Mn spins, the exchange, and the single-ion anisotropy interactions which yields:

$$E_{\text{tot}}(\alpha, H_c) = -E_0 \cos(2\alpha) - 2D \sin(\alpha) - \frac{\mu_B}{k_B} M_{\text{Mn}}(\alpha) H_c - \frac{g_c \mu_B}{2k_B} H_c - E_{\text{ex}}(\alpha) - \Lambda[2 \cos(\alpha)]^2 \quad (7.25)$$

with

$$M_{\text{Mn}}(\alpha) = g_{\text{Mn}} S_{\text{Mn}} \sin(\alpha) = 4 \sin(\alpha) \quad (7.26)$$

$$E_{\text{ex}}(\alpha) = \frac{\mu_B a}{2k_B} M_{\text{Mn}}(\alpha). \quad (7.27)$$

For $H = 0$ we know the energy gain due to the exchange coupling:

$$E_{\text{ex}}^{H=0} = \frac{\mu_B a}{2k_B} M_0 = \Delta_0/2 = 10.3 \text{ K} \quad (7.28)$$

The minimization of Eq. 7.25 is now straightforward: First $\partial E_{\text{tot}}(\alpha)/\partial \alpha = 0$ is solved for $H = 0$ under the additional condition Eq. 7.28, yielding the values for M_0 , α_0 and a . Then Eq. 7.25 is minimized again for a field $H_c^f > 0$, yielding the values M_f and α_f . Then, χ_{Mn} is calculated by

$$\chi_{\text{Mn}} = (M_f - M_0)/H_f. \quad (7.29)$$

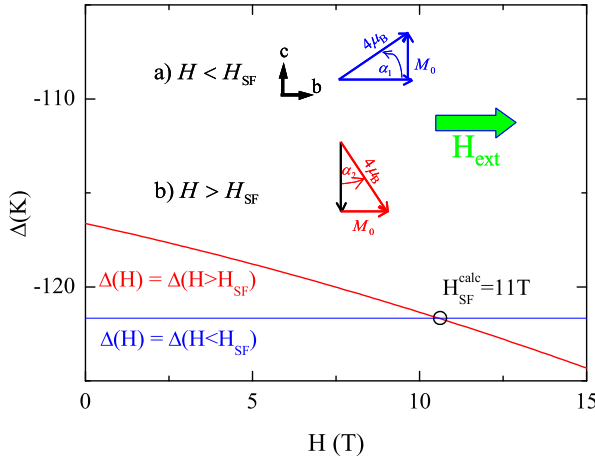


Figure 7.15.: Calculation of the spin flop field in NdMnO₃.

Finally, g_c is calculated from Eq. 7.17 (setting $H_c = 0$). The resulting values are listed in Tab. 7.4 in the line termed EM.

A comparison of the different results shows, that a unique set of parameters cannot be established. Comparing the results from TM and EM, the TM results with smaller g values give a better agreement with the other parameters. The g factor from CF is too large, which is presumably caused by the difference of the CF of NdMnO₃ to the used CF parameters from NdGaO₃. We suspect, that the van Vleck contribution coming from the CF calculation is also too small, even if the discrepancy is not as large as in the $H \parallel b$ configuration.

7.4.5. The Spin-Flop Transition

In a simple antiferromagnet with uniaxial anisotropy a spin-flop transition occurs when the field is applied parallel to the spins. The reason is, that the energy gain through the canting in the field is larger than the uniaxial anisotropy energy. In NdMnO₃ the situation is more complex, but the idea is the same: one has to compare the energies of both phases. Herefore we adapt Eq. 7.25 for $H \parallel b$ in the following cases:

- $H < H_{\text{SF}}$: This is the situation shown in Fig. 7.15a. The angle $\alpha_1 = 8^\circ$ is determined by the previously calculated zero-field canting due to the DM interaction. Since we assume that the spin canting is parallel to the c direction, the magnetic field term cancels. Further we do not include the Nd Zeeman term, since it is the same for both phases.
- $H > H_{\text{SF}}$: This is the situation shown in Fig. 7.15b. Here, the DM term cancels, since the spin canting has no c component. The sine of the single-ion anisotropy has to be replaced by a cosine in the chosen angle parameterization. The angle $\alpha_2 H_b = 8.9^\circ + (3.9 \cdot 10^{-5})^\circ/\text{G}$, which depends on the magnetic field, has been calculated according to the previous section, with the same modifications used in Eq. 7.30. We assume, that the Mn-Nd exchange constant a is isotropic and end with the following equations:

$$\Delta^{H < H_{\text{SF}}}(H_b) = -E_0 \cos 2\alpha_1 - 2D \sin(\alpha_1) - \frac{\mu_B a}{2k_B} \cdot M_0 - \Lambda[2 \cos(\alpha_1)]^2 \quad (7.30)$$

$$\Delta^{H > H_{\text{SF}}}(H_b) = -E_0 \cos 2\alpha_2 - \frac{4\mu_B}{k_B} \sin(\alpha_2) H_b - \frac{\mu_B a}{2k_B} \cdot M(\alpha_2) - \Lambda[2 \sin(\alpha_2)]^2 \quad (7.31)$$

In Fig. 7.15 the calculated values are shown. The term for $H < H_{\text{SF}}$ gives a constant offset. The term for $H > H_{\text{SF}}$ starts at a higher value but has a negative slope. The value $\Lambda = 0.9 \text{ K}$ is taken from PrMnO_3 [304]. The intersection of the curves gives the spin-flop field of $H_{\text{SF}} = 11 \text{ T}$. This is in a good agreement with the expected zero-temperature spin-flop field of $\approx 9.5 \text{ T}$ (see Sec. 7.4.2).

These considerations are only valid for $T = 0$. For larger temperatures, thermal activation becomes important. In this case we expect a decrease of the angles α_i . Furthermore the parallel susceptibility of the Mn is no longer negligible, and the spontaneous moment M_0 will change. The unusual temperature dependence of T_{SF} is likely to result from the complex interplay of the different parameters.

7.4.6. Uniaxial Pressure Dependences

In this section the measured uniaxial pressure dependences of the energy gap (shown in Fig. 7.9) will be analyzed quantitatively.¹⁰

Uniaxial Pressure Dependence: $H \parallel b$

For $H \parallel b$ the field dependence of the energy gap is given by Eq. 7.13. We restrict the analysis to the field range below the spin-flop transition. The uniaxial pressure dependence for the energy gap along the b axis is given by

$$\frac{\partial \ln(\Delta(H_b))}{\partial p_b} = \frac{\Delta_0 \frac{\partial \Delta_0}{\partial p_b} + \frac{2\mu_B^2 g_b}{k_B^2} \frac{\partial g_b}{\partial p_b} \cdot H_b^2}{\Delta_0^2 + \frac{\mu_B^2 g_b^2}{k_B^2} \cdot H_b^2} \quad (7.32)$$

This function depends on Δ_0 and g_b , which we calculated, and on the pressure dependences $\Delta_0/\partial p_b$ and $\partial g_b/\partial p_b$. Fig. 7.9 shows a fit of Eq. 7.32 to the measured uniaxial pressure dependence. The data are described very well by the fit. The resulting uniaxial pressure dependences are $\partial \Delta_0/\partial p_b = 4 \text{ \%/GPa}$ and $\partial g_b/\partial p_b = -7.4 \text{ \%/GPa}$.

		A (G/GPa)	B (10^{-7} /GPa)	aM_0 (10^5 G)	$a\chi_{Mn} + g_c$ ()	$\frac{\partial \ln(\Delta_0)}{\partial p_i}$ %/GPa
α_b	$H \parallel c$	0.144	6.8	3.1	3.35	4.7
α_c	$H \parallel c$	-0.035	-18	3.1	3.35	-1
		$\Delta_0 \frac{\partial \Delta_0}{\partial p_b}$ ($10^{-4} \text{ K}^2/\text{GPa}$)	$\frac{2\mu_B^2 g_b}{k_B^2} \frac{\partial g_b}{\partial p_b}$ ($10^{-14} \text{ K}^2/\text{G}^2 \text{ GPa}$)	Δ_0^2 (K^2)	$\frac{\mu_B^2 g_b^2}{k_B^2}$ ($10^{-8} \text{ K}^2/\text{G}^2$)	$\frac{\partial \ln(\Delta_0)}{\partial p_b}$ %/GPa
α_b	$H \parallel b$	1.7	-1.8	441	2.4	4.0

Table 7.5.: Parameters of the analysis of the Schottky contribution in NdMnO_3 . For $H \parallel c$ the measurement direction i of α_i is either b or c .

¹⁰In the following H_b (H_c) means a field in b (c) direction, respectively.

Uniaxial Pressure Dependence: $H \parallel c$

For $H \parallel c$ the relative pressure dependence of the gap is given by

$$\frac{\partial \ln \Delta(H_c)}{\partial p_i} = \frac{\frac{\partial a}{\partial p_i} M_0 + a \cdot \frac{\partial M_0}{\partial p_i} + \left(\frac{\partial a}{\partial p_i} \cdot \chi_{\text{Mn}} + a \cdot \frac{\partial \chi_{\text{Mn}}}{\partial p_i} + \frac{\partial g_{\text{Nd}}}{\partial p_i} \right) \cdot H_c}{a M_0 + (a \chi_{\text{Mn}} + g_{\text{Nd}}) \cdot H_c} \equiv \frac{A + B \cdot H_c}{a M_0 + (a \chi_{\text{Mn}} + g_{\text{Nd}}) \cdot H_c} \quad (7.33)$$

with

$$A = \frac{\partial a}{\partial p_i} \cdot M_0 + a \cdot \frac{\partial M_0}{\partial p_i} \quad [\text{G/GPa}] \quad (7.34)$$

$$B = \frac{\partial a}{\partial p_i} \cdot \chi_{\text{Mn}} + a \cdot \frac{\partial \chi_{\text{Mn}}}{\partial p_i} + \frac{\partial g_{\text{Nd}}}{\partial p_i} \quad [1/\text{GPa}] \quad (7.35)$$

and $i = b, c$. The parameters A and B are obtained by fitting the $\frac{\partial \ln(\Delta)}{\partial p_i}(H_c)$ curves. The fits are shown as solid lines in Fig. 7.9 and yield a good description for $\alpha_{b,c}$ with $H \parallel c$. For $H = 0$ the uniaxial pressure dependence of Δ_0 follows from Eq. 7.33:

$$\frac{\partial \ln \Delta_0}{\partial p_i} = \frac{A}{a M_0} \quad (7.36)$$

yielding the values $\partial \Delta_0 / \partial p_b = 4.7\%/\text{GPa}$ and $\partial \Delta_0 / \partial p_c = -1\%/\text{GPa}$. Because Δ_0 is independent of the field direction, the measurements with $H \parallel b$ and $H \parallel c$ should give the same result within the experimental uncertainty, which is the case.

The equations Eq. 7.34 and 7.35 contain five possible pressure dependent parameters. In Eq. 7.34 $\partial a / \partial p_i$ as well as $\partial M_0 / \partial p_i$ are presumably pressure dependent since these parameters are related to the structural distortion. Therefore it is not possible to further dissolve the Eqs. 7.34 and 7.35.

7.4.7. Specific Heat

For a quantitative analysis of κ the magnetic contribution C_m to the specific heat is needed [305, 306]. To determine C_m , the other contributions to C have to be subtracted. The background contribution C_{bg} in NdMnO₃ is given by acoustic and optical phonons as well as the Schottky specific heat of the Nd-doublet CF excitations. Because of $C_{\text{bg}} \gg C_m$, a calculation of C_{bg} with the required precision is difficult. Therefore we will use NdGaO₃ as a reference compound. From Sec. 2.1.6 we know that the crystal field splitting is presumably very similar in NdGaO₃ and NdMnO₃, except of the additional splitting of the ground state due to the Mn exchange field. Fig. 7.16a shows the specific heat of NdMnO₃ [307] and NdGaO₃ [22]. At high temperatures the curves are nearly identical showing that the phononic and Schottky contributions are indeed very similar for NdGaO₃ and NdMnO₃. Therefore we calculate

$$C_m = C(\text{NdMnO}_3) - C(\text{NdGaO}_3) - C_{\text{sch}}^{\Delta_0}. \quad (7.37)$$

The latter term is calculated by Eq. 7.5 and takes the additional splitting of the Nd ground-state doublet in NdMnO₃ into account. The resulting C_m is shown in Fig. 7.16a and with a logarithmic y scale in panel b). C_m monotonously increases up to T_N where the peak of the phase transition is visible. Above T_N , still a sizeable contribution of C_m is present which slowly decays. To check this analysis, we calculate

$$S_m(T) = \int_0^T \frac{C_m}{T} dT, \quad (7.38)$$

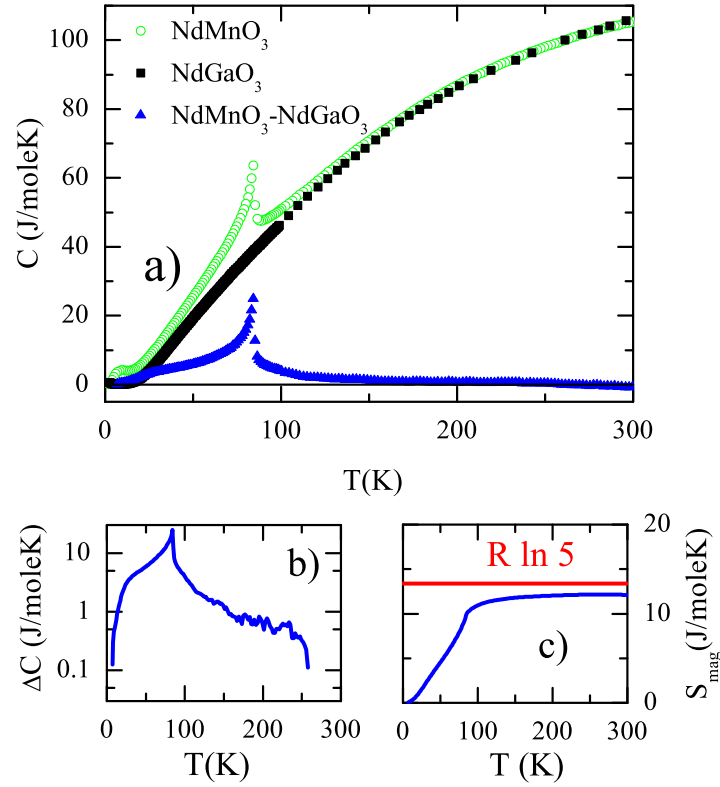


Figure 7.16.: a) Specific heat of NdMnO_3 , NdGaO_3 and extracted magnetic contribution. b) Magnetic contribution C_m to the specific heat in double-logarithmic scales. c) Calculated magnetic entropy. The line is the estimated total entropy of the Mn moments.

which is the magnetic entropy of the Mn moments. The total entropy of the Mn moments is given by $R \ln(2S + 1) = 13.4 \text{ J/MoleK}$, where R is the gas constant. This condition is well fulfilled as seen in Fig. 7.16c.

7.4.8. Thermal Conductivity of NdMnO_3 : Scattering by Magnetic Excitations

From Fig. 7.6 it is obvious that the observed sharp dip in κ is related to the Néel transition. The influence of the Néel transition on the thermal conductivity was investigated theoretically in Refs. [305, 306]. An additional scattering rate

$$\tau_m^{-1} = MT^2 C_m(T) \omega^4 \quad (7.39)$$

is derived, where M gives the scattering strength, and C_m is the magnetic specific heat of the system. Note, that fluctuations cause a sizeable contribution to C_m above T_N . Fig. 7.17a shows the thermal conductivity of NdMnO_3 in zero field. For the fit the scattering rate Eq. 7.39 was included in the Debye formula Eq. 2.5. The fit parameters are listed in Tab. 7.6. The fit gives an approximate description of the data for $T > T_N$. Below T_N a large increase of the fit occurs. Thus the anomalous high-temperature behavior of the thermal conductivity of NdMnO_3 can be explained by a strong suppression of the phononic κ due to scattering

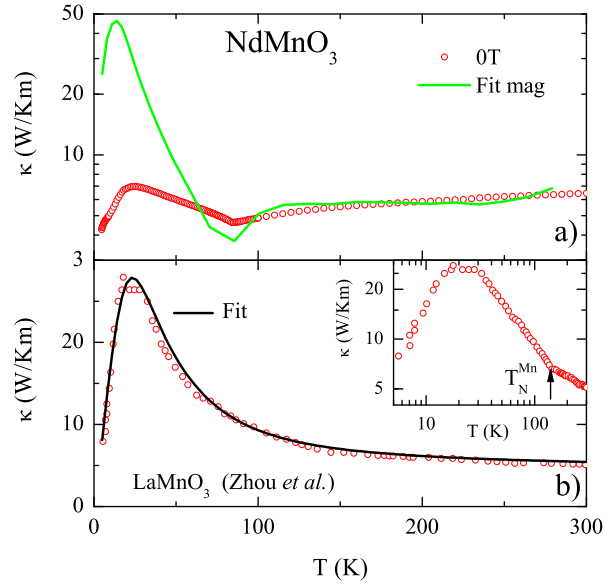


Figure 7.17.: a) Thermal conductivity κ_b of NdMnO₃. The solid line is a fit with the extended Debye model, see text. The y axis is shown on a logarithmic scale. b) Thermal conductivity of LaMnO₃ from Ref. [272] and fit. Inset: κ of LaMnO₃ on double-logarithmic scales.

by magnetic excitations of the antiferromagnetic ground state of Mn. This explains the decreasing temperature dependence from room temperature down to T_N^{Mn} and the following increase. Since at lowest temperatures the magnetic excitations freeze out, an restoration of κ is expected¹¹. The absence of the increase at low temperatures will be addressed in the next section.

For comparison, Fig. 7.17b shows the thermal conductivity of LaMnO₃ taken from Ref. [308]. In contrast to NdMnO₃ the anomaly at T_N^{Mn} is only very weak (see inset). The Debye fit applied without an additional scattering describes the data very well. This shows that the influence of the antiferromagnetic transition acts differently for the different compounds.

	$P [10^{-43} \text{ s}^3]$	$U [10^{-31} \text{ s}^2/\text{K}]$	u	$Ds [\text{s}]$	$\ell_{\min} [\text{\AA}]$	$M [10^{-41} \text{ m}^3 \text{ s}^3/\text{KJ}]$
LaMnO ₃	3.1	11.4	1	33	5.5	
NdMnO ₃	10	2.5	13	5	2.8	2.8

Table 7.6.: Fit parameter Debye fits for LaMnO₃ and NdMnO₃. The Debye temperature $\Theta_D = 600 \text{ K}$ was determined from the specific heat [55]. The sound velocity $v_s = 4200 \text{ m/s}$ was estimated with Eq. 2.10.

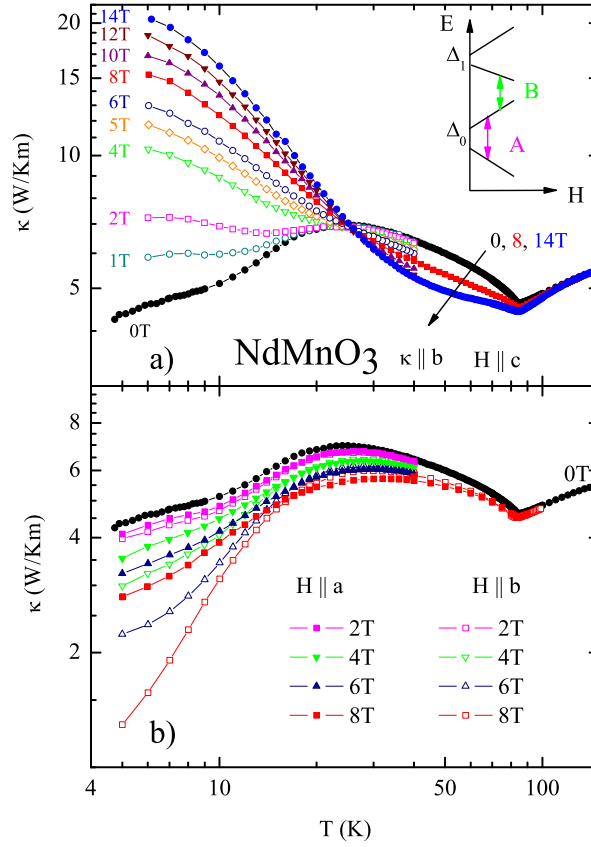


Figure 7.18.: a) Thermal conductivity of NdMnO_3 along the b axis in magnetic fields up to 14 T with $H \parallel c$. Inset: Schematic picture of the splitting of the Nd $4f$ moments in magnetic fields b) κ_b in magnetic fields up to 8 T with $H \parallel b$ and $H \parallel a$.

7.4.9. Thermal Conductivity of NdMnO_3 : Influence of Magnetic Fields

Fig. 7.18 shows the magnetic-field dependent measurements of κ of NdMnO_3 . All curves were obtained with one setup. The measurements for $H \parallel a$ and $H \parallel c$ were performed in a transverse-field cryostat. For these field directions, a Hall probe mounted close to the sample was used to orient the sample with respect to the magnetic field direction. This restricts the misalignment error to a few percent. Fig. 7.18a shows the data with $H \parallel c$ in fields up to 14 T. The influence of the magnetic field can be grouped into two regions: Below 25 K, κ monotonously increases with the field, causing a strong enhancement of κ at the lowest temperature. At $T \simeq 25$ K all curves intersect, and above this temperature κ is gradually suppressed by the field. This suppression is most pronounced around 50 K and is monotonously lowered at higher temperatures, but is still present at T_N^{Mn} . The field dependence at the lowest temperature (≈ 6 K) can be understood as follows: In zero-field, κ is suppressed by resonant scattering processes on the two-level system of the Nd ground-state multiplet with the splitting $\Delta_0 \approx 20$ K. From the thermal expansion with $H \parallel c$ we know, that the splitting $\Delta(H)$ strongly increases, up to ≈ 50 K at 14 T. This decreases the probability

¹¹Such a behavior is e.g. observed for $\text{GdFe}_3(\text{BO}_3)_4$, see Sec. A.3.

of the resonant processes and leads to an enhancement of κ with magnetic field. The large absolute values of κ at 14 T clearly show that the low zero-field values of κ are not related to a poor sample quality. This also shows that the scattering by the $4f$ moments is the dominant process at low temperatures.

The additional resonant scattering explains, why the quantitative calculation of the previous section is not able to explain κ below T_N . For all fields, κ is far below the fit shown in Fig. 7.17. In order to explain the observed field dependences at intermediate temperatures, the next excited doublet of Nd may also play a significant role. This could e.g. explain the sign change of the field dependence at $T \approx 35$ K: If the lower branch of the first excited doublet of the Nd comes close to the upper branch of the ground state doublet, scattering between these levels may become relevant (see the sketch in Fig. 7.18a. This process requires a thermal population of the states and is therefore not effective at low temperatures. However, the energy scheme of the first excited level is not known. Furthermore, it is not known how the phonon scattering by the magnetic excitations changes in a magnetic field. The consequence is that there are too many uncertainties for a more elaborated analysis.

Fig. 7.18b shows κ for the other field directions. In contrast to $H \parallel c$, κ is monotonously suppressed in the whole temperature range. The effect for $H \parallel a$ and $H \parallel b$ is almost the same. Below ≈ 20 K the suppression is stronger for $H \parallel b$. The gap Δ increases only weakly for $H \parallel b$. This would imply a weak increase of κ following the picture from above. Since this is not the observed behavior, another mechanism seems to be present. For $H \parallel b$, a possible origin is the presence of fluctuations as a precursor of the spin-flop transition. The onset of the spin-flop transition is visible in the magnetostriction already above 6 T, what supports this picture. However, data above 8 T are not available for this field-direction, so this is not clear. Furthermore, the thermal conductivity is also suppressed for $H \parallel a$, where no spin-flop occurs. Since the sample is weakly twinned [55], this could be a reason for the suppression along the a direction.

7.5. TbMnO_3

Before we will present the magnetic-field dependent measurements of κ , a short introduction into the phase diagram of TbMnO_3 will be given. TbMnO_3 is the first compound of the RMnO_3 series in which ferroelectricity is established over a large temperature and magnetic-field range. In Ref. [289] the phase diagram was explored via polarization and dielectric measurements. In zero field the polarization points along the c direction. A refined phase diagram based on thermal expansion measurements in Ref. [287] is shown in Fig. 7.19. In zero field, the system transforms from a paramagnetic phase into an incommensurate antiferromagnetic phase (HT-ICAFM) at $T_N = 41$ K. At $T_c = 27$ K, a transition into another incommensurate antiferromagnetic phase with a different propagation vector (LT-ICAFM) occurs. These phase boundaries are hardly magnetic-field dependent. For $H \parallel a$ and $H \parallel b$, the application of magnetic fields leads to a transition into a commensurate canted antiferromagnetic phase (CAFM), which is accompanied by a polarization flop from $P \parallel c$ to $P \parallel a$. The thermal-expansion measurements show that no direct transition from the HT-ICAFM to the CAFM phase occurs. Even at the highest fields, the system passes the LT-ICAFM phase. The main difference between $H \parallel a$ and $H \parallel b$ (above 10 K) is the much larger hysteresis of the LT-ICAFM \rightarrow CAFM transition for $H \parallel a$. The application of high magnetic fields along the c axis leads to a transition into a paraelectric canted AFM phase, instead of a polarization

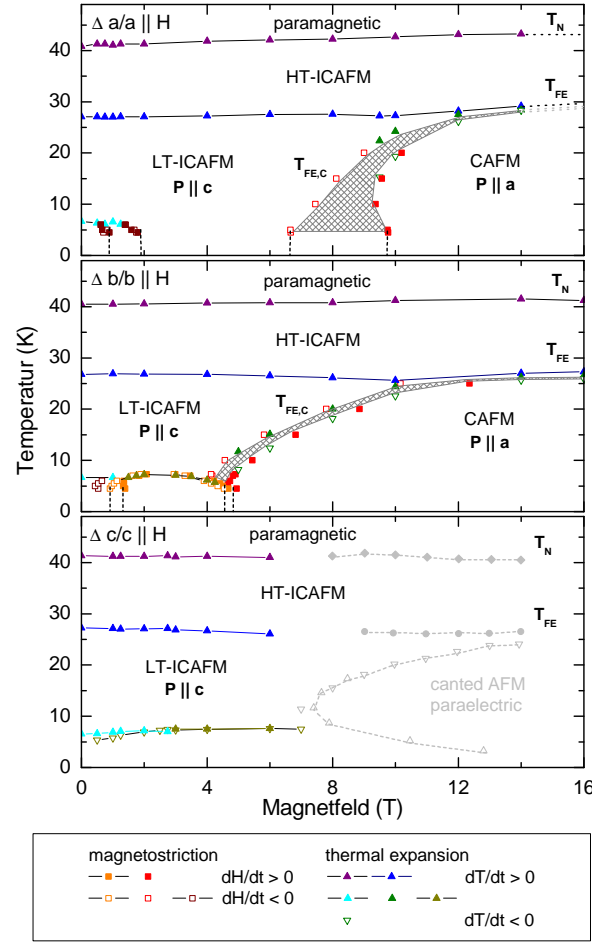


Figure 7.19.: $H - T$ phase diagram of TbMnO_3 derived from thermal expansion and magnetostriction [273, 291]. For $H||c > 8$ T the phase boundaries are taken from Ref. [289].

flop. Note that thermal expansion for $H \parallel c$ could only be measured for $H \leq 7$ T. Therefore the phase boundaries with $H > 8$ T shown in Fig. 7.19 are taken from Ref. [289].

For all magnetic field directions a very complex low-temperature and low-field behavior with various transitions is observed below 10 K. The reason for these effects is presumably the interplay of different interactions (Tb-Mn, Tb-Nd, etc.) which have similar energy scales. The details of these mechanisms are presently not understood. The thermal conductivity measurements below 10 K turned out to be very sensitive to these transitions. However, the present knowledge does not allow a detailed interpretation of this low-temperature behavior of κ . In this chapter only the results with $T \geq 10$ K will be discussed. The whole set of measurements is shown in the appendix (Sec. A.1).

7.5.1. Thermal Conductivity

Fig. 7.20 presents the thermal conductivity κ of TbMnO_3 along the b direction. In zero field, κ monotonously decreases from a value of 5 W/Km at room temperature down to a minimum

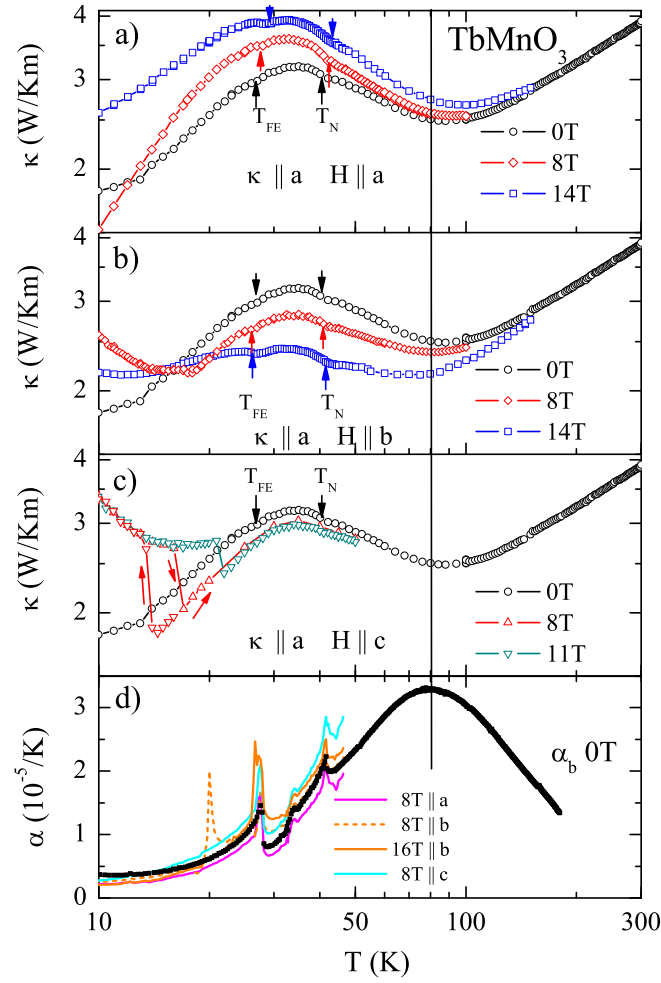


Figure 7.20.: Thermal conductivity κ_a of TbMnO_3 . a) $H \parallel a$. b) $H \parallel b$. c) $H \parallel c$. d) Thermal expansion α_b in zero field, and with magnetic fields applied along a , b , and c .

at $T \approx 90$ K. Further lowering the temperature, κ increases and a maximum at $T = 34$ K with a relatively low absolute value $\kappa \approx 3$ W/Km is reached. Comparing the thermal conductivity with the thermal expansion, see panel d), a maximum of α_b is reached at the same temperatures where κ runs through its minimum. The maximum in α_b is presumably caused by a Schottky contribution from the $4f$ states of Tb^{3+} [287]. The $J = 6$ state of Tb^{3+} splits into 13 singlets in an orthorhombic crystal field. To my knowledge, the energy level scheme is not known¹², and there have also been no investigations of the crystal-field splitting of other orthorhombic TbAO_3 compounds in the literature. The analysis of the thermal expansion data by Eq. 7.5 yields an energy gap¹³ of ≈ 190 K [287]. From the comparison with thermal expansion it is likely that the minimum of κ at ≈ 100 K is caused by a resonant scattering process, as discussed

¹²In Ref. [304] a peak at 4 meV was observed in a neutron scattering experiment, which was attributed to a CF excitation. These measurements are restricted to 10 meV.

¹³In principle, a mixture of several Schottky contributions, or a (approximate) degeneracy of the levels is also possible.

for PrCoO_3 in Sec. 5.4.10. This scenario is supported by the magnetic field dependences of κ and α . For $H \parallel a$ and $H \parallel c$, κ is suppressed over a broad temperature range, whereas for $H \parallel b$, an enhancement of κ is observed. In a field of 14 T the field dependence of κ is detectable up to a comparatively high temperature of 150 K. To compare the field dependence of κ to the Schottky peak in α_b , Fig. 7.20 shows magnetic-field dependent measurements of α_b with the field applied along all crystallographic axes. Although the magnetic-field curves of α_b only extend to 50 K, it is clearly seen that the Schottky contribution is either enhanced or suppressed for the different field directions. From the comparison of the field dependences of α and κ , we can derive the direct correlation: When α_b increases, κ is suppressed, while κ is enhanced, when α_b decreases. This correlation clearly suggests that the suppression of κ is a consequence of resonant scattering between CF levels of the $4f$ shell of Tb^{3+} .

The influence of T_N and T_{FE} on κ is hardly detectable. Weak dips are observed at the transition temperatures (see arrows in Fig. 7.20). However, the shape of the thermal conductivity curves is not changed. Because of the low absolute values of κ , we conclude that these effects play almost no role, since the scattering by the $4f$ moments is dominant.

Below T_{FE} one can distinguish the measurements with H parallel to the a and b axis, where a transition from the LT-ICAFM to the cAFM phase occurs, from those with $H \parallel c$, where the system turns from the LT-ICAFM to the paraelectric cAFM phase, if a large field is applied. For the latter case, a sharp increase of κ is observed when the paraelectric cAFM phase is reached, see Fig. 7.20c. The pronounced hysteresis of the 8 T curve, shows the first order nature of the transition. At 11 T the transition shifts to a higher temperature, but the curves at 8 T and 11 T are almost identical, if the system is in the same phase. For $H = 8 \text{ T} \parallel b$, a sudden increase is observed when the system goes from the LT-ICAFM phase to the cAFM phase (see Fig. 7.20b). Since at the same time a polarization flop from $P \parallel a$ to $P \parallel c$ takes place, one may suspect that this increase is related to the formation of ferroelectric domains. However, we could rule out this possibility as will be shown in the next section. Another possible explanation is that the additional suppression of the thermal conductivity in the LT-ICAFM phase is caused by the incommensurability: The symmetry of the system is lowered, causing additional thermal resistance.

Thermal Conductivity in Electric Fields

As in the magnetic equivalent, ferroelectric domains occur in the ferroelectric state, if the system is cooled in zero electric field. To investigate, whether the additional disorder caused by the domains has an influence on the thermal conductivity, measurements under application of electric fields were performed, which will be presented in this section.

For the electric-field dependent measurements one needs two capacitor plates, which are realized by sputtering gold on two opposite sides of the samples (see Sec. 3.5 for experimental details). Since the electric field is given by $E = U/d$, where U is the applied voltage, and d the distance between the capacitor plates, large fields may be achieved by making the samples thin in the direction of E . The electric field was applied along the c direction. Therefore sample B was cut with a small c length of 0.14 mm.

To check the existence of domains, first the polarization P_c was measured. For the experimental details of the polarization measurements see Sec. 3.5. Fig. 7.21a shows the results of the measurements of P_c below 30 K with $H \parallel b$. For $H = 0 \text{ T}$ the transition to the polarized state is clearly seen at 28 K. Below, P_c increases until it reaches its saturation value at low temperatures. For $H = 3 \text{ T}$ no change is observed, except below 10 K, which is due to the

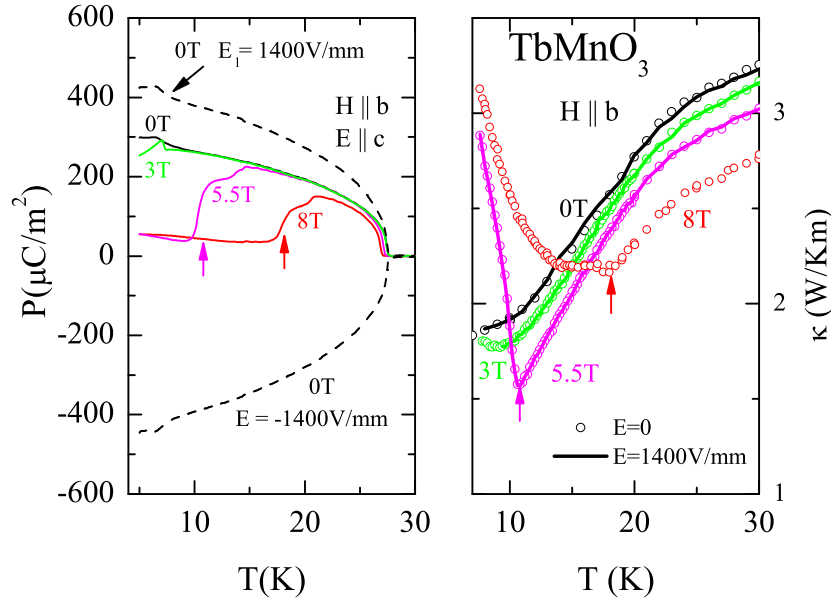


Figure 7.21.: a) Polarization P of TbMnO_3 . All measurements with $H > 0$ T were done without a polling field. b) Thermal conductivity of TbMnO_3 without (symbols) and with application of electric fields (lines).

above-mentioned complex low-temperature phases. For $H = 5.5$ T the polarization flop to the $P||a$ phase is observed as expected from the phase diagram (Fig. 7.19). Below the transition temperature the polarization $P||c$ drops to zero¹⁴.

The polarization of TbMnO_3 was investigated in detail in [289]. The comparison to the literature data yields lower values for our sample, which can be explained by the formation of domains. The literature data were measured in a FC configuration. This means that a large electric field is applied above the transition temperature, and then the sample is cooled to the starting temperature of the measurement, which hinders the domain formation. Then the electric field is turned off, and the measurements are performed without an applied field. In contrast, the presented measurements were performed without the application of an electric field. To prove the existence of domains, some zero-field measurements were performed with a field cooled configuration. The dashed line in Fig. 7.21a shows P measured after cooling the sample in a field of 1400 V/mm, having about 30% larger absolute values. Further, the application of a negative voltage aligns the electric polarization with a different sign, as seen by the measurement in -1400 V/mm. The application of electric fields (not shown) up to 7200 V/mm did not cause a further change of P . We conclude that we are able to control the domain structure. Fig. 7.21a shows κ_b with $H = 0, 3, 5.5$, and 8 T applied along the b direction. For the thermal conductivity, the application of electric fields up 1400 V/mm yields exactly the same results as for the measurements without electric field. We conclude that the ferroelectric domain structure is not the reason for the increase of κ in the $P||c$ phase.

¹⁴The residual Polarization below 10 K and $H > 5$ T arises from the drift of the background signal, see Sec. 3.5.

7.6. Conclusions

In this chapter we presented thermal conductivity measurements of the orthorhombic manganites $RMnO_3$ with $R = \text{Nd, Gd, and Tb}$. The thermal conductivity of NdMnO_3 shows a very unusual behavior. The antiferromagnetic transition at $T_N = 81 \text{ K}$ leads to a strong suppression of the thermal conductivity over a large temperature range. This is in contrast to LaMnO_3 , where a much weaker influence of the Néel transition to the heat transport was observed. The calculated scattering rates using the magnetic specific heat qualitatively describe the observed behavior around T_N and at higher temperatures. At low temperatures the thermal conductivity is further suppressed by another scattering mechanism. The ground-state doublet of Nd is split by $\Delta \approx 20 \text{ K}$ due to exchange interaction with the canted Mn moments. Additional resonant scattering processes by this two-level system further suppress the thermal conductivity. A systematic investigation of the thermal expansion in magnetic fields up to 14 T shows that Δ strongly increases in magnetic fields applied along the c axis. A detailed analysis in combination with the magnetic susceptibility clarified details of this mechanism. The increase of Δ in magnetic fields has a large impact on the heat transport. With increasing magnetic field, a strong increase of κ at low temperatures is observed. For higher temperatures a gradual change to a suppression of κ with increasing magnetic field takes place. A possible explanation of the sign change of the field dependence is that phonon-scattering by the first excited Nd doublet becomes also important. However, the interplay of the scattering mechanism of magnetic excitations and $4f$ moments as well as the lack of the knowledge of the Nd energy scheme prevent a more quantitative analysis in this temperature range difficult. In TbMnO_3 a strongly suppressed thermal conductivity is observed in the whole temperature range, too. As the main mechanism suppressing κ we identified resonant scattering by the Tb $4f$ moments. This conclusion was drawn from the comparison of the temperature and field dependences of κ with those of the thermal expansion α . In contrast, the transitions at T_c and T_{FE} only cause very weak anomalies in κ . At low temperatures complex field dependences occur. The transition from the LT-ICAFM into the cAFM phase for $H||a, b$ and into the paraelectric canted AFM phase for $H||c$ leads to an increase of the thermal conductivity. The ferroelectric domain structure has no influence on the heat transport, as shown by measurements of the polarization and of the thermal conductivity under application of electric fields. The additional suppression of κ seems to be caused by the incommensurability of the LT-ICAFM phase, which lowers the lattice symmetry. In GdMnO_3 κ shows very low absolute values at low temperatures. This is in contrast to the literature data [272]. The observed behavior seems to reflect non-intrinsic properties and we did not further consider the measurements on this sample. In Ref. [272] Zhou *et al.* proposed that the low absolute values of the thermal conductivity of TbMnO_3 are caused by complex magnetic and electric ordering phenomena. However, such an explanation is much too simplistic, since scattering by the crystal-field split $4f$ orbitals of Tb^{3+} is neglected. Our results of κ of NdMnO_3 and TbMnO_3 show that such resonant scattering strongly suppresses κ . All measurements not discussed in this chapter, are shown in the appendix.

8. Summary

In this thesis the thermal transport properties of transition-metal oxides were investigated. In the rare-earth cuprates $R_2\text{CuO}_4$ with $R = \text{La, Pr, Nd, Sm, Eu, and Gd}$ the role of magnetic excitations for the heat transport was studied. For the cobaltates $R\text{CoO}_3$ with $R = \text{La, Pr, Nd, and Eu}$ the goal was to study the influence of the spin-state transition on the thermal conductivity κ . In the Sr-doped cobaltates $\text{La}_{1-x}\text{Sr}_x\text{CoO}_3$ with $0 \leq x \leq 0.3$ and $\text{La}_{0.75-x}\text{Eu}_{0.25}\text{Sr}_x\text{CoO}_3$ with $0 \leq x \leq 0.4$ the thermoelectric properties and the thermoelectric figure of merit were the focus of the investigation. In the orthorhombic manganites $R\text{MnO}_3$ with $R = \text{Nd, Gd, and Tb}$ the question was addressed, to which extent magnetic and electric ordering phenomena influence the thermal conductivity.

The unconventional thermal conductivity of the layered cuprates has been controversially discussed in the literature. Nakamura *et al.* [6] suggested a magnetic contribution of κ , whereas Cohn *et al.* [81] proposed a purely phononic scenario. To clarify this issue, a systematic study by thermal conductivity measurements of $R_2\text{CuO}_4$ with $R = \text{La, Pr, Nd, Sm, Eu, and Gd}$ was carried out. The zero-field thermal conductivity is studied in a temperature range of $5\text{ K} \leq T \leq 300\text{ K}$ for both, a heat current perpendicular ($R = \text{Pr and Gd}$) and parallel ($R = \text{Pr, Nd, Sm, Eu, and Gd}$) to the CuO_2 planes. The out-of-plane thermal conductivity shows the typical temperature dependence of a purely phononic thermal conductivity with a low-temperature maximum, whose magnitude depends on the crystal quality. In contrast, the in-plane conductivity for all crystals exhibits a pronounced double-peak structure consisting (i) of a low-temperature peak similar to that of the out-of-plane thermal conductivity and (ii) of an anomalous high-temperature contribution with a broad maximum around 250 K. Such an anisotropy between the in-plane and the out-of-plane thermal conductivity is also observed in La_2CuO_4 by several authors. The fact that the double-peak is present in the structurally stable $R_2\text{CuO}_4$ with $R = \text{Pr, Nd, and Sm}$ unambiguously rules out the possibility that the double-peak structure is caused by a structural instability, which is present for $R = \text{La, Eu, and Gd}$. The qualitative anisotropy between the in-plane and the out-of-plane thermal conductivity and the rather similar high-temperature behavior of the out-of-plane thermal conductivity for all the different crystals gives clear evidence that this additional high-temperature contribution arises from a sizeable heat transport by magnetic excitations within the CuO_2 planes. The data analysis yields a magnetic contribution to the in-plane thermal conductivity between about 7 to 25 W/Km depending on the R system. In weakly charge-carrier doped La_2CuO_4 , this magnetic contribution is strongly suppressed showing that scattering of magnetic excitations by mobile charge carriers plays an important role. In contrast, the structural instability does hardly influence the magnetic thermal conductivity indicating that scattering of magnetic excitations by soft or anharmonic phonons plays a minor role. To compare the principle behavior of the thermal conductivity of the two-dimensional square lattice with one-dimensional systems, the energy diffusion constant $D_E(T)$ is calculated for La_2CuO_4 and compared with $D_E(T)$ obtained for various one-dimensional chains with $S = 1/2$ and $S = 1$. The heat transport in the one-dimensional systems is anomalously enhanced, since the estimated $D_E(T)$ is much larger than an estimate using the calculated correlation length. In contrast, a rather

conventional behavior of the thermal transport in the two-dimensional square lattice is found. The observation of a large magnetic contribution on the heat transport is just a consequence of the large coupling constant J , which causes a sizeable contribution to κ , and the fact that $J \gg \Theta_D$, allowing the distinction of κ_{mag} from the phononic heat conductivity.

A second focus is the influence of magnetic fields on the thermal conductivity. At low temperatures large magnetic-field effects are observed for the in-plane thermal conductivity of Nd_2CuO_4 and Gd_2CuO_4 , a smaller effect in Pr_2CuO_4 , and no magnetic-field dependences in Sm_2CuO_4 and Eu_2CuO_4 . It is shown, that resonant scattering processes by the $4f$ orbitals can consistently describe the observed behavior. This conclusion is in contrast to the magnon heat transport proposed for Nd_2CuO_4 by Jin *et al.* [80] and Li *et al.* [10]. A comparative analysis of the different experimental results of Nd_2CuO_4 analysis reveals, that the proposed methods to extract the possible magnon contributions are highly uncertain. Moreover, the observed magnetic-field dependences in Nd_2CuO_4 are much smaller than those observed e.g. in NdMnO_3 , where the effect is unambiguously caused by the $4f$ orbitals. This shows that the attribution of the observed magnetic-field dependences to a magnon contribution to κ , as proposed by Li *et al.*, is highly questionable.

The influence of the spin-state transition to the thermal conductivity of Cobaltates is investigated in $R\text{CoO}_3$ with $R = \text{La}, \text{Pr}, \text{Nd}, \text{and Eu}$. A main result is that the unconventional thermal conductivity of LaCoO_3 can be attributed to the spin-state transition. At low temperatures, a maximum of κ with an unusual temperature and magnetic-field dependence is observed. The low-temperature behavior of the thermal conductivity is systematically investigated on five different LaCoO_3 crystals. It is shown that non-intrinsic strong scattering processes caused by paramagnetic impurity levels governs the heat transport in this temperature range. The measured thermal conductivity could be correlated to the paramagnetic impurity content of the samples obtained via magnetization measurements. The effectiveness of these processes may be enhanced due to the formation of magnetic polarons. Concerning the $R\text{CoO}_3$ series, a systematic increase of the thermal conductivity from $R = \text{La}$ to Eu is observed. At low temperatures, this observation cannot directly be attributed to the spin-state transition. The analysis of the thermal conductivity in combination with susceptibility measurements suggests a scenario, where magnetic polarons significantly scatter phonons at low temperatures. Because the polaron formation becomes less likely when the spin gap is increased, the systematic increase of the thermal conductivity from La to Eu results. Above $T \approx 30 \text{ K}$, a strong suppression of the thermal conductivity is observed in all samples. The resulting very low absolute value of the thermal conductivity up to room temperature is an intrinsic feature of the thermal conductivity of LaCoO_3 . This unusual behavior of the heat transport is a consequence of the spin-state transition. The Co^{3+} ion has a larger ionic radius in the thermally activated higher-spin state than in the low-spin ground state. The random distribution of the low-spin and the higher-spin states causes an additional lattice disorder which strongly suppresses the thermal conductivity. To check this scenario also quantitatively, the additional scattering-rate due to the spin-state transition is estimated. Herefore EuCoO_3 is used as a reference compound, where the influence of the spin-state transition is negligible below room temperature. The temperature dependence of the additional phonon scattering can be described by a model based on the Nordheim rule. Such a model was successfully used in the literature to describe the thermal conductivity of mixed semiconductor alloys. The proposed model works well with both, the low-spin/intermediate-spin scenario with a spin gap of 186 K estimated by susceptibility measurements as well as with the recently proposed model based on a spin-orbit coupled high-spin state.

In PrCoO_3 and NdCoO_3 , the spin-state transition shifts gradually to higher temperatures. The spin-state transition influences the thermal conductivity at high temperatures in PrCoO_3 and NdCoO_3 in the same way as in LaCoO_3 . The change of the scattering rates due to the spin-state transition can be modeled using the parameters estimated from LaCoO_3 . This is clear evidence that the spin-state transition indeed causes the suppression of the thermal conductivity due to the additional disorder. The scattering mechanism is explored in detail and the scattering strength for LaCoO_3 is quantitatively described. The results show that the static volume changes of the Co^{3+} ions caused by the spin-state transition are sufficient to explain the observed behavior of the thermal conductivity. This is in contrast to the scenario given by Yan *et al.*[9], which proposes that dynamic fluctuations are responsible for the strong suppression of the thermal conductivity. In PrCoO_3 , an additional scattering mechanism could be identified, which is attributed to resonant scattering by the $4f$ orbitals of Pr^{3+} .

The thermal conductivity of $\text{La}_{1-x}\text{Sr}_x\text{CoO}_3$ for $0 \leq x \leq 0.3$ is strongly suppressed for all x . For small finite x , a spin-state transition of the Co^{3+} ions may be induced by the neighboring magnetic Co^{4+} ions, and so-called high-spin polarons can be formed. For larger x this effect becomes less important, but scattering of phonons by mobile charge carriers also plays a role for the suppression of the thermal conductivity. For finite doping a large, positive thermopower is observed, which strongly depends on temperature and doping. The room temperature values of the thermopower follow a doping dependence that is expected from a modified Heikes formula. In nominally pure LaCoO_3 the different crystals either have a large positive or a large negative thermopower. We suspect that this is a consequence of weak deviations from the nominal oxygen content causing small amounts of hole or electron doping. For the sample with $x = 0.25$ both, the thermal conductivity and the thermopower show a significant magnetic-field dependence in the temperature range around the ferromagnetic ordering temperature. The field dependence of the thermal conductivity can be traced back to a field-dependent charge carrier contribution to the heat current, and the field dependence of the thermopower indicates that it contains a sizeable contribution arising from magnetic entropy. For the intermediate doping $x = 0.125$ rather large values of the thermoelectric figure merit are found, which is calculated from the resistivity, thermopower and thermal conductivity data. This value is large, but yet too small for technical applications.

The thermal conductivity of the orthorhombic manganites $R\text{MnO}_3$ with $R = \text{Nd}, \text{Gd},$ and Tb turned out to be very complex. In particular, the thermal conductivity of NdMnO_3 shows a very unusual behavior. The antiferromagnetic transition at $T_N = 81 \text{ K}$ causes a strong suppression of the thermal conductivity over a large temperature range. This is contrast to LaMnO_3 , where a much weaker influence of the Néel transition to the heat transport was observed in the literature. The calculated scattering rates using the magnetic specific heat qualitatively describe the observed behavior of the thermal conductivity in NdMnO_3 around T_N and at higher temperatures. At low temperatures the thermal conductivity is also influenced by another scattering mechanism. The ground-state doublet of Nd is split by $\Delta \approx 20 \text{ K}$ due to exchange interaction with the canted Mn moments. Additional resonant scattering processes by this two-level system further suppress the thermal conductivity. A systematic investigation of the thermal expansion in magnetic fields up to 14 T shows that Δ strongly increases in magnetic fields applied along the c axis. A detailed analysis in combination with the magnetic susceptibility clarified details of this mechanism. The increase of Δ in magnetic fields has a large impact on the heat transport. With increasing magnetic field, a strong increase of κ at low temperatures is observed. At higher temperatures, κ is determined by the interplay of the scattering mechanism caused by the antiferromagnetic transitions and the $4f$ orbitals. In

TbMnO₃, a strongly suppressed thermal conductivity is observed in the whole temperature range, too. As the main mechanism suppressing κ resonant scattering by the Tb 4*f* orbitals can be identified. This conclusion is drawn from the comparison of the temperature and field dependences of κ with those of thermal expansion α . In contrast, the transitions at T_c and T_{FE} only cause very weak anomalies in κ . At low temperatures complex field dependences occur. The transition from the low-temperature incommensurate antiferromagnetic into the canted antiferromagnetic phase for $H||a,b$ and into the paraelectric canted antiferromagnetic phase for $H||c$ leads to an increase of the thermal conductivity. The electrical domain structure has, however, no influence on the heat transport, as shown by measurements of the electrical polarization and of the thermal conductivity under application of electrical fields. The additional suppression of κ seems to be caused by the incommensurability of the low-field low-temperature phase, which reduces the lattice symmetry. Zhou *et al.* [272] proposed that the low absolute values of the thermal conductivity of TbMnO₃ are caused by the complex magnetic and electric ordering phenomena. However, such an explanation is much too simplistic, since scattering by the crystal-field split 4*f* orbitals of Tb³⁺ is neglected. The results of κ of NdMnO₃ and TbMnO₃ clearly show that such resonant scattering strongly suppresses κ . Therefore, in TbMnO₃ the ferroelectric and magnetic transitions at low temperature have no additional effect.

In conclusion, complex temperature and magnetic-field dependences occurred in all investigated transition-metal oxide classes. Two important effects related to the transition-metal ions have been found: Heat transport by magnetic excitations in the cuprates, and a large suppression of the thermal conductivity in the cobaltates induced by the disorder due to the spin-state transition. Moreover, complex low-temperature and field dependences arise as a consequence of resonant scattering mechanisms, either by paramagnetic impurities, or by the 4*f* orbitals of the rare-earth ions. In some cases, mostly pronounced in NdMnO₃, the interplay of the transition-metal and rare-earth ions significantly influences the thermal conductivity, too.

A. Additional Measurements

A.1. TbMnO₃

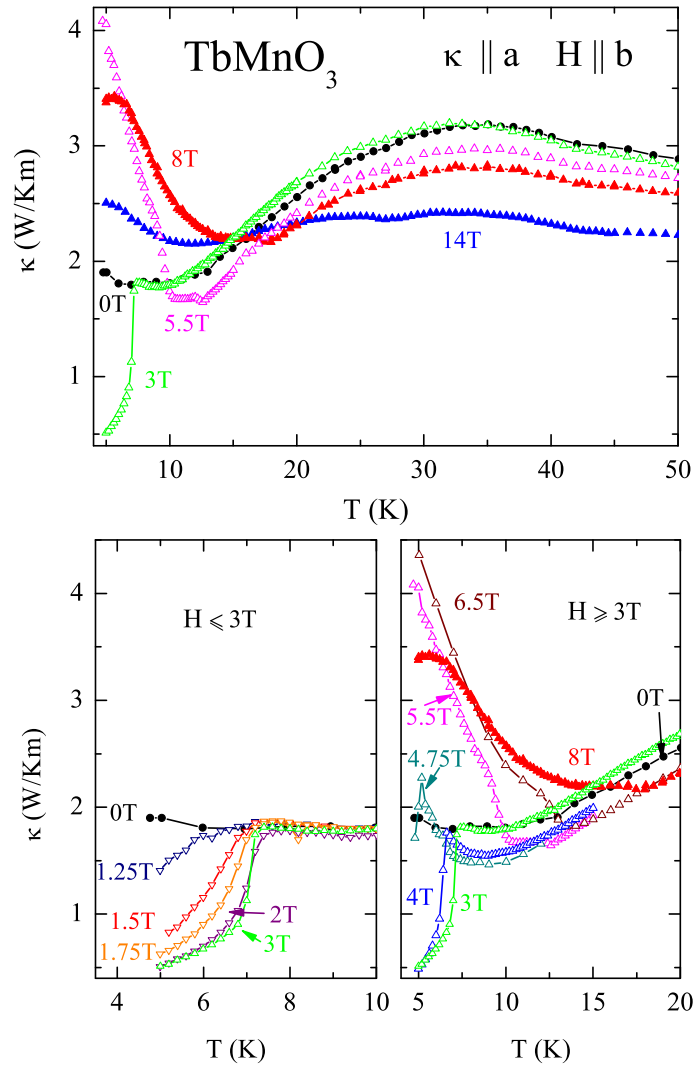


Figure A.1.: Thermal conductivity of TbMnO₃, $\kappa \parallel a$, $H \parallel b$. a) Selected magnetic fields between 0 T and 14 T. b) Magnetic fields between 0 T and 3 T. c) Magnetic fields between 3 T and 8 T. (Δ, \blacktriangle): Measurements with increasing T . ($\nabla, \blacktriangledown$): Measurements with decreasing field. The hysteretic behavior of the field curves is shown in Fig. A.3. The sudden increase of κ with decreasing temperature for $H \geq 5.5$ T

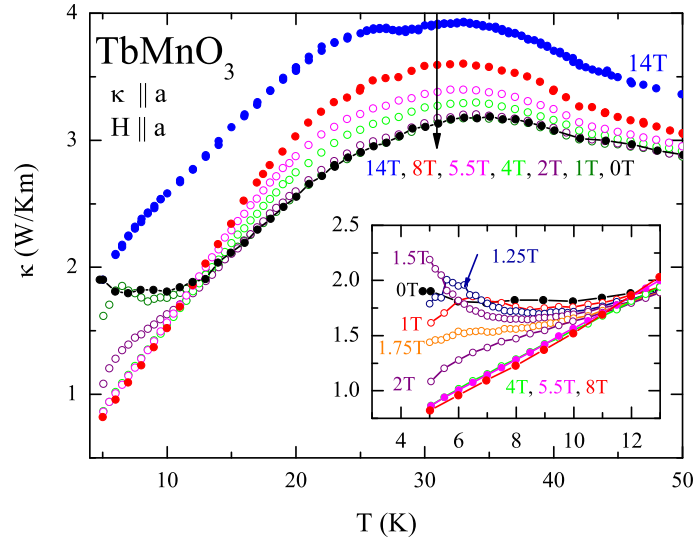


Figure A.2.: Thermal conductivity of TbMnO_3 , $\kappa \parallel a$, $H \parallel b$. $H = 0 \dots 14$ T. Inset: Field range up to 8 T in detail.

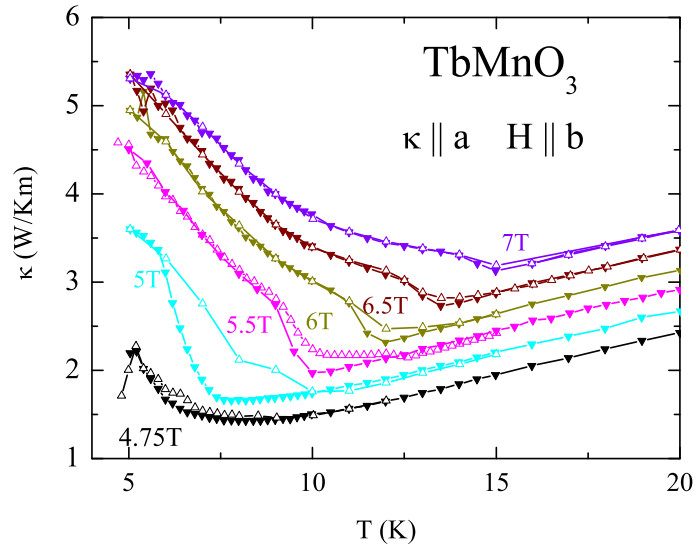


Figure A.3.: Thermal conductivity of TbMnO_3 , $\kappa \parallel a$, $H \parallel b$, hysteretic behavior of the measurements in magnetic fields. (Δ, \blacktriangle) : Measurements with increasing T . $(\nabla, \blacktriangledown)$: Measurements with decreasing field.

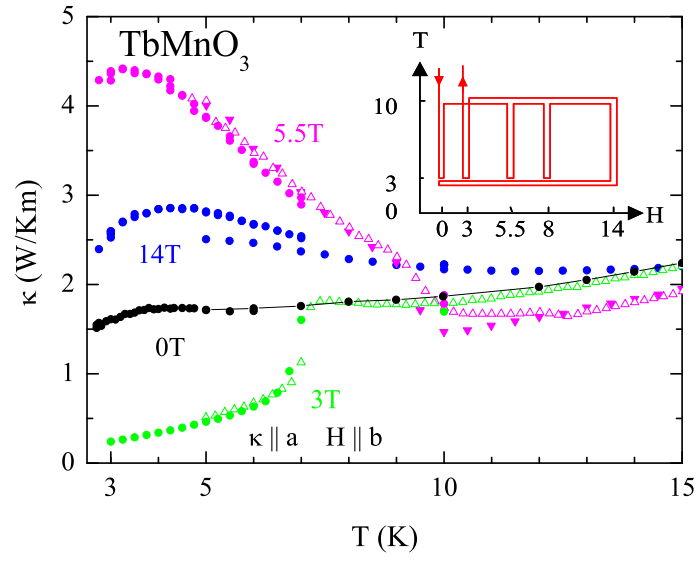


Figure A.4.: Thermal conductivity TbMnO_3 , $\kappa \parallel a$, $H \parallel b$. Additional measurements down to 3 K (●) in combination with the measurements from Fig. A.1.

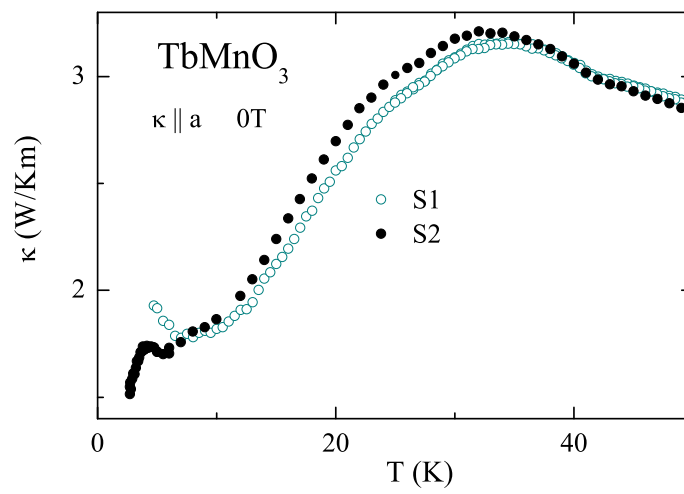


Figure A.5.: Thermal conductivity TbMnO_3 , $\kappa \parallel a$. Zero-field data of the two different samples.

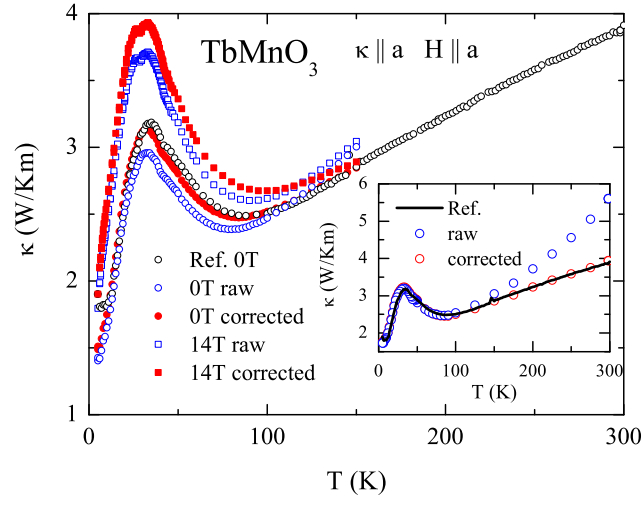


Figure A.6.: Correction of the radiation losses of κ_b of the small TbMnO_3 sample. The reference is the measurement on the large sample (see Tab. 7.2).

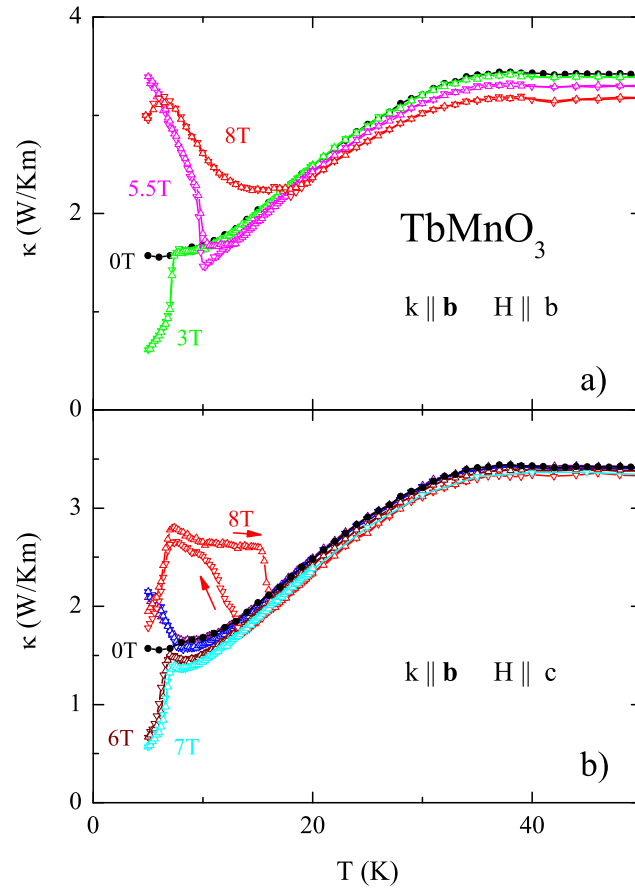


Figure A.7.: Thermal conductivity of TbMnO_3 , $\kappa \parallel b$. a) Measurements with $H \parallel b$. b) Measurements with $H \parallel c$.

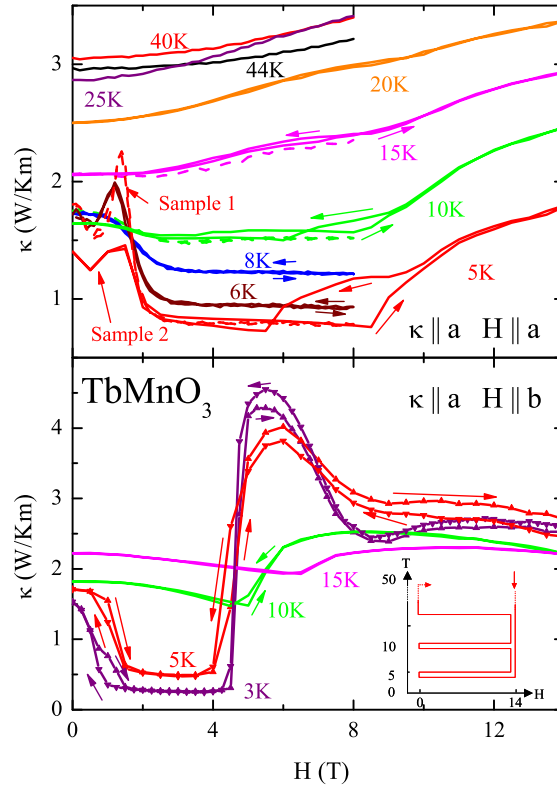


Figure A.8.: Thermal conductivity of TbMnO_3 , $\kappa||a$, $H||b$. Measurements of $\kappa(H)$ at fixed temperatures. a) Measurements with $H||a$. The data up to 8 T are from Sample S1, the data up to 14 T from sample S2. Differences are present at low fields and low temperatures (see also Fig. A.5). b) Measurements with $H||b$. At low temperatures hysteresis effects are present. The sketch shows how the points were taken in the H - T plane. For the 3 K curve see Fig. A.4.

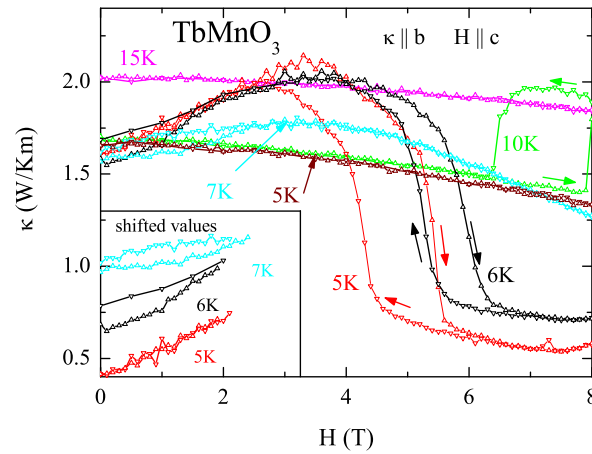


Figure A.9.: Thermal conductivity of TbMnO_3 , $\kappa||b$, $H||c$. Measurements of $\kappa(H)$ at fixed temperatures. Inset: Low-field hysteric behavior, values shifted by a constant offset).

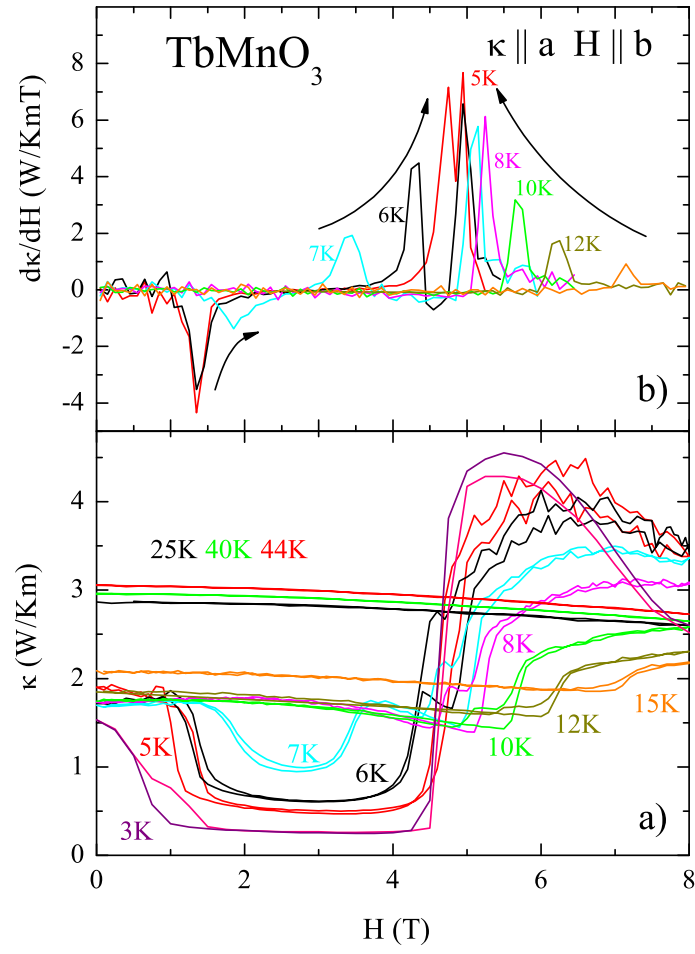


Figure A.10.: a) Thermal conductivity of TbMnO_3 , $\kappa \parallel a$, $H \parallel b$. Measurements of $\kappa(H)$ at fixed temperatures. b) Derivative $d\kappa/dH$ vs. H for low temperatures.

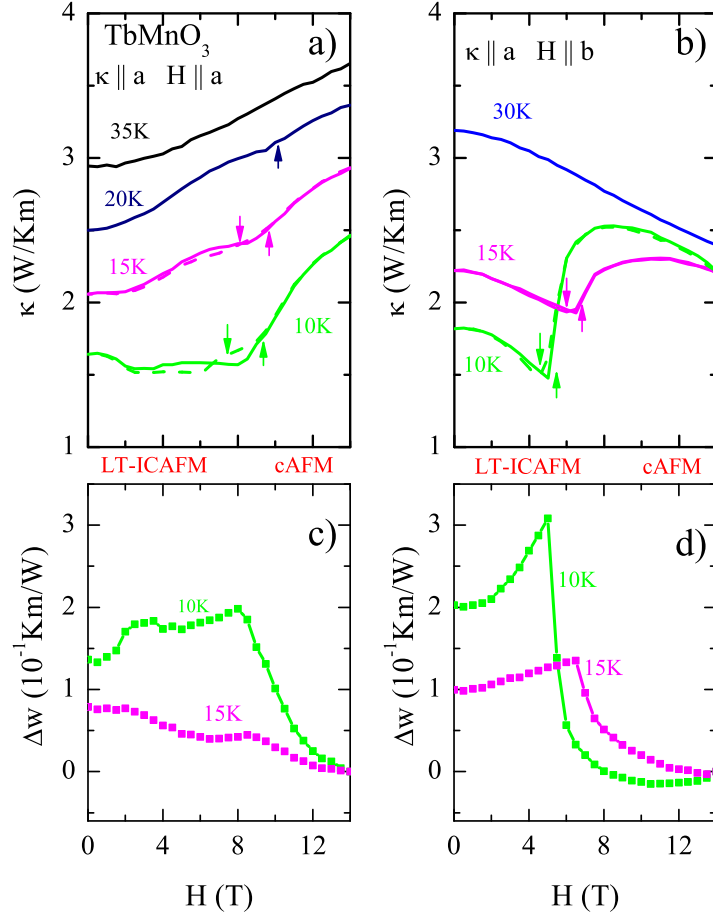


Figure A.11.: Thermal conductivity κ_b of TbMnO_3 vs. H at fixed temperatures. a) Measurements at 10 K, 15 K and 30 K. with $H \parallel a$. b) Measurements at 10 K, 15 K and 35 K. with $H \parallel b$. To analyze the change of the thermal conductivity at the transition from the LT-ICAFM to the cAFM phase, Fig. A.11 a) and b) shows κ vs. H with fields applied along the a and b direction. We attribute the field dependencies above 20 K to the scattering by the $4f$ moments. From the curve at 10 K with $H \parallel b$ we conclude that in the LT-ICAFM phase an additional scattering rate is present, which disappears at the transition field. Since at high fields the slope of κ vs. H is the same like for $T = 30$ K, we conclude that the additional low-temperature scattering mechanism totally disappears. Furthermore, the scattering due to the $4f$ moments seems to change not much between 35 K and 10 K. This allows to calculate the relative change of the thermal resistance due to the phase transition by $\Delta w = 1/\kappa(H) - \Delta w_{4f} - w_{\text{static}}$. The thermal resistance change Δw_{4f} due to the $4f$ moments is estimated from the measurement at 35 (30) K. The field-independent scattering by static effects is given by the constant w_{static} , based on the assumption that the additional low-field scattering vanishes at 14 T. The result of this estimation is shown in Fig. A.11 c) and d). At the same temperature, the additional thermal resistance of the LT-ICAFM phase is very similar for both field directions. The responsible scattering mechanism disappears if the cAFM phase is reached. The only difference between the both field directions is that for $H \parallel a$ the transition is much broader than for $H \parallel b$. This supports the results from the thermal expansion, where also a much broader transition was observed for $H \parallel a$.

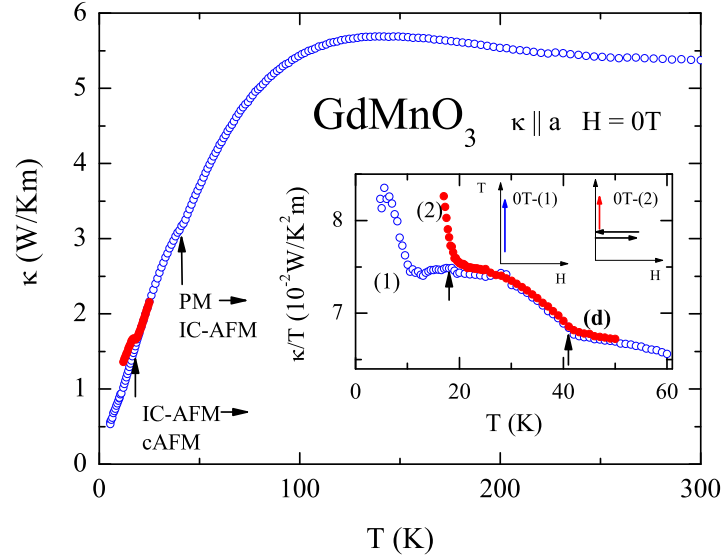
A.2. GdMnO_3 

Figure A.12.: Zero-field thermal conductivity of GdMnO_3 along the a direction. At room temperature, κ has a value of 6 W/Km, which stay approximately constant down to 100 K. Below 100 K, κ decreases linearly with temperature, and reaches very low absolute values. The temperature dependence reminds to the thermal conductivity of highly disordered crystals, where the low-temperature phonon peak is completely suppressed. At the transition from the PM to the IC-AFM phase, a small anomaly is seen in κ . To resolve this in more detail, the inset shows κ/T vs. T below 50 K. At the second transition from the IC-AFM phase no anomaly is observed. However, as known from the thermal expansion measurements, for the zero-field measurements no pure cAFM phase is present, and only a coexistence region of both phases is realized. To examine the zero-field thermal conductivity in the pure cAFM phase, the same idea like in Refs. [273, 291] was applied: The sample was cooled down to 12 K, then a magnetic field of 8 T with $H \parallel a$ was applied and removed without changing the temperature. Then κ was measured with increasing temperature. The resulting curve has an anomaly at the transition temperature, and has higher absolute values in the cAFM phase. This is consistent with the expectation, that the additional disorder in a mixed phase further suppresses κ . However, the resulting thermal conductivity is still very low, and decreasing with decreasing temperature. The conclusion is that still another very effective scattering mechanism is present at low temperatures.

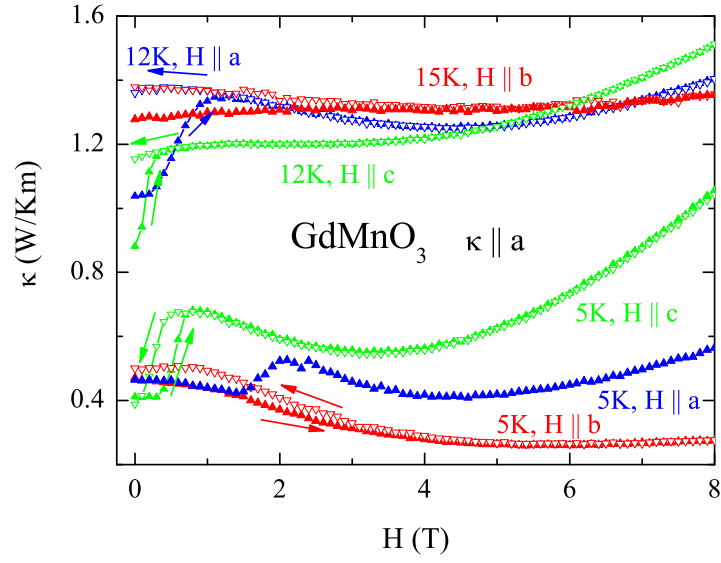


Figure A.13.: Thermal conductivity vs. H of GdMnO_3 . Shown are measurements at 5 K and 12 K with fields applied along all crystallographic axes. At 12 K with $H \parallel a$ the thermal conductivity of the zero field curve has a value of $\approx 0.8 \text{ W/Km}$, which increases to $\approx 1.3 \text{ W/Km}$ at 1 T. For higher fields only a small further increase is observed. Removing the field, κ does not follow the curve with increasing field, instead the value of $\approx 1.3 \text{ W/Km}$ remains down to 0 T. At 5 K the sudden increase is observed at about 2 T. Here the curve should drop down to the zero-field value if the field is removed. Unfortunately the sample fell of the samples holder at 8 T in two different setups when the field of 8 T with $H \parallel a$ was applied. The reason is the large torque moments acting on the sample. However, for $H \parallel c$ in principle the same behavior is expected from the phase diagram, just with a smaller coexistence region. The measurements along this field direction show the expected behavior: At 12 K the sample remains in the cAFM phase, whereas the this phase is (partly) left at 5 K, seen in a downturn of the curve with decreasing field at 1 T.

[r]]

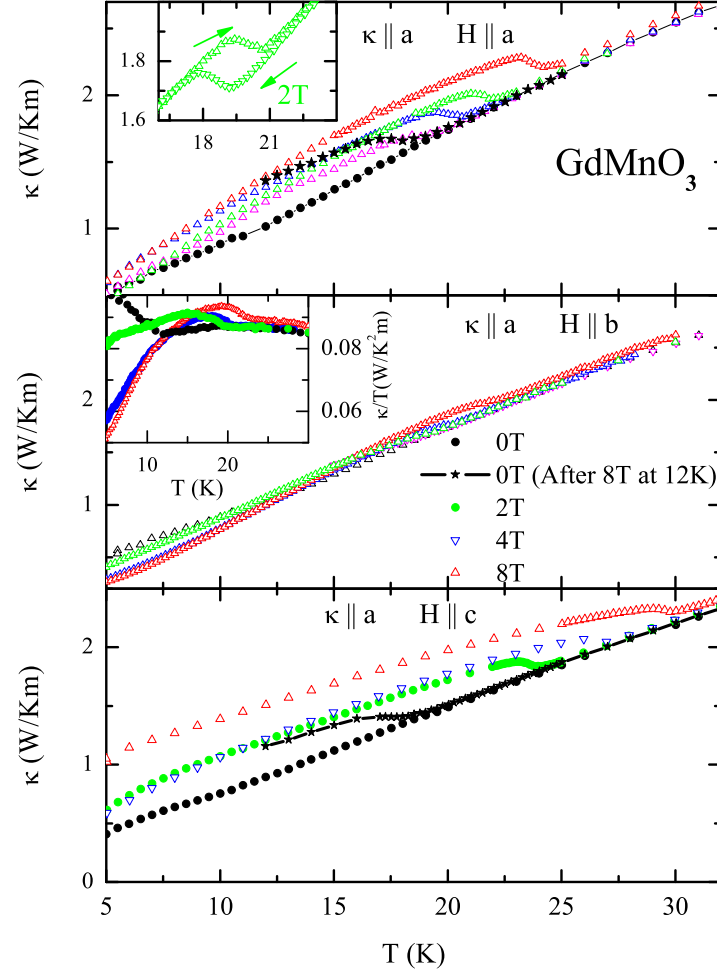


Figure A.14.: Thermal conductivity κ of GdMnO_3 in magnetic fields. a) $H \parallel a$. Inset: Hysteresis at T_c for $H_a = 2$ T. b) $H \parallel b$ Inset: κ/T . c) $H \parallel c$. For $H \parallel a$ and $H \parallel c$ the thermal conductivity increases at the transition to the cAFM phase if the temperature is lowered. Further decreasing the temperature, the decreasing behavior of κ is restored a few Kelvin lower. For $H \parallel a$ a hysteretic behavior is observed in all investigated fields, as shown exemplarily in the inset for $H = 2$ T. For $H \parallel c$ each magnetic field curve was only measured along one direction, but according to the phase diagram no pronounced hysteresis is expected. In contrast, for $H \parallel b$ the magnetic field dependence is less pronounced. At the transition to the cAFM phase in magnetic fields, the anomaly is much weaker than for the other field directions. The inset shows κ/T , where the weak anomaly at T_c is better resolved. In contrast to the other magnetic-field directions, here the field curves cross the zero field curve and the following decrease is stronger. Whereas the ferroelectric transitions produces sharp transitions in the thermal expansion, here, below 10 K no anomalies are identifiable. This corresponds to the almost field independent measurements at 5 K and 12 K in Fig. A.13. Here, only a small hysteretic behavior is observed for fields below ≈ 2 T. From these observations one can summarize, that T_N and T_C can be observed in small anomalies, which show the same hysteretic behavior like observed in the thermal expansion, especially the low-field coexistence region of the IC-AFM and the cAFM phase. The ferroelectric phase transition, however, seems to have a minor influence on κ . However, from the absolute values one can conclude that these are only minor effects and that a very effective scattering mechanism suppresses κ in the whole temperature range.

A.3. $\text{GdFe}_3(\text{BO}_3)_4$

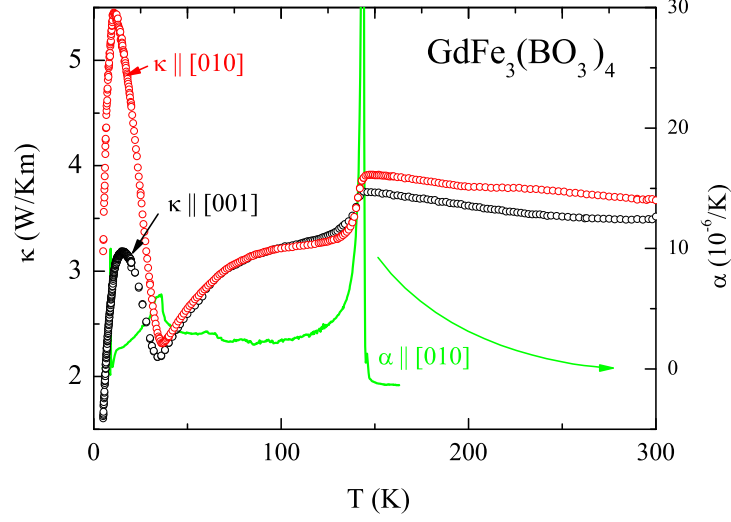


Figure A.15.: Thermal conductivity of $\text{GdFe}_3(\text{BO}_3)_4$ in zero field along the [010] and the [001] axis. The $\text{GdFe}_3(\text{BO}_3)_4$ crystal is from A. Vasiliev (Moskau State University). It was cutted to a cuboid with the dimensions $1 \times 1 \times 2 \text{ mm}^3$. Note, that because of the trigonal structure the following relations between direct and reciprocal space hold: $[010] = (120)$, $(001) = [001]$, $(100) = [2-10]$. The thermal conductivity shows two anomalies: One caused by a structural phase transition at 150 K and second caused by an transition to an antiferromagnetic ordered state. For further information about the system see Refs. [309–316]. Line: Thermal expansion measured by D. Meier [287].

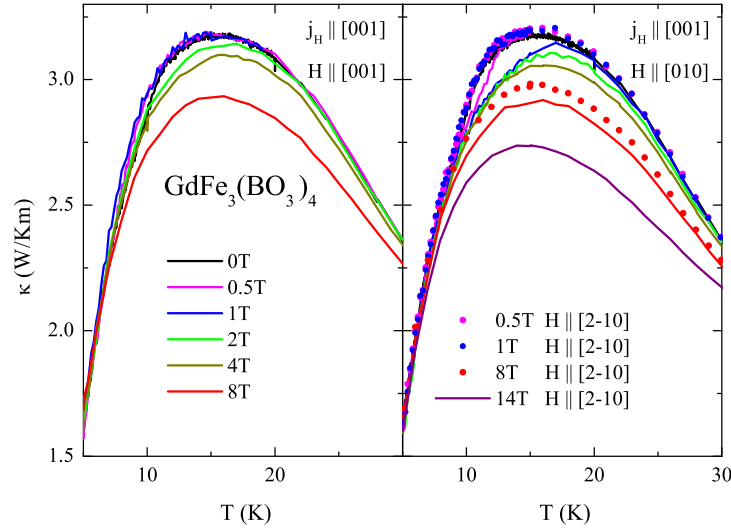


Figure A.16.: Thermal conductivity of $\text{GdFe}_3(\text{BO}_3)_4$ with $j_H || [001]$. Left panel: $H || [001]$. Right panel: $H || [010]$ and $[2-10]$.

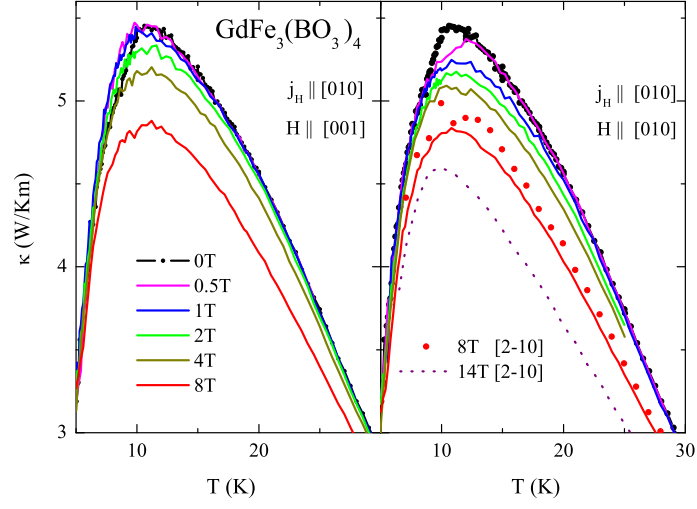


Figure A.17.: Thermal conductivity of $\text{GdFe}_3(\text{BO}_3)_4$ with $j_H \parallel [010]$. Left panel: $H \parallel [001]$. Right panel: $H \parallel [010]$ and $[2-10]$.

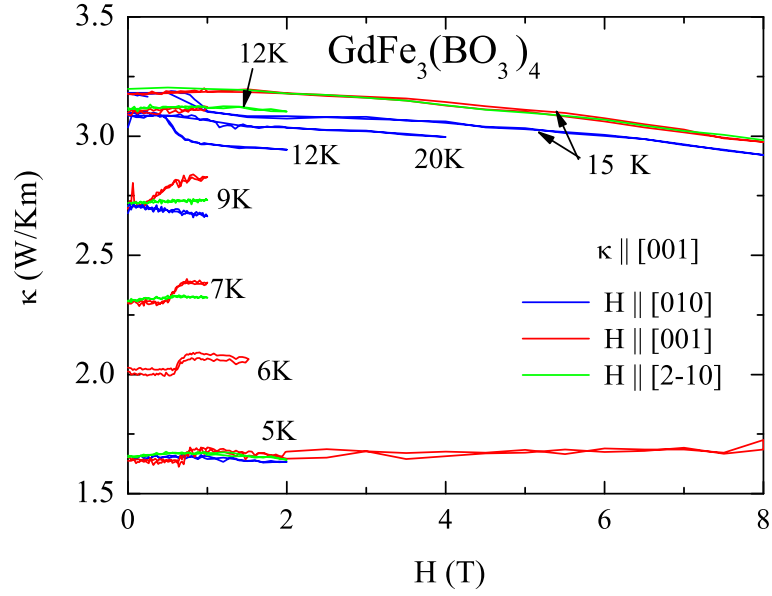


Figure A.18.: Thermal conductivity κ vs H of $\text{GdFe}_3(\text{BO}_3)_4$ at fixed temperatures with $j_H \parallel [001]$ and $H \parallel [010]$, $[001]$, and $[2-10]$.

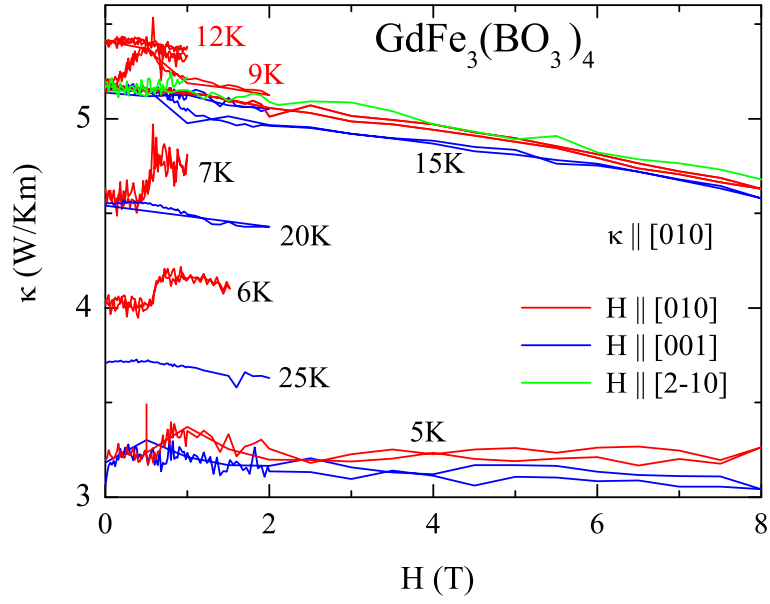


Figure A.19.: Thermal conductivity κ vs H of $\text{GdFe}_3(\text{BO}_3)_4$ at fixed temperatures with $j_H || [010]$ and $j_H || [010], [001]$, and $[2-10]$.

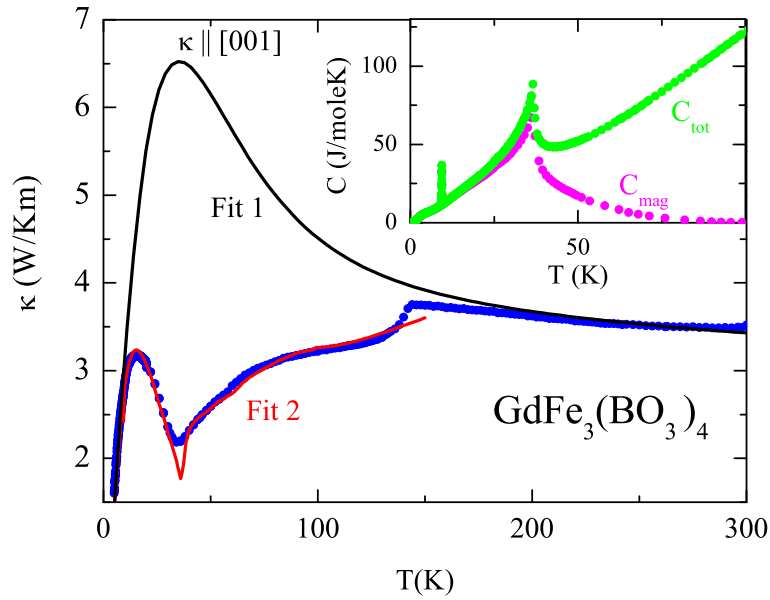


Figure A.20.: Analysis thermal conductivity $\text{GdFe}_3(\text{BO}_3)_4$. Fit1: Debye fit using only conventional scattering mechanisms. Fit2: Debye fit using the additional scattering term of Eq. 7.39. The used magnetic contribution to the specific heat is shown in the inset, together with the lattice specific heat [317].

A.4. Bechgaard Salts

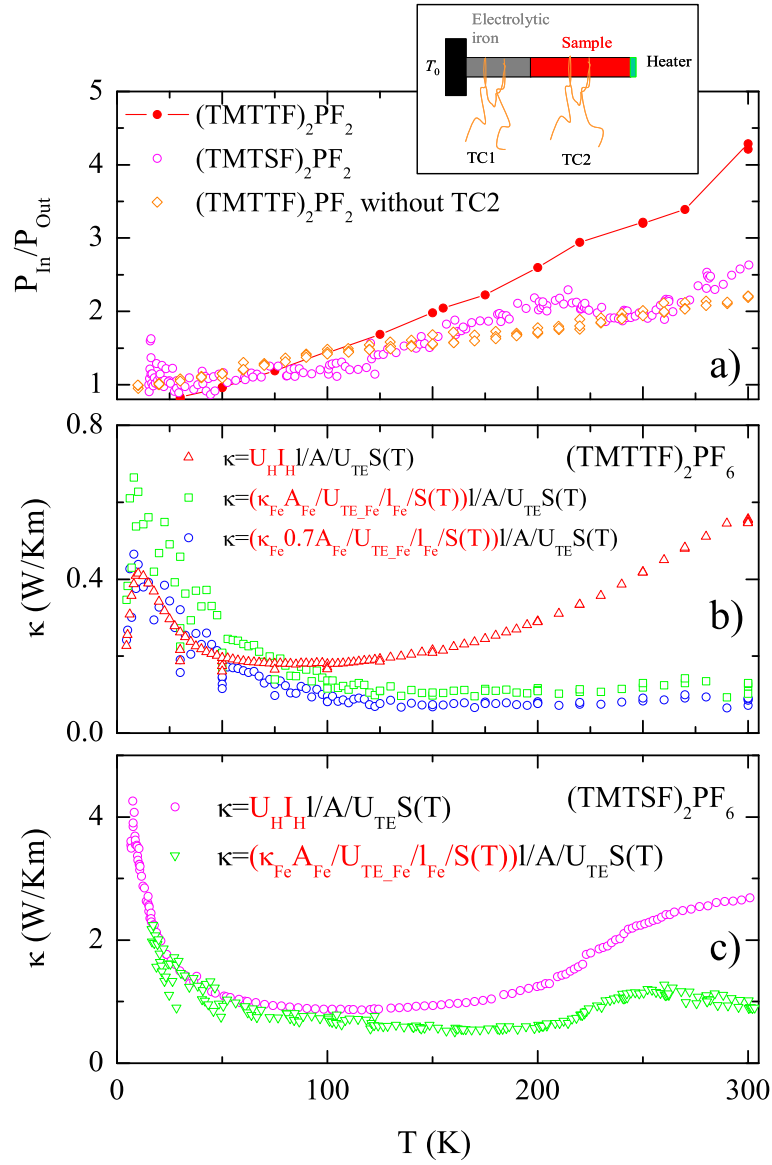


Figure A.21.: Thermal conductivity of Bechgaard salts. The samples are from M. Dressel. The thermal conductivity has been remeasured after it turned out that the data in [318, 319] suffer from large systematic errors due to the used wiring. The setup was extended by the use of an electronic iron sample connected in series with the actual sample. From the temperature gradient over the iron sample the heat current was calculated via the known thermal conductivity. This allowed the estimation of the radiation losses by the subtraction of the power applied to the sample heater, and the power which reached the iron sample.

A.5. Spin Ladders

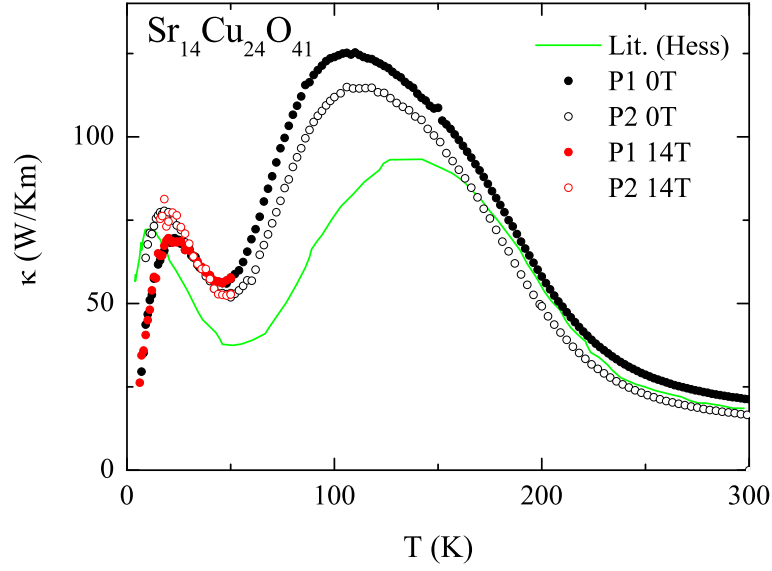


Figure A.22.: Thermal conductivity of $\text{Sr}_{14}\text{Cu}_{24}\text{O}_{41}$, measured on two different samples. The samples were grown by M. Reuther [214]. In addition to the low-temperature maximum a huge high-temperature maximum is observed. The qualitative agreement to the literature data from Ref. [3] is well. The samples show an even larger high-temperature peak. No magnetic field dependence is observed at low temperatures.

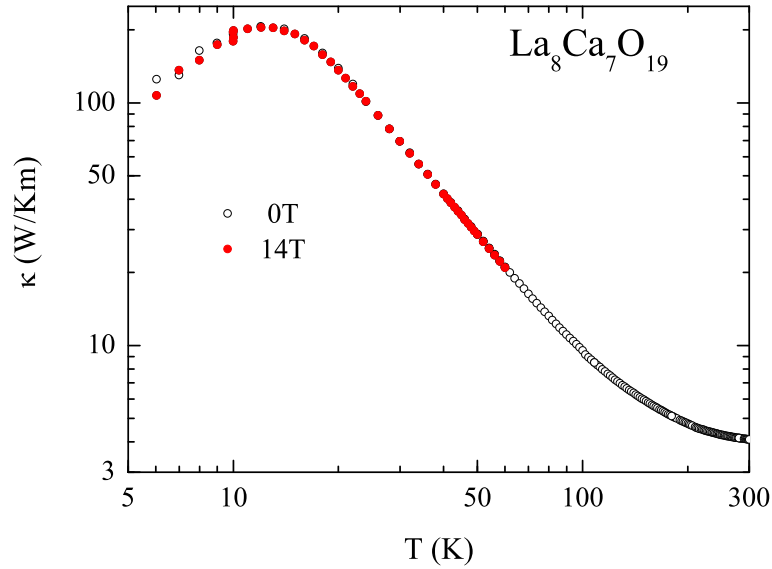


Figure A.23.: Thermal conductivity of the four-rung ladder compound $\text{La}_8\text{Ca}_7\text{O}_{19}$ along the ladder direction. The sample was grown by M. Reuther [214]. In contrast to $\text{Sr}_{14}\text{Cu}_{24}\text{O}_{41}$, no unusual temperature dependence is observed.

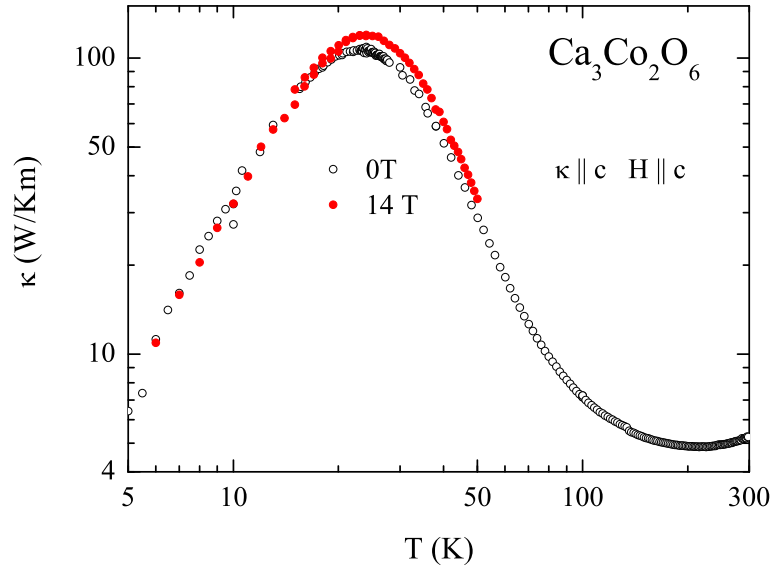
A.6. $\text{Ca}_3\text{Co}_2\text{O}_6$ 

Figure A.24.: Thermal conductivity of $\text{Ca}_3\text{Co}_2\text{O}_6$. The sample is from A. Maignan (Laboratoire CRISMAT, France). The thermal shows a conventional phononic behavior.

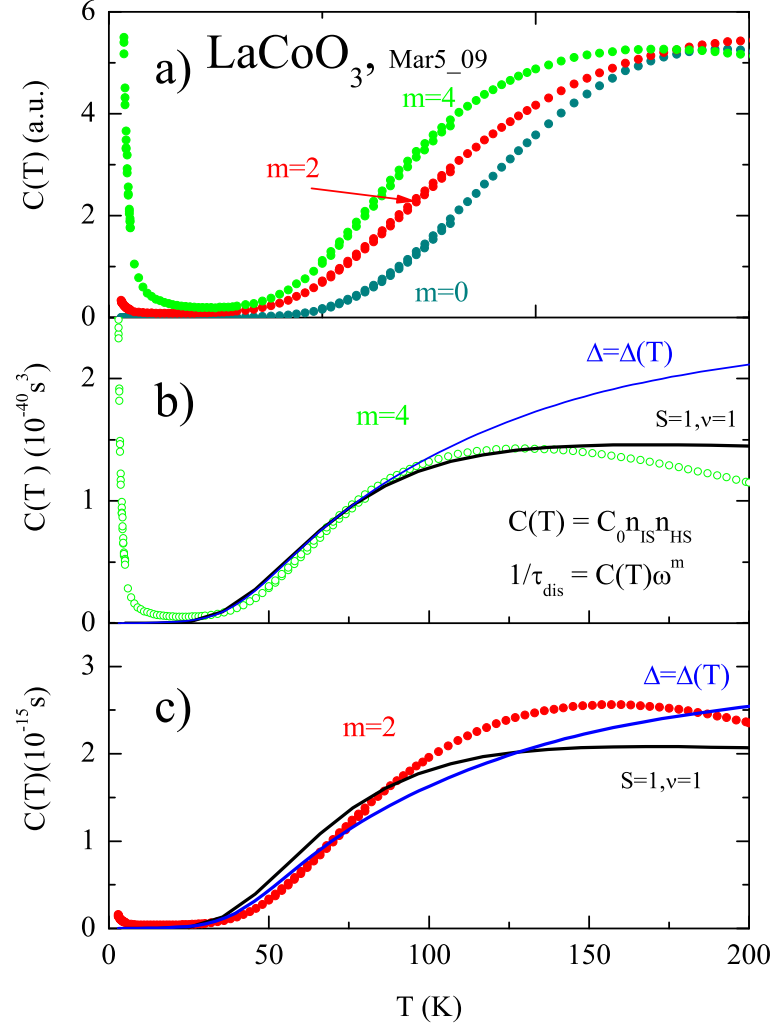
A.7. LaCoO₃

Figure A.25.: Estimated scattering rates $C(T)$ for LaCoO₃ according to Eq. 5.16. The calculation with Eq. 5.12 are shown as solid lines. Different ω^m dependencies of the disorder-scattering rate were used.

List of Figures

2.1. Thermal conductivity of LiF and NdGaO ₃	4
2.2. Sketch resonant scattering	6
2.3. Thermal resistance and level scheme of Holmium ethylsulfate.	7
2.4. Energy levels $4f^2$	10
3.1. Setup for thermal conductivity.	17
3.2. Thermal conductivity of small samples	18
3.3. Setup low-temperature thermal conductivity measurements	20
3.4. Setup Heliox	21
3.5. Setup κ in E field and electrical polarization	22
3.6. Data analysis electrical Polarization	23
3.7. Thermal conductivity of reference samples	25
3.8. Thermocouple test; magnetic field dependence	26
4.1. Crystal structure T and T'-phase	30
4.2. Specific heat of $R_2\text{CuO}_4$ with $R=\text{Sm, Gd}$	33
4.3. Magnetic structures of $R_2\text{CuO}_4$ with $R=\text{Sm, Gd}$	33
4.4. Literature $\text{La}_{2-x}\text{Sr}_x\text{CuO}_4$	36
4.5. Literature data Nd_2CuO_4 by Jin <i>et al.</i>	37
4.6. κ_{mag} vs. T^3 Nd_2CuO_4 by Li <i>et al.</i>	37
4.7. Susceptibility $R_2\text{CuO}_4$	38
4.8. $4f$ level scheme for Pr_2CuO_4 , Nd_2CuO_4 , and Sm_2CuO_4	39
4.9. Magnetic susceptibility of $R_2\text{CuO}_4$	40
4.10. Thermal expansion α for $R_2\text{CuO}_4$ with $R = \text{Sm, Eu, and Gd}$	42
4.11. Magnetization of Sm_2CuO_4 and Eu_2CuO_4	43
4.12. Thermal Conductivity of Gd_2CuO_4	44
4.13. Thermal Conductivity of Pr_2CuO_4	45
4.14. κ vs. temperature in zero field for $R_2\text{CuO}_4$ with $R=\text{Nd, Eu, and Sm}$	46
4.15. thermal conductivity and resistivity of $\text{La}_2\text{CuO}_{4+\delta}$	47
4.16. Magnetic contributions to κ in $R_2\text{CuO}_4$	49
4.17. Mean free path and magnetic correlation length for $R_2\text{CuO}_4$	50
4.18. Diffusion constants low-dimensional spin-systems	52
4.19. κ vs. temperature for Nd_2CuO_4 in magnetic fields	53
4.20. κ vs. magnetic field for Nd_2CuO_4	54
4.21. κ vs. Temperature for Pr_2CuO_4	55
4.22. κ vs. magnetic field for Pr_2CuO_4	56
4.23. Thermal conductivity of Sm_2CuO_4 in magnetic fields.	57
4.24. κ vs. T ; whole temperature range.	57
4.25. κ vs. T and field for Gd_2CuO_4 at low temperatures	57

4.26. κ_{ab} of Gd_2CuO_4 in magnetic fields	58
4.27. Thermal conductivity of Eu_2CuO_4 in magnetic fields.	59
4.28. $\kappa(14\text{ T})/\kappa(0\text{ T})$ for $R_2\text{CuO}_4$ with $R = \text{Pr, Sm, Eu, and Gd}$	60
4.29. $\kappa(T, H)$ for Nd_2CuO_4 in comparison to the literature	61
4.30. Estimated magnetic contributions Nd_2CuO_4	62
4.31. Relative magnetic-field dependence for $R_2\text{CuO}_4$ at 5 K	65
5.1. Structure of $R\text{CoO}_3$	69
5.2. $3d$ orbital in a crystal field and spin states.	70
5.3. Co^{3+} susceptibility of LaCoO_3 and EuCoO_3	71
5.4. Susceptibility of $R\text{CoO}_3$ for $R = \text{La, Pr, Nd, and Eu}$	74
5.5. CF calculation susceptibility and magnetization of PrCoO_3 and NdCoO_3	75
5.6. Temperature-dependent energy gap Δ_{Co} for LaCoO_3 and $\alpha(T)$	76
5.7. $\chi(T)$ for different LaCoO_3 samples	76
5.8. $M(T)$ LaCoO_3	77
5.9. $M(T)$ for different	77
5.10. Magnetization and susceptibility of PrCoO_3 and NdCoO_3	79
5.11. Thermal conductivity and thermal expansion in LaCoO_3	81
5.12. Thermal conductivity of $R\text{CoO}_3$ with $R = \text{La, Pr, Nd, and Eu}$	82
5.13. Literature data LaCoO_3 , PrCoO_3 , and LaCoO_3	83
5.14. Thermal conductivity of LaCoO_3 down to 300 mK	84
5.15. κ vs. H for LaCoO_3 , sample Mar5b_07, down to 300 mK.	85
5.16. κ vs. H for LaCoO_3 , down to 3 K for several samples.	86
5.17. κ vs. T for all LaCoO_3 samples in various magnetic fields.	87
5.18. κ of LaCoO_3 for all investigated samples.	88
5.19. Sketch $\kappa(\omega)$	88
5.20. κ_{\min} LaCoO_3	89
5.21. Thermal resistivity w for LaCoO_3 and EuCoO_3	90
5.22. Calculated scattering rates $C(T)$ for LaCoO_3	91
5.23. Modelation of κ for LaCoO_3	92
5.24. Scaling of thermal expansion and specific heat of EuCoO_3	93
5.25. Sketch of volume changes LaCoO_3	94
5.26. Thermal conductivity of $R\text{CoO}_3$ in magnetic fields	96
5.27. Scattering rates for PrCoO_3 and NdCoO_3	97
5.28. Schottky contributions to thermal expansion and specific heat $R\text{CoO}_3$	98
5.29. Resonant scattering in PrCoO_3	99
6.1. Resistivity of $\text{La}_{1-x}\text{Sr}_x\text{CoO}_3$	103
6.2. Thermal conductivity LaCoO_3	104
6.3. Thermal conductivity LaCoO_3 in magnetic fields	105
6.4. Thermopower of LaCoO_3	106
6.5. Thermopower of undoped LaCoO_3	107
6.6. Figure of Merit of LaCoO_3	108
6.7. Resistivity of $\text{La}_{0.75-x}\text{Eu}_{0.25}\text{Sr}_x\text{CoO}_3$	110
6.8. Thermopower of $\text{La}_{0.75-x}\text{Eu}_{0.25}\text{Sr}_x\text{CoO}_3$	111
6.9. Thermal conductivity of $\text{La}_{0.75-x}\text{Eu}_{0.25}\text{Sr}_x\text{CoO}_3$	111
6.10. Figure of Merit of $\text{La}_{0.75-x}\text{Eu}_{0.25}\text{Sr}_x\text{CoO}_3$	112

7.1. Structure $RMnO_3$	115
7.2. Phase diagram of $RMnO_3$	116
7.3. Thermal conductivity of $RMnO_3$ for various R and literature data	119
7.4. Magnetization and specific heat of $NdMnO_3$	120
7.5. Thermal expansion of $NdMnO_3$ in zero field	121
7.6. κ and C/T of $NdMnO_3$	122
7.7. Thermal expansion α_b of $NdMnO_3$ for $H \parallel c$	123
7.8. Thermal expansion α_c of $NdMnO_3$ for $H \parallel c$	124
7.9. Schottky contribution to α in $NdMnO_3$	125
7.10. Thermal expansion α_b of $NdMnO_3$ for $H \parallel b$	126
7.11. Magnetostriction $NdMnO_3$	127
7.12. Calculation of the total effective field.	128
7.13. Magnetization $M(H)$ of $NdMnO_3$ and model calculations	129
7.14. Schematic picture for the calculation Mn Canting in $NdMnO_3$	132
7.15. Calculation spin-flop field in $NdMnO_3$	133
7.16. Specific heat analysis $NdMnO_3$ and $LaMnO_3$	136
7.17. Analysis thermal conductivity $NdMnO_3$ and $LaMnO_3$	137
7.18. Thermal conductivity of $NdMnO_3$ along the b axis in magnetic fields	138
7.19. $H - T$ phase diagram of $TbMnO_3$	140
7.20. Thermal conductivity κ_b of $TbMnO_3$	141
7.21. Polarization of $TbMnO_3$ and κ in electric fields	143
A.1. Thermal conductivity of $TbMnO_3$, κa , $H \parallel b$	149
A.2. Thermal conductivity of $TbMnO_3$, κa , $H \parallel a$	150
A.3. Thermal conductivity of $TbMnO_3$, κa , $H \parallel b$, hysteresis	150
A.4. Thermal conductivity $TbMnO_3$, κa , $H \parallel b$, low-temperature measurements	151
A.5. Thermal conductivity $TbMnO_3$, κa , zero field	151
A.6. Thermal conductivity $TbMnO_3$, correction radiation losses	152
A.7. Thermal conductivity of $TbMnO_3$, κb , $H \parallel b$, $H \parallel c$	153
A.8. κ vs. H of $TbMnO_3$, κa , $H \parallel b$	154
A.9. κ vs. H of $TbMnO_3$, κb , $H \parallel c$	154
A.10. Thermal conductivity of $TbMnO_3$, κa , $H \parallel b$	155
A.11. Thermal conductivity κ_b of $TbMnO_3$ vs. H	156
A.12. Thermal conductivity of $GdMnO_3$ in zero field	157
A.13. Thermal conductivity vs. H of $GdMnO_3$	158
A.14. Thermal conductivity of $GdMnO_3$ in magnetic fields.	159
A.15. Thermal conductivity of $GdFe_3(BO_3)_4$ in zero field	160
A.16. Thermal conductivity of $GdFe_3(BO_3)_4$ with $j_H [001]$	160
A.17. Thermal conductivity of $GdFe_3(BO_3)_4$ with $j_H [010]$	161
A.18. κ vs H of $GdFe_3(BO_3)_4$ with $j_H [001]$	161
A.19. κ vs H of $GdFe_3(BO_3)_4$ with $j_H [010]$	162
A.20. $[\kappa$ of $GdFe_3(BO_3)_4$, analysis	162
A.21. Thermal conductivity of Bechgaard Salts	163
A.22. Thermal conductivity of $Sr_{14}Cu_{24}O_{41}$	164
A.23. Thermal conductivity of $La_8Ca_7O_{19}$	164
A.24. Thermal conductivity of $Ca_3Co_2O_6$	165
A.25. Scattering rates $C(T)$ for $LaCoO_3$, different ω^m dependencies	166

List of Tables

2.1.	Crystal field energies PrMO_3 and NdMO_3	13
2.2.	Some properties of R^{3+} ions	13
2.3.	Parameters R^{3+}	14
3.1.	Estimated radiation losses	19
3.2.	Sample dimensions of the used reference samples	24
4.1.	Samples properties and Debye fit parameters for $R_2\text{CuO}_4$	29
4.2.	J , T_N , and magnetic groundstate for $R_2\text{CuO}_4$	31
4.3.	Parameters low-temperature susceptibility for $R_2\text{CuO}_4$ and $\text{Sr}_2\text{CuO}_2\text{Cl}_2$	42
5.1.	Sample sizes $R\text{CoO}_3$	72
5.2.	$R\text{CoO}_3$: Key parameters	73
5.3.	Parameters LaCoO_3 , impurity estimation	78
5.4.	κ in $R\text{CoO}_3$: Some κ and S values.	80
5.5.	Fit parameter Debye fits LaCoO_3	91
5.6.	Parameters scattering strength caused by volume differences of the Co^{3+} ions.	95
6.1.	Oxygen content δ of the $\text{La}_{1-x}\text{Sr}_x\text{CoO}_{3+\delta}$ crystals	102
7.1.	Exchange constants and MF calculations $R\text{MnO}_3$	117
7.2.	Sample sizes $R\text{MnO}_3$	118
7.3.	Fit-parameters Schottky contribution of NdMnO_3	125
7.4.	Parameters for the susceptibility analysis in NdMnO_3	130
7.5.	Parameters Schottky peak NdMnO_3	134
7.6.	Fitparameter $R\text{MnO}_3$	137

Bibliography

- [1] J.G. Bednorz and K.A. Müller. Z. Physik B **64**, 189–193 (1986). [1](#), [27](#)
- [2] J.M.D. Coey, M. Viret, and S. v. Molnár. Adv. in Phys. **48**, 167–293 (1999). [1](#)
- [3] C. Hess, C. Baumann, U. Ammerahl, B. Büchner, F. Heidrich-Meisner, W. Brenig, and A. Revcolevschi. Phys. Rev. B **64**, 184305 (2001). [1](#), [28](#), [50](#), [164](#)
- [4] A.V. Sologubenko, K. Gianno, H.R. Ott, U. Ammerahl, and A. Revcolevschi. Phys. Rev. Lett. **84**, 2714 (2000). [1](#), [28](#), [50](#)
- [5] M. Hofmann, T. Lorenz, A. Freimuth, G.S. Uhrig, H. Kageyama, Y. Ueda, G. Dhalenne, and A.M. Revcolevschi. Physica B **312**, 597 (2002). [1](#), [28](#), [84](#)
- [6] Y. Nakamura, S. Uchida, T. Kimura, N. Motohira, K. Kishio, K. Kitazawa, T. Arima, and Y. Tokura. Physica C **185-189**, 1409 (1991). [1](#), [27](#), [28](#), [29](#), [35](#), [36](#), [46](#), [48](#), [49](#), [50](#), [66](#), [145](#)
- [7] X.F. Sun, J. Takeya, S. Komiya, and Y. Ando. Phys. Rev. B **67**, 104503 (2003). [1](#), [27](#), [28](#), [29](#), [35](#), [46](#), [48](#), [49](#), [66](#)
- [8] C. Hess, B. Büchner, U. Ammerahl, L. Colonescu, F. Heidrich-Meisner, W. Brenig, and A. Revcolevschi. Phys. Rev. Lett. **90**, 197002 (2003). [1](#), [27](#), [28](#), [35](#), [46](#), [49](#), [66](#)
- [9] J.-Q. Yan, J.-S. Zhou, and J.B. Goodenough. Phys. Rev. B **69**, 134409 (2004). [1](#), [2](#), [50](#), [67](#), [69](#), [71](#), [82](#), [83](#), [94](#), [100](#), [147](#)
- [10] S.Y. Li, L. Taillefer, C.H. Wang, and X.H. Chen. Phys. Rev. B **95**, 156603 (2005). [1](#), [28](#), [35](#), [36](#), [37](#), [60](#), [61](#), [62](#), [67](#), [146](#)
- [11] J.-Q. Yan, J.-S. Zhou, and J.B. Goodenough. Phys. Rev. B **68**, 104520 (2003). [1](#), [27](#), [28](#), [29](#), [31](#), [35](#), [41](#), [46](#), [48](#), [49](#), [50](#), [52](#), [66](#)
- [12] C. Zobel, M. Kriener, D. Bruns, J. Baier, M. Grüninger, T. Lorenz, P. Reutler, and A. Revcolevschi. Phys. Rev. B **66**, 020402 (2002). [1](#), [70](#), [71](#), [72](#), [100](#), [101](#), [102](#)
- [13] M.W. Haverkort, Z. Hu, J.C. Cezar, T. Burnus, H. Hartmann, M. Reuther, C. Zobel, T. Lorenz, A. Tanaka, N.B. Brookes, H.H. Hsieh, H.-J Lin, C.T. Chen, and L.H Tjeng. Accepted by PRL (2006). [2](#), [70](#), [74](#), [100](#)
- [14] T. Kimura, S. Ishihara, H. Shintani, T. Arima, K.T. Takahashi, K. Ishizaka, and Y. Tokura. Nature **426**, 55–58 (2003). [2](#), [23](#), [115](#), [117](#)
- [15] T. Goto, T. Kimura, G. Lawes, A.P. Ramirez, and Y. Tokura. Phys. Rev. Lett. **92**, 257201 (2004). [2](#), [116](#)
- [16] C. Kittel. *Einführung in die Festkörperphysik*. R. Oldenburg Verlag 12. edition (1999). [3](#), [5](#), [39](#), [70](#), [76](#), [128](#)

- [17] R. Bermann. *Thermal Conduction in Solids*. Clarendon Press Oxford (1976). 3, 64
- [18] R.D. Barnard. *Thermoelectricity in Metals and Alloys*. Taylor and Francis Ltd London (1972). 3, 9
- [19] R.R. Heikes. *Thermoelectricity*. Interscience Publishers New York (1961). 3, 9
- [20] F.J. Blatt and P.A. Schroeder. *Thermoelectric Power of Metals*. Plenum Press New York (1976). 3, 9
- [21] R. Berman and J.C.F. Brock. Proc. Roy. Soc. Lond. **A289**, 46 (1965). 4, 5
- [22] W. Schnelle, R. Fischer, and E. Gmelin. J. Phys. D – Applied Phys. **34**, 846 (2001). 4, 5, 80, 95, 135
- [23] C.V. Briscoe and C.F. Squire. Phys. Rev. **106**, 1175 (1957). 4, 5
- [24] P.G. Klemens. Proc. Phys. Soc. **A68**, 1113 (1955). 5, 93
- [25] D.G. Cahill, S.K. Watson, and R.O. Pohl. Phys. Rev. B **46**, 6131 (1992). 6, 89
- [26] P.V.E. McClintock, I.P. Morton, R. Orbach, and H.M. Rosenberg. Proc. Roy. Soc. Lond. **A298**, 359 (1967). 7, 84
- [27] M. Hofmann. PhD thesis, Universität zu Köln (2001). 6, 7, 28, 29, 47, 84
- [28] M. Hofmann, T. Lorenz, G.S. Uhrig, H. Kierspel, O. Zabara, A. Freimuth, H. Kageyama, and Y. Ueda. Phys. Rev. Lett. **87**, 047202 (2001). 7, 28
- [29] C.K. Chau. Phys. Rev. B **6**, 287 (1972). 7, 84
- [30] R. Orbach. Phys. Rev. Lett. **8**, 393 (1962). 7
- [31] R. Orbach. Proc. Roy. Soc. Lond. **77**, 821 (1961). 7
- [32] N.W. Ashcroft and N.D. Mermin. *Solid State Physics*. Saunders College Publishing New York (1976). 8, 9, 117
- [33] C. Zobel. PhD thesis, Universität zu Köln (2002). 8, 16, 69, 72, 101, 102, 103, 104, 105, 106, 107, 185, 186
- [34] M. Haverkort. PhD thesis, Universität zu Köln (2005). 10
- [35] U. Walter. J. Phys. Chem. Solids **45**, 401 (1984). 11, 13
- [36] CrystalFieldTheory version 0.0756, Mathematica package by M. Haverkort (2006). 11, 39, 41, 128
- [37] M. Loewenhaupt. Physica B **163**, 479 (1990). 11, 13
- [38] A. Podlesnyak, S. Rosenkranz, F. Fauth, W. Marti, H.J. Scheel, and A. Furrer. J. Phys. – Condens. Matter **6**, 4099 (1994). 11, 13
- [39] R. Kajimoto, H. Mochizuki, H. Yoshizawa, H. Shintani, T. Kimura, and Y. Tokura. J. Phys. Soc. Japan **74**, 2430 (2005). 11, 13, 117
- [40] I. Sosnowska and P. Fischer. J. Less Common Metals **111**, 109 (1985). 13

-
- [41] K. Feldmann, K. Hennig, L. Kaun, B. Lippold, M.M. Lukina, S. Matthies, W. Matz, and E. Warming. *phys. stat. sol. (b)* **72**, 817 (1975). 13
- [42] W. Marti, P. Fischer, F. Altorfer, H.J. Scheel, and M. Tadin. *J. Phys. – Condens. Matter* **6**, 127 (1994). 13
- [43] P. Lacorre, J.B. Torrance, J. Pannetier, A.I. Nazzal, P.W. Wang, and T.C. Huang. *J. of Solid State Chem.* **91**, 225 (1991). 13
- [44] S. Rosenkranz, M. Medarde, F. Fauth, J. Mesot, M. Zolliker, A. Furrer, U. Staub, P. Lacorre, R. Osborn, R.S. Eccleston, and V. Trounov. *Phys. Rev. B* **60**, 14857 (1999). 13, 73, 75, 98, 99
- [45] H.W. Brinks, H. Fjellvåg, A. Kjekshus, and B.C. Hauback. *J. of Solid State Chem.* **147**, 464–477 (1999). 13, 73
- [46] W. Marti, P. Fischer, J. Schefer, and F. Kubel. *Z. f. Krist.* **211**, 891 (1996). 13
- [47] A. Podlesnyak, S. Rosenkranz, F. Fauth, W. Marti, A. Furrer, A. Mirmelstein, and H.J. Scheel. *J. Phys. – Condens. Matter* **5**, 8973 (1993). 13, 73, 75
- [48] W. Marti, M. Medarde, S. Rosenkranz, P. Fischer, A. Furrer, and C. Klemenz. *Phys. Rev. B* **52**, 4275 (1995). 13, 128
- [49] V.A. Streltsov and N. Ishizawa. *Acta. Cryst. B* **55**, 1 (1999). 13
- [50] R. Przenioslo, I. Sosnowska, M. Loewenhaupt, and A. Taylor. *J. Magn. Magn. Mat.* **140**, 2151 (1995). 13
- [51] J.L. Garciamunoz, J. Rodriguezcarvajal, P. Lacorre, and J.B. Torrance. *Phys. Rev. B* **46**, 4414 (1992). 13
- [52] H. Taguchi. *J. of Solid State Chem.* **122**, 297–302 (1996). 13, 73
- [53] T. Mori, N. Kamegashira, K. Aoki, T. Shishido, and T. Fukuda. *Materials Letters* **54**, 238 (2002). 13
- [54] R.D. Shannon. *Acta. Cryst. A* **32**, 751 (1976). 13, 73, 94, 109
- [55] J. Hemberger, M. Brando, R. Wehn, V.Yu. Ivanov A.A. Mukhin, A.M. Balbashov, and A. Loidl. *Phys. Rev. B* **69**, 064418 (2004). 13, 117, 120, 121, 122, 126, 128, 129, 131, 137, 139
- [56] Private communication, M. Haverkort, (2006). 14
- [57] K. Berggold. diploma thesis, Universität zu Köln (2002). 15, 16, 17, 18, 19, 20, 24, 27, 29, 44, 45, 46, 49, 50, 53, 61, 69, 79, 80, 82
- [58] C. Heß. PhD thesis, Universität zu Köln (2002). 17, 18
- [59] N. Johannsen. diploma thesis, Universität zu Köln (2003). 19
- [60] T. Zabel. PhD thesis, Universität zu Köln (2004). 20
- [61] O. Heyer. diploma thesis, Universität zu Köln (2005). 20, 122

- [62] Photograph by O. Heyer, (2005). 21
- [63] Private communication, A. Sologubenko (2006). 21
- [64] B. Zeini. PhD thesis, Universität zu Köln (1997). 21
- [65] W.C. Myers and R.T. Bate. Rev. Sci. Instrum. **31**, 464 (1960). 22
- [66] J.G. Hust. Nat. Bur. Stand. Special Publication **260-89** (1984). 24
- [67] *Report of Investigation, Research Materials 8420 and 8421 (Datenblatt)*. National Bureau of Standards (1984). 24
- [68] P.A. Lee, N. Nagaosa, and X.G. Wen. Rev. Mod. Phys. **78**, 17 (2006). 27
- [69] Y. Tokura, H. Takagi, and S. Uchida. Nature **337**, 345 (1989). 27
- [70] J.T. Markert, E.A. Early, T. Bjornholm, S. Ghamaty, B.W. Lee, J.J. Neumeier, R.D. Price, C.L. Seaman, and M.B. Maple. Physica C **158**, 178 (1989). 27
- [71] M.A. Kastner, R.J. Birgeneau, G. Shirane, and Y. Endoh. Rev. Mod. Phys. **70**, 897 (1998). 27, 28, 31, 50, 51
- [72] D.C. Johnston. *Normal-state magnetic properties of single-layer cuprate high-temperature superconductors and related materials*. Elsevier Science B.V. (1997). 27, 30, 31, 46, 51
- [73] K. Berggold, T. Lorenz, J. Baier, M. Kriener, D. Senff, H. Roth, A. Severing, H. Hartmann, A. Freimuth, S. Barilo, and F. Nakamura. Phys. Rev. B **73**, 104430 (2006). 27, 31, 39, 44, 45, 46, 49, 53, 61
- [74] K. Berggold, T. Lorenz, J. Baier, M. Kriener, D. Senff, S.D Barilo, and A. Freimuth. Physica B **378**, 1064 (1996). 27, 44, 45
- [75] A.V. Sologubenko, K. Gianno, H.R. Ott, A. Vietkine, and A. Revcolevschi. Phys. Rev. B **64**, 054412 (2001). 28, 50, 51, 52
- [76] Y. Ando, J. Takeya, D.L. Sisson, S.G. Doettinger, I. Tanaka, R.S. Feigelson, and A. Kapitulnik. Phys. Rev. B **58**, R2913 (1998). 28
- [77] A.V. Sologubenko, S.M. Kazakov, H.R. Ott, T. Asano, and Y. Ajiro. Phys. Rev. B **68**, 094432 (2003). 28, 51, 52
- [78] K. Kordonis, A.V. Sologubenko, T. Lorenz, S. W. Cheong, and A. Freimuth. Phys. Rev. Lett. **97**, 115901 (2006). 28, 51, 52, 67
- [79] B.C. Sales, M.D. Lumsden, S.E. Nagler, D. Mandrus, and R. Jin. Phys. Rev. Lett. **88**, 095901 (2002). 28
- [80] R. Jin, Y. Onose, Y. Tokura, D. Mandrus, P. Dai, and B.C. Sales. Phys. Rev. Lett. **91**, 146601 (2003). 28, 29, 31, 35, 36, 37, 41, 45, 46, 48, 49, 55, 59, 60, 61, 62, 67, 146
- [81] J.L. Cohn, C.K. Lowe-Ma, and T.A. Vanderah. Phys. Rev. B **52**, R13134 (1995). 28, 35, 145

-
- [82] M. Hofmann, T. Lorenz, K. Berggold, M. Grüninger, A. Freimuth, G.S. Uhrig, and E. Brück. Phys. Rev. B **67**, 184502 (2003). 28, 29, 47, 48, 50
- [83] A. Junod. in *Physical Properties of High Temperature Superconductors* volume 2. D.M. Ginsberg (Ed.), World Scientific Singapore (1989). 29
- [84] T. Suzuki, T. Fukase, S. Wakimoto, and K. Yamada. Physica B **284-288**, 479 (2000). 29
- [85] M.F. Hundley, J.D. Thompson, S-W. Cheong, Z. Fisk, and S.B. Oseroff. Physica C **158**, 102 (1989). 29, 31, 40
- [86] D.V. Fil, I.G. Kolobov, V.D. Fil, S.N. Barilo, and D.I. Zhigunov. Czech. J. Phys. **46**, Supp. 4, 2155 (1996). 29, 64
- [87] S.L. Cooper, G. A. Thomas, A. J. Millis, P. E. Sulewski, J. Orenstein, D. H. Rapkine, S-W. Cheong, and P.L. Trevor. Phys. Rev. B **42**, R10785 (1990). 29, 31
- [88] M. Grüninger, D. van der Marel, A. Damascelli, A. Erb, T. Nunner, and T. Kopp. Phys. Rev. B **62**, 12422 (2000). 29
- [89] J. Lorenzano and G.A. Sawatzky. Phys. Rev. B **52**, 9576 (1995). 29, 31
- [90] C.Y. Chen, R.J. Birgeneau, M.A. Kastner, N.W. Preyer, and T. Thio. Phys. Rev. B **43**, 392 (1991). 29
- [91] M. Braden, W. Schnelle, W. Schwarz, N. Pyka, G. Heger, Z. Fisk, K. Gamayunov, I. Tanaka, and H. Kojima. Z. Physik B **94**, 29 (1994). 30
- [92] P. Allenspach, S.W. Cheong, A. Dommann, P. Fischer, Z. Fisk, A. Furrer, H.R. Ott, and B. Rupp. Z. Physik B **77**, 185 (1989). 31
- [93] D.E. Cox, A.I. Goldman, M.A. Subramanian, J. Gopalakrishnan, and A.W. Sleight. Phys. Rev. B **40**, 6998 (1989). 31, 49
- [94] M. Matsuda, K. Yamada, K. Kakurai, H. Kadowaki, T.R. Thurston, Y. Endoh, Y. Hidaka, R.J. Birgeneau, M.A. Kastner, P.M. Gehring, A.H. Moudden, and G. Shirane. Phys. Rev. B **42**, 10098 (1990). 31, 49, 50
- [95] T.R. Thurston, M. Matsuda, K. Kakurai, K. Yamada, Y. Endoh, R.J. Birgeneau, P.M. Gehring, Y. Hidaka, M.A. Kastner, T. Murakami, and G. Shirane. Phys. Rev. Lett. **65**, 263 (1990). 31, 51
- [96] J. Akimitsu, H. Sawa, T. Kobayashi, H. Fujiki, and Y. Yamada. J. Phys. Soc. Japan **58**, 2646 (1989). 31
- [97] Y. Endoh, M. Matsuda, K. Yamada, K. Kakurai, Y. Hidaka, G. Shirane, and R. J. Birgeneau. Phys. Rev. B **40**, 7023 (1989). 31
- [98] G.M. Luke, B.J. Sternlieb, Y.J. Uemura, J.H. Brewer, R. Kadono, R.F. Kiefl, S.R. Kretzmann, T.M. Riseman, J. Gopalakrishnan, A.W. Sleight, M.A. Subramanian, S. Uchida, H. Takagi, and Y. Tokura. Nature **338**, 49 (1989). 31

- [99] J.W. Lynn, I.W. Sumarlin, S. Skanthakumar, W-H. Li, R.N. Shelton, J.L. Peng, Z. Fisk, and S-W. Cheong. Phys. Rev. B **41**, 2569 (1990). 31
- [100] S. Skanthakumar, H. Zhang, T.W. Clinton, W.H. Li, and J.W. Lynn. Physica C **160**, 124 (1989). 31
- [101] S. Skanthakumar and J.W. Lynn. Physica C **170**, 175 (1990). 31
- [102] S. Skanthakumar, J.W. Lynn, J.L. Peng, and Z.Y. Li. J. Magn. Magn. Mat. **104**, 519 (1992). 31
- [103] S. Skanthakumar, J.W. Lynn, J.L. Peng, and Z.Y. Li. Phys. Rev. B **47**, 6173 (1993). 31
- [104] S. Skanthakumar, J.W. Lynn, J.L. Peng, and Z.Y. Li. J. Appl. Phys. **69**, 4866 (1991). 31
- [105] Y. Dalichaouch, B.W. Lee, C.L. Seaman, J.T. Markert, and M.B. Maple. Phys. Rev. B **64**, 599 (1990). 31
- [106] S. Ghamaty, B.W. Lee, J.T. Markert, E.A. Early, T. Bjornholm, C.L. Seaman, and M.B. Maple. Physica C **160**, 217–222 (1989). 31
- [107] B. Jiang, B.-H O, and J.T. Markert. Phys. Rev. B **45**, 2311 (1992). 31
- [108] C.L. Semann, N.Y. Ayoub, T. Bjørnholm, E.A. Early, S. Ghamaty, B.W. Lee, J.T. Markert and J.J Neumeier, P.K. Tsai, and M.B. MAPLE. Physica C **159**, 391 (1989). 31
- [109] T. Chattopadhyay, J.W. Lynn, N. Rosov, T.E. Grigereit, S.N. Barilo, and D.I. Zhigunov. Phys. Rev. B **49**, 9944 (1994). 31, 32
- [110] T. Chattopadhyay, P.J. Brown, B. Roessli, A.A. Stepanov, S.N. Barilo, and D.I. Zhigunov. Phys. Rev. B **46**, 5731 (1992). 31
- [111] S. Oseroff, D. Rao, F. Wright, M. Tovar, D.C. Vier, S. Schultz, J.D. Thompson, Z. Fisk, and S.W. Cheong. Sol. State Commun. **70**, 1159 (1989). 31
- [112] J.D. Thompson, S-W. Cheong, S.E. Brown, Z. Fisk, S.B. Oseroff, M. Tovar, D.C. Vier, and S. Schultz. Phys. Rev. B **39**, 6660 (1989). 31, 32
- [113] G. Xiao, M.Z. Cieplak, and C.L. Chien. Phys. Rev. B **40**, 4538 (1989). 31
- [114] T. Chattopadhyay, P.J. Brown, A.A. Stepanov, A.I. Zvyagin, S.N. Barilo, and D.I. Zhigunov. J. Magn. Magn. Mat. **104**, 607 (1992). 31
- [115] P. Adelman, R. Ahrens, G. Czjzek, G. Roth, H. Schmidt, and C. Steinleitner. Phys. Rev. B **46**, 3619 (1992). 31
- [116] J-M. Louis, G. Chouteau, A.A. Stepanov, J. Voiron, S.N. Barilo, and D.I. Zhigunov. Phys. Rev. B **46**, 14301 (1992). 31
- [117] A.S. Cherny, E.N. Khatsko, G. Chouteau, J.M. Louis, A.A. Stepanov, P. Wyder, S.N. Barilo, and D.I. Zhigunov. Phys. Rev. B **45**, 12600 (1992). 31

-
- [118] M. Tovar, D. Rao, J. Barnett, S.B. Oseroff, J.D. Thompson, S-W. Cheong, Z. Fisk, D.C. Vier, and S. Schultz. *Phys. Rev. B* **39**, 2661 (1989). [32](#), [40](#), [41](#)
- [119] M. Braden, W. Paulus, A. Cousson, P. Vigoureux, G. Heger, A. Goukassov, P. Bourges, and D. Petitgrand. *Europhys. Lett.* **25**, 625 (1994). [32](#)
- [120] P. Vigoureux, A. Gukasov, S.N. Barilo, and D. Zhigunov. *Physica B* **234**, 815 (1997). [32](#)
- [121] A.A. Stepanov, P. Wyder, T. Chattopadhyay, P.J. Brown, G. Fillion, I.M. Vitebsky, A. Deville, B. Gaillard, S.N. Barilo, and D.I. Zhigunov. *Phys. Rev. B* **48**, 12979 (1993). [32](#)
- [122] T. Chattopadhyay, P. J. Brown, and B. Roessli. *J. Appl. Phys.* **75**, 6816 (1994). [32](#)
- [123] J. Mira, J. Rivas, D. Fiorani, R. Caciuffo, D. Rinaldi, C. Vázquez-Vázquez, J. Mahía, M.A. López-Quintela, and S.B. Oseroff. *Phys. Rev. B* **52**, 16020 (1995). [32](#), [39](#)
- [124] A. Butera, M. Tovar, S.B. Oseroff, and Z. Fisk. *Phys. Rev. B* **52**, 13444 (1995). [32](#)
- [125] V.A. Pashchenko, S. Huant, A.A. Stepanov, and P. Wyder. *Phys. Rev. B* **61**, 6889 (2000). [32](#)
- [126] H. Martinho, A.A. Martin, N.O. Moreno, J.A. Sanjurjo, C. Rettori, S.B. Oseroff, Z. Fisk, P.G. Pagliuso, and J.L. Sarrao. *Physica B* **305**, 48 (2001). [32](#), [60](#)
- [127] A.D. Alvarenga, D. Rao, J.A. Sanjurjo, E. Granado, I. Torriani, C. Rettori, S. Oseroff, J. Sarrao, and Z. Fisk. *Phys. Rev. B* **53**, 837 (1996). [32](#)
- [128] T. Holubar, H. Michor, G. Chaudyand, G. Hilscher, M. Vybornov, and P. Rogl. *Physica B* **194**, 201–202 (1994). [33](#), [34](#), [58](#)
- [129] T. Holubar, G. Schaudy, N. Pillmayr, G. Hilscher, M. Divis, and V. Nekvasil. *J. Magn. Magn. Mat.* **104**, 479 (1992). [33](#), [34](#), [58](#)
- [130] H. Wiegmann, I.M. Vitebsky, A.A. Stepanov, A.G.M. Jansen, and P. Wyder. *Phys. Rev. B* **55**, 15304 (1997). [33](#), [34](#)
- [131] T. Chattopadhyay, P.J. Brown, A.A. Stepanov, P. Wyder, J. Voiron, A.I. Zvyagin, S. N. Barilo, D. I. Zhigunov, and I. Zobkalo. *Phys. Rev. B* **44**, 9486 (1991). [34](#), [58](#)
- [132] D. Petitgrand, S.V. Maleyev, Ph. Bourges, and A.S. Ivanov. *Phys. Rev. B* **59**, 1079 (1999). [35](#), [36](#)
- [133] D.T. Morelli, J. Heremans, G. Doll, P.J. Picone, H.P. Jenssen, and M.S. Dresselhaus. *Phys. Rev. B* **39**, 804 (1989). [35](#)
- [134] O. Baberski, A. Lang, O. Maldonado, M. Hücker, B. Büchner, and A. Freimuth. *Europhys. Lett.* **44**, 335 (1998). [35](#)
- [135] M. Sera, K. Yamamoto, M. Hiroi, N. Kobayashi, O. Fujita, A. Ogiwara, and J. Akimitsu. *Phys. Rev. B* **56**, 14771 (1997). [35](#)
- [136] M. Sera, M. Maki, M. Hiroi, N. Kobayashi, T. Suzuki, and T. Fukase. *Phys. Rev. B* **52**, R735 (1995). [35](#)

- [137] D.G. Hawthorn, R.W. Hill, C. Proust, F. Ronning, M. Sutherland, E. Boaknin, C. Lupien, M.A. Tanatar, J. Paglione, S. Wakimoto, H. Zhang, L. Taillefer, T. Kimura, M. Nohara, H. Takagi, and N.E. Hussey. Phys. Rev. Lett. **90**, 197004 (2003). 35
- [138] X.F. Sun, S. Komiya, J. Takeya, and Y. Ando. Phys. Rev. Lett. **90**, 117004 (2003). 35
- [139] X.F. Sun, Y. Kurita, T. Suzuki, S. Komiya, and Y. Ando. Phys. Rev. Lett. **92**, 047001 (2004). 35, 66
- [140] C. Hess, B. Buchner, U. Ammerahl, and A. Revcolevschi. Phys. Rev. B **68**, 184517 (2003). 35
- [141] X.F. Sun, S. Komiya, and Y. Ando. Phys. Rev. B **67**, 184512 (2003). 35
- [142] M.F. Hundley, R.S. Kwok, S.W. Cheong, J.D. Thompson, and Z. Fisk. Physica C **172**, 455 (1991). 35, 46
- [143] A.V. Inyushkin, A.N. Taldenkov, L.N. Demyanets, T.G. Uvarova, and A.B. Bykov. Physica B **194-196**, 479 (1994). 35, 44
- [144] X.F. Sun, I. Tsukada, T. Suzuki, S. Komiya, and Y. Ando. Phys. Rev. B **72**, 104501 (2005). 35, 36, 43
- [145] J.M. Ziman. *Electrons and Phonons*. Oxford University Press (1960). 36
- [146] D. Vaknin, S.K. Sinha, C. Stassis, L.L. Miller, and D.C. Johnston. Phys. Rev. B **41**, 1926 (1990). 37, 42, 43
- [147] Measurements of $\chi(T)$ for Gd_2CuO_4 by J. Baier and H. Roth. 38
- [148] Determination of T_N of Pr_2CuO_4 by D. Senff. 38
- [149] Measurements of $\chi(T)$ for La_2CuO_4 by H. Hartmann. 38
- [150] R. Sachidanandam, T. Yildirim, A.B. Harris and A. Aharony, and O. Entin-Wohlman. Phys. Rev. B **56**, 260 (1997). 39, 40
- [151] M. Hücker. PhD thesis, Universität zu Köln (1999). 40, 41
- [152] S.N. Barilo, D.I. Zhigunov, and S.V. Shiryayev. *Physico-Chemical Fundamentals of Growth and Properties of $R_{2-x}\text{Me}_x\text{CuO}_4$ ($\text{Me}=\text{Sr}, \text{Ce}$)*. In: *High Temp. Supercond.* volume 1. H.S. Freyhardt, R. Flukiger, M. Peuckert, Informationsgesellschaft Verlag (1993). 38
- [153] P.W. Klamut. Phys. Rev. B **50**, 13009 (1994). 39
- [154] A.T. Boothroyd, S.M. Doyle, D.M.K. Paul, and R. Osborn. Phys. Rev. B **45**, 10075 (1992). 39
- [155] T. Strach, T. Ruf, M. Cardona, C.T. Lin, S. Jandl, V. Nekvasil, D.I. Zhigunov, S.N. Barilo, and S.V. Shiryayev. Phys. Rev. B **54**, 4276 (1996). 39
- [156] T. Thio, T.R. Thurston, N.W. Preyer, P.J. Picone, M.A. Kastner, H.P. Jenssen, D.R. Gabbe, C.Y. Chen, R.J. Birgeneau, and A. Aharony. Phys. Rev. B **38**, R905 (1988). 41

-
- [157] Measurements of $\alpha(T)$ for Sm_2CuO_4 and Gd_2CuO_4 by M. Kriener, see [205] (2005). 42
- [158] Measurements of $\alpha(T)$ for Eu_2CuO_4 by J. Baier, see [273] (2005). 42
- [159] D.C. Johnston, S.K. Sinha, A.J. Jacobson, and J.M. Newsam. *Physica C* **153**, 572 (1988). 45
- [160] N.W. Preyer, R.J. Birgeneau, C.Y. Chen, D.R. Gabbe, H.P. Jenssen, M.A. Kastner, P.J. Picone, and T. Thio. *Phys. Rev. B* **39**, 11563 (1989). 45
- [161] J.D. Jorgensen, B. Dabrowski, S.S. Pei, D.G. Hinks, L. Soderholm, B. Morosin, J.E. Schirber, E.L. Venturini, and D.S. Ginley. *Phys. Rev. B* **38**, 11337 (1988). 46
- [162] J.D. Yu, Y. Inaguma, M. Itoh, M. Oguni, and T. Kyomen. *Phys. Rev. B* **54**, 7455 (1996). 46
- [163] J.D. Yu, M. Itoh, T. Huang, Y. Inaguma, and T. Nakamura. *Physica C* **235**, 1323 (1994). 46
- [164] M. Hücker, V. Kataev, J. Pommer, J. Haraß, A. Hosni, C. Pflictsch, R. Gross, and B. Büchner. *Phys. Rev. B* **59**, R725 (1999). 49
- [165] I.W. Sumarlin, J.W. Lynn, T. Chattopadhyay, S.N. Barilo, D.I. Zhigunov, and J.L. Peng. *Phys. Rev. B* **51**, 5824 (1995). 49
- [166] K. Berggold, M. Kriener, C. Zobel, A. Reichel, M. Reuther, R. Müller, A. Freimuth, and T. Lorenz. *Phys. Rev. B* **72**, 155116 (2005). 50, 69, 101, 102, 104, 105, 106, 107
- [167] T. Oguchi. *Phys. Rev.* **117**, 117 (1960). 50
- [168] K. Sun, J.H. Cho, F.C. Chou, W.C. Lee, L.L. Miller, D.C. Johnston, Y. Hidaka, and T. Murakami. *Phys. Rev. B* **43**, 239 (1991). 51
- [169] A.V. Sologubenko, H.R. Ott, G. Dhalenne, and A. Revcolevschi. *Europhys. Lett.* **62**, 540 (2003). 51, 52
- [170] B. Sales, R. Jin, and D. Mandrus. *cond-mat/0401154* (2004). 55
- [171] G.A. Slack. *Phys. Rev. B* **122**, 1451 (1961). 56
- [172] R.F. Jardim, C.H. Westphal, C.C. Becerra, and A. Paduan-Filho. *Phys. Rev. B* **45**, 10485 (1992). 58
- [173] R.O. Pohl and B. Stritzker. *Phys. Rev. B* **25**, 3608 (1982). 64
- [174] N.T. Hien, V.H.M. Duijn, J.H.P. Colpa, J.J.M. Franse, and A.A. Menovsky. *Phys. Rev. B* **57**, 5906 (1998). 65
- [175] J.B. Goodenough and P.M. Raccah. *J. Appl. Phys.* **36**, 1031 (1965). 69
- [176] M.A. Señarís-Rodríguez and J.B. Goodenough. *J. of Solid State Chem.* **116**, 224 (1995). 69, 70, 101, 102, 109, 113
- [177] H. Anapa. diploma thesis, Universität zu Köln (2004). 69, 71, 101, 110, 184, 186

- [178] J. Baier, S. Jodlauk, M. Kriener, A. Reichl, C. Zobel, H. Kierspel, A. Freimuth, and T. Lorenz. Phys. Rev. B **71**, 014443 (2005). [69](#), [70](#), [71](#), [72](#), [73](#), [74](#), [102](#), [109](#)
- [179] A. Reichl. diploma thesis, Universität zu Köln (2002). [69](#), [72](#), [73](#), [102](#), [109](#)
- [180] G. Demazeau, M. Pouchard, and P. Hagenmuller. J. of Solid State Chem. **9**, 202 (1974). [69](#)
- [181] G. Thornton, B.C. Tofield, and A.W. Hewat. J. of Solid State Chem. **61**, 301 (1986). [69](#)
- [182] S. Yamaguchi, Y. Okimoto, and Y. Tokura. Phys. Rev. B **54**, R11022 (1996). [69](#)
- [183] S. Sugano, Y. Tanabe, and H. Kamimura. *Multiplets of Transition-Metal Ions in Crystals*. Academic Press New York and London 1. edition (1970). [70](#)
- [184] R.H. Potze, G.A. Sawatzky, and M. Abbate. Phys. Rev. B **51**, 11501 (1995). [70](#)
- [185] M.A. Korotin, S.Y. Ezhov, I.V. Solovyev, V.I. Anisimov, D.I. Khomskii, and G.A. Sawatzky. Phys. Rev. B **54**, 5309 (1996). [70](#), [101](#)
- [186] M. Itoh, M. Mori, M. Sugahara, T. Yamauchi, and Y. Ueda. Physica B **230-232**, 756–758 (1997). [70](#)
- [187] T. Saitoh, T. Mizokawa, A. Fujimori, M. Abbate, Y. Takeda, and M. Takano. Phys. Rev. B **55**, 4257 (1997). [70](#)
- [188] S. Stølen, F. Grønvd, H. Brinks, T. Atake, and H. Mori. Phys. Rev. B **55**, 14103 (1997). [70](#), [90](#)
- [189] S. Yamaguchi, Y. Okimoto, and Y. Tokura. Phys. Rev. B **55**, 8666 (1997). [70](#), [101](#)
- [190] K. Asai, A. Yoneda, O. Yokokura, J.M. Tranquada, G. Shirane, and K. Kohn. J. Phys. Soc. Japan **67**, 290 (1998). [70](#), [101](#)
- [191] Y. Tokura, Y. Okimoto, S. Yamaguchi, H. Taniguchi, T. Kimura, and H. Takagi. Phys. Rev. B **58**, 1699 (1998). [70](#)
- [192] Y. Kobayashi, N. Fujiwara, S. Murata, K. Asai, and H. Yasuoka. Phys. Rev. B **62**, 410 (2000). [70](#)
- [193] Y. Kobayashi, N. Fujiwara, S. Murata, K. Asai, and Y. Yasuoka. Physica B **281&282**, 512–513 (2000). [70](#)
- [194] S. Xu, Y. Moritomo, K. Mori, T. Kamiyama, T. Saitoh, and A. Nakamura. J. Phys. Soc. Japan **70**, 3296 (2001). [70](#)
- [195] S.R. English, J. Wu, and C. Leighton. Phys. Rev. B **65**, 220407 (2002). [70](#)
- [196] P. Ravindran, H. Fjellvåg, A. Kjekshus, P. Blaha, K. Schwarz, and J. Luitz. J. Appl. Phys. **91**, 291 (2002). [70](#)
- [197] G. Maris, Y. Ren, V. Volotchaev, C. Zobel, T. Lorenz, and T.T.M. Palstra. Phys. Rev. B **67**, 224423 (2003). [70](#), [71](#)

-
- [198] I.A. Nekrasov, S.V. Streltsov, M.A. Korotin, and V.I. Anisimov. Phys. Rev. B **68**, 235113 (2003). 70
- [199] T. Vogt, J.A. Hriljac, N.C. Hyatt, and P. Woodward. Phys. Rev. B **67**, 140401(R) (2003). 70
- [200] O. Haas, R.P.W.J. Struis, and J.M. McBreen. J. of Solid State Chem. **177**, 1000–1010 (2004). 70, 73
- [201] A. Ishikawa, J. Nohara, and S. Sugai. Phys. Rev. Lett. **93**, 136401 (2004). 70, 71
- [202] Measurements of the susceptibility for LaCoO_3 and EuCoO_3 by M. Kriener and J. Baier, see Refs.[302] (2001) and [206] (2002). 70, 71, 74
- [203] Z. Hu, H. Wu, M. W. Haverkort, H. H. Hsieh, H.-J. Lin, T. Lorenz, J. Baier, A. Reichl, I. Bonn, C. Felser, A. Tanaka, C. T. Chen, and L. H. Tjeng. Phys. Rev. Lett. **92**, 207402 (2004). 70, 101
- [204] S. Noguchi, S. Kawamata, K. Okuda, H. Nojiri, and M. Motokawa. Phys. Rev. B **66**, 94404 (2002). 70, 73
- [205] M. Kriener. PhD thesis, Universität zu Köln (2005). 70, 71, 72, 73, 74, 75, 76, 90, 93, 94, 98, 101, 102, 103, 104, 105, 108, 121, 181
- [206] J. Baier. diploma thesis, Universität zu Köln (2002). 71, 109, 117, 183
- [207] M. Benomar. PhD thesis, Universität zu Köln (in Vorbereitung). 71, 72
- [208] H.A. Jahn and E. Teller. Proc. Roy. Soc. Lond. **161**, 220 (1937). 71
- [209] Z. Ropka and R. J. Radwanski. Physica B **312-313**, 777–779 (2002). 71
- [210] F. Fauth, E. Suard, and V. Caignaert. Phys. Rev. B **65**, 060401 (2001). 71
- [211] D. Louca and J.L. Sarrao. Phys. Rev. Lett. **91**, 155501 (2003). 71
- [212] D. Louca. Physica B **329-333**, 835–836 (2003). 71
- [213] M. Kriener, C. Zobel, A. Reichl, J. Baier, M. Cwik, K. Berggold, H. Kierspel, O. Zabara, A. Freimuth, and T. Lorenz. Phys. Rev. B **69**, 094417 (2004). 72, 102, 103, 104, 105, 108, 113
- [214] M. Reuther. diploma thesis, Universität zu Köln (2005). 72, 164
- [215] S. Yamaguchi, Y. Okimoto, H. Taniguchi, and Y. Tokura. Phys. Rev. B **53**, 2926 (1996). 72, 78, 104
- [216] J.H. van Vleck. *The Theory of Electric and Magnetic Susceptibilities*. Oxford University Press (1965). 72
- [217] Measurements of the susceptibility for PrCoO_3 and NdCoO_3 by S. Jodlauk, see Ref.[320] (2005). 74
- [218] Measurements of $\chi(T)$ and $M(H)$ for the samples Mar5b_07, Mar5a_08, Mar5_09, and ZO104 by H. Hartmann, see [321] (2005). 76

- [219] F. Bartolome, M.D. Kuzmin, J. Bartolome, J. Blasco, J. Garcia, and F. Sapina. Sol. State Commun. **91**, 177 (1994). [79](#), [98](#)
- [220] Y. Kobayashi, T.S. Naing, M. Suzuki, M. Akimitsu, K. Asai, K. Yamada, J. Akimitsu, P. Manuel, J.M. Tranquada, and G. Shirane. Phys. Rev. B **72**, 174405 (2005). [80](#)
- [221] Measurements of the thermal conductivity for PrCoO_3 and NdCoO_3 by H. Anapa, see Ref.[\[177\]](#) (2004). [80](#)
- [222] C.G.S. Pillai and A.M. George. Int. J. Thermophys. **12**, 207 (1991). [82](#)
- [223] P. Gerthsen and F. Kettel. J. Phys. Chem. Solids **25**, 1023 (1964). [82](#)
- [224] G.A. Toombs and F.W. Sheard. J. Phys. – Condens. Matter **6**, 1467 (1973). [84](#)
- [225] S. Murata, S. Isida, M. Suzuki, Y. Kobayashi, K. Asai, and K. Kohn. Physica B **263-264**, 647–249 (1999). [89](#), [90](#), [94](#)
- [226] L. Nordheim. Phys. Rev. B **401**, 607 (1931). [90](#)
- [227] B. Abeles. Phys. Rev. **131**, 1906 (1963). [93](#)
- [228] J.-S Zhou, J.-Q Yan, and J.B. Goodenough. Phys. Rev. B **71**, 220103 (2005). [93](#), [94](#)
- [229] P.G. Radaelli and S.-W. Cheong. Phys. Rev. B **66**, 94408 (2002). [94](#)
- [230] G.A. Slack and D.W. Oliver. Phys. Rev. B **4**, 592 (1971). [97](#)
- [231] J.L. Prather. *Atomic energy levels in crystals*. National Bureau of Standards monograph 19 (1961). [99](#)
- [232] C. Hanebeck. diploma thesis, Universität zu Köln (2002). [101](#), [102](#), [109](#), [112](#), [186](#)
- [233] G.H. Jonker and J.H. Van Santen. Physica **XIX**, 120 (1953). [101](#)
- [234] K. Asai, O. Yokokura, N. Nishimori, H. Chou, J.M. Tranquada, G. Shirane, S. Higuchi, Y. Okajima, and K. Kohn. Phys. Rev. B **50**, 3025 (1994). [101](#)
- [235] T. Vogt, P.M. Woodward, P. Karen, B.A. Hunter, P. Henning, and A.R. Moodenbaugh. Phys. Rev. Lett. **84**, 2969 (2000). [101](#)
- [236] E. Suard, F. Fauth, V. Caignaert, I. Mirebeau, and G. Baldinozzi. Phys. Rev. B **61**, 11871 (2000). [101](#)
- [237] Y. Moritomo, T. Akimoto, M. Takeo, A. Machida, E. Nishibori, M. Takata, M. Sakata, K. Ohoyama, and A. Nakamura. Phys. Rev. B **61**, R13325 (2000). [101](#)
- [238] M. Respaud, C. Frontera, J.L. García-Muñoz, M.A.G. Aranda, B. Raquet, J.M. Broto, H. Rakoto, M. Goiran, A. Llobet, and J. Rodríguez-Carvajal. Phys. Rev. B **64**, 214401 (2001). [101](#)
- [239] H. Wu. Phys. Rev. B **64**, 92413 (2001). [101](#)
- [240] J. Wang, Weiyi Zhang, and D. Y. Xing. Phys. Rev. B **64**, 64418 (2001). [101](#)
- [241] S. Roy, M. Khan, Y.Q. Guo, J. Craig, and N. Ali. Phys. Rev. B **65**, 64437 (2002). [101](#)

-
- [242] E. Rose. diploma thesis, Universität zu Köln (2006). 101
- [243] K. Takada, H. Sakurai, E. Takayama-Muromachi, F. Izumi, R.A. Dilanian, and T. Sasaki. *Nature* **422**, 53 (2003). 101
- [244] K. Takahata, Y. Iguchi, D. Tanaka, T. Itoh, and I. Terasaki. *Phys. Rev. B* **61**, 12551 (2000). 101, 109
- [245] R. Venkatasubramanian, E. Siivola, T. Colpitts, and B. O’Quinn. *Nature* **413**, 597 (2001). 101
- [246] T.C. Harmann, P.J. Taylor, M.P. Walsh, and B.E. LaForge. *Science* **297**, 2229 (2002). 101
- [247] I. Terasaki, Y. Sasago, and K. Uchinokura. *Phys. Rev. B* **56**, R12685 (1997). 101
- [248] Y. Wang, N.S. Rogado, R.J. Cava, and N.P. Ong. *Nature* **423**, 425 (2003). 101, 107
- [249] M.A. Se  ar  s-Rodr  guez and J.B. Goodenough. *J. of Solid State Chem.* **118**, 323 (1995). 101, 102, 106
- [250] P.S. Anil Kumar, P.A. Joy, and S.K. Date. *J. Appl. Phys.* **83**, 7375 (1998). 102
- [251] M. Itoh, I. Natori, S. Kubota, and K. Motoya. *J. Phys. Soc. Japan* **63**, 1486 (1994). 102
- [252] S.R. Sehlin, H.U. Anderson, and D.M. Sparlin. *Phys. Rev. B* **52**, 11681 (1995). 102, 109, 113
- [253] Measurements of the oxygen content of $\text{La}_{1-x}\text{Sr}_x\text{CoO}_3$ with $x = 0 \dots 0.3$ by T. Lorenz and S. Heiligen (2005). 102
- [254] R. Lengsdorf, M. Ait-Tahar, S.S. Saxena, M. Ellerby, D.I. Khomskii, H. Micklitz, T. Lorenz, and M.M. Abd-Elmeguid. *Phys. Rev. B* **69**, 140403(R) (2004). 102
- [255] A. Maignan, D. Flahaut, and S. H  bert. *The European Phys. J. B* **39**, 145–148 (2004). 102, 108
- [256] A. Maignan, V. Caignaert, B. Raveau, D. Khomskii, and G. Sawatzky. *Phys. Rev. Lett.* **93**, 026401 (2004). 102
- [257] M. James, D. Cassidy, D.J. Goossens, and R.L. Withers. *J. of Solid State Chem.* **177**, 1886–1895 (2004). 103
- [258] D.J. Goossens, K.F. Wilson, M. James, A.J. Studer, and X.L. Wang. *Phys. Rev. B* **69**, 134411 (2004). 103
- [259] K. Conder, E. Pomjakushina, A. Soldatov, and E. Mitberg. *Mater. Res. Bull.* **40**, 257–263 (2005). 103
- [260] Measurements of the zero-field resistivity for $\text{La}_{1-x}\text{Sr}_x\text{CoO}_3$ by C. Zobel, see Ref.[33] (2002). 103
- [261] Measurements of the field-dependent resistivity for $\text{La}_{1-x}\text{Sr}_x\text{CoO}_3$ with $x = 0.25$ by M. Zittarz, see Ref.[322] (2002). 103

- [262] Measurements of the thermal conductivity $\text{La}_{1-x}\text{Sr}_x\text{CoO}_3$ for $x = 0.002 \dots 0.18$ by C. Zobel, see Ref.[33] (2002). 104, 105
- [263] R. Mahendiran and A.K. Raychaudhuri. Phys. Rev. B **54**, 16044 (1996). 105
- [264] Measurements of the thermopower in $\text{La}_{1-x}\text{Sr}_x\text{CoO}_3$ for $x = 0.002 \dots 0.18$ by C. Zobel, see Ref.[33] (2002). 106
- [265] Measurements of the thermopower in $\text{La}_{1-x}\text{Sr}_x\text{CoO}_3$ for $x = 0.002 \dots 0.18$ and for crystal EKPari by C. Zobel, see Ref.[33] (2002). 107
- [266] P.M. Chaikin and G. Beni. Phys. Rev. B **13**, 647 (1976). 107
- [267] W. Koshibae, K. Tsutsui, and S. Maekawa. Phys. Rev. B **62**, 6869 (2000). 107, 108, 113
- [268] Measurements of the resistivity for $\text{La}_{0.75-x}\text{Eu}_{0.25}\text{Sr}_x\text{CoO}_3$ with $x = 0.1, 0.2, 0.3$, and 0.4 by C. Hanebeck, see Ref.[232] (2002). 110
- [269] Measurements of the thermopower for $\text{La}_{0.75-x}\text{Eu}_{0.25}\text{Sr}_x\text{CoO}_3$ with $x = 0, 0.1, 0.2, 0.3$, and 0.4 by H. Anapa, see Ref.[177] (2004). 111
- [270] Measurements of the thermal conductivity for $\text{La}_{0.75-x}\text{Eu}_{0.25}\text{Sr}_x\text{CoO}_3$ with $x = 0, 0.1, 0.2, 0.3$, and 0.4 by H. Anapa, see Ref.[177] (2004). 110, 111
- [271] Measurements of the resistivity for $\text{La}_{0.75-x}\text{Eu}_{0.25}\text{Sr}_x\text{CoO}_3$ with $x = 0, 0.1, 0.2, 0.3$, and 0.4 by C. Hanebeck, see Ref.[232] (2002). 109
- [272] J.S. Zhou and J.B. Goodenough. Phys. Rev. Lett. **96**, 247202 (2006). 115, 118, 119, 137, 144, 148
- [273] J. Baier. PhD thesis, Universität zu Köln (2006). 116, 118, 119, 120, 122, 140, 157, 181
- [274] T. Arima, T. Goto, Y. Yamasaki, S. Miyasaka, K. Ishii, M. Tsubota, T. Inami, Y. Murakami, and Y. Tokura. Phys. Rev. B **72**, 100102(R) (2005). 116, 117
- [275] J. Rodríguez-Carvajal, M. Hennion, F. Moussa, A.H. Moudden, L. Pinsard, and A. Revcolevschi. Phys. Rev. B **57**, R3189 (1998). 116
- [276] Masatoshi Imada, Atsushi Fujimori, and Yoshinori Tokura. Rev. Mod. Phys. **70**, 1039 (1998). 116
- [277] J.S. Zhou and J.B. Goodenough. Phys. Rev. B **68**, 144406 (2003). 116
- [278] B. Dabrowski, S. Kolesnik, A. Baszczuk, O. Chmaissem, T. Maxwell, and J. Mais. J. of Solid State Chem. **178**, 629 (2005). 116
- [279] G. Maris, V. Volotchaev, and T.T.M. Palstra. New J. Phys. **6**, 153 (2004). 116
- [280] J.B. Goodenough, A. Wold, R.J. Arnott, and N. Menyuk. Phys. Rev. **124**, 373 (1961). 116
- [281] E.O. Wollan and W.C. Koehler. Phys. Rev. **100**, 545 (1955). 116
- [282] S. Ishihara, J. Inoue, and S. Maekawa. Phys. Rev. B **55**, 8280 (1997). 116
- [283] D. Senff. diploma thesis, Universität zu Köln (2003). 116

-
- [284] F. Moussa, M. Hennion, J. Rodriguez-Carvajal, H. Moudden, L. Pinsard, and A. Revcolevschi. *Phys. Rev. B* **54**, 15149 (1996). 116, 117
 - [285] Private communication, D. Senff (2006). 117
 - [286] K. Hirota, N. Kaneko, A. Nishizawa, and Y. Endoh. *J. Phys. Soc. Japan* **65**, 3736 (1996). 117
 - [287] D. Meier. diploma thesis, Universität zu Köln (2006). 117, 118, 120, 121, 122, 139, 141, 160
 - [288] M. Paraskevopoulos, F. Mayr, J. Hemberger, A. Loidl, R. Heichele, D. Maurer, V. Muller, A.A. Mukhin, and A.M. Balbashov. *J. Phys. – Condens. Matter* **12**, 3993 (2000). 117
 - [289] T. Kimura, G. Lawes, T. Goto, Y. Tokura, and A.P. Ramirez. *Phys. Rev. B* **71**, 224425 (2005). 117, 139, 140, 143
 - [290] N. Aliouane, D.N. Argyriou, J. Strempfer, I. Zegkinoglou, S. Landsgesell, and M.v. Zimmermann. *Phys. Rev. B* **73**, 020102 (2006). 117
 - [291] J. Baier, D. Meier, K. Berggold, J. Hemberger, A. Balbashov, J.A. Mydosh, and T. Lorenz. *Phys. Rev. B* **73**, 100402(R) (2006). 117, 118, 119, 140, 157
 - [292] M. Kenzelmann, A.B. Harris, S. Jonas, C. Broholm, J. Schefer, S.B. Kim, C.L. Zhang, S.-W. Cheong, O.P. Vajk, and J.W. Lynn. *Phys. Rev. Lett.* **95**, 087206 (2005). 117
 - [293] T. Kimura, S. Ishihara, H. Shintani, T. Arima, K.T. Takahashi, K. Ishizaka, and Y. Tokura. *Phys. Rev. B* **68**, 060403(R) (2003). 117
 - [294] S. Quezel, F. Tcheou, J. Rossat-Mignoda, G. Quezel, and E. Roudaut. *Physica B* **86-88**, 916–918 (1977). 117
 - [295] J. Zukrowski, M. Wasniowska, Z. Tarnawski, J. Przewoznik, J. Chmista, A. Kozłowski, K. Krop, and M. Sawicki. *Acta Physica Polonica B* **34**, 1533–1535 (2003). 117
 - [296] T. Goto, Y. Yamasaki, H. Watanabe, T. Kimura, and Y. Tokura. *Phys. Rev. B* **72**, 220403(R) (2005). 117
 - [297] J.-S. Zhou, J.B. Goodenough, J.M. Gallardo-Amores, E. Morán, M.A. Alario-Franco, and R. Caudillo. *Phys. Rev. B* **74**, 014422 (2006). 117, 118
 - [298] A.M. Balbashov, S.G. Karabashev, Y.M. Mukovskiy, and S.A. Zverkov. *J. Crystal Growth* **167**, 365 (1996). 118
 - [299] A.A. Mukhin, V.Y. Ivanov, V.D. Travkin, and A.M. Balbashov. *J. Magn. Magn. Mat.* **226**, 1139 (2001). 120
 - [300] J.G. Cheng, Y. Sui, Z.N. Qian, Z.G. Liu, J.P. Miao, X.Q. Huang, Z. Lu, Y. Li, X.J. Wang, and W.H. Su. *Sol. State Commun.* **134**, 381 (2005). 121, 122
 - [301] S. Stark. diploma thesis, Universität zu Köln (in Vorbereitung). 122
 - [302] M. Kriener. diploma thesis, Universität zu Köln (2001). 122, 183

- [303] Private communication, J. Hemberger (2006). 127
- [304] R. Kajimoto, H. Yoshizawa, H. Shintani, T. Kimura, and Y. Tokura. Phys. Rev. B **70**, 012401 (2004). 132, 134, 141
- [305] K. Kawasaki. Prog. Theor. Phys. **29**, 801 (1963). 135, 136
- [306] H. Stern. J. Phys. Chem. Solids **26**, 153 (1965). 135, 136
- [307] Private communication, J. Hemberger (2006). 135
- [308] J.-Q. Yan, J.-S. Zhou, and J.B. Goodenough. Phys. Rev. B **70**, 014402 (2004). 137
- [309] A.I. Pankrats, G.A. Petrakovskii, L.N. Bezmaternykh, and O.A. Bayukov. Sov. Phys. JETP **99**, 766 (2004). 160
- [310] A.K. Zvezdin, S.S. Krotov, A.M. Kadomtseva, G.P. Vorob'ev, Y.F. Popov, A.P. Pyatakov, L.N. Bezmaternykh, and E.A. Popova. JETPL **81**, 272 (2005). 160
- [311] F. Yen, B. Lorenz, Y.Y. Sun, C.W. Chu, L.N. Bezmaternykh, and A.N. Vasiliev. Phys. Rev. B **73**, 054435 (2006). 160
- [312] S.A. Klimin, D. Fausti, A. Meetsma, L.N. Bezmaternykh, P.H.M. van Loosdrecht, and T.T.M. Palstra. Acta. Cryst. B **61**, 481 (2005). 160
- [313] A.M. Kadomtseva, Yu.F. Popov, G.P. Vorob'ev, K.I. Kamilov, A.P. Pyatakov, V.Yu. Ivanov, A.A. Mukhin, and A.M. Balbashov. Sov. Phys. JETP Lett. **81**, 22–26 (2005). 160
- [314] R.Z. Levitin, E.A. Popova, R.M. Chtsherbov, A.N. Vasiliev, M.N. Popova, E.P. Chukalina, S.A. Klimin, P.H.M. van Loosdrecht, D. Fausti, and L.N. Bezmaternykh. Sov. Phys. JETP Lett. **79**, 423 (2004). 160
- [315] A.D. Balaev, L.N. Bezmaternykh, I.A. Gudim, V.L. Temerov, S.G. Ovchinnikov, and S.A. Kharlamova. J. Magn. Magn. Mat. **258**, 532 (2003). 160
- [316] A.N. Vasiliev, E.A. Popova, L.N. Bezmaternykh, V.L. Temerov, and Z. Hiroi. Sov. Phys. JETP **102**, 262 (2006). 160
- [317] J.-S. Zhou, J.-Q. Yan, and J.B. Goodenough. J. Magn. Magn. Mat. **300**, 382 (2006). 162
- [318] T. Lorenz, M. Hofmann, M. Gruninger, A. Freimurth, G.S. Uhrig, M. Dumm, and M. Dressel. Nature **418**, 614 (2002). 163
- [319] T. Lorenz, M. Hofmann, M. Gruninger, A. Freimurth, G.S. Uhrig, M. Dumm, and M. Dressel. Nature **440**, 707 (2006). 163
- [320] S. Jodlauk. diploma thesis, Universität zu Köln (2005). 183
- [321] H. Hartmann. diploma thesis, Universität zu Köln (2005). 183
- [322] M.A. Zittartz. PhD thesis, Universität zu Köln (2003). 185

Publikationsliste

Teilpublikationen dieser Arbeit

1. **Evidence for large magnetic heat current in insulating layered cuprates**
M. Hofmann, T. Lorenz, K. Berggold, M. Grüninger, A. Freimuth, G.S. Uhrig, and E. Brück
Physical Review B **67**, 184502 (2003)
2. **Magnetic heat transport in R_2CuO_4 with $R = La, Pr, Nd, Sm, Eu$, and Gd**
K. Berggold, T. Lorenz, J. Baier, M. Kriener, D. Senff, H. Roth, A. Severing, H. Hartmann, A. Freimuth, S. Barilo, and F. Nakamura
Physical Review B **73**, 104430 (2006)
3. **Thermal conductivity of R_2CuO_4 , with $R = La, Pr$ and Gd**
K. Berggold, T. Lorenz, J. Baier, M. Kriener, D. Senff, S. Barilo, and A. Freimuth
Physica B **378**, 1064 (2006)
4. **Thermal Conductivity, thermopower, and figure of merit of $La_{1-x}Sr_xCoO_3$**
K. Berggold, M. Kriener, C. Zobel, A. Reichel, M. Reuther, R. Müller, A. Freimuth, and T. Lorenz
Physical Review B **72**, 155116 (2005)
5. **Uniaxial pressure dependencies of the phase transitions in $GdMnO_3$**
J. Baier, D. Meier, K. Berggold, J. Hemberger, A. Balbashov, J.A. Mydosh, and T. Lorenz
cond-mat/0605515, akzeptiert bei Journal of Magnetism and Magnetic Materials (Proceedings of ICM'06)
6. **Hysteresis effects in the phase diagram of multiferroic $GdMnO_3$**
J. Baier, D. Meier, K. Berggold, J. Hemberger, A. Balbashov, J.A. Mydosh, and T. Lorenz
Physical Review B **73**, 100402(R) (2006)
7. **Tagungsbeiträge zu**
 - Frühjahrstagungen der Deutschen Physikalischen Gesellschaft, Arbeitskreis Festkörperphysik in den Jahren 2003 bis 2006
 - International Workshop of SFB 608 on *Strongly Correlated Transition Metal Compounds*, Köln, 2003
 - The International Conference on Strongly Correlated Electron Systems (SCES), Wien, 2005
 - Joint Symposium of SFB 608 and „Graduiertenkolleg“ 549 on *Functional Transition Metal Compounds & Multiferroics*, Köln, 2005
 - DPG - spring meeting of the Division Condensed Matter and EPS - 21st General Conference of the Condensed Matter Division, Dresden, 2006

Weitere Publikationen

1. **Structure, magnetization, and resistivity of $\text{La}_{1-x}\text{M}_x\text{CoO}_3$ ($M=\text{Ca}$, Sr , and Ba)**
M. Kriener, C. Zobel, A. Reichl, J. Baier, M. Cwik, K. Berggold, H. Kierspel, O. Zabara, A. Freimuth, and T. Lorenz
Physical Review B **69**, 094417 (2004)
2. **Magnetoresistance, specific heat and magnetocaloric effect of equiatomic rare-earth transition-metal magnesium compounds**
H. Hartmann, K. Berggold, S. Jodlauk, I. Klassen, K. Kordonis, T. Fickenscher, R. Pöttgen, A. Freimuth, and T. Lorenz.
Journal of Physics - Condensed Matter **17**, 7731 (2005).

Danksagung

An dieser Stelle möchte ich allen danken, die zum Erfolg dieser Arbeit und zu einer schönen Zeit beigetragen haben.

Bei Herrn Prof. Freimuth möchte ich mich bedanken, dass er mir es ermöglicht hat, diese Arbeit anzufertigen. Seine Vorlesung hat mich einst in die Festkörperphysik gebracht, und durch sein Engagement für den SFB hat er hervorragende Bedingungen für das Anfertigen dieser Arbeit geschaffen. Insbesondere möchte ich mich dafür bedanken, dass er mir bei meinem Wunsch nach einem Auslandsaufenthalt sehr behilflich war und mir sehr interessante sechs Monate in San Diego ermöglicht hat.

Herrn Prof. Mydosh danke ich für sein großes Engagement als Lehrstuhlvertreter.

Mein ganz besonderer Dank gilt Thomas Lorenz für seinen unermüdlichen Einsatz im Dienste der Wissenschaft, ohne den ich um einiges unwissender wäre. „Gib mir mal nen Zettel...“ endete meistens in vielen Zetteln, die auf weit verzweigte Weise oft schon die Lösung des Problems enthielten. Insbesondere möchte ich auch für die sehr hilfreichen Korrekturen¹, auch zu den unmöglichsten Zeiten („Ich les das noch.“) danken, (samt den anschaulichen Beispielen), ohne die die Arbeit wohl mehr eine Art Stilblütensammlung wäre (mit sprechenden Tabellen usw).

Herrn Prof. Braden danke ich für die Bereitschaft das Gutachten zu erstellen, und für diverse Erklärungen zu den Kupraten (was sind das denn für Striche an den m's?).

Herrn Prof. Rosch danke ich für die Bereitschaft, das zweite Gutachten zu erstellen.

Joachim Hemberger danke ich für Proben, Daten, und die vielen bunten Bilder die daraus resultiert sind

I would like to thank Prof. Maple for the opportunity to work in his lab and for an very interesting time at the UCSD.

Maurits Haverkort danke ich für die geduldige Einführung in das „CFT“ package, und für die Gabe und die Bereitschaft die Physik dahinter so schön zu erklären, dass auch „Laien“ was verstehen.

I'd like to thank Alexandr Sologubenko for the very helpful discussions about the interpretation of the data.

Meinem treuen Gegenüber seit... ich weiß nicht vielen Jahre, Jörg Baier, gilt mein persönlicher Dank für eine tolle Zeit, viele lustige Momente, das Segeln, für unzählige Ratschläge in allen Lebenslagen, die Kunst des Reklamierens, die Hilfsbereitschaft in jeder Hinsicht, die gute Laune, und die Liste ließe sich endlos fortführen.

Auch meinen anderen Bürogefährten möchte ich für das beste Büro überhaupt danken, Eva für ihre (immer freundliche) Abwehr von meinem auswucherndem Blätterwald, diversen Hilfen bei „schwierigsten“ Rechnungen, ..., Reinhard danke ich für die immer wieder neuen (fast) nobelpreiswürdigen Ideen und für ausführlichste Erläuterungen zur Gruppentheorie im allgemeinen und im besonderen ... nur den Kobold der immer die Stifte der Anderen stiehlt, den hab ich leider nie erwischt.

¹Hierbei danke ich auch für das Durchgehenlassen des 4004-Niveausystems.

Dem Botschafter der Wahrheit, Niko Johannsen danke ich für großartige Ideen die Welt zu verbessern, die Wahrheit, und für apt-get install.

Chrischtina Hilgers danke ich für für diverse nette Schwätzchen, kleine „Gemeinheiten“, und fürs Grillen.

Alex Gößling danke ich für Mathematica-Hilfen, den Ringaustausch, und sonntägliche Kaffeepausen.

Kostas Kordonis danke ich für die Einführung in die Transportmesserei, und für Fishermans und Obst.

Markus Kriener danke ich für die Hilfsbereitschaft in vielen Dingen, und seit neuestem dem Bericht aus Fernost.

Olli Heyer danke ich, dass ich das tolle Dilatometer auch mal benutzen durfte, und dafür das es so robust ist.

Den Werkstätten und Angestellten des Instituts danke ich für die Anfertigung von vielerlei Dingen, die Reparaturen, das Helium, die Erledigung des Papierkrams, und für vieles mehr.

Carmen Handels danke ich für die allmorgendliche freundliche Begrüßung, und ihre Hilfsbereitschaft in all den kleinen wichtigen Alltagsdingen.

Allen nicht namentlich genannten gegenwärtigen und ehemaligen Mitgliedern des zweiten Institutes sei für die vielen Hilfestellungen in vielerlei Hinsicht gedankt.

Den guten Kaffee- und Wasser-geistern dank ich für die lebenswichtigen Getränke.

Der anderen Seite des Ganges, Matthias Cwik, Daniel Senff, Olaf Schumann und Paul Steffens danke ich für viele Hilfen auf den Gebieten Computer, Manganante, Neutronen, Flowerpower, Kobaltate, Hirn, und vieles mehr.

To the Maple group: Thanks for the nice time!

Dano: Thanks for the friendship and all the fun stuff!

Der DPG danke ich dafür, dass die Frühjahrstagungen meistens nicht in Regensburg stattgefunden haben.

Sebastian Stark danke ich für die abendlichen Spaziergänge und fürs Gute-Nacht sagen.

den Radfahrern danke ich für schnelle Dienstagsrunden und eine tolle Alpentour (das waren doch die Alpen, oder???)

Den Kletterern dank ich für das Radfahrersatzprogramm (was keine Latexabart ist)

Thomas Fuchs danke ich für die tolle Zusammenarbeit während des Physikstudiums.

Dank gilt auch Annette, Anne, Albert, Aleks, Arnd, Claudi, Doris, Eva, Frank, Jens, Jiri, Michael, Roswitha, Sandra, Thorsten, Yvonne, Wolfgang; für schöne Jahre.

Meinen Brüdern Malte, Lars und Jan danke ich für die schönen (leider viel zu seltenen) Besuche.

Meinen Eltern danke ich für die Unterstützung und dafür dass sie mir diesen Lebensweg möglich gemacht haben.

Mein ganz besonderer Dank geht an Anja, für alles.

Offizielle Erklärung

Ich versichere, dass ich die von mir vorgelegte Dissertation selbständig angefertigt, die benutzten Quellen und Hilfsmittel vollständig angegeben und die Stellen der Arbeit - einschließlich Tabellen, Karten und Abbildungen -, die anderen Werken im Wortlaut oder dem Sinn nach entnommen sind, in jedem Einzelfall als Entlehnung kenntlich gemacht habe; dass diese Dissertation noch keiner anderen Fakultät oder Universität zur Prüfung vorgelegen hat; dass sie - abgesehen von den in der Publikationsliste angegebenen Teilpublikationen - noch nicht veröffentlicht worden ist sowie, dass ich eine solche Veröffentlichung vor Abschluss des Promotionsverfahrens nicht vornehmen werde. Die Bestimmungen dieser Promotionsordnung sind mir bekannt. Die von mir vorgelegte Dissertation ist von Prof. Dr. A. Freimuth betreut worden.

Köln, den 28. September 2006

Kai Berggold

Zusammenfassung

Gegenstand der vorliegenden Arbeit ist die Untersuchung der thermischen Transporteigenschaften dreier Klassen von Übergangsmetalloxiden: Kupraten, Kobaltaten und Manganaten. Die geschichteten Kuprate $R_2\text{CuO}_4$ mit $R = \text{La, Pr, Nd, Sm, Eu}$ und Gd zeigen eine ungewöhnliche Wärmeleitfähigkeit κ . Zwei Maxima werden für κ als Funktion der Temperatur für einen Wärmestrom entlang der CuO_2 -Ebenen beobachtet, während für einen Wärmestrom senkrecht zu den CuO_2 -Ebenen nur ein konventionelles phononisches Tieftemperaturmaximum auftritt. Es wird gezeigt, dass das Hochtemperaturmaximum durch Wärmetransport magnetischer Anregungen auf dem CuO_2 Quadratgitter verursacht wird. Ein weiteres Ergebnis ist, dass das komplexe Tieftemperatur- und Magnetfeldverhalten von κ in Nd_2CuO_4 am wahrscheinlichsten durch zusätzliche Phononenstreuung verursacht wird anstatt durch magnonischen Wärmetransport, wie es in der Literatur vorgeschlagen wurde. In den Kobaltaten $R\text{CoO}_3$ mit $R = \text{La, Pr, Nd}$ und Eu wird ein temperaturgetriebener Spinübergang der Co^{3+} -Ionen beobachtet. Es wird gezeigt, dass die zusätzliche Gitterunordnung durch die zufällige Verteilung der besetzten angeregten Spinzustände eine starke Unterdrückung der Wärmeleitfähigkeit von LaCoO_3 für Temperaturen oberhalb von 25 K verursacht. Dieser Effekt ist in NdCoO_3 und PrCoO_3 wegen der größeren Spin-Anregungslücke viel schwächer ausgeprägt. Eine quantitative Analyse wird durchgeführt, basierend auf EuCoO_3 als Referenzsubstanz. Ein wesentliches Ergebnis ist, dass statische Unordnung ausreicht die Unterdrückung von κ zu erklären. Eine dynamische Jahn-Teller Verzerrung, wie sie in der Literatur vorgeschlagen wurde, ist nicht notwendig um die Stärke der Streuung zu beschreiben. Unterhalb von 25 K wird κ im wesentlichen durch resonante Streuung an paramagnetischen Verunreinigungszuständen bestimmt, welche z.B. durch nicht stöchiometrischen Sauerstoffgehalt verursacht werden können. Eine derartige Unterdrückung der Wärmeleitfähigkeit durch resonante Streuprozesse ist z.B. von Holmiumethylsulfat bekannt. Dieser Effekt ist in LaCoO_3 am ausgeprägtesten, vermutlich durch die Bildung magnetischer Polaronen. In den dotierten $\text{La}_{1-x}\text{Sr}_x\text{CoO}_3$ Verbindungen mit $0 \leq x \leq 0.25$ wird eine große Thermokraft, eine niedrige Wärmeleitfähigkeit und ein nennenswerter thermoelektrischer Nutzfaktor gefunden. Hier wird κ in Folge der durch Sr-Substitution induzierten magnetischen Polaronen stark unterdrückt, wogegen die große Thermokraft durch einen großen Entropiebeitrag verursacht wird, der durch die unterschiedlichen Spinzustände von Co^{3+} und Co^{4+} zustande kommt. In den orthorhombischen Manganaten NdMnO_3 und TbMnO_3 werden komplexe Temperatur- und Magnetfeldabhängigkeiten von κ beobachtet. In Kombination mit magnetfeldabhängigen Messungen der thermischen Ausdehnung wird gezeigt, dass der dominierende Effekt, der κ beeinflusst, durch resonante Streuung an $4f$ -Momenten gegeben ist. Sowohl die komplexe magnetische Struktur von TbMnO_3 bei tiefen Temperaturen als auch die Ferroelektrizität scheinen nur einen schwachen Einfluss auf die Wärmeleitfähigkeit zu haben.

Abstract

The subject of this thesis is the investigation of the thermal transport properties of three classes of transition-metal oxides: Cuprates, cobaltates, and manganites.

The layered cuprates $R_2\text{CuO}_4$ with $R = \text{La, Pr, Nd, Sm, Eu, and Gd}$ show an anomalous thermal conductivity κ . Two maxima of κ are observed as a function of temperature for a heat current within the CuO_2 planes, whereas for a heat current perpendicular to the CuO_2 planes only a conventional phononic low-temperature maximum of κ is present. Evidence is provided that the high-temperature maximum is caused by heat-carrying excitations on the CuO_2 square lattice. Moreover, it is shown that the complex low-temperature and magnetic-field behavior of κ in Nd_2CuO_4 is most likely caused by additional phonon scattering rather than by heat-carrying Nd magnons, as it was proposed in the literature. In the cobaltates $R\text{CoO}_3$ with $R = \text{La, Pr, Nd, and Eu}$, a temperature-induced spin-state transition of the Co^{3+} ions occurs. It is shown that the additional lattice disorder caused by the random distribution of populated higher spin states causes a large suppression of the thermal conductivity of LaCoO_3 for $T > 25 \text{ K}$. The effect is much weaker in PrCoO_3 and NdCoO_3 due to the increased spin gap. A quantitative analysis of the responsible mechanisms based on EuCoO_3 as a reference compound is provided. A main result is that the static disorder is sufficient to explain the suppression of κ . No dynamical Jahn-Teller distortion, as proposed in the literature, is necessary to enhance the scattering strength. Below 25 K, κ is mainly determined by resonant phonon scattering on paramagnetic impurity levels, e.g. caused by oxygen non-stoichiometry. Such a suppression of the thermal conductivity by resonant scattering processes is e.g. known from Holmium ethylsulfate. This effect is most pronounced in LaCoO_3 , presumably due to magnetic polaron formation. In the doped compounds $\text{La}_{1-x}\text{Sr}_x\text{CoO}_3$ with $0 \leq x \leq 0.25$, a large thermopower, a low thermal conductivity, and a considerable large thermoelectric figure of merit is found. Here, κ is strongly suppressed by the Sr-induced magnetic polarons, whereas the large thermopower arises from a large entropy contribution due to the different spin states of Co^{3+} and Co^{4+} . In the orthorhombic manganites NdMnO_3 and TbMnO_3 complex temperature and field dependencies of κ are observed. In combination with magnetic-field dependent thermal expansion measurements it is shown that the dominating effect determining κ is resonant phonon scattering by the $4f$ orbitals of the R^{3+} ions. The complicated magnetic structure of TbMnO_3 at low temperature as well as the ferroelectricity has only a minor influence on the thermal conductivity.

Lebenslauf

Kai Berggold

Adresse
Vogelsanger Str. 64
50823 Köln

Geburtsdatum
14. 03. 1975
Geburtsort
Rottweil
Familienstand
ledig

Schulausbildung

1981 - 1985
Grundschule, Rottweil
1985 - 1994
Droste-Hülshoff-Gymnasium, Rottweil
Juli 1994
Abitur

Wehrdienst

Juli 1994 - Juni 1996

Studium

Oktober 1996 - März 2003
Physik-Studium an der Universität zu Köln
März 2002 - März 2003
Diplomarbeit bei Prof. Dr. A. Freimuth
II. Physikalisches Institut, Universität zu Köln
Thema: Wärmetransport in den Übergangsmetalloxiden
 $R\text{CoO}_3$ ($R=\text{La, Eu}$) und $R_2\text{CuO}_4$ ($R=\text{La, Pr, Nd, Gd}$)

Promotion

März 2003 - Dezember 2006
Promotion bei Prof. Dr. A. Freimuth
II. Physikalisches Institut, Universität zu Köln
Thema: Thermal Transport in
Cuprates, Cobaltates, and Manganites
Februar 2004 - August 2004
Forschungsaufenthalt bei
Prof. M. B. Maple
University of California, San Diego